



**HAL**  
open science

# Implication of LXRs in the myelination of the peripheral nervous system

Tatiana El Jalkh

► **To cite this version:**

Tatiana El Jalkh. Implication of LXRs in the myelination of the peripheral nervous system. Neuro-science. Université Paris Cité, 2021. English. NNT : 2021UNIP5026 . tel-04147754

**HAL Id: tel-04147754**

**<https://theses.hal.science/tel-04147754v1>**

Submitted on 1 Jul 2023

**HAL** is a multi-disciplinary open access archive for the deposit and dissemination of scientific research documents, whether they are published or not. The documents may come from teaching and research institutions in France or abroad, or from public or private research centers.

L'archive ouverte pluridisciplinaire **HAL**, est destinée au dépôt et à la diffusion de documents scientifiques de niveau recherche, publiés ou non, émanant des établissements d'enseignement et de recherche français ou étrangers, des laboratoires publics ou privés.

# Université de Paris

École doctorale [Médicament Toxicologie Chimie Imagerie- MTCI ED 563](#)

*Laboratoires*      [INSERM 1124 – Toxicité Environnementale, Cibles  
Thérapeutiques, Signalisation Cellulaire et Biomarqueurs  
EC2M, Faculté des Sciences, Fanar, Liban](#)

## *Implication of LXRs in the myelination of the peripheral nervous system*

Par Tatiana EL JALKH

Thèse de doctorat de [Neurosciences](#)

Dirigée par Pr. Sophie BERNARD  
Et par Dr. Frédéric HARB

Présentée et soutenue publiquement le [01/07/2021](#)

Devant un jury composé de :

Michael SCHUMACHER, DR, Université Paris Saclay, Rapporteur

Jean-Marc LOBACCARO, PU, Université de Clermont Auvergne, Rapporteur

Olivier LAPREVOTE, PU-PH, Université de Paris, Examineur

Amalia TROUSSON, MCU, Université de Clermont Auvergne, Examinatrice

Robert FLEDERICH, Group Leader, University of Leipzig, Examineur

Adina-Nicoleta LAZAR, MCU, INSA Lyon, Université de Lyon, Examinatrice

Frédéric HARB, MCU, Université Libanaise, Co-directeur de thèse

Sophie BERNARD, PU, Université de Paris, Directrice de thèse



Except where otherwise noted, this is work licensed under  
<https://creativecommons.org/licenses/by-nc-nd/3.0/fr/>

## ACKNOWLEDGMENTS

I would like to start by expressing my deepest gratitude towards my thesis Director Pr. Sophie Bernard who has been a great mentor, and simply a person to look up to. Thank you for always pushing me forward, for your support and guidance.

I express my deepest thanks to my thesis director Dr. Frédéric Harb. Thank you for being a great mentor, for always being available for scientific discussions and for your constant motivation and support.

I would like to thank Pr. Robert Barouki for welcoming me in the U1124 T3S and would like to extend special thanks to Pr. Charbel Massaad who has welcomed me in his team. Thank you for all the scientific discussions around the LXR project and for always being available to help. Additionally I would like to thank Pr. Roland Habchi for welcoming me in the EC2M lab.

I would like to sincerely thank the jury members for their time and efforts in reviewing my thesis.

Thank you for all the team members of the T3S team and EC2M team who have been of great help with experiments and discussions; Dr. Zied Ferjaoui, Dr. Hugo Salmon, Dr. Christel Becker, Dr. Delphine Meffre, Pr. Mehrnaz Jafarian-Tehrani, Dr. Anne Simon, Céline Becker, Dr. Damien Le Menuet, Fatima El Ouazzani and Julia Montanaro and my intern Perla Khoueiry. Special thanks to Dr. Julien Grenier for all the scientific discussions and for his positivity.

Thank you to the PhD students Venkat Krishnan Sundaram, Rasha Barakat, Aïda Padilla-Ferrer, Julia Fath and Alex Carreté who have made this journey unforgettable, thank you for all the laughs, support and motivation. Special thanks goes to Venkat Krishnan Sundaram for his immeasurable help during the whole PhD journey and Rasha Barakat for being there for me on a daily.

Additionally, I would like to thank Pr. Frédéric Charbonnier and his team members for being the extended version of our lab and for their immense help during my thesis, special thanks to Dr. Olivier Biondi and Mirella El Khoury.

Last but not Least I would like to thank my family and friends for their love and support.

To my parents Ghazi and Hoda and my sister Lina, thank you for believing in me and for all the sacrifices you made for me to be where I am at, I dedicate this work to you.

I would like to thank my grandmother and role model Rahil, the most hardworking life loving person I know. I wish you could have attended my thesis defense but I know you are watching from up above.

I would like to thank my partner Maher, you mean the world to me, thank you for your love, endless support and for being there every step at a time throughout this whole journey.

## RESUME DE THESE

La gaine de myéline est une couche isolante formée par les cellules gliales autour des axones. Elle est essentielle au bon fonctionnement du système nerveux ; notamment en isolant l'axone, en augmentant la vitesse de l'influx nerveux par conduction saltatoire et en assurant un support trophique aux axones.

Les cellules de Schwann (SC) et les oligodendrocytes sont respectivement les cellules gliales responsables de la myélinisation du système nerveux périphérique et central. Dans cette étude, nous nous intéressons au système nerveux périphérique, par la suite nous aborderons uniquement le rôle des cellules de Schwann dans la formation de la gaine de myéline. La lignée Schwannienne doit passer par différentes étapes de développement pour se différencier en cellules de Schwann myélinisantes ou non myélinisantes. Chaque cellule de Schwann myélinisante s'associe avec un seul axone et enroule sa membrane plasmique autour de l'axone plusieurs fois pour former la gaine de myéline.

Cette dernière possède une composition très particulière : environ 70 % des constituants de la membrane plasmique sont des lipides - spécialement enrichis en cholestérol et en phospholipides - et 30% des constituants sont des protéines. Le processus de myélinisation est étroitement régulé, donc des altérations de l'expression des gènes impliqués dans ce processus peuvent engendrer des conséquences sur la myélinisation du système nerveux.

Les LXRs (Liver X Receptors) sont des récepteurs nucléaires, initialement considérés comme récepteurs orphelins. Il a finalement été montré que les oxystérols endogènes – qui sont des formes oxydées du cholestérol – pouvaient lier et activer ces récepteurs qui existent sous deux isoformes : LXR  $\alpha$  (NR1H3) et LXR  $\beta$  (NR1H2). Le LXR  $\beta$  est exprimé de manière ubiquitaire tandis que le LXR  $\alpha$  est principalement exprimé dans la rate, la glande surrénale, les intestins, le tissu adipeux, les macrophages, les poumons et les reins. Les LXRs ont plusieurs fonctions mais ils régulent surtout l'homéostasie du cholestérol, la lipogenèse et l'inflammation. Les LXRs sont impliqués dans de nombreuses maladies métaboliques et neurodégénératives du système nerveux central et périphérique. L'évaluation du rôle du LXR dans la myélinisation serait cruciale pour comprendre son implication dans l'initiation et la régulation de ce processus complexe qui nécessite la biosynthèse de quantités importantes de cholestérol et de phospholipides.

Des études antérieures, menées par notre équipe, ont montré que les mutants totaux  $LXR\alpha/\beta^{-/-}$  présentent une dérégulation de l'expression des protéines de la myéline, des gaines de myéline plus minces et des niveaux de stress oxydatif élevés. Par contre, le modèle mutant utilisé - invalidé pour les  $LXR\alpha$  et  $\beta$  - ne dévoile pas la cause exacte de ces modifications.

Cependant, plusieurs questions doivent être abordées : Quelle est l'origine de ces conséquences ? Est-elle neuronale ou Schwannienne ? Quel est l'isoforme fonctionnel dans le système nerveux périphérique ?

Etant intéressés par la myélinisation du système nerveux périphérique - assuré par les cellules de Schwann - et ayant obtenu des résultats préliminaires qui suggèrent que le  $LXR\beta$  est l'isoforme prédominant et fonctionnel dans le système nerveux périphérique, notre équipe a conçu un modèle murin spécifique, invalidant cet isoforme uniquement dans les cellules de Schwann. Ce modèle est réalisé en croisant des souris transgéniques floxées  $LXR\beta$  avec des souris exprimant la Cre recombinase sous le contrôle du promoteur Desert Hedgehog (Dhh). La reconnaissance des sites flox et la délétion du  $LXR\beta$  se fait alors par la Cre recombinase qui est sous le contrôle de l'expression du Dhh spécifique des cellules de Schwann dans le système nerveux périphérique et exprimé à partir du jour embryonnaire 12.5.

L'invalidation spécifique du  $LXR\beta$  ( $LXR\beta$  SC KO) dans la cellule de Schwann a engendré un phénotype grave et inattendu qui ne ressemble pas aux conséquences subtiles de l'invalidation totale des deux isoformes  $\alpha$  et  $\beta$ .

Par conséquent, nous avons cherché à comprendre les conséquences du  $LXR\beta$  SC KO sur l'intégrité structurale, les propriétés biophysiques et biochimiques des nerfs sciatiques. Ainsi, les principaux axes abordés dans cette étude sont les conséquences de l'ablation spécifique de  $LXR\beta$  dans les cellules de Schwann sur :

- Le comportement des souris, la conduction nerveuse et la myélinisation.
- L'organisation structurelle du nerf sciatique et les propriétés biophysiques des fibres nerveuses.

- La composition lipidique du nerf sciatique et l'effet de l'inactivation du LXR $\beta$  spécifiquement dans les cellules de Schwann sur l'homéostasie du cholestérol et des lipides.
- Et finalement, l'évaluation des causes probables conduisant à ce phénotype.

Nos résultats montrent de graves déficits comportementaux et locomoteurs mis en évidence chez les souris LXR $\beta$  SC KO par différents tests comportementaux. Les images de microscopie électronique dévoilent la présence de très peu d'axones myélinisés dans les nerfs sciatiques de souris LXR $\beta$  SC KO à 8 semaines. Des mesures électrophysiologiques par CMAP (Compound Muscle Action Potential) ont mis en évidence une altération marquée de la conduction nerveuse.

Le profil topographique obtenu par microscopie à force atomique (AFM) a montré que le diamètre apparent des fibres nerveuses LXR $\beta$  SC KO est plus petit que celui des contrôles. Par contre, les résultats des mesures de forces, réalisés également par AFM, sont inattendus et montrent que les propriétés mécaniques des fibres nerveuses ne sont pas affectées chez les souris LXR $\beta$  SC KO. La présence d'un nombre réduit de fibres myélinisées chez les souris LXR $\beta$  SC KO, observé par immuno-marquage, pourrait expliquer la différence entre les diamètres apparents des deux groupes, par contre la myélinisation ne s'avère pas corrélée à l'élasticité des fibres nerveuses. Les résultats des études publiées récemment nous ont incités à évaluer l'implication de la matrice extracellulaire et de la lame basale dans la préservation de l'intégrité des fibres nerveuses après compression. L'implication de la lame basale n'est pas valide dans nos conditions puisqu'on observe un nombre très réduit de fibres nerveuses myélinisées dans les nerfs de souris LXR $\beta$  SC KO. Alors, nous avons commencé par évaluer la teneur en collagène du nerf sciatique – le composant majeur de la matrice extracellulaire – qui s'est révélé être être très significativement augmentée chez les souris LXR $\beta$  SC KO. Cette concentration élevée de collagène pourrait être le facteur responsable du maintien de la rigidité similaire dans les deux groupes et donc de l'intégrité des fibres nerveuses.

Nous avons ensuite évalué la possibilité de l'implication des autres composants cellulaires du nerf sciatique afin de maintenir l'intégrité des fibres nerveuses. Nous avons premièrement évalué la présence de cellules endoneuriales, connues pour leur contribution à l'expression du collagène. L'immuno-marquage de Thy1, une protéine permettant l'identification des cellules endoneuriales,

est plus visible dans les nerfs sciatiques LXR $\beta$  SC KO. Ceci pourrait expliquer l'augmentation du dépôt de collagène dans les nerfs sciatiques des souris LXR $\beta$  SC.

L'implication d'une autre composante a également été remise en cause. Sur la base des observations faites en microscopie électronique, nous avons remarqué des faisceaux nerveux plus petits entourés par un type cellulaire inhabituel qui ressemble aux cellules périneuriales. Ainsi, nous avons immuno-marqué ZO-1, un marqueur pour les cellules périneuriales dans le système nerveux périphérique. A notre grande surprise, l'ensemble du nerf sciatique des souris LXR $\beta$  SC KO semble être restructuré par ces cellules périneuriales qui se sont infiltrées dans l'espace endoneurial. Ces modifications structurales du nerf sciatique pourraient expliquer l'absence de différence entre le module de Young des fibres nerveuses des souris contrôles et LXR $\beta$  SC KO et pourrait être défini comme une tentative de maintien de l'intégrité du nerf.

Nous avons, ensuite, évalué les conséquences de l'inactivation du LXR  $\beta$  spécifiquement dans les cellules de Schwann sur la composition lipidique des nerfs sciatiques par imagerie par spectrométrie de masse ToF-SIMS (Time of Flight Secondary Ion Mass Spectrometry) et observé une diminution drastique de la quantité de cholestérol. La baisse des niveaux d'ARN messagers des enzymes clés impliquées dans la biosynthèse et la régulation du cholestérol, telles que HMGCR (3-hydroxy-3-methylglutaryl-coenzyme A reductase) et SREBP2 (Sterol Regulatory Element Binding Protein 2), a aussi été observée. Par contre, les niveaux d'ARNm d'ABCA1 (ATP Binding Cassette transporter) et d'ApoE (Apolipoprotein), cibles directes du LXR impliquées dans le transport et l'efflux du cholestérol, sont plus élevés dans le nerf sciatique des souris LXR $\beta$  SC KO comparés aux souris contrôles. L'inactivation du LXR $\beta$  spécifiquement dans les cellules de Schwann n'a pas affecté la synthèse et la disponibilité des acides gras dans les nerfs sciatiques. Cependant, la sphingomyéline, un phospholipide enrichi dans la gaine myéline du système nerveux périphérique, est plus abondante dans les nerfs sciatiques des souris LXR $\beta$  SC KO que dans les souris contrôles.

Nos résultats mettent donc en évidence l'altération des propriétés structurales et biochimiques du nerf sciatique en raison de l'inactivation spécifique du LXR $\beta$  ainsi qu'une tentative des composants cellulaires du nerf sciatique de préserver son intégrité en modifiant sa composition.



Nos résultats montrent des conséquences délétères suite à l'invalidation du LXR $\beta$  spécifiquement dans les cellules de Schwann mais quelles sont les éléments qui ont induit ce phénotype très marqué ?

Nous nous sommes donc interrogés sur la présence de cellules de Schwann et leur capacité à myéliniser. Nous avons évalué les niveaux d'expression des ARNm des protéines de la gaine de myéline : PMP22 (Peripheral Myelin Protein) et MPZ (Myelin Protein Zero) dans les nerfs sciatiques des souris LXR $\beta$  SC KO à 8 semaines. Les taux d'expression de ces ARNm sont considérablement réduits ainsi que l'expression des marqueurs cellulaires de la cellule Schwann tels que le S100 $\beta$ , Dhh, SOX10 et Krox20. Ces résultats pourraient expliquer l'absence de myélinisation observée par microscopie électronique. Nous avons de plus évalué la présence des cellules de Schwann myélinisantes en immuno-marquant Krox20 et toutes les cellules de la lignée Schwannienne en marquant SOX10. La présence de cellules Krox20 positives est minime dans les nerfs sciatiques des souris LXR $\beta$  SC KO, ce qui est logique puisque nous avons observé une présence très réduite de fibres nerveuses myélinisées par microscopie électronique et immuno-marquage de MPZ. Par contre, la faible présence de cellules de la lignée Schwannienne positives pour SOX10 est inattendue. Quelles sont les causes pour lesquelles la présence de cellules de Schwann serait autant réduite à 8 semaines et sont-elles présentes à des stades de développement plus précoces ?

Les recherches en cours dans notre laboratoire ont révélé que la présence réduite des cellules de Schwann est même observée au cours des stades précoces de développement (E 18,5). Les co-cultures dissociées de DRG (Dorsal Root Ganglia) à partir d'embryons LXR  $\beta$  SC KO à E13,5 ont révélé que les progéniteurs des cellules de Schwann commencent à se détacher au jour 7 (DIV7) *in vitro*. Afin d'identifier à quel stade de développement les cellules de Schwann à DIV7 correspondent *in vivo*, nous avons étudié l'expression des marqueurs de différenciation de ces dernières au cours du temps. Nous avons montré que la période entre DIV5 et DIV7 correspond à la transition des précurseurs des cellules de Schwann au stade immature et, par conséquent, mis en évidence que le LXR $\beta$  joue un rôle crucial pour leur survie lors de cette transition.

En conclusion, nos résultats dévoilent que le LXR $\beta$  joue un rôle essentiel dans la survie et la différenciation des cellules de Schwann qui sont nécessaires pour le maintien de l'intégrité des nerfs périphériques.

**Mots clés :** Récepteur LXR  $\beta$ , myéline, système nerveux périphérique, homéostasie du cholestérol, cellules de Schwann, cellules périneuriales.

## ABSTRACT

The Liver X Receptors (LXRs) are members of the nuclear receptor superfamily, initially considered as orphan receptors. The discovery of LXR ligands, the endogenous oxysterols, deorphanized LXRs and hinted at their functions. LXR is present in two isoforms: LXR $\alpha$  (NR1H3) and LXR $\beta$  (NR1H2). LXR $\beta$  is ubiquitously expressed while LXR $\alpha$  is mainly expressed in the spleen, adrenal gland, intestines, adipose tissue, macrophages, lung and kidney. LXRs have multiple functions but most importantly they regulate: cholesterol homeostasis, lipogenesis and inflammation. Moreover, LXRs are implicated in many metabolic diseases and neurodegenerative diseases in the Central and Peripheral Nervous Systems.

Previous studies, led by our team, have shown that LXR $\alpha/\beta$ <sup>-/-</sup> total mutants show dysregulation of myelin gene expression, thinner myelin sheaths and elevated oxidative stress levels. LXR $\beta$  has been shown to be the predominant isoform of the LXR in the PNS, therefore we were interested in using a specific knock out model of the LXR $\beta$  isoform uniquely in Schwann cells; the myelinating glia of the PNS. We constructed this mouse model by cross breeding LXR $\beta$  floxed mice with Desert Hedgehog:Cre mice. Therefore, LXR $\beta$  deletion by Cre recombinase was under the control of Desert Hedgehog (Dhh) expression, specific to Schwann cells at Embryonic day 12.5 (E12.5). Surprisingly, the LXR $\beta$  Schwann Cell specific Knock-Out (LXR $\beta$  SC KO) mice manifested severe behavioral and locomotive deficits and the presence of very few myelinated axons. Therefore, we aimed to understand the consequences of LXR $\beta$  SC KO on the structural integrity, biophysical properties and lipid homeostasis of the sciatic nerves. For this reason, electrophysiological measurements were conducted on these nerves and revealed a drastic decrease of nerve conduction. Subsequently, force measurements by atomic force microscopy showed that the mechanical properties of the KO nerve fibers were not affected. Structural reorganization of the sciatic nerve following LXR $\beta$  ablation was put into question in order to explain these results. Increased collagen deposition as well as increased number of Endoneurial Fibroblasts-Like (EFLCs) and the infiltration of perineurial cells into the endoneurial space were all observed in LXR $\beta$  SC KO sciatic nerve. Furthermore, we assessed the lipid composition of the sciatic nerve by Time-of-Flight Secondary Ion Mass Spectrometry and observed an immense decrease in cholesterol levels accompanied with the downregulation of mRNA levels of key enzymes involved in cholesterol biosynthesis and regulation such as HMGCR and SREBP2. Nonetheless, ABCA1

and ApoE mRNA levels, which are LXR direct targets involved in cholesterol transport and efflux, were upregulated in LXR $\beta$  SC KO sciatic nerve. LXR $\beta$  SC KO did not affect fatty acid synthesis and availability in the SNs. However, to our surprise, sphingomyelin, a myelin enriched phospholipid, is more abundant in the sciatic nerves of LXR $\beta$  SC KO mice. Thus, our results highlight the alteration of sciatic nerve structural and biochemical properties due to the specific ablation of LXR $\beta$  and the attempt of SN cellular components in rescuing the sciatic nerve integrity.

We then questioned the presence of Schwann cells and their ability to myelinate. Therefore, we evaluated the expression levels of Peripheral Myelin Protein 22 (PMP22) and Myelin Protein Zero (MPZ) transcripts in the sciatic nerves of LXR $\beta$  SC KO mice and we found that they were drastically reduced as well as Schwann cell markers, explaining the absence of myelination observed by electron microscopy.

The ongoing research in our lab revealed that Schwann cell absence is even observed during earlier developmental stages. DRG dissociated co-cultures from LXR $\beta$  SC KO E13.5 embryos revealed that SC progenitors start detaching at Day 7 *in vitro* (DIV7). In order to identify the SC developmental stage at DIV7, we conducted a study to understand the different SC developmental stages of *in vitro* cultured DRGs. We have shown that the period between DIV5 to DIV7 corresponds to the transition from SC precursors to immature SCs. Consequently, we can conclude that the LXR $\beta$  is of crucial importance during this transition for SC survival, differentiation and maintaining the integrity of the peripheral nerves.

**Key words:** Liver X Receptor  $\beta$ , Myelin, Peripheral Nervous System, Cholesterol Homeostasis, Schwann Cells, Perineurial Cells.

## List of Abbreviations

ABCA1: ATP Binding Cassette Subfamily A Member1

AFM: Atomic Force Microscopy

ANS: Autonomic Nervous System

APOE: Apolipoprotein

BACE1: Beta Secretase 1

BDNF: Brain-derived neurotrophic factor

BL: Basal Lamina

BMP: Bone Morphigenic Protein

cAMP: cyclic Adenosine Monophosphate

CNS: Central Nervous System

CMAP: Compound Muscle Action Potential

DIV: Days *in vitro*

Dhh: Desert Hedgehog

DRG: Dorsal Root Ganglia

ECM: Extracellular Matrix

EFLCs: Endoneurial Fibroblast-like Cells

FA: Fatty Acid

FGF: Fibroblast Growth Factor

GDNF: Glial cell line-derived neurotrophic factor

GFAP: Glial Fibrillary Acidic Protein

HMGCR: 3-Hydroxy-3-Methylglutaryl-CoA Reductase

IGF2: Insulin-like Growth Factor 2

IPL: Intraparodontal Line

iSC: immature Schwann Cells

KO: Knock-Out

Krox20/ Egr2: Early Growth Response protein 2

LIF: Leukemia Inhibitory Factor

LXR: Liver X Receptor

MAPK: Mitogen-Activated Protein Kinase

MBP: Myelin Basic Protein

MDL: Major Dense Line

MPZ: Myelin Protein Zero

MSE : Myelin Specific Enhancer

mTOR: mechanistic Target Of Rapamycin

NCCs: Neural Crest Cells

Necl: Nectin-like Proteins

NFATc: Nuclear Factor of Activated T-cells

NG2: Neuron-glia antigen 2

NGF: Nerve Growth Factor

NRG1: Neuregulin 1

NT3: Neurotrophin 3

Oct6: Octamer-Binding Transcription Factor 6

OL: Oligodendrocyte

PMP22: Peripheral Myelin Protein 22

PNS: Peripheral Nervous System

RXR: Retinoid X Receptor

SC: Schwann Cell

SCAP: SREBP Cleavage Activation Protein

SCP: Schwann Cell Precursor

SEM: Scanning Electron Microscopy

SLI: Schmidt Lanterman Incisures

SN: Sciatic Nerve

SREBP: Sterol Regulatory Binding Protein

SOX10: SRY)-box Transcription Factor 10

SQS: Squalene Synthase

TEM: Transmission Electron Microscopy

TF: Transcription Factor

TFAP2 $\alpha$ : Transcription Factor AP-2 Alpha (Activating Enhancer-Binding Protein 2 Alpha)

THY1: Thymus cell antigen 1

ToF-SIMS: Time of Flight Secondary Ion Mass Spectrometry

TrK: Tropomyosin receptor Kinase

YY1: Yin Yang 1

ZO-1: Zonula Occludens 1

# Table of Content

INTRODUCTION.....	1
CHAPTER I: LITERATURE REVIEW .....	3
I.    The Peripheral Nervous System.....	3
1.    The anatomy of the PNS .....	4
2.    Origin and development of the Peripheral Nervous System .....	12
II.   The Myelin sheath.....	26
1.    Myelin sheath ultrastructure and characteristics.....	27
2.    Composition of the myelin sheath.....	29
3.    Lipid/ protein interaction.....	46
III.  Liver X Receptor in the Peripheral Nervous System .....	48
1.    Liver X Receptor .....	48
2.    Oxysterols .....	50
3.    Functions of Liver X Receptors: Cholesterol homeostasis and lipid biogenesis .....	51
4.    Liver X Receptor and myelination.....	52
5.    Liver X Receptor in pathology.....	53
CHAPTER II: MATERIAL AND METHODS.....	56
1.    Ethical approval procedures .....	56
2.    Genotyping.....	56
3.    Behavioral testing and electrophysiological assessment .....	57
4.    Histological characterization of the Sciatic nerves .....	60
5.    Biophysical characterization by Atomic Force Microscopy .....	63
6.    Scanning Electron Microscopy (SEM) .....	68
7.    Lipid composition of the SN characterization using the Time of Flight – Secondary Ion Mass Spectrometry (ToF-SIMS).....	68
8.    Primary co-culture of dissociated DRGs at E13.5.....	72
9.    Evaluation of mRNA expression levels by RT-qPCR .....	74
10.   Statistical Analysis.....	75
CHAPTER III: RESULTS.....	76
1.    LXR $\beta$ specific deletion in Schwann Cells presents deleterious consequences on behavioral performance, myelination and nerve conduction.....	76
1.1.  Animal model design.....	76



1.2. Phenotypic description of the LXR $\beta$ Schwann cells specific knock-out mouse model. ....	80
1.3. Electrophysiological assessment of nerve conduction in LXR $\beta$ SC KO mice. ....	84
2. LXR $\beta$ specific deletion does not affect the biophysical properties of the nerve fibers but leads to sciatic nerve structural reorganization. ....	87
2.1. Investigating the effect of LXR $\beta$ SC KO on the structural characteristics of the sciatic nerve fibers .....	87
2.2. Investigating the effect of LXR $\beta$ SC KO on the biomechanical properties sciatic nerve fibers. ....	91
2.3. Assessment of cellular organization and collagen deposition in the sciatic nerves of LXR $\beta$ SC KO mice.....	96
3. LXR $\beta$ specific deletion in Schwann cells alters sciatic nerve lipid composition and homeostasis.....	99
CHAPTER IV: DISCUSSION .....	139
1. Consequences of LXR $\beta$ SC KO on mice behavioral performance and nerve ultrastructure. ....	139
2. Maintenance of Sciatic nerve fiber biomechanical integrity in the LXR $\beta$ SC KO mutant mice by collagen deposition.....	140
3. Perineurial/Schwann cell communication .....	142
4. Alteration of lipid composition in LXR $\beta$ SC KO SNs .....	143
5. Unraveling the cause of reduced myelin presence.....	144
CHAPTER V: PERSPECTIVES AND CONCLUSION .....	146
1. Which type of collagen is responsible for the maintenance of nerve fiber biomechanical integrity after LXR $\beta$ SC KO? .....	146
2. Is the increase of sphingomyelin concentration a compensation for cholesterol reduction? .....	146
3. Is the lipid alteration the cause or the consequence of the observed phenotype in LXR $\beta$ SC KO? .	147
Conclusion.....	149
References .....	150

## INTRODUCTION

The myelin sheath is a specialized insulating layer formed around the axons and is essential for the healthy functioning of the nervous system especially by insulating the axon and increasing the nerve conduction velocity by saltatory propagation of the action potentials. The Schwann cells (SCs) and oligodendrocytes (OLs) are the glia responsible for myelination of the peripheral and central nervous system respectively. In this study, we are working on the Peripheral Nervous System (PNS) therefore, we will be addressing only the role of SCs in myelin formation. SC lineage has to go through different developmental stages to become either myelinating or non myelinating SCs. The myelinating SCs associate in a 1:1 ratio and wrap their plasma membrane around the axons multiple times to form the myelin sheath. The latter has a very distinctive composition; around 70% of the plasma membrane constituents are lipids especially enriched in cholesterol and phospholipids. The myelination process is tightly regulated and alterations to genes involved in this process would have consequences on the correct myelination of the PNS.

Liver X Receptors (LXRs), found in isoforms  $\alpha$  and  $\beta$ , are nuclear receptors, activated by their natural ligands; the oxysterols –oxidized form of cholesterol– and function as cholesterol “sensors”. The activation by oxysterols leads to the transcription of genes involved in cholesterol efflux and lipogenesis, therefore, they play a crucial role in the cholesterol and lipid homeostasis. Since the myelin sheath is highly rich in cholesterol and phospholipids; the implication of LXR in this process was evaluated by our team. Our teams’ findings have shown that the  $LXR\alpha/\beta^{-/-}$  total mutants show dysregulation of myelin gene expression, thinner myelin sheaths and elevated oxidative stress levels.

LXR $\beta$  has been shown to be the predominant isoform of the LXR in the PNS, therefore, we were interested in evaluating this isoform's contribution to the process of myelination by specifically deleting it in the myelinating glia of the PNS. Accordingly, we would only observe consequences related to its function in the Schwann cells and this may help to understand its role in the PNS. We constructed a specific knock-out model of the LXR $\beta$  isoform uniquely in Schwann cells (SCs). We bred LXR $\beta$  Floxed mice with Desert Hedgehog: Cre mice, thus the deletion of LXR $\beta$  happens at embryonic day E13 following the expression of Dhh. This model did not phenocopy the LXR $\alpha/\beta$ <sup>-/-</sup> total mutants and showed a more severe phenotype.

The main axes addressed in this study are the consequences of the LXR $\beta$  specific ablation in SCs on:

1. Behavioral performance, nerve conduction and myelination.
2. Structural organization of the sciatic nerve (SN) and biophysical properties of the nerve fibers.
3. Lipid composition of the SN and effect of LXR $\beta$  SC KO on cholesterol and lipid homeostasis.
4. The probable causes leading to this phenotype.

# CHAPTER I: LITERATURE REVIEW

The nervous system is the most complex part of the body. It is a highly organized hub of connections responsible for our cognition, behavior, regulation of all vital organs, reflexes, locomotion and much more. The nervous system has long been an intriguing domain of research that is still far from being fully understood.

In this introductory chapter, the Peripheral Nervous System and the cellular components of the peripheral nerves will be detailed, with a special focus on the description of Schwann cell development, the induction of myelination and myelin sheath composition. Furthermore, the Liver X Receptors are introduced and their roles in the PNS myelination and pathology are reported.

## I. The Peripheral Nervous System

The vertebrate nervous system is divided into the Central Nervous System (CNS) which consists of the brain and spinal cord, and the Peripheral Nervous System (PNS) which consists of the nerves emerging out of and back into the CNS (Figure 1A) (Dale Purves, 2018).

The nerves of the PNS are made of sensory (afferent) and motor (efferent) components. The neural system acquires sensory information from its receptors sensitive to internal and external environments of the body and sends the information through the nerve fibers to be processed in the CNS. The motor components are further divided into two functions; firstly carrying the motor commands of the CNS to the muscles (Somatic Nervous System) and secondly regulating the involuntary autonomic body functions (Autonomic Nervous System) (Figure 1B).

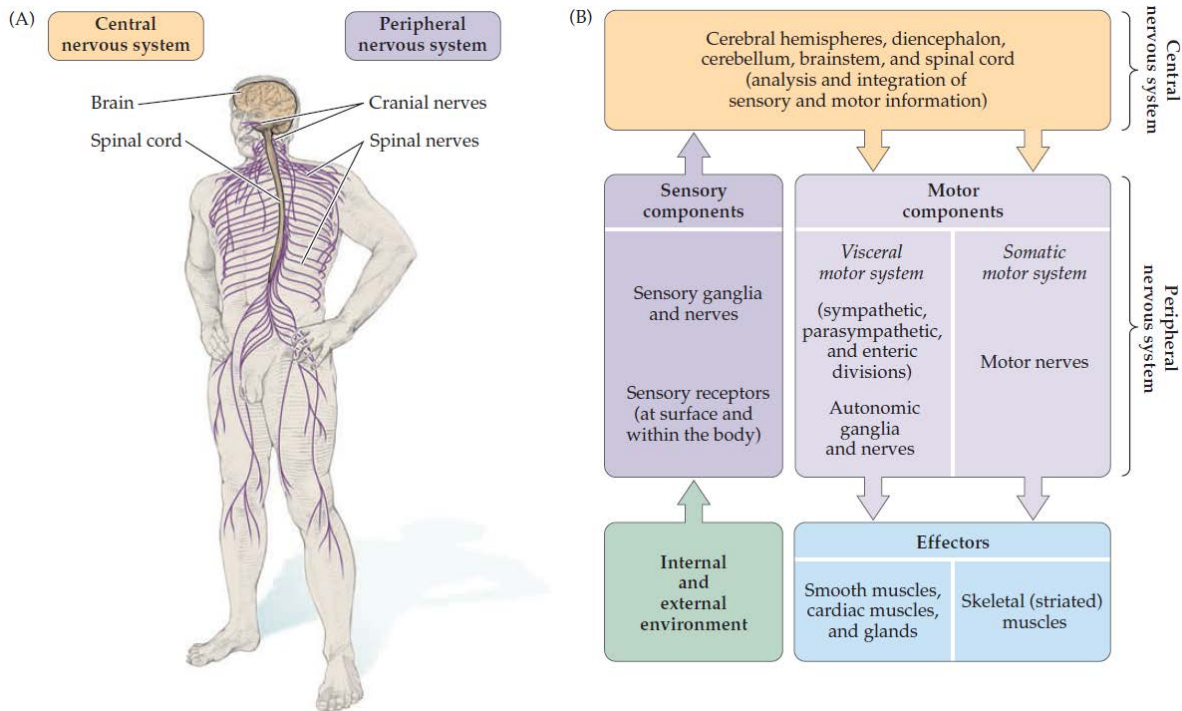


**Figure 1.** A. The Nervous System. B. Components and functions of the Peripheral Nervous System (Dale Purves, 2018).

## 1. The anatomy of the PNS

The functions of the PNS are assured by nerves; made of sensory neurons, somatic motor neurons and autonomic motor neurons bundled by specific cell types in a very organized and structured configuration. The human body possesses 12 cranial nerves and 31 pairs of spinal nerves. These nerves retain their names from their site of emergence (Dale Purves, 2018).

### 1.1. The Cranial Nerves

The cranial nerves emerge from the brain and brain stem and serve the sensory and/or motor functions of the area surrounding their site of emergence (mostly in head and neck) and autonomic functions such as digestion. The nature and function of each nerve are detailed in Table 1. It is important to note that the first two out of the total 12 cranial nerves, the olfactory and optic nerves, are considered part of the CNS because they are myelinated by CNS glia that are different from PNS glia (Dale Purves, 2018).

<b>Cranial Nerve</b>	<b>Name</b>	<b>Sensory and/or Motor</b>	<b>Major Function</b>
I	Olfactory nerve	Sensory	Sense of smell
II	Optic nerve	Sensory	Vision
III	Oculomotor nerve	Motor	Eye movements; pupillary constriction and accommodation; muscle of upper eyelid
IV	Trochlear nerve	Motor	Eye movements (intorsion, downward gaze)
V	Trigeminal nerve	Sensory and motor	Somatic sensation from face, mouth, cornea; muscles of mastication
VI	Abducens nerve	Motor	Eye movements (abduction or lateral movements)
VII	Facial nerve	Sensory and motor	Controls the muscles of facial expression; taste from anterior tongue; lacrimal and salivary glands
VIII	Vestibulocochlear (auditory) nerve	Sensory	Hearing; sense of balance
IX	Glossopharyngeal nerve	Sensory and motor	Sensation from posterior tongue and pharynx; carotid baroreceptors and chemoreceptors; salivary gland
X	Vagus nerve	Sensory and motor	Autonomic functions of gut; cardiac inhibition; sensation from larynx and pharynx; muscles of vocal cords; swallowing
XI	Spinal accessory nerve	Motor	Shoulder and neck muscles
XII	Hypoglossal nerve	Motor	Movements of tongue

**Table 1.** Location and function of the cranial nerves. Figure by Patrick J. Lynch, medical illustrator derivative work: Beao derivative work: Dwstultz [CC BY 2.5], via Wikimedia Commons, Table (Dale Purves, 2018).

## 1.2.The Spinal nerves

The eminence of the spinal nerves can be perceived from their name. Spinal nerves are mixed in nature and are responsible for the communication of sensory, motor and autonomic signals between the body and the spinal cord (CNS). In the human body, there are 31 pairs of spinal nerves, classified according to the spinal region into cervical, thoracic, lumbar and coccygeal nerve pairs (See figure 2).

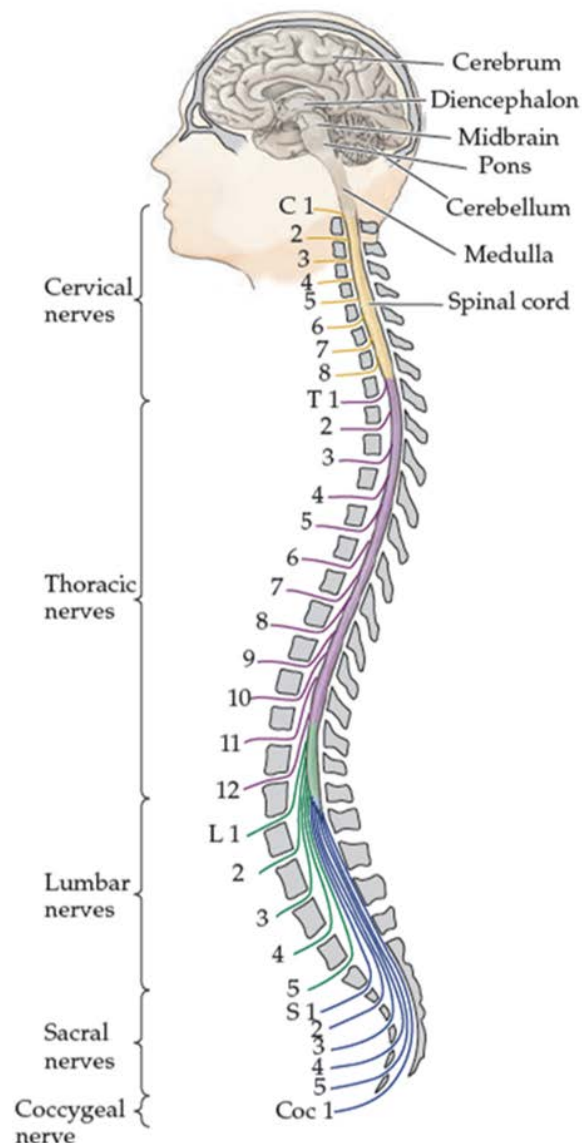


**Figure 2.** The Spinal Nerves. The human body has 8 cervical nerve pairs (C1- C8), 12 thoracic nerve pairs (T1-T12), 5 lumbar nerve pairs (L1-5) and one coccygeal nerve pair (Dale Purves, 2018).

The neural circuitry in the spinal cord is very organized. The somatic motor neuron (efferent) cell bodies are found in the ventral horn of the spinal cord and innervate the skin and skeletal muscles. The soma of the sensory neurons (afferent), responsible for innervating the body, are found in the Dorsal Root Ganglia (DRG). However, the case is different for the autonomic nervous system (ANS) which is responsible of the innervation of smooth muscles, glands and different organs. The ANS is further divided into sympathetic and parasympathetic. The ANS motor neurons emerging from the lateral horn of the spinal cord are called the preganglionic neurons, which then synapse, at the level of ganglions located outside of the spinal cord, to the post ganglionic neurons that will be responsible of innervating their targets. The sympathetic ganglia can be found close to the spinal cord however the parasympathetic ganglia are close to the innervated organs. Figure 3 summarizes the functions of the sympathetic and parasympathetic divisions (Dale Purves, 2018).

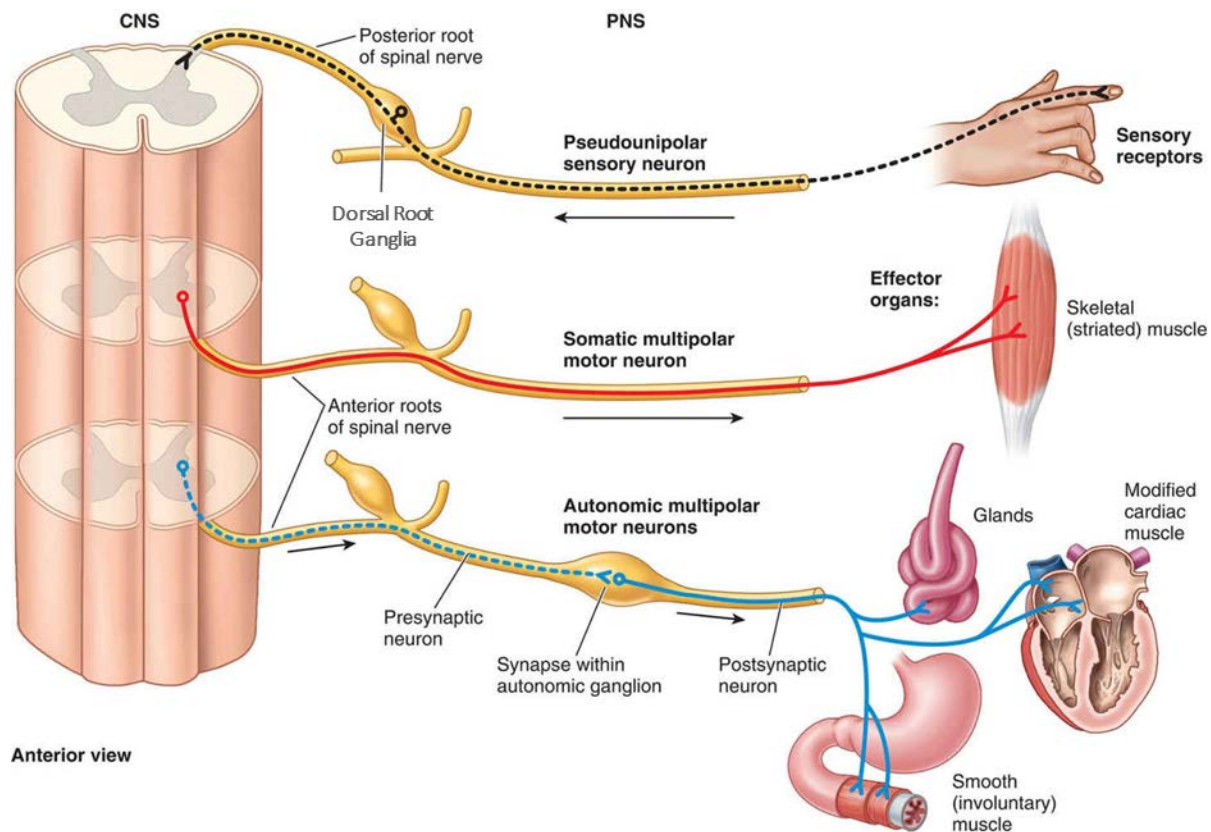


**Figure 3.** Section of the spinal cord showing the localization of the cell bodies of neurons forming the peripheral nerves and the innervation of their targets (Walters Klower).



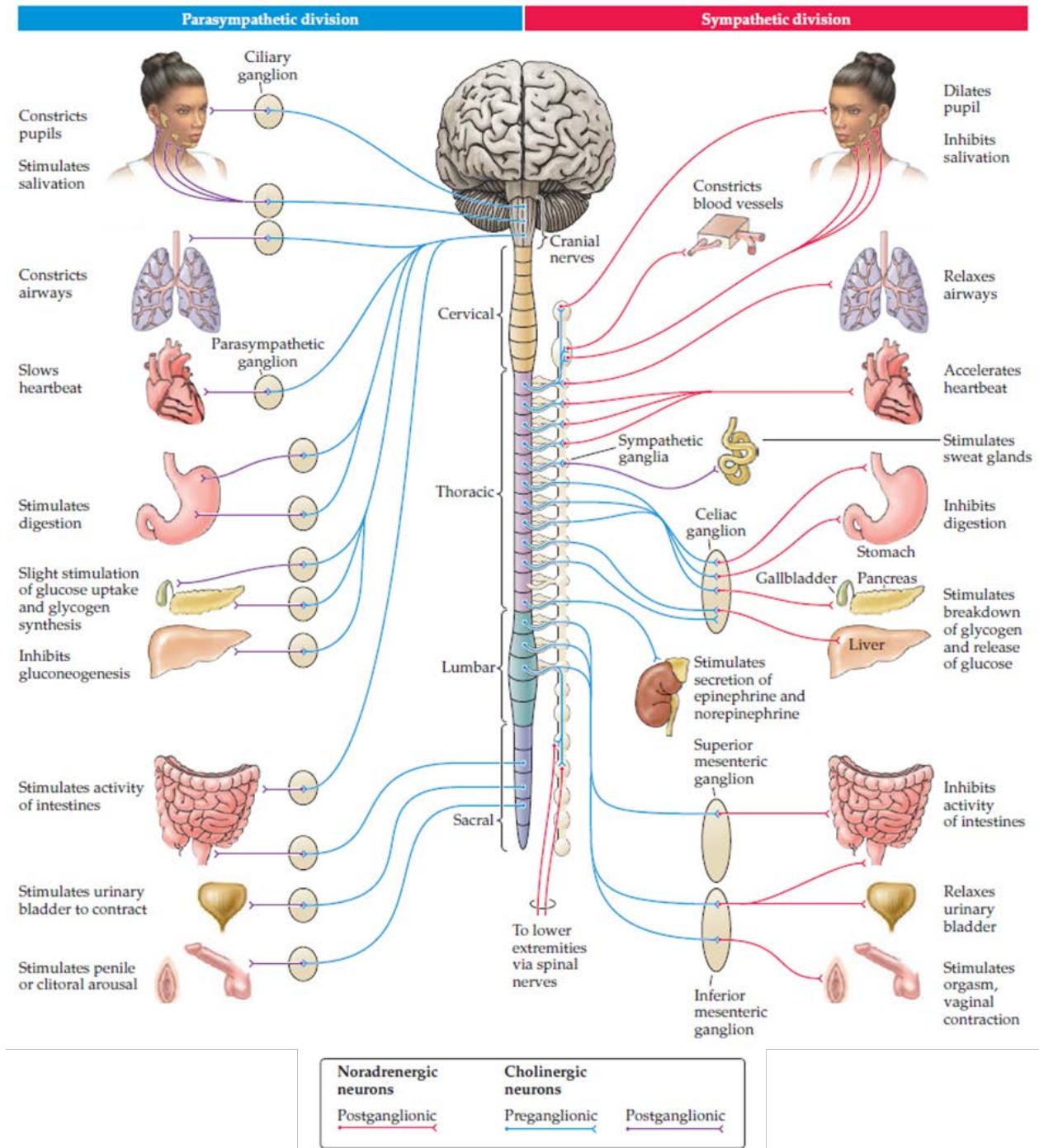


**Figure 4.** Sympathetic and parasympathetic divisions of the Autonomic Nervous System and their functions (Dale Purves, 2018)

### 1.1. The Sciatic Nerves

The Sciatic Nerve (SN) is the largest peripheral nerve in the PNS innervating the lower leg muscles (Giuffre et al., 2020), it is predominantly used by researchers invested in understanding the PNS. In the human body, the SN originates from L5 to S3, however, in mice it originates from L3 and L4 spinal nerves (Rigaud et al., 2008) (Figure 5).

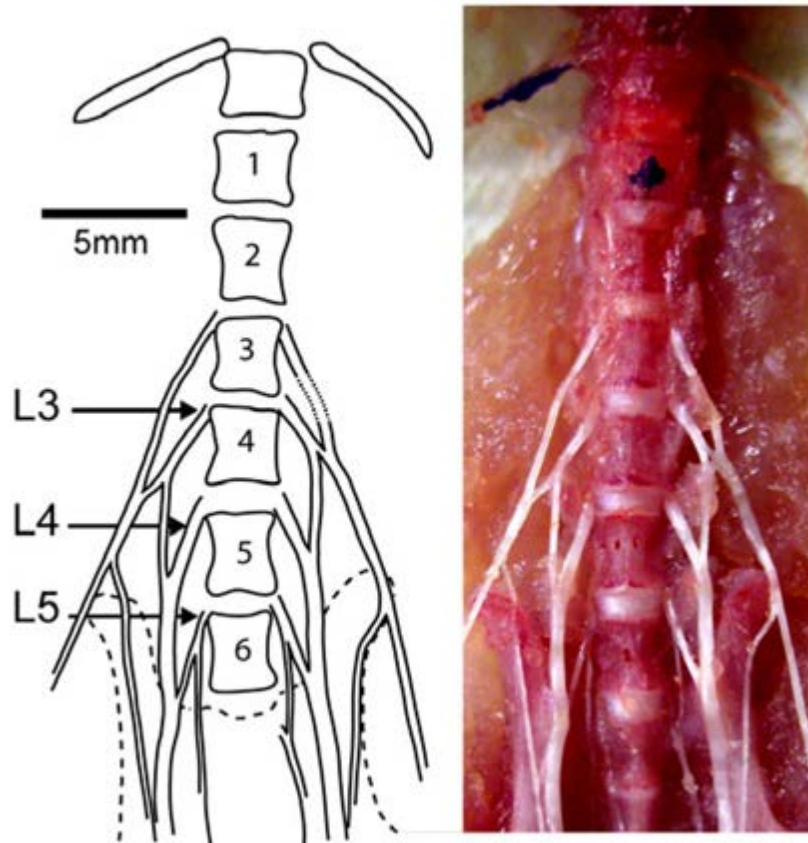


**Figure 5.** Scheme and image of a C57Bl/6 mouse lumbar spinal nerve pairs forming the sciatic nerve (Rigaud et al., 2008).

The PNS is most often portrayed to be more vulnerable to stresses from the external environment than the Central Nervous System (CNS) due to the absence of bone structure protection. However, the nerves of the PNS have a very characteristic organization, which plays a great role in absorbing and minimizing stresses and injuries (Ross, 2014).

In the PNS, the axons extending from the CNS and PNS ganglia are insulated and grouped by glial and stromal cells, forming peripheral nerves. Peripheral nerves contain three layers of connective tissue: the endoneurium, perineurium and epineurium (Figure 6).

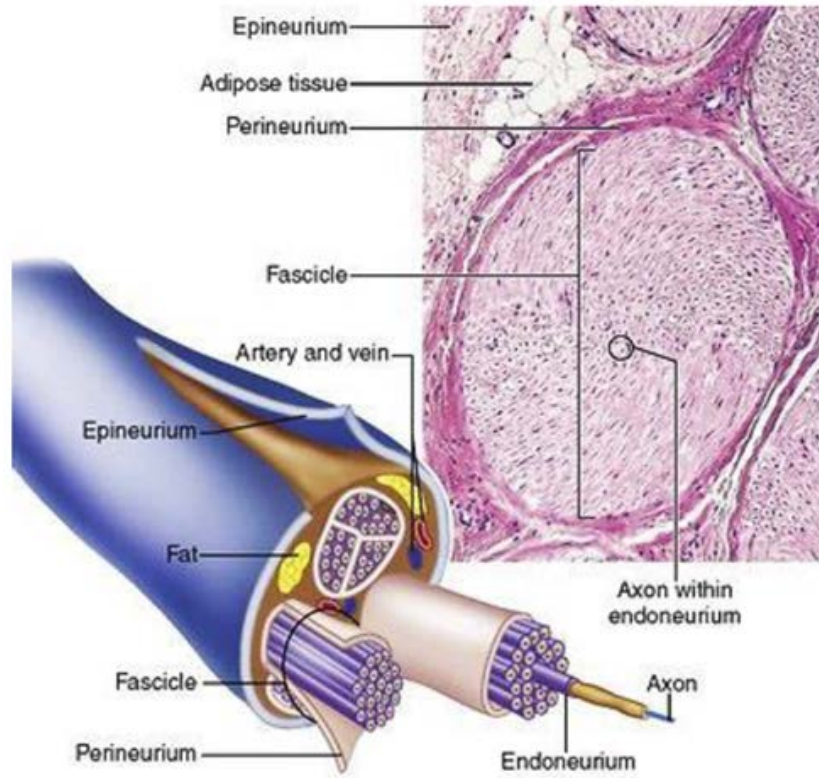


**Figure 6.** Schematic representation of the Sciatic Nerve layers (Patton et al., 2018).

The innermost layer of the peripheral nerve is the endoneurium; where axons and Schwann cells are surrounded by a loose connective tissue mostly produced by the endoneurial cells, also containing blood vessels. Schwann cells (SCs) are the myelinating glia of the PNS and play a crucial role in maintaining the integrity and function of the axons by providing trophic support and insulation. In addition to being responsible for the radial sorting of the axons, SCs associate in a 1:1 ratio with large caliber axons  $\sim 1\mu\text{m}$  then wrap and condense their plasma membrane around them, forming the highly rich in lipids myelin sheath. Oligodendrocytes (OLs) are responsible for the ensheathment of the neurons of the Central Nervous System (CNS) whereas Schwann Cells (SCs) are responsible for the ensheathment of the neurons of the Peripheral Nervous System (PNS) (Nave et al., 2014). SCs wrap their plasma membrane around a single axon while OLs extend numerous processes and can myelinate multiple axons at the same time.

The smaller caliber axons are bundled together by single non myelinating SCs forming Remak bundles. During development, Schwann cell precursors initiate the deposition of extracellular matrix (ECM) components like laminin which would become the basal lamina (BL) surrounding myelinating and unmyelinating SCs (Jessen et al., 2005).

The second layer of connective tissue is called the perineurium; formed by perineurial cells and layers of collagen holding together several nerve bundles to form fascicles. The composition and structure of the perineurium provide high mechanical strength to the nerve. These nerve fascicles are then grouped with the fatty tissue and blood supply by the outermost connective tissue layer called the epineurium (Schanthaveerappa et al., 1962; T. Shanthaveerappa et al., 1966).

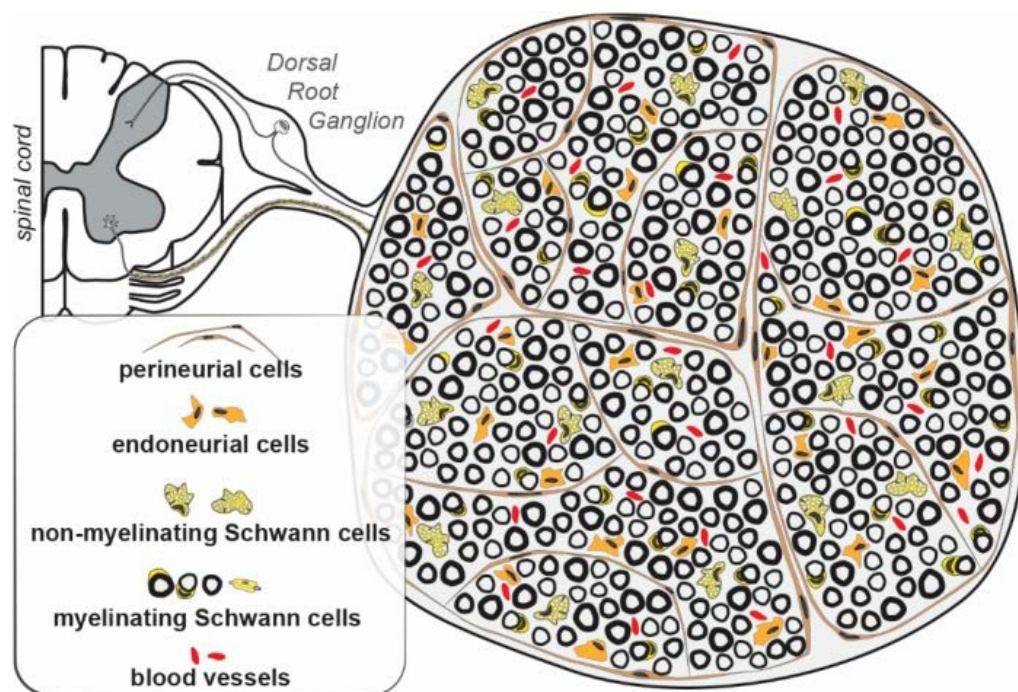


**Figure 7.** Cellular components of the Sciatic Nerve (V. K. Sundaram et al., 2019).

## 2. Origin and development of the Peripheral Nervous System

Not all cells forming the peripheral nerves have the same origin, however a large majority of them derive from the same population. The PNS glial cells (Schwann cells, Boundary Cap Cells and Satellite glia) as well as sensory neurons and endoneurial cells originate from the migrating Neural Crest Cells (NCCs) (Hall, 1999; Joseph et al., 2004). During neurulation, the folding of the neural plate gives rise to crest cells on either side of the plate: the Neural Crest Cells. Following different developmental cues, the NCCs detach from the neural plate and migrate in different waves to give rise to the multiple cell types (Bhatt et al., 2013). For the pertinence of this study, we will only be describing the wave that gives rise to the cells of the peripheral nerves.

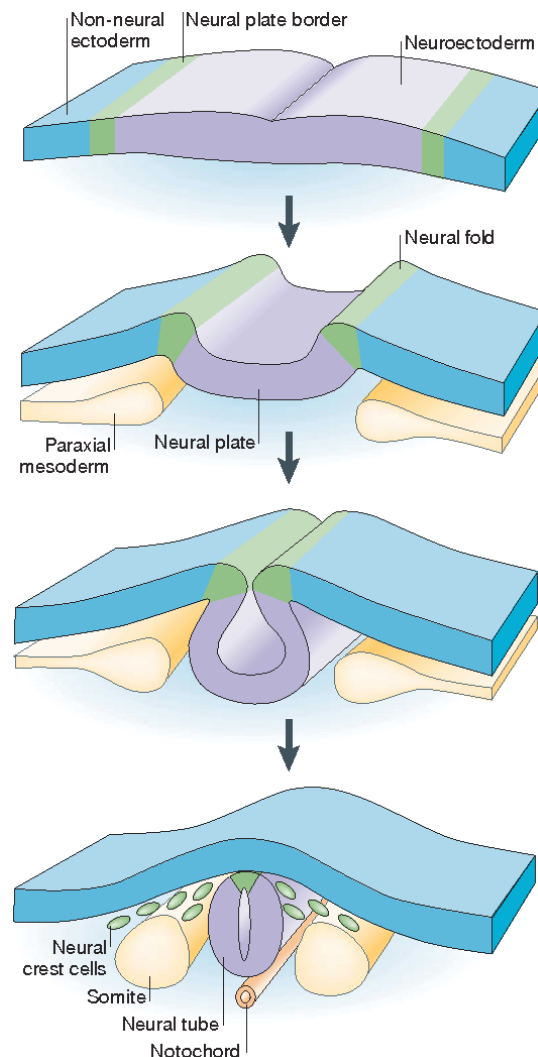


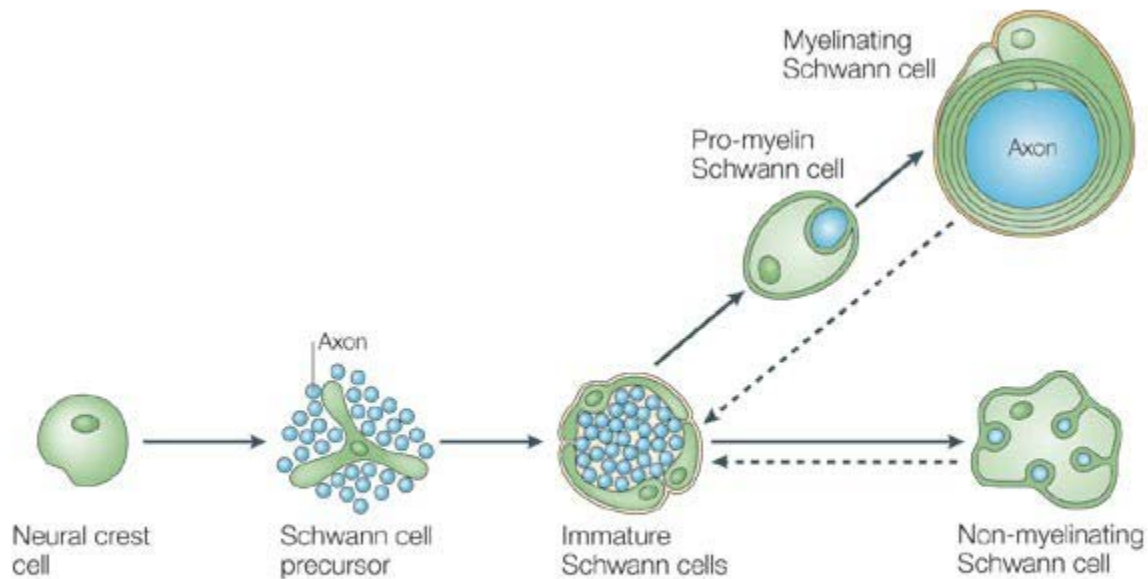
**Figure 8.** Neural tube folding and Neural Crest Cell formation (Gammill et al., 2003).

## 2.1. Sensory Neuron Generation

The sensory neurons of the PNS originate from the population of NCCs that migrate during development and form the Dorsal Root Ganglia (DRG). The differentiation of NCCs into sensory neurons progenitors takes place around embryonic day 10 (E10) in mice and precedes all other cell differentiation (Prendergast et al., 2014). Bone Morphogenic Protein (BMP) signaling is crucial for the migration of the NCCs and its expression is necessary for the NCCs to gain a neural fate. BMP signaling also drives the expression of neurogenins, and transcription factors (TFs) involved in the regulation of neuronal differentiation (Ma et al., 1999). Neurogenins drive the expression of TFs Brn3a and Islet1 that would consequently activate the expression of the Runx family of transcription factors TFs (Dykes et al., 2011). Then, the Runx family of TFs promotes the expression of three types of Tropomyosin receptor Kinase (TrK) A, B and C. These receptors will dictate the functional type of the sensory neurons of the DRG along with other factors (Bhatt et al., 2013; Ma et al., 1999).

## 2.2. Schwann Cell Lineage

SCs are the primary glial cells of the PNS. They play a crucial role in development, neuronal survival and myelination. Schwann cells derive from the NCCs and go through three distinct developmental stages to become differentiated into either myelinating or non-myelinating glia (Jessen et al., 2005) (Figure 9).

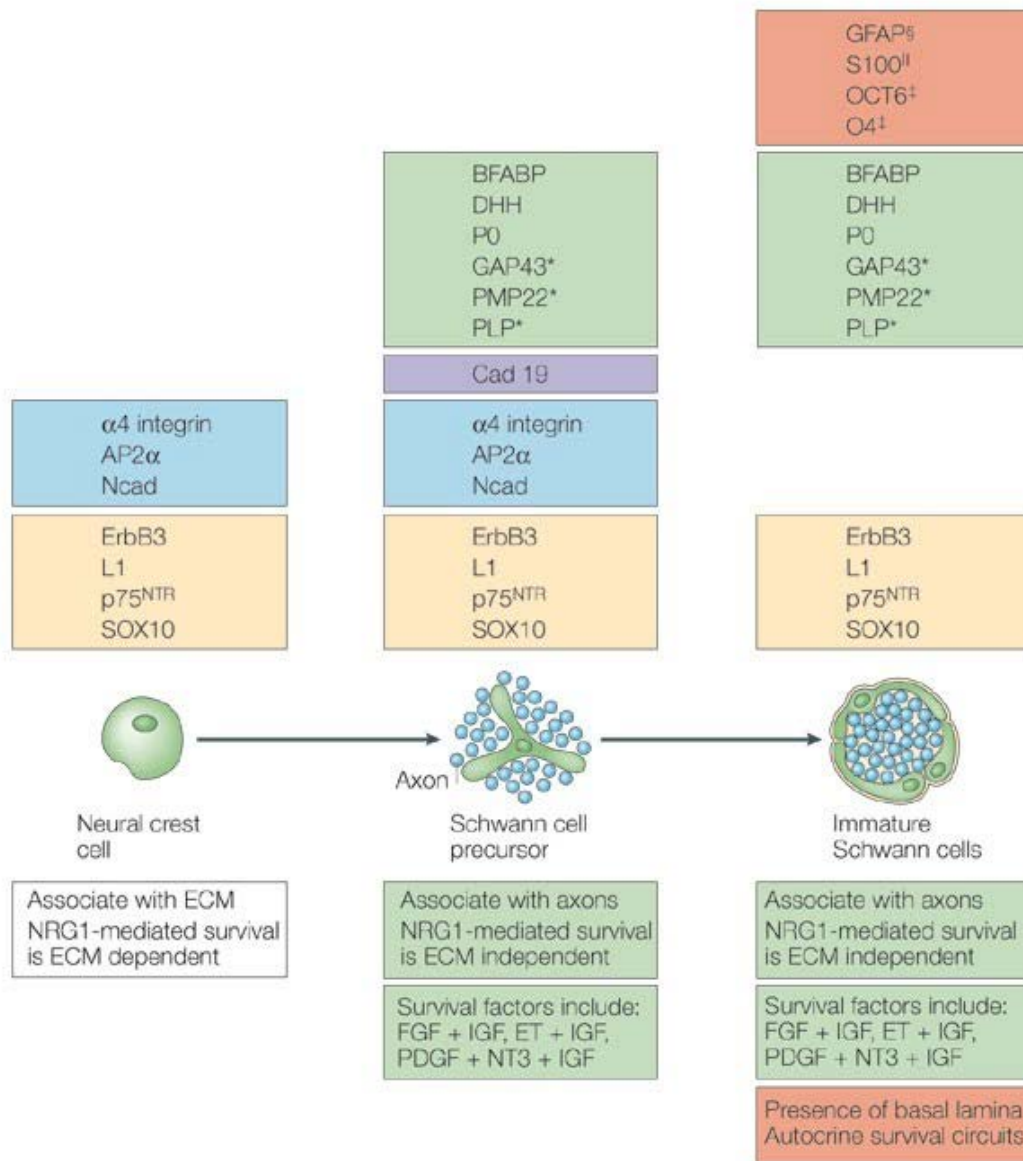


Copyright © 2005 Nature Publishing Group  
Nature Reviews | Neuroscience

**Figure 9.** Schwann cell development (Jessen et al., 2005).

These transitions are under the regulation of a large spectrum of genes, transcription factors, axonal factors and cytoskeleton associated molecules, all orchestrating the proliferation and differentiation of the SC lineage. During the first transition, NCCs give rise to Schwann Cell Precursors (SCPs), which differentiate into immature Schwann Cells (iSCs). iSCs will later on differentiate into either myelinating or non-myelinating SCs (Jessen et al., 2005; Monk et al., 2015).

A complex set of markers defines each differentiation stage. The phenotypic profile of the SC lineage is summarized in Figure 10. Some factors and markers are present in all phases of differentiation and are crucial for the correct generation of SCs such as Neuregulin 1 and SOX10 (Box 1), and other factors are specific to certain stages and considered as markers of differentiation (Jessen et al., 2005)



Copyright © 2005 Nature Publishing Group  
Nature Reviews | Neuroscience

**Figure 10.** Factors and markers expressed in the differentiation of the SC lineage (Jessen et al., 2005).



## **BOX 1. Neuregulin 1 and SOX10 expression in SC development**

### **Neuregulin 1- Axon/Schwann cell communication**

A master regulator of the PNS axo-glial communication, present in all SC developmental stages and a key factor in SC lineage survival, differentiation and myelination (Birchmeier et al., 2008).

Neuregulin 1 (NRG1) is a member of the epidermal growth factor (EGF) family present at the level of the neuroblast and later differentiated sensory neuron axolemma. NRG1 type III is the most expressed isoform on axonal surface amongst the types I to III, (Taveggia et al., 2005).

NRG1 Type III is localized at the level of axonal membrane and is cleaved by the protease BACE1 (beta-site amyloid precursor protein-cleaving enzyme 1) and works in juxtacrine manner (Willem et al., 2006). NRG1 Type III binds to its receptors from the family of Tyrosine Kinase ErbB2/3 heterodimer presented by the Schwann cell progenitors and activates different downstream cascades involved in SC progenitor's migration, survival and proliferation. NRG also plays a role in radial sorting, SC fate differentiation and myelination (Monk et al., 2015; J. Newbern et al., 2010).

### **Sox10**

SOX10 (Sex Determining Region Y (SRY)-box Transcription Factor 10) is a transcription factor, member of the SOX family (SRY-related HMG-box), that plays a role in cell fate determination and development. SOX10 couples with other proteins to form a protein complex and activate the transcription of its target genes.

SOX10 is expressed by all NCC lineage and is essential for the determination of a glial fate, it is also expressed during all stages of SC development and its deletion is detrimental (Britsch et al., 2001; Finsch et al., 2010).

### 2.2.1. Neural Crest Cells to Schwann Cell Precursors transition

The transition of NCCs towards Schwann Cell Precursors (SCPs) takes place around E12-13 in mice. SCPs are multipotent cells that give rise to various cell types such as melanocytes, chromaffin cells, endoneurial fibroblasts and many more. The transition of SCPs towards the glial fate is mostly initiated by signals that arise from the neuronal cells. During this step, the SCPs clustered in the DRGs proliferate and migrate on newly sprouting axons. SCPs are implicated in the process of nerve fasciculation since they start associating to axonal bundles and help in guiding the axons reach their targets (Jessen et al., 2019).

The transition of NCCs to SCPs is initiated by FGF2 (Fibroblast Growth Factor 2) signaling – suspected to be expressed by the surrounding neuroblasts. FGF2 binds to its receptor the FGF-R, presented by the NCC, and promotes the expression of Notch which further drives the expression of ErbB2 (Dong et al., 1999; Jessen et al., 2005). At the same time, SOX10 promotes the expression of ErbB3, which dimerizes with ErbB2 and interacts with NRG1 type III presented by the neuroblast to promote the glial fate through signaling cascades (Britsch et al., 2001).

Epigenetic modifications also promote the glial fate of NCC by regulating the gene expression of glial markers through SOX10 and Pax3 (Jacob et al., 2014) (See figure 11).

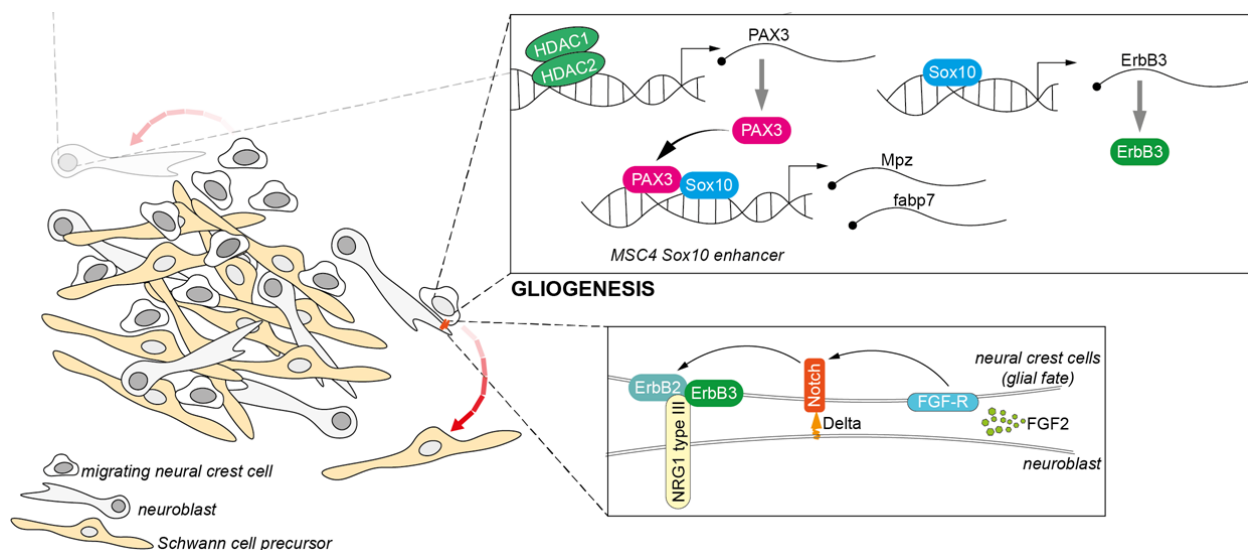


**Figure 11.** Molecular machinery responsible for the differentiation of NCCs into SCPs (Artistic elaboration by J. Grenier).

In SOX10 knock-out models, the glial differentiation of NCCs is blocked and diverged into neuron generation also affecting the differentiation of NCCs into satellite glial cells of the DRGs. Therefore, SOX10 plays a crucial role in ensuring the glial fate of the crest cells (Britsch et al., 2001). NCC/SCP transition does not require Neuregulin, however SCP proliferation and survival do. The survival of SCPs is also dependent on desert hedgehog (Dhh) expression - a transmembrane protein involved in signaling that additionally highlights the role of SCPs in the correct structuration of the forming perineurium (Parmantier et al., 1999).

### **2.2.2. Schwann Cell Precursors to immature Schwann Cell transition**

The SCP to immature SCs (iSCs) transition takes place around E15-16 in mice. During this transition, the fibroblasts, that produce the connective tissue present around the nerves, enter the endoneurial space, which was so far only made of big bundles of neurons surrounded by SCPs. Then, SCPs come into contact with ECM molecules produced by the fibroblasts such as collagen that plays an important role in the transitioning of SCPs into iSCs (Jessen et al., 2019).

The most important role of iSCs is the sorting of axons during their maturation, a process known as radial sorting (M. Laura Feltri et al., 2016) (Refer to Box 2).

The hallmark of SCP to iSCs transition is that iSCs start supporting their own survival in an autocrine manner by secreting multiple factors such as IGF2, NT3, LIF and LPA and forming the basal lamina (Jessen et al., 2019).

Several factors are involved in this transition especially NRG1 and Notch signaling. SCP to iSC transition comes with the downregulation of TFAP2 $\alpha$ ,  $\alpha$ 4 integrin and N-cadherin (Buchstaller et al., 2004). Another negative regulator of the SCP differentiation is endothelins; the deletion of its receptors causes the premature presence of iSCs. At this step, SOX10 plays a role in transition and is recruited to promote the expression of Pou3f1 (Oct6/Scip) (Finzsch et al., 2010; Schreiner et al., 2007). Many markers are upregulated such as S100 $\beta$  and GFAP which and are considered as pan iSC and SC markers (Buchstaller et al., 2004).

## BOX 2. Radial Sorting

The main role of iSCs is the radial sorting of the peripheral axons. The sorting is based on the axonal caliber where large caliber axons are, later on, destined for myelination whereas the smaller caliber axons are segregated into Remak Bundles by one non-myelinating SC. iSCs start by segregating the axons into smaller bundles; radially pull the large caliber axons to the periphery and make a 1:1 relationship with large caliber axons and bundle small caliber axons together (M. Laura Feltri et al., 2016).

The radial sorting process is complex, governed by multiple factors and requires high proliferation rates of the iSCs to reach the necessary numbers that is needed to associate with the axons. Radial sorting deregulation leads to pathological development (Figure 12)

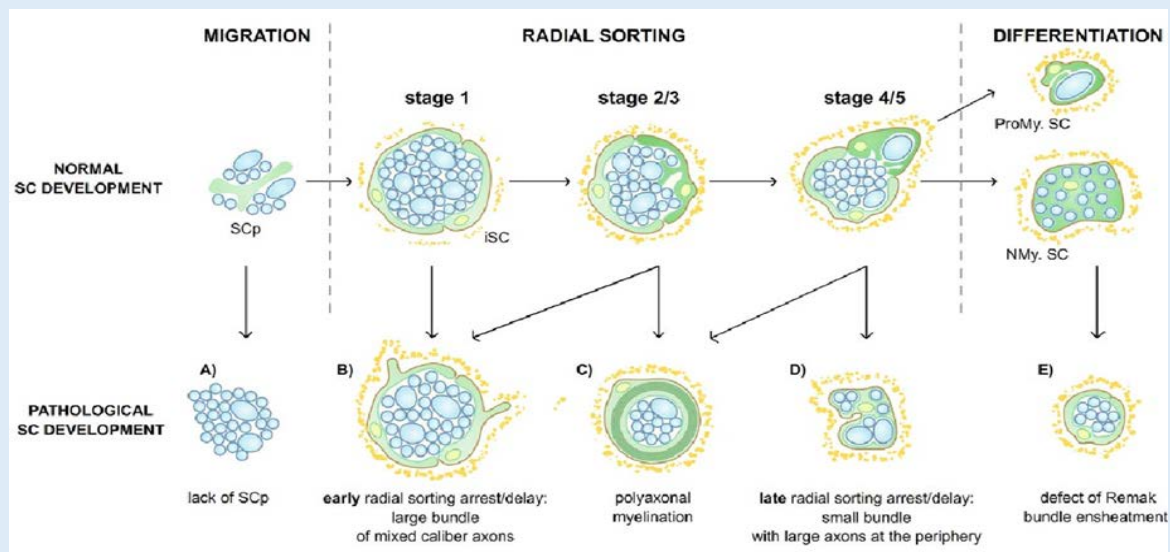


**Figure 12.** Normal and pathological SC development (M. Laura Feltri et al., 2016).

Two important players in radial sorting are the extracellular matrix molecules and the NRG1 mediated axo-glia axis. The interaction between ECM molecules and iSCs affect radial sorting, where ECM molecules help iSC polarization, processes extension and activate signaling cascades involved in iSC proliferation.

Axonal NRG1 Type III- Schwann ErbB2/3 receptor axis is a key player in radial sorting. NRG1 Type III null mice are not viable, however haplo-insufficient mutants have proven that NRG1 Type III is crucial for the myelination of large caliber axons (Taveggia et al., 2005). NRG1 type III is more expressed on large caliber axons than in smaller caliber ones, thus becoming an important cue for the SC sorting and myelination.

ECM molecules govern actin remodeling by the activation of Rho GTPases as well as inducing proliferation by activating the canonical cAMP pathway (M. L. Feltri et al., 2008; Monk et al., 2015). Many more factors are involved in this process: other axo-glia axes are important contributors in radial sorting and the disruption of their normal functioning results in radial sorting defects, delay or arrest.

### 2.2.3. Maturation of Schwann Cells

#### 2.2.3.1. Immature SCs to myelinating SCs transition

The induction of myelination is a complex process orchestrated by external and internal stimuli provided by growth factors, contact with the axon and a tightly regulated gene expression and molecular signaling (Emery, 2013; Pertusa et al., 2007; Svaren et al., 2008). Myelinating SCs go through an intermediate step of promyelination controlled by transcription factors before committing to the myelinating fate (Jaegle et al., 2003).

#### *External signals*

At this step, Notch signaling deactivation is necessary to proceed to the non-proliferative myelinating fate of the SCs (Woodhoo et al., 2009). As in all other stages of SC development, the NRG1 type III/ErbB2/3 axo-glia communication governs the process of myelination by activating several signaling cascades promoting the expression of myelin genes. NRG1 type III deletion leads to hypomyelination and its overexpression leads to hypermyelination (Michailov et al., 2004). Another axo-glia dependent communication plays an important role in myelination: the Nectin like proteins (Nec1) presented on both SCs and neurons. The interplay of Nec14 presented by the SCs and Nec11 and 2 presented by the axons have been shown to affect myelination; the SC specific deletion of Nec14 leads to myelin defects (Maurel et al., 2007). Neurotrophins such as BDNF, NGF, NT3 and GDNF are also promoters of myelination, and their presence is often imperative *in vitro* for the induction of myelination (Meier et al., 1999).

#### *Internal signals*

The internal signals are mostly induced by the binding of NRG1 type III to the ErbB2/3 tyrosine receptor kinase. Three signaling cascades are activated and mediate the expression of myelin specific genes and are required for proper myelination of the axons.

##### *1. PLC $\gamma$ / Calcineurin/ NFAT signaling*

The activation of this signaling cascade leads to increased intracellular calcium levels that activate Calcineurin B. Calcineurin B dephosphorylates NFAT which translocate to the nucleus and promote the expression of Krox20 by forming a complex with SOX10 (Kao et al., 2009).

## 2. MAPK pathway

Through the activation of ERK, the MAPK pathway regulates the expression of genes implicated in myelination, namely an important transcription factor Yin Yang (YY1) (He et al., 2010; J. M. Newbern et al., 2011).

## 3. PI3K/ Akt/ mTOR

The activation of this PI3K pathway leads to the phosphorylation of Akt. Akt activates the mTORC1 complex and regulates RXR $\gamma$ , which is recruited to the promoter region of a major regulator of lipogenesis; the Sterol Regulatory Element Binding Protein 1c (SREBP1c) (Norrmen et al., 2014).

Another mediator of myelination is the increase of GPCR independent cAMP levels that promote the expression of Krox20 and other genes implicated in the myelination process (Arthur-Farraj et al., 2011; Monje, 2015) (Figure 13).

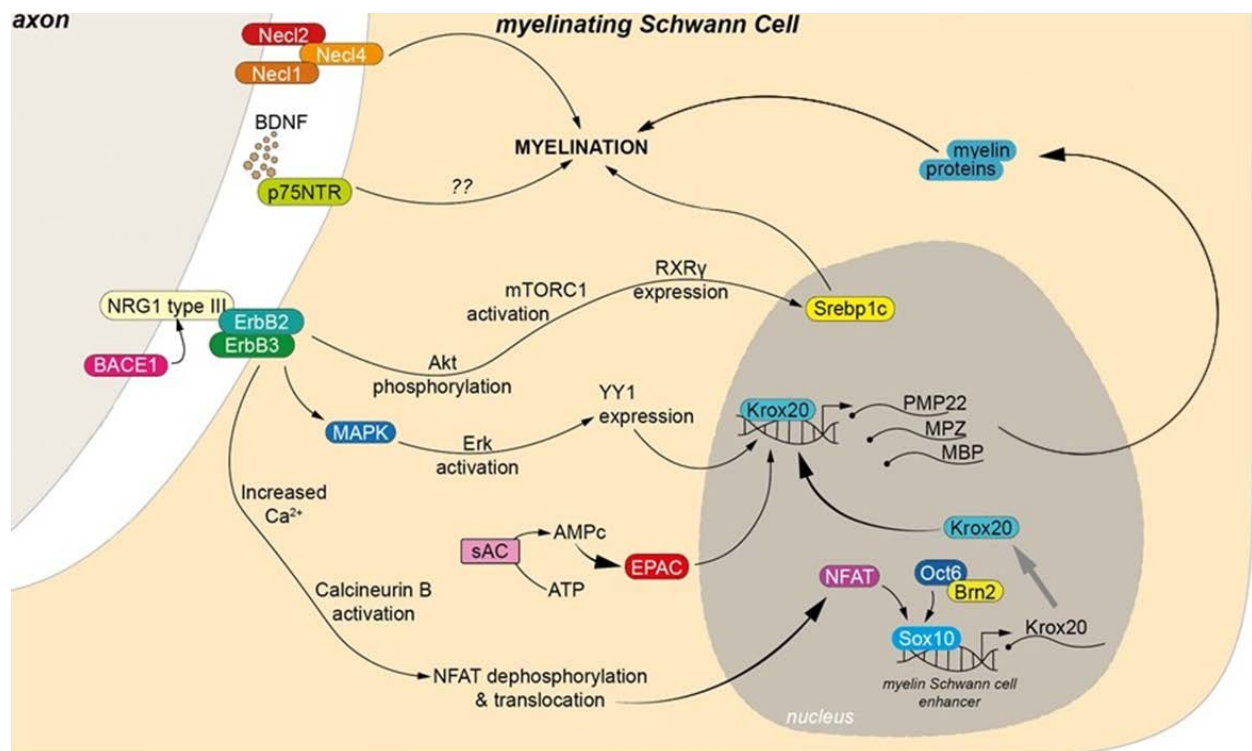


**Figure 13.** External and internal factors inducing myelination (Artistic elaboration by J. Grenier).

### ***Transcriptional networks regulating myelin gene expression in the SCs***

The different stimuli activating signaling cascades converge to TFs that drive the differentiation and myelination. Transcriptional networks regulating myelination give us an understanding of how the SCs transition from the iSC state to a myelinating SC going through an intermediate stage of promyelination. These transitions rely on the timely activation or upregulation of the TFs in a feedforward loop manner (J. L. Salzer, 2015). The major drivers of myelination are SOX10, Oct6 (Octamer-Binding Transcription Factor 6- POU3F1), Brn2 (POU3F2), Yin Yang (YY1), NFATc4 (Nuclear factor of the activated T cells) and Krox20 (Egr2 Early Growth Response protein 2) (Emery, 2013; He et al., 2010).

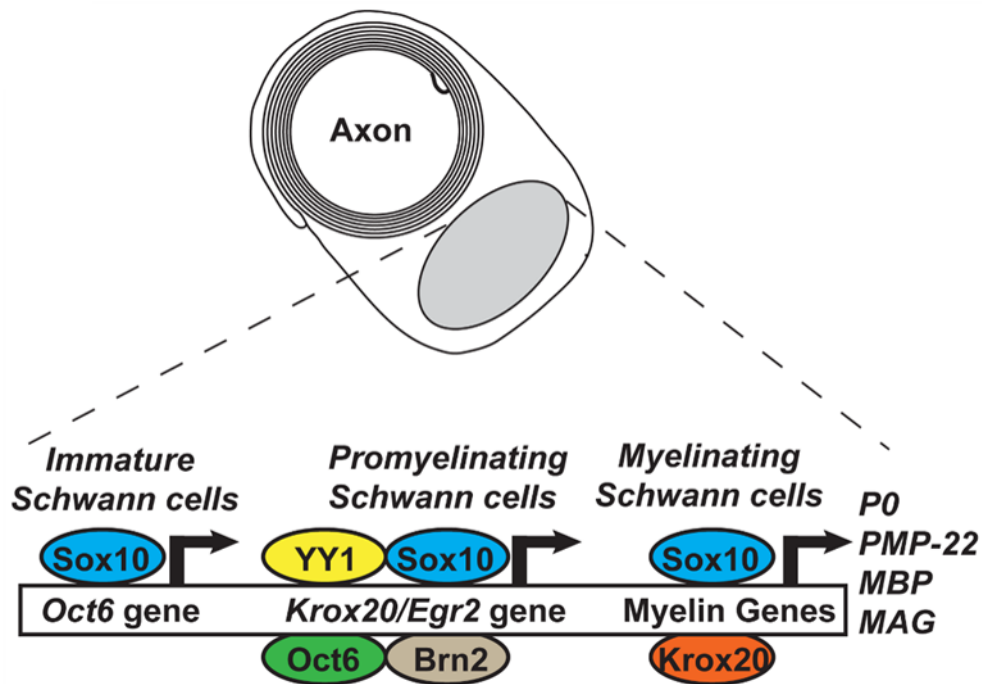


**Figure 14.** Transcriptional network responsible for myelinating SC maturation (Emery, 2013).

### ***iSC/ promyelinating SC transition***

The iSC to promyelinating step requires the upregulation of the Transcription factor Oct6 (Pou3f1); a specific marker of the promyelination step, however, its downregulation is necessary for the transition from the promyelinating to the myelinating step (Jaegle et al., 2003). Oct6 upregulation is mediated by the molecular cascades of NRG1 and cAMP (Jagalur et al., 2011; Taveggia et al., 2005). NRG1 signaling cascade converges to the Schwann Cell Enhancer (SCE)

element of the Oct6/Scip gene and regulates its expression. Additionally, the SCE element contains Sox protein binding sites and defective SOX10 homodimerization can support the development of SCs however, it is unable to upregulate Oct6 in order to proceed in myelination. This confirms the regulatory role that SOX10 plays on Oct6 (Jagalur et al., 2011).

### ***Promyelinating/ myelinating SC Transition***

The induction of myelination is mediated by the upregulation of the zinc finger transcription factor Krox20, considered to be the marker of myelinating SCs. Oct6 and Brn2 are major activators of the Krox20 gene, however their expression is quickly shutdown once Krox20 expression is induced (Jaegle et al., 2003). Through the NGR1 signaling cascades, NFATc4 and YY1 promote the expression of Krox20 (He et al., 2010; Kao et al., 2009). Furthermore, SOX10 and NFATc4 act together and recruit a mediator complex that recognizes the myelin specific enhancer (MSE) specific to the SC and present on the Krox20 gene (J. L. Salzer, 2015; Vogl et al., 2013).

Thus, Krox20 activation leads to the expression of myelin specific genes such as Myelin Protein Zero (MPZ) and Peripheral Myelin Protein 22 (PMP22) (Topilko et al., 1994).

On the other hand, Krox20 deletion leads to the arrest of the SCs at the promyelinating stage. Its expression is also crucial for maintaining the myelination phenotype (Decker et al., 2006).

### **2.2.3.2. Immature SC to non-Myelinating SCs transition**

The molecular mechanisms involved in the Remak SC's fate are not fully elucidated. However, certain players have been identified. Notch signaling is active and counteracts the activation of Krox20 (Woodhoo et al., 2009). Therefore, in contrast to myelinating SCs, the non-myelinating SCs do not express Krox20.

Brain Derived Neurotrophic Factor (BDNF) promotes the differentiation of Remak Schwann Cells (RSCs) through its receptor P75NTR, yet, its mechanism of action is not known (Jessen et al., 2005).

As previously mentioned, NRG1 expression by large caliber axons is the cue for iSCs to associate in a 1:1 ratio with large caliber axons. The specific knock-out of NRG1 in sensory neurons led to the formation of larger Remak bundles and thinner myelin sheath around the myelinated axons (Fricker et al., 2009). Also deleting the expression of NTE (Neuropathy Target Esterase) and Lrp1 (LDL Receptor-related Protein 1) results in an incomplete Remak bundling, aberrant formation of



Remak bundles and hypomyelination of the axons respectively (McFerrin et al., 2017). A tightly regulated Akt/mTORC axis is also necessary for the differentiation of RSCs. A balanced regulation of the Akt/mTORC and SC mitochondrial metabolism are put forward as essential in the differentiation and maturation of RSCs (Domènech-Estévez et al., 2016; Normén et al., 2014).

### **2.3. Endoneurial Fibroblast Like Cells (EFLCs)**

The Endoneurial cells or Endoneurial Fibroblast-Like Cells (EFLCs) make up around 2% to 9% of the cells present in the peripheral nerves. The EFLCs are scattered in the endoneurial space and mostly found next to the blood vessels and adjacent to the perineurial cells. The morphology of the endoneurial cells is different from that of the other cells of the peripheral nerve. The nucleus of the EFLC is paler than that of the SC and the cytoplasm presents long processes that interact with neighboring EFLCs. In contrast to SCs, pericytes and perineurial cells, the EFLCs do not present a continuous basal lamina (Richard et al., 2012).

The role of EFLCs is mainly producing the ECM component type I collagen that is essential for basal lamina formation and induction of myelination in SCs. Although, it is not the only role that EFLCs undertake in the PNS nerves. EFLCs are often termed as the resident immune cells or resident macrophages of the peripheral nerves. They act as immune surveyors and may present MHC II molecules. They are also known for pro-inflammatory cytokine production and for being activated following an injury to the nerve before the infiltration of hematogenous macrophages. It has been recently suggested that EFLCs might be able to generate other cell types after injury (Richard et al., 2012).

Although the presence of EFLCs in the peripheral nerves has long been described, their origin remained unknown till recently. N. Joseph and colleagues showed that the EFLCs are of NCC lineage and originate from a Dhh expressing progenitor the SCPs. SCP were only thought to differentiate into glial cells; yet, it was not the case. EFLCs do not retain Dhh and P75NTR expression but are Thy1 positive + (Thymus cell antigen 1)- considered as a marker of EFLCs (Joseph et al., 2004). N. Joseph et al. additionally showed that culturing neural crest stem cells *in vitro* in a medium supplemented with BMP4, NRG1 and Delta Fc increased the generation Thy1 positive cells (Joseph et al., 2004). EFLCs also express Neuron-Glial Proteoglycan 2 (NG2) and

CD34 (the haemopoietic stem cell marker) (Richard et al., 2014), which brings ambiguity to EFLCs' origin as some studies might hint to a bone marrow origin.

## 2.4. Perineurial Cells

Peripheral nerves have a characteristic structure that depends on the fasciculation of the nerve fibers into bundles innervating the same target and delimiting the endoneurial space containing the EFLCs, the vasculature, axons and myelinating or non-myelinating Schwann Cells. The perineurium is composed of several layers of perineurial cells that form tight junctions to maintain the structure of the perineurium and limit the infiltration of external substances into the endoneurial space (T. R. Shanthaveerappa et al., 1966). The expression of tight junction proteins is one of the markers of perineurial cells such as Zonula Occludens1 (ZO-1) and glucoprotein Podoplanin. Perineurial cells have been thought to arise from the mesoderm since they resemble, though this hypothesis was dismissed because of the many differences in structure and function. Fibroblasts are unable to surround small axonal bundles at the level of nerve terminals, do not present a double basal lamina, and are not assembled in a very organized way (Kucenas, 2015). Ongoing research is aiming to clarify the origin of the perineurial cell by studying the development of the PNS in zebrafish and mice. A neural crest origin was refuted by the work of Joseph et al. using the Wnt1-Cre+loxP/Rosa+ mice, where only a very small subpopulation of perineurial cells was of NCC origin (Joseph et al., 2004). The other speculation of perineurial cell origin was the neural tube, with work showing that a population of perineurial cells origin form the motor exit points (ventral root of the spinal nerve). Some perineurial cells express the NKx2.2 transcription factor implicated in the differentiation of some CNS derived cells. Nkx2.2 deletion disturbed the myelination and development of neuromuscular junctions (Clark et al., 2014; Kucenas et al., 2008). However, more research is necessary to confirm the origin of all perineurial cell subpopulations. The function of perineurial cells is not only limited to a barrier function, it has been shown that perineurial cells with help of Boundary cap cells play a crucial role in closing the boundaries between CNS and PNS (Kucenas et al., 2009). Zebrafish studies have shown that perineurial cells play a role in nerve regeneration and emphasized an interaction between perineurial cells and SCs for correct nerve development. This was further observed in Parmentier's work on Dhh knock-out mice models, where the absence of Dhh expression in SCs lead to the infiltration of perineurial cells into the endoneurial space and form smaller fascicles around the axons (Parmentier et al., 1999).

## II. The Myelin sheath

The myelin sheath is a specialized insulating layer formed around the axons by the myelinating glia of the PNS, the Schwann cells. The myelin sheath is crucial for healthy functioning of the nervous system. The myelinated section is impermeable to ions and consequently the ion channels are condensed in the region between two consecutive myelinated sections called the Node of Ranvier. This repartition of the ion channels is responsible for the increase of nerve conduction in myelinated fibers as opposed to unmyelinated fibers. The action potential of the nerve propagates from one node to another and is referred to as the saltatory conduction (Girault et al., 2002). OLs and SCs' plasma membranes therefore act as electrical insulators speeding up action potential conduction, reducing current leak out of the axon and reducing axonal energy consumption (D Purves et al., 2001).

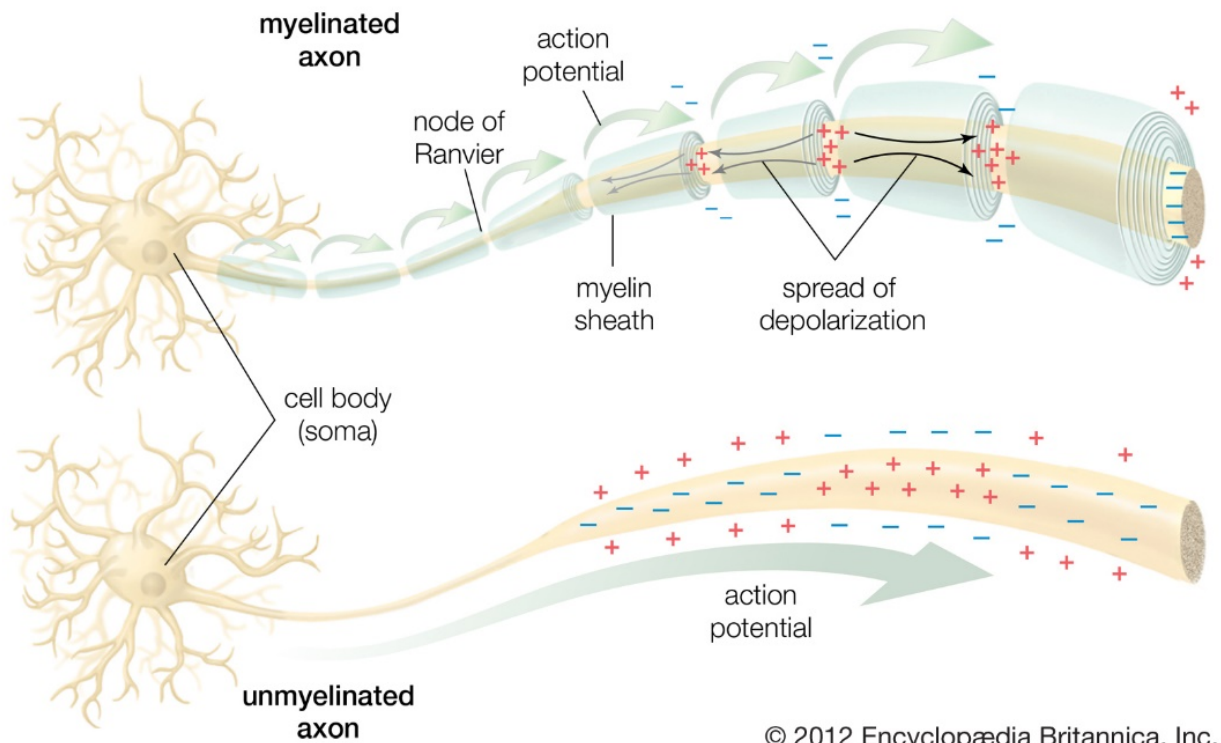


**Figure 15.** Schematic representation of action potential propagation in a myelinated axon (top) and in an unmyelinated axon (bottom) (From: ("Demyelinating Disorders - Physiopedia,")).

## 1. Myelin sheath ultrastructure and characteristics

The SC plasma membrane spiraling around the axons forms the multilamellar myelin sheath (Figure 16A.). Electron Microscopy allows the identification of structural differences between CNS and PNS myelinating cells; for example lamellar periodicity is more prominent in the PNS than in the CNS. (Morell P., 1999). The inner surfaces of the SC cytoplasm condense by the help of proteins to become compact myelin and are referred to as the Major Dense Lines (MDL). The outer surfaces of the cytoplasm are also connected by proteins and are referred to as the Intraperiod Line (IPL) of myelin (Figure 16B.). Another important difference observed by electron microscopy is the presence of a basal lamina (BL) secreted uniquely by the Schwann cells (Figure 16C.). This basal lamina is rich in laminin and plays a significant role in myelination (Court et al., 2006).

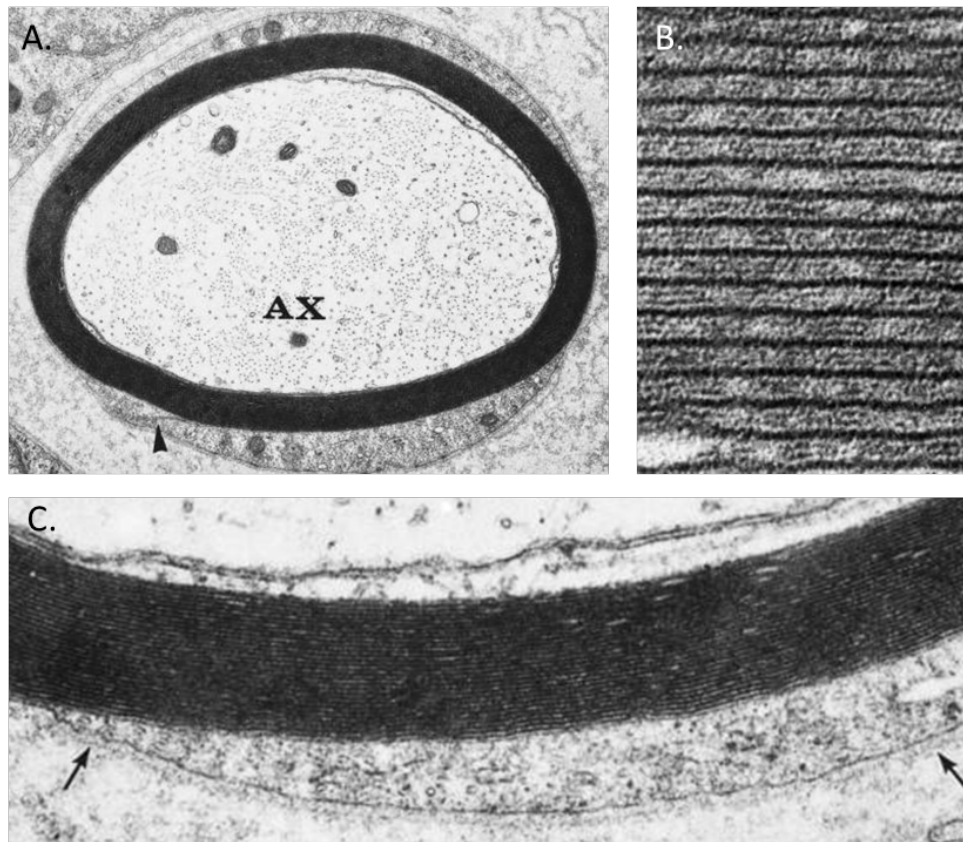


**Figure 16.** Electron microscopy images of a single rabbit sciatic nerve myelinated axon. **A.** myelinated axon. **B.** increased magnification on the myelin sheath, where IPL (light lines) and MDL (dark lines) are observable. **C.** Basal lamina surrounding the myelinated axon (arrows) (Morell P., 1999).

The cytoplasm of the myelinating SCs is not completely compacted and we observe uncompacted regions, such as Schmidt Lanterman Incisures (SLI), Cajal bands, paranodal and juxtaparanodal loops that play a role in myelin maintenance and are enriched in junction proteins and complexes (Figure 17) (J. Salzer et al., 2016).

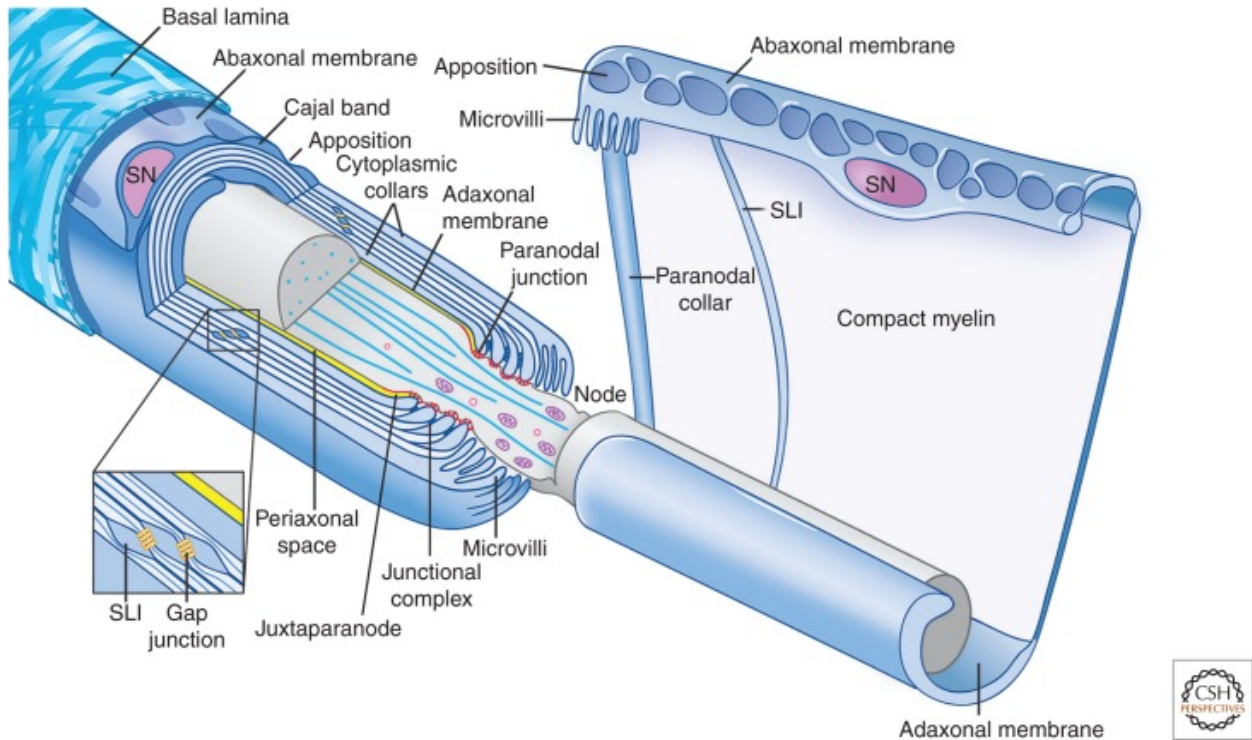


**Figure 17.** Representation of a myelinating Schwann cell at the level of the Node of Ranvier (J. Salzer et al., 2016).

## 2. Composition of the myelin sheath

The insulating characteristic of the myelin sheath is determined by the composition of the plasma membrane. The myelin sheath has a specific birefringence under polarized light that depends on its constituents and which was later described as a mosaic of both lipid and protein layers (Morell P., 1999).

The myelin sheath is distinguished from other plasma membranes by its high lipid to protein ratio. Myelin dry weight is mainly composed of lipids which make up to 70% of the sheath while proteins make up only 30% (Schmitt et al., 2015). The exact myelin sheath lipid composition is not fully defined, studies have shown that the composition of the plasma membrane depends on the specie, the cell type and its stage of development (Noutsu et al., 2016).

### 2.1. Myelin proteins:

Myelin proteins represent 20-30% of the myelin sheath dry weight and are specific. Some are found in the compacted regions and others are found in the uncompact regions of the myelin sheath. A handful of proteins have been identified and in contrast to the CNS the majority of these proteins are glycoproteins such as Myelin Protein Zero (P0), Peripheral Myelin Protein 22 (PMP22), Myelin Associated Glycoprotein (MAG) and Epithelial Cadherin (E-Cadherin). A second prominent category of myelin proteins are the basic proteins such as Myelin Basic Protein (MBP) and Protein 2 (P2). Other types of proteins are also found in the myelin sheath of the PNS like 2'3'-cyclic nucleotide 3'-phosphodiesterase (CNP), Proteolipid Proteins (PLP/DM20) and Connexin 32 (CX32). The expression of these proteins contributes to different aspects of SC development and mostly in the structural integrity, compaction and stabilization of the myelin sheath (Garbay et al., 2000; Morell P., 1999).

#### **Myelin Protein Zero (P0)**

The most prominent protein found in the myelin sheath is Myelin Protein Zero (P0, MPZ). P0 is specific to the PNS. P0 is a 28 kDa integral membrane glycoprotein that is responsible for the compaction of apposing membranes of the myelinating SC through homophilic binding creating the intra-period line (Filbin et al., 1990; Raasakka et al., 2020). P0 null mice emphasized its role in myelination, compaction and maintenance, where in heterozygous P0<sup>-/-</sup> mice thinly myelinated

and uncompacted SC loops were observed as early as postnatal day 4 followed by demyelination at later stages. These mice also showed poor motor coordination, tremors and occasional convulsions (Giese et al., 1992; Rudolf Martini et al., 1995)

### **Myelin Basic Protein (MBP)**

MBP is a strongly basic intrinsically disordered protein found abundantly in both the CNS and PNS. MBP electrostatically interacts with the cytoplasmic leaflets mediating compaction and closing the cytoplasmic regions (R. Martini et al., 1995). Many isoforms of MBP are found, the most notable are the 18.5 kDa and 14.5 kDa proteins. MBP knock out in the PNS results in reduction of myelin thickness and compaction, also an increase in the number of SLIs (Gould et al., 1995).

### **Peripheral Myelin Protein 22 (PMP22)**

PMP22 is a four transmembrane glycoprotein that is found in compact myelin. One of its extracellular loops interacts with another PMP22 protein through homophilic binding, and the other extracellular loop interacts with P0 (Naef et al., 1998). PMP22 only represents 2 to 5% of myelin proteins however different types of mutations to this gene are responsible for the majority of inherited peripheral neuropathies (van Paassen et al., 2014). The structure of PMP22 hints at its functional role in correct myelin formation, maintaining stability and compaction of the myelin sheath. However, PMP22 is also involved in SC proliferation, apoptosis, migration and adhesion functions mediated through actin microfilaments (S. Lee et al., 2014; Sancho et al., 2001)

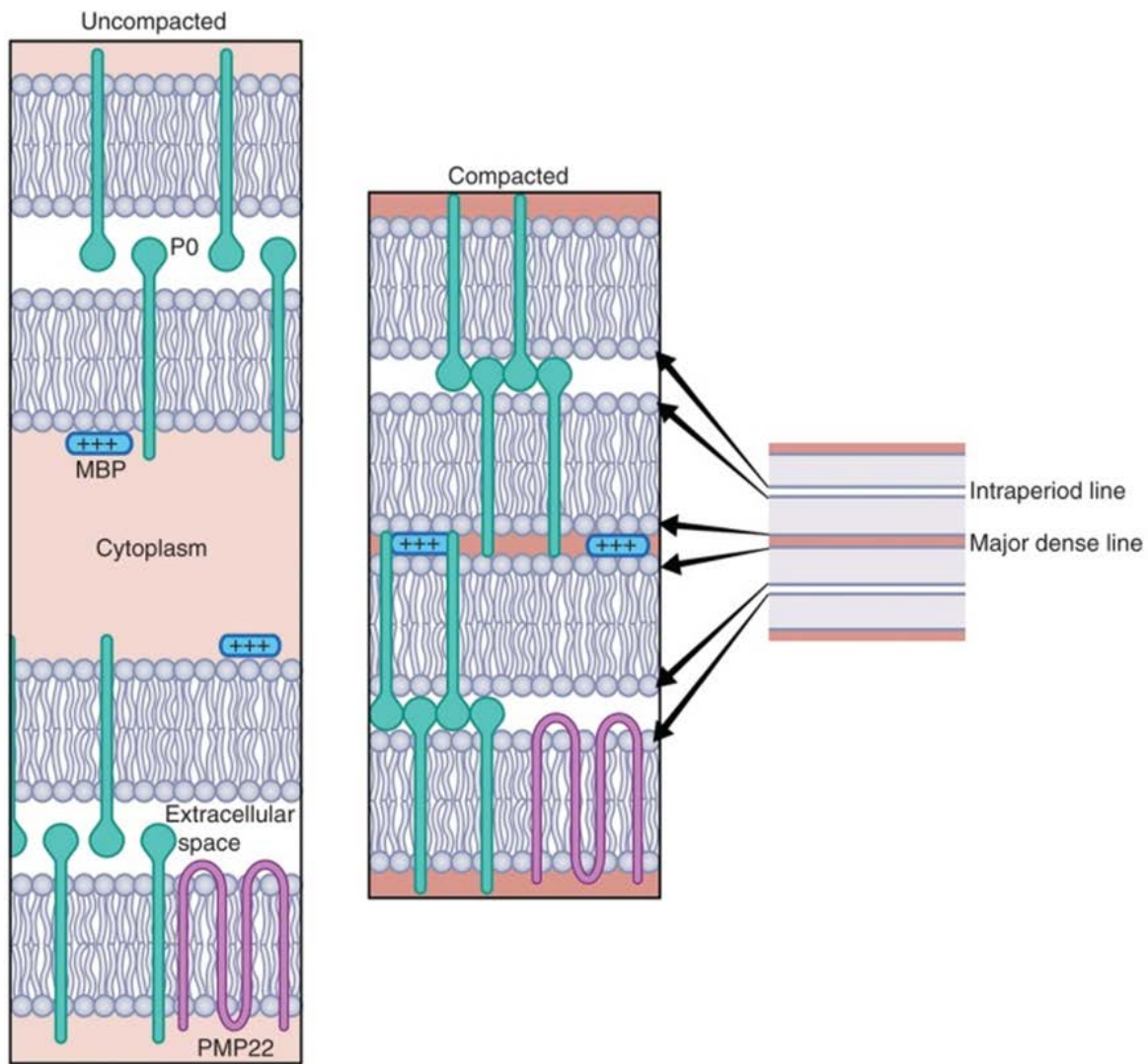


**Figure 18.** Schematic representation of the localization and role of myelin proteins in the compaction of the myelin sheath (J. Salzer et al., 2016).





## 2.2.Lipids of the Myelin sheath

Many studies have evaluated the lipid composition of the PNS myelin from mice, rats, bovine and human sciatic nerves. While CNS and PNS specific proteins have been identified no myelin-specific lipids have been cited, as all major lipid classes are present in the myelin. The difference resides in the concentration of certain lipids that would be more important in a system than in the other. The lipid classes involved in myelin sheath composition are: phospholipids, glycolipids and cholesterol (Siegel, 1999), with a remarkably higher presence of sphingomyelin and phosphatidylcholine in the PNS compared to the CNS (Heape et al., 1986). In the following sections the major classes of lipid present in the myelin sheath will be detailed with a special focus on the PNS. Table 2 summarizes the lipid composition of CNS versus PNS myelin.

	PNS <sup>a</sup>	CNS <sup>b</sup>
Cholesterol	41%	46%
Glycolipid	11%	20%
↳ Galactosylceramide	10%	17%
↳ Sulfatide	1%	3%
Phospholipid	29%	26%
↳ Plasmalogen	12%	13%
↳ Phosphatidylcholine	10%	7%
↳ Other Phospholipid	7%	7%
Sphingomyelin	13%	6%
Other lipids	6%	2%

**Table 2.** Lipid composition of bovine spinal root and brain (Poitelon et al., 2020) adapted from (O'Brien et al., 1967)

### **BOX 3. Methods of lipid composition analysis**

The widely used techniques for evaluating lipid composition of tissue are chromatography, nuclear magnetic resonance (NMR) and mass spectrometry (MS). The most commonly used techniques for myelin sheath lipid analysis are chromatography based techniques coupled to mass spectrometry for a thorough analysis of the lipids; like gas chromatography mass spectrometry (GC-MS) and high performance liquid chromatography mass spectrometry (HPLC-MS) (S. N. Fewou et al., 2009). Although GC-MS and HPLC-MS require the extraction of lipids from the sample and potentially damage the native conformation of the lipids; the detection of lipids is much more sensitive than techniques that do not require extraction for example NMR (van Echten-Deckert et al., 2006). In notably recent years, matrix assisted laser desorption and ionization mass spectrometry (MALDI-MS) as well as time of flight secondary ion mass spectrometry (ToF-SIMS) have been applied to lipid analyses. MALDI-MS and ToF-SIMS techniques are less sensitive than GC-MS and HPLC-MS, however they offer the advantage of measuring the composition of thin tissue sections and visualization of the spatial distribution of lipids (McDonnell et al., 2007).

Unfortunately, no single technique can characterize all lipids due to their diverse physical and structural properties of these biomolecules.

### 2.2.1. Cholesterol

The most abundant component of the PNS myelin is cholesterol, making up 30 to 40% of dry weight of total PNS myelin. Cholesterol plays a major role in myelin multilamellar membrane insulation, stabilization, compaction and viscosity. It also plays a role in protein regulation and transport (Saher et al., 2009).

Cholesterol availability is very critical for PNS myelin formation and is mainly, locally produced by Schwann cells using the *de novo* synthesis (Fu et al. 1998). Cholesterol synthesis first starts with the mevalonate dependent isoprenoid pathway by the condensation of two molecules of Acetyl-CoA into Acetoacetyl-CoA, followed by a second condensation with an Acetyl-CoA molecule to form the 3-hydroxy-3-methylglutaryl-CoA (HMG-CoA). HMG-CoA reductase then converts HMG-CoA into mevalonate, this step is known as the rate limiting step in the cholesterol biosynthesis pathway. HMG-CoA reductase (HMGCR) competitive inhibition by statins was discovered to be a very potent therapeutic drug for lowering cholesterol levels in patients. By a series of phosphorylation, mevalonate is converted into Geranyl-P-P then into Farnesyl-P-P. Farnesyl-P-P conversion into squalene by the squalene synthase is the first step into the sterol pathway. Squalene synthase (SQS; farnesyl-diphosphate farnesyl transferase) is also considered as a rate limiting enzyme in the biosynthesis of cholesterol. Squalene is converted into squalene epoxide, then is cyclized to lanosterol. Through a series of enzymatic reactions lanosterol is then converted to cholesterol (Cortes et al., 2014).

Cholesterol biosynthesis is very energy demanding, expression levels of cholesterol biosynthesis enzymes increase by more than 3 folds during early myelinogenesis (between postnatal day P2 and P10), to accumulate cholesterol in the myelin membrane, and then decrease to maintain a baseline expression level in adult stages (Verheijen et al., 2003).

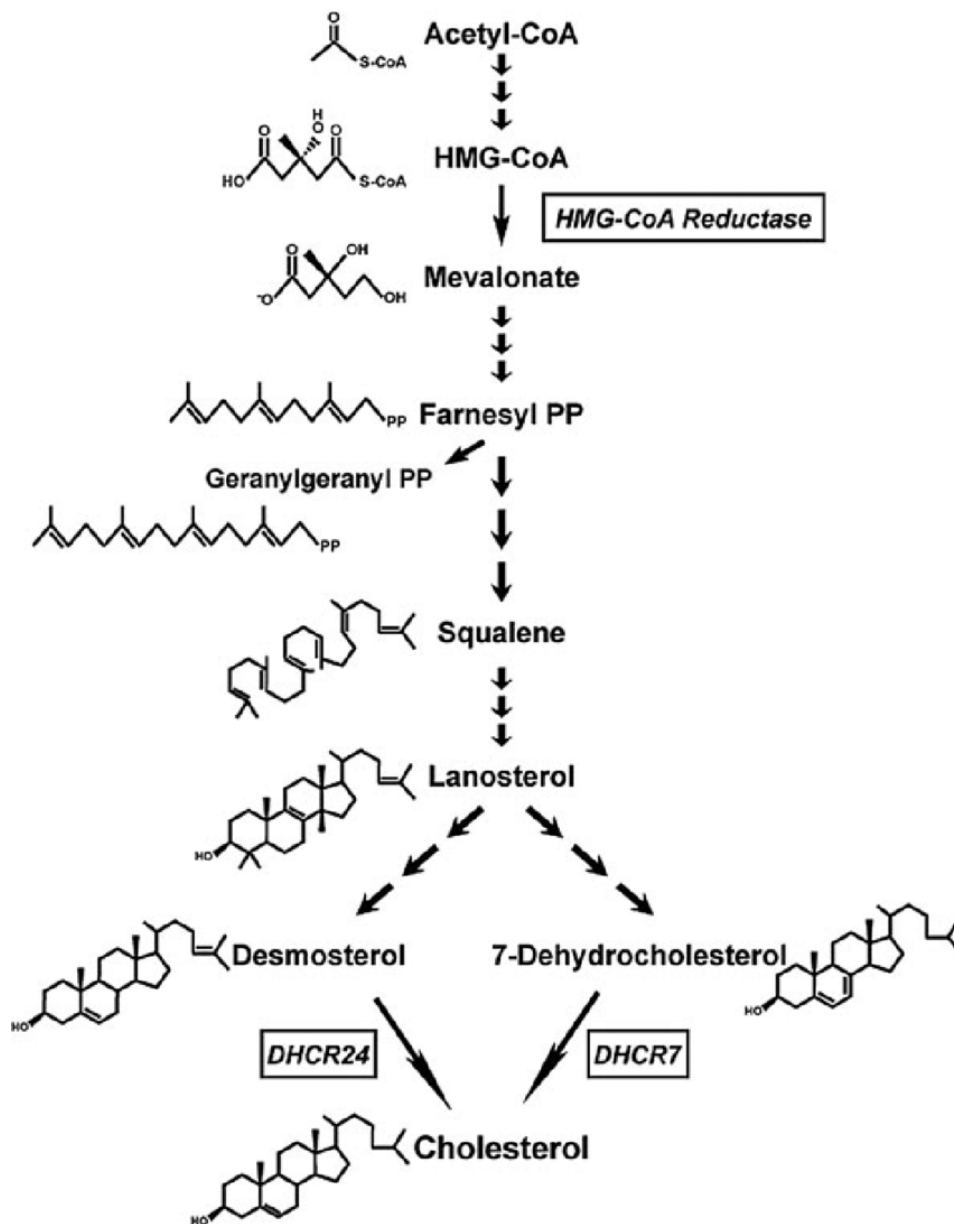


**Figure 19.** Cholesterol biosynthesis (Cortes et al., 2014).

Cholesterol and lipid synthesis is tightly regulated by Sterol Regulatory Element Binding Proteins (SREBPs); a family of transcription factors that are sensitive to sterol levels. The SREBP are firstly bound to the membranes of the Endoplasmic Reticulum bound to SREBP Cleavage-Activating Protein (SCAP).

When cholesterol levels are elevated, the relocation of SREBP to the Golgi apparatus is halted, cholesterol binds to SCAP followed by the binding of INSIG (insulin Induced Gene) which inhibits the translocation.

In the absence or reduced levels of cholesterol levels SREBP is translocated to the Golgi apparatus, then cleaved by resident proteases the S1P and S2P (site 1 and site 2 proteases), releasing the SREBP from the Golgi. SREBP then translocate to the nucleus and binds to Sterol Regulatory Elements (SRE) found on DNA and activates transcription of genes responsible for the biosynthesis of cholesterol and fatty acids such as HMGCR and FASN (Fatty Acid Synthase) (Brown, 1997).

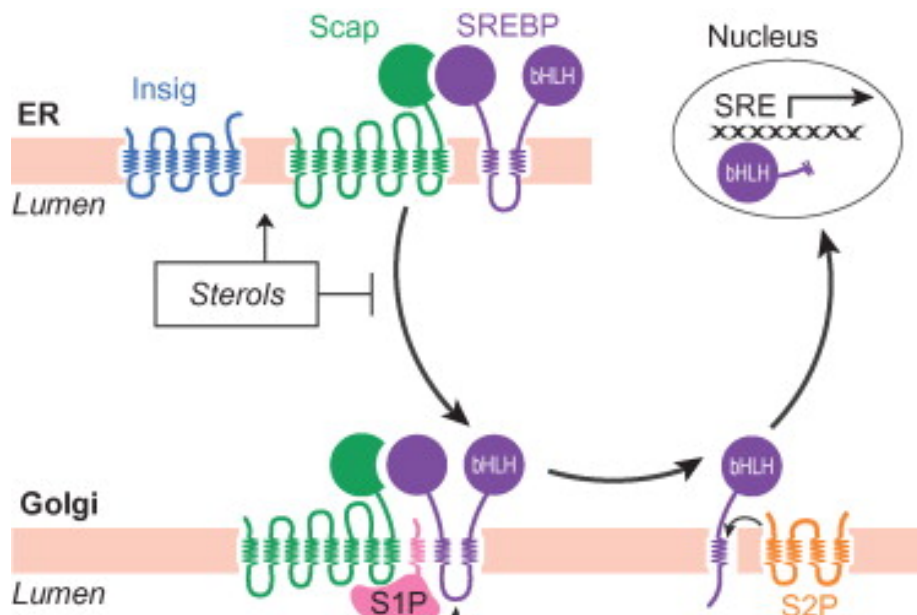


**Figure 20.** Schematic representation of SREBPs mechanism of action (Radhakrishnan et al., 2010).

SREBP has three isoforms SREBP1a, SREBP1c and SREBP2. SREBP2 is responsible for cholesterol biosynthesis. SREBP1 is not as sensitive to cholesterol levels as SREBP2, it is mostly induced by insulin and glucose. SREBP1c is responsible for the regulation of lipogenesis however SREBP1a regulates both lipid and cholesterol biosynthesis (Radhakrishnan et al., 2010).

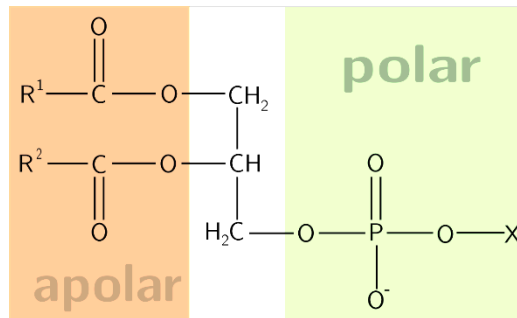
Disruption of cholesterol synthesis by elimination of SCAP (also affecting the lipid metabolism) or SQS- a rate limiting enzyme of cholesterol synthesis- showed respectively hypomyelination and dysmyelination of the nerves of the PNS (Saher et al., 2011; Verheijen et al., 2009). SQS mutants could not recover from this phenotype however SCAP mutants were able to uptake lipids from external sources and enhance myelination over time nevertheless, myelin thickness did not reach normal levels.

These findings implicate that cholesterol is essential for maintaining the integrity of the myelin sheath however, there are means of cholesterol uptake independent of the *de novo* synthesis by the help of Low-Density Lipoprotein receptors (LDLr). After facing nerve injury, SCs uptake cholesterol and lipids from neighboring cells forming the LDLs and reutilize them. The fact that LDLr knockout mice are able to uptake cholesterol after injury without the upregulation of HMGCR also points out to the presence of different cholesterol and lipid uptake players (Rothe et al., 1991).

The role of cholesterol is not limited to being a structural element of the myelin sheath, it also plays a role in the regulation of major myelin specific proteins such as P0. Cholesterol is responsible for the regulation of P0 export from the endoplasmic reticulum to the myelin compartment of Schwann cells, and its reduced availability leads to myelin sheath structural abnormalities (Saher et al., 2009).

### 2.2.2. Glycerophospholipids

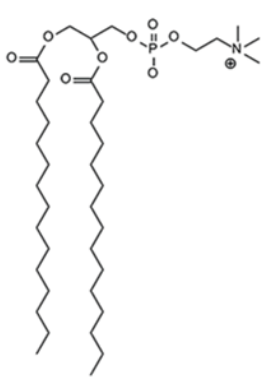
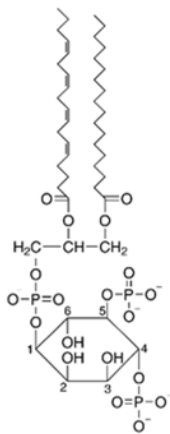
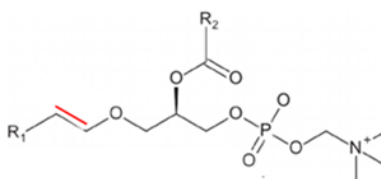
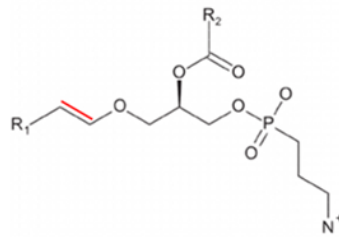
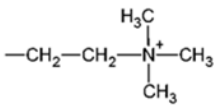
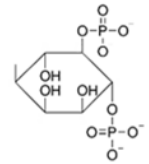
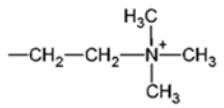
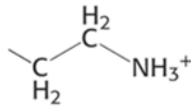
Glycerophospholipids constitute the second most abundant lipid class in the PNS myelin sheath also known to be the anchoring lipids of the plasma membrane. Glycerophospholipids play crucial structural and metabolic roles in cells also in the myelin sheath. Glycerol serves as the alcohol backbone of this lipid class (Aggarwal et al., 2011). Two fatty acid groups are attached to glycerol as esters and are non-polar thus hydrophobic. A phosphatidyl ester group is attached to the third carbon of glycerol backbone and is considered the polar head with hydrophilic properties.



**Figure 21.** Structural representation of a glycerophospholipid (Phospholipid.svg. (2020, September 20). Retrieved from Wikimedia Commons, the free media repository).

The amphipathic nature of this lipid class is what leads to the formation of the phospholipid bilayer, where the hydrophobic tails of fatty acids are pointing inwards and the polar groups are pointing outwards. There is a variety of phospholipids; they differ by the head group attached to the glycerol backbone like phosphatidylcholine, phosphatidylserine, phosphatidylinositol or by the presence of a vinyl ether and ester bonds like plasmalogens (S. Fewou et al., 2009).

The distribution of the glycerophospholipids is not homogeneous some are present at the outer leaflet of the plasma membrane and others are found on the inner leaflet (Poitelon et al., 2020).

Name of glycerophospholipid	Phosphatidylcholine	Phosphatidylinositol 4,5-bisphosphate	Plasmalogens	
			Phosphatidylcholine Plasmalogen	Phosphatidylethanolamine Plasmalogen
Structure				
Name of head group	Choline	Myo-Inositol 4,5-bisphosphate	Choline	Ethanolamine
Head group structure				
Role in the PNS myelin	Structural component of the myelin sheath.  Plays a role in the initiation of the myelin sheath, its compaction and maintenance (Heffernan et al., 2017).	Structural component of the myelin sheath.  Interacts with myelin proteins and regulate cellular processes; endocytosis, actin remodeling and cell growth (Alvarez-Prats et.al, 2018)	Structural component of the myelin sheath.  Most abundant glycerophospholipid in the PNS myelin sheath.  Role in myelin stabilization by bond strengthening with other lipids of the membrane. Plasmalogen absence in the PNS leads to a distorted sorting of the axons and hypomyelination. Plasmalogens are thus critical for axon-glia recognition and normal myelination (da Silva et al., 2014)	

**Table 3.** Structure and role of the glycerophospholipids in the PNS.



### 2.2.3. Sphingolipids

Sphingolipids are a major class of lipids found in all cell plasma membranes, and especially in the membranes of myelinating glia. All sphingolipids are composed of a sphingosine backbone linked to a fatty acyl chain at the C2-amino group thus synthesizing ceramide, the building block of complex sphingolipids (Gault et al., 2010). Ceramide is known to play a role in diverse mechanisms such as cell proliferation, apoptosis and differentiation (Riebeling et al., 2013). Ceramide production takes place in the endoplasmic reticulum and is transported to the Golgi, by the ceramide transport protein (CERT) to give rise to the complex sphingolipids (Wattenberg, 2019), as represented in Figure 22.

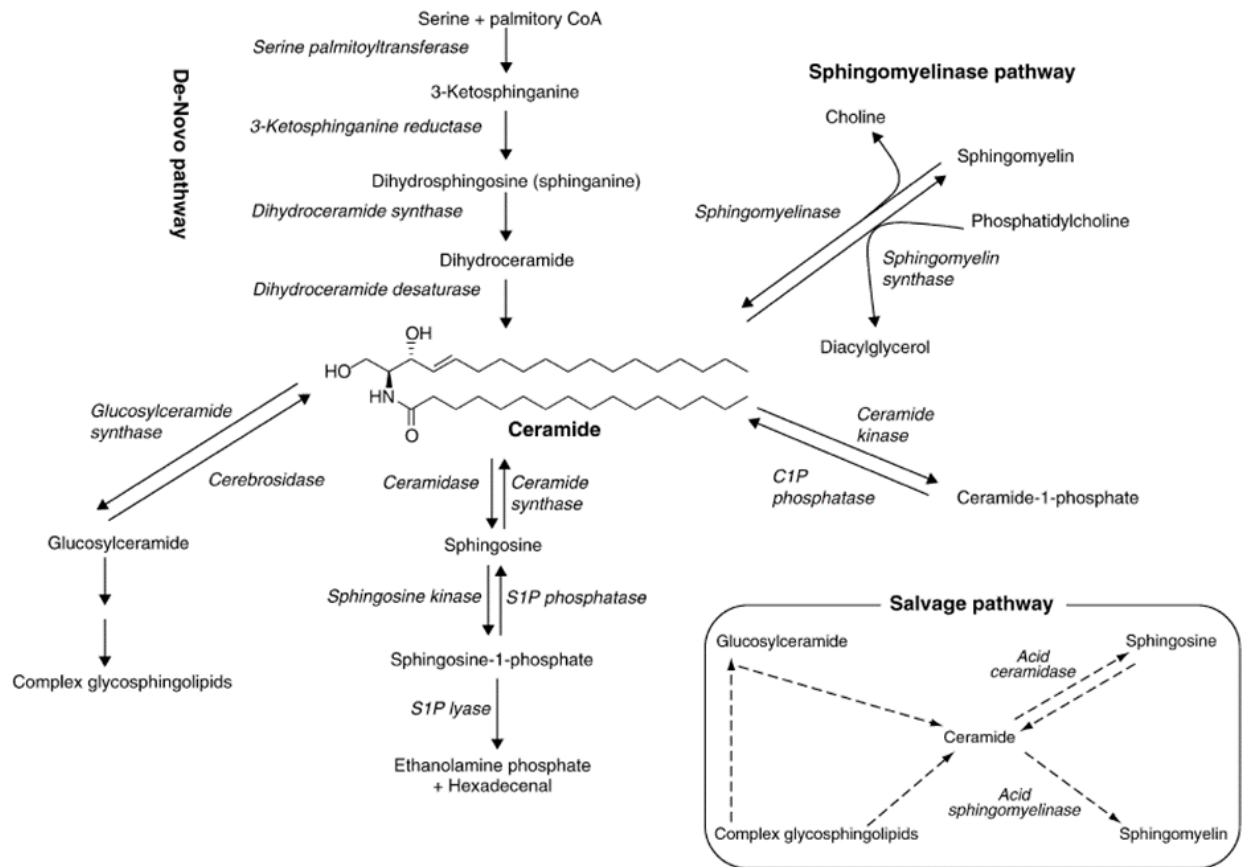


**Figure 22.** Sphingolipid metabolism (Lajtha et al., 2009)

Ceramide is considered as the entry point to the metabolism of the different sphingolipids, which are very diverse in structure and functionality. Sphingolipids differ by the head group added to ceramide with the help of different enzymes. Two major subclasses of sphingolipids found in the myelin sheath are **sphingomyelin and glycosphingolipids**.

In the CNS the disruption of sphingolipid metabolism leads to numerous diseases, as seen in Figure 23, which have been reviewed recently by Giussani and collaborators (Giussani et al., 2020). In this study, the focus will be directed on their role in the peripheral nervous system.

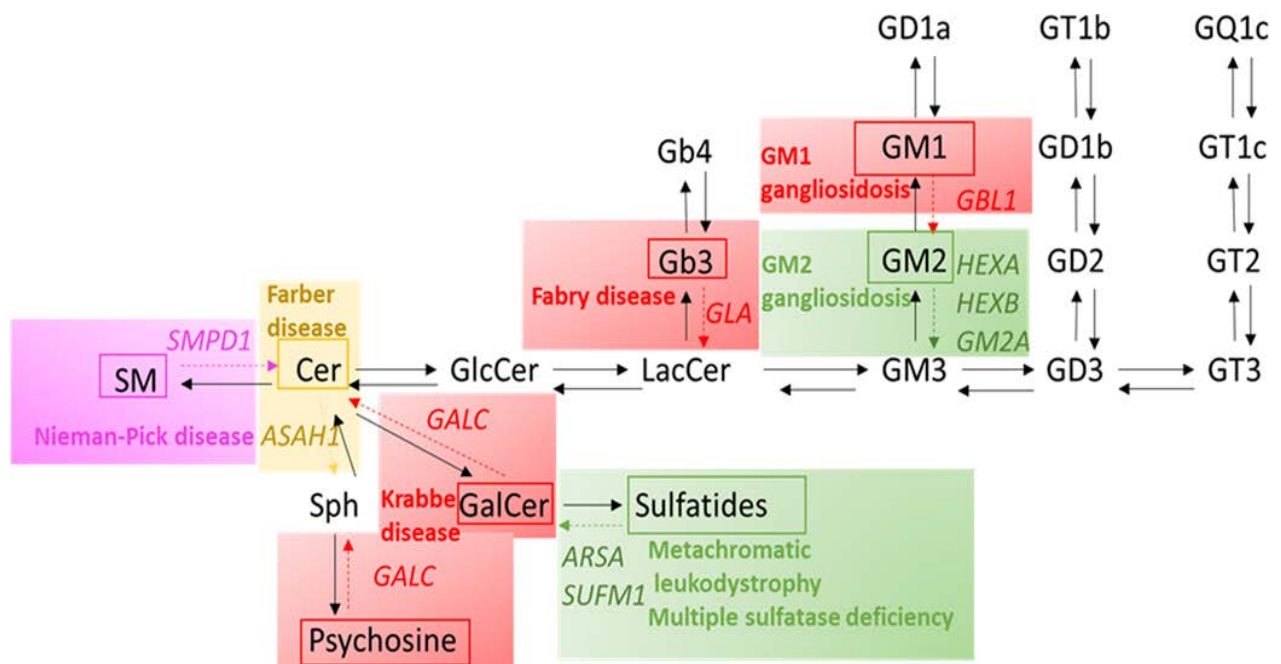


**Figure 23.** Sphingolipid metabolism and pathologies resulting of its disruption in the CNS (Giussani et al., 2020).

### **A. Glycolipids -Galactosylceramide and Sulfatide**

Although there are no myelin specific lipids, Galactosylceramide or galactocerebroside (GalC) and its sulfated derivative, Sulfatide (sGalC), are specifically abundant in the membranes of myelinating glia of the CNS and PNS (Norton et al., 1984). Galactolipids are composed of a sphingosine backbone, a very long chain fatty acid tail group and a galactose head group. Approximately 5% of the galactolipids at early stages of myelination are hydroxylated at the C-2 position of their fatty acids (FA) chain. The length of the FA chains as well as the 2- hydroxylation increase during myelination and are important for the maintenance of the myelin sheath (Maldonado et al., 2008; Zöller et al., 2008). Very hydrophobic bonds are formed between the fatty acid chain tails which give high stability to the myelin sheath, the bonds are often referred to as membrane zippering.

GalC is mostly found in the compact part of myelin and sulfatide is found in the non-compact myelin. GalC and sulfatide are generated by the addition of a galactose (from a UDP-galactose), to a ceramide by the UDP-galactose:ceramide galactosyl-transferase (CGT) (Morell et al., 1970)

CGT null mice, unable to express GalC or sGalC, exhibit a disruption of nerve conduction and motor deficits however myelin specific proteins were reported to be expressed normally (Bosio et al., 1996; Coetzee et al., 1996). Earlier studies could not detect the anatomical and structural consequences of GCT<sup>-/-</sup> on the myelin sheath that would explain the phenotype, but showed an altered myelin lipid composition. Sulfated glucosylceramide as well as  $\alpha$ -hydroxy substituted fatty-acids of ceramide and sphingomyelin were detected in the knockouts while they were non-detectable in the wild types (Bosio et al., 1996; Coetzee et al., 1996). Later studies solely targeting sulfatide expression revealed that its ablation leads to abnormal paranodal regions and elongation of nodal sodium channels areas, leading to an altered ion permeability both in the CNS and PNS (Hayashi et al., 2013; Hoshi et al., 2007; Marcus et al., 2006). These studies highlight the role of GalC and sGalC in myelin stability, insulation and proper function of the myelinated axons.

### **B. Sphingomyelin**

The only remarkable difference between CNS and PNS myelin lipid composition is the enrichment of PNS myelin sheath with sphingomyelin (SM). SM represents 10-35% of lipid dry weight in the PNS (Garbay et al., 2000) however it only represents 3-7% in the CNS (Brady, 2005).

Sphingomyelin is synthesized by the addition of a phosphocholine head group to a ceramide by the help of sphingomyelin synthase (SMS), isoform 1 and 2 residing in the Golgi and plasma membrane respectively. In non-neuronal cells SM synthesis is described to primarily take place in the Golgi by SMS1, however in neuronal cells more SM are synthesized at the level of the plasma membrane by SMS2, up to 50% in the plasma membrane of oligodendrocytes (Poitelon et al., 2020; van Echten-Deckert et al., 2006). SM incorporates at the outer leaflet of the plasma membrane and plays an important role in forming protein/lipid complexes, in myelin membrane protein trafficking (Kim et al., 1999) and signaling transduction pathways (Hannun, 1994).

Knockout mouse models of SMS1 and SMS2 showed no consequences on central or peripheral myelin (Li et al., 2012). SMS2 deficiency in mice showed neuroprotective effect in cerebral ischemic reperfusion injury, by suppression of microglia activation and reducing levels of proinflammatory cytokines (Hailemariam et al., 2008; Xue et al., 2019). In a previous review, the authors hypothesized that SMS2 might have a late onset discrete phenotype where structural consequences may be detected at developed stages.

On the other hand, SM homeostasis is very important in the CNS where the knockout of acid Sphingomyelinase (ASMase) – enzyme responsible for the hydrolysis of SM back into ceramide – enhances the recovery of the oligodendrocytes after cuprizone treatment (Chami et al., 2017). However, SM accumulation caused by acid sphingomyelinase enzymatic deficiency in Nieman-Pick disease type A leads to neurodegeneration (Giussani et al., 2020).

A scarce number of studies evaluate role of sphingomyelin in the PNS, only a recent study suggested that the index of presence of SM in human CSF might be a potential biomarker of PNS demyelinating neuropathies (Capodivento et al., 2017).

#### 2.2.4. Fatty Acids (FAs)

In Schwann cells as in all other cell types, the majority of the fatty acids – the fundamental units of all myelin lipids except cholesterol – come from food intake and can be transported by Fatty Acid Transport Proteins (FATP), Fatty Acid Translocase (CD36) or can diffuse passively through the membrane (Schwenk et al., 2010). However due to the high demand of FA during myelination and maintenance of the myelin sheath, the non-essential fatty acids are also greatly synthesized in the cytoplasm of the SCs. Essential fatty acids (major families of omega-3 and omega-6) like Linoleic Acid and  $\alpha$ -linoleic acid can only be provided by food intake (Trapp et al., 1978).

FA synthesis starts by the carboxylation of acetyl CoA into malonyl-CoA. Then, through the action of Fatty Acid Synthase (FASN), a multienzyme complex, and the presence of NADPH, the acetyl-CoA moiety, is released and the 2 carbon chain is extended to 16 saturated carbons resulting in the formation of Palmitic Acid (C16:0) (Cassagne et al., 1986). The elongation or reduction of the FA carbon chain length is provided by other enzymes and the chain length can vary from 2 to 30 carbons. Another important feature of the FAs is the levels of saturation which directly affect the fluidity of the membrane.

FAs are crucial for the normal myelination onset and composition, the expression of FASN is timely with myelination and is tightly regulated by SREBP1c in Schwann cells (De Preux et al., 2007).

The length of the FA carbon chain is not specific to a particular lipid. However, the length can be suggestive, in some cases, of a certain lipid class. The diversity of lipid extraction and detection techniques do not allow us to compare the findings of all studies to one another, nevertheless all studies have stated a distinctive distribution of FAs in the myelin sheath (Figure 24).

The myelin sheath is known for its high content of 16 and 18 carbon chain FAs all throughout development and myelin maintenance, with Oleic Acid [C18:1 (n-9)] being the major form found in the PNS myelin (around 30 to 40% of PNS FAs) (Fressinaud et al., 1986; Pratt et al., 1969). Garbay and colleagues evaluated the FAs of rat SNs during development in normal and hypomyelinated nerves, and stated that the C18:1/C18:2 ratio is a good indicator of the myelin status during the development of the PNS. Fatty aldehydes of C16:0, C18:0 and C18:1 derivatives are usually found in the ether linked glycerophospholipid; plasmalogens (Garbay et al., 2000).

Another distinguishing trait of the myelin sheath is the important presence of very long chain fatty acids (VLCFAs), from 20 to 24 carbon FA chains which are metabolized in peroxisomes. VLCFAs are mostly integrated in sphingolipids and the most abundant form of VLCFAs is lignoceric acid (C24:0). The majority of the VLCFAs are saturated and play an important role in the stabilization the myelin sheath (Heape et al., 1986).

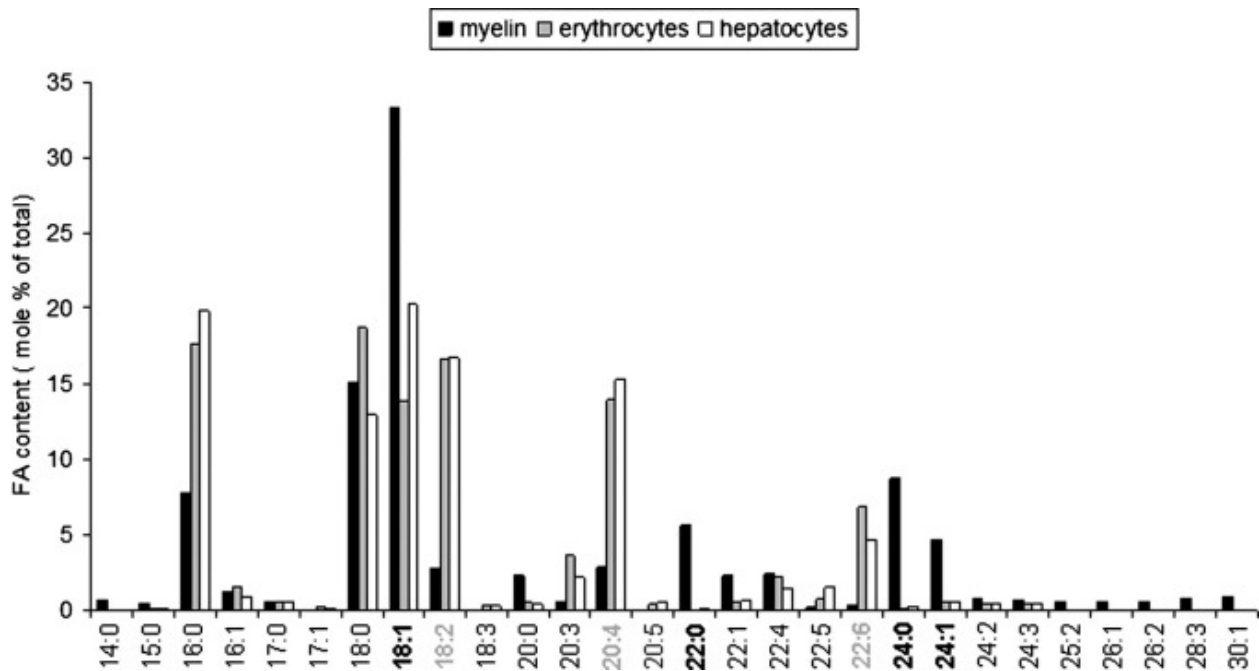


**Figure 24.** Comparison of Fatty Acid content in PNS myelin versus erythrocyte and hepatocyte plasma membranes in mice (Chrast et al., 2011).

The importance of FAs is highlighted by the numerous knock out models that target FA synthesis, transport and supplementation.

The FASN conditional knock out model in SCs during myelination has shown that SCs are able to survive and proliferate however there is a defective myelination onset, and an impairment in lipid composition due to the lack of Palmitate and different lipids. This model also highlighted the gene modulatory role FAs play by their interplay with Peroxisome proliferator-activated receptors (PPARs). The attempt of compensating FASN absence by high fat diet in order to regain normal lipid distribution and composition, was not successful in this context (Montani et al., 2018). However in a recent study, giving CMT1A model rats (reduction of Lipid biosynthesis) a specific diet rich in ameliorated the phenotype (Fledrich et al., 2018).

### 3. Lipid/ protein interaction

The myelination process requires large amounts of lipids and proteins to be produced and transferred to the wrapping plasma membrane of SCs. The high content of lipids is very specific in myelinating glial plasma membrane and does not resemble other plasma membranes majorly enriched in proteins (Morell P., 1999). SCs have been described as epithelial polarized resembling cells that present apical and basolateral membranes with different compositions and transport. The apical membrane resembling myelin sheath is even more complex where lipid and protein distribution is asymmetric in the leaflets of the membrane bilayers (Trapp et al., 1995). Phospholipids such as phosphatidylserine, phosphatidylinositol and plasmalogen are found at the level of the inner cytoplasmic leaflet of the myelin sheath. As for the outer leaflet, it is highly enriched in sphingolipids such as SM, GalCer also phosphatidylcholine and cholesterol (Figure 25).

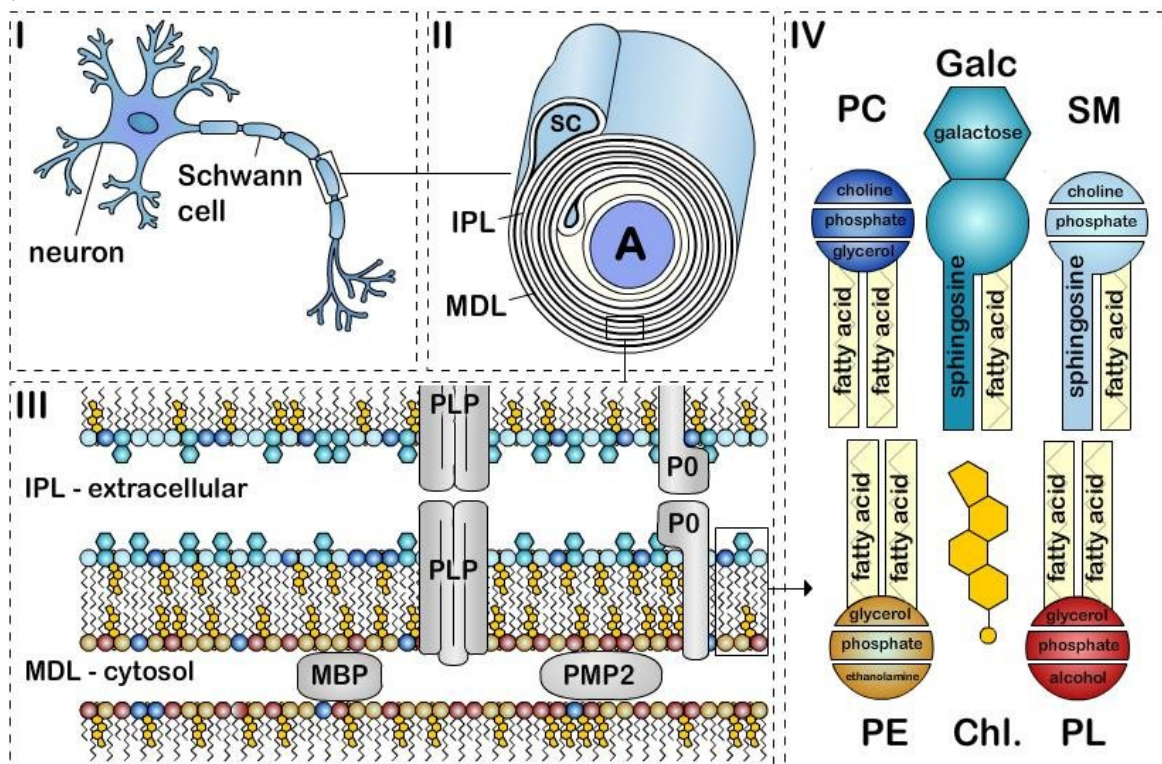


**Figure 25.** Localization of myelin lipids and proteins in the myelin sheath of the PNS (Poitelon et al., 2020).

The outer leaflet is very rich in cold detergent resistant microdomains termed lipid rafts (A. G. Lee, 2001). Lipid rafts formation is mediated by the tight packing of long saturated FA chains presented by the sphingolipids (forming solid domains); however, the rafts are not only enriched

by sphingolipids but is also very rich in cholesterol. Cholesterol plays an essential role on lipid packing and forms a liquid ordered state, increases lateral fluidity and limit small molecules diffusion (Munro, 2003). The lipid raft is a dynamic domain that plays a role in the regulation of myelin protein trafficking, myelin formation and stability. Recent studies have been highlighting the role of the trans-Golgi network in the assembly of the lipid rafts that also incorporates proteins and mediate their transport to the plasma membrane (Baron et al., 2010). Many major PNS myelin proteins have been found in these lipids' rafts and have shown specific binding to the lipids of the rafts. For example, P0 binds specifically to cholesterol through its CRAC motif. The work of Saher and colleagues revealed that P0 exiting from the ER is cholesterol dependent and essential for correct myelin formation (Saher et al., 2009). Recent and ongoing work has also proven that PMP22 is found in the lipid rafts and plays a role in the sequestration of cholesterol at the level of the plasma membrane mostly through its CRAC motif (S. Lee et al., 2014; Zhou et al., 2020; Zhou et al., 2019). MAG has been shown to bind to GalCer and Sulfatide at the level of the uncompacted regions of the myelin sheath and are necessary for its correct organization (Erne et al., 2002). Therefore, specific lipids/proteins play multiple roles in maintaining the integrity and homeostasis of the myelinating SCs.



### III. Liver X Receptor in the Peripheral Nervous System

#### 1. Liver X Receptor

The Liver X Receptor (LXR) is a member of the nuclear receptor superfamily, discovered in 1994 by multiple research groups (Apfel et al., 1994). LXR was initially considered as an orphan receptor and given different names. The discovery of its ligands, the endogenous oxysterols, deorphanized LXR and hinted at its functions. LXR is present in two isoforms: LXR- $\alpha$  (NR1H3) and LXR- $\beta$  (NR1H2) encoded by the genes present on human chromosomes 11 (chromosome 2 in mice) and 19 (chromosome 7 in mice) respectively and present around 80% homology in the proteins amino acid sequence.

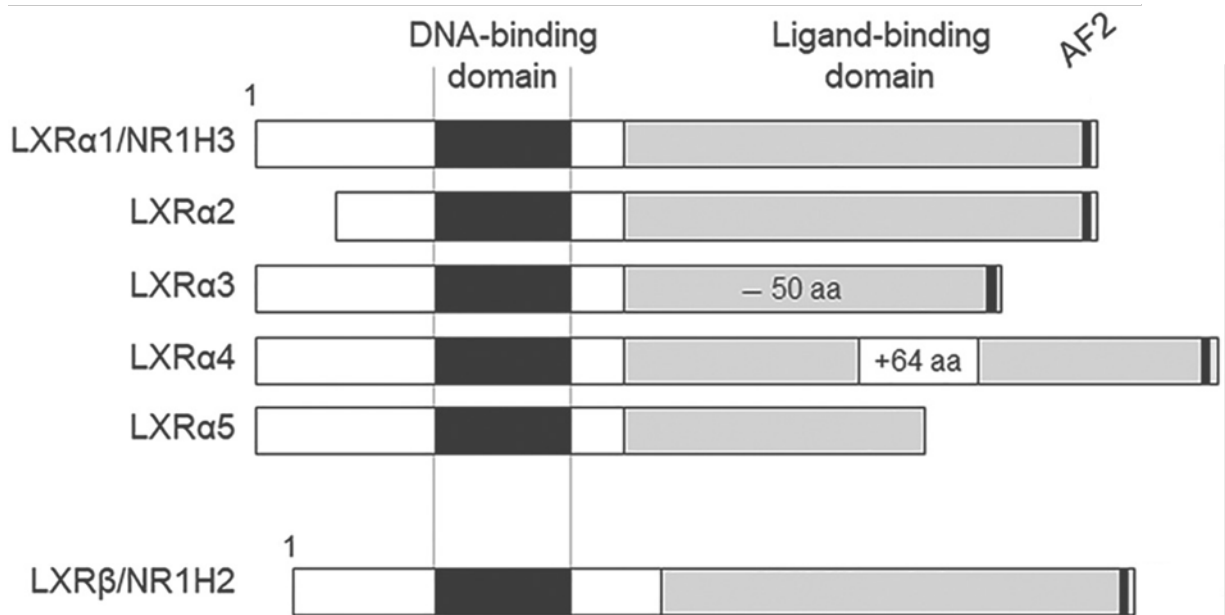


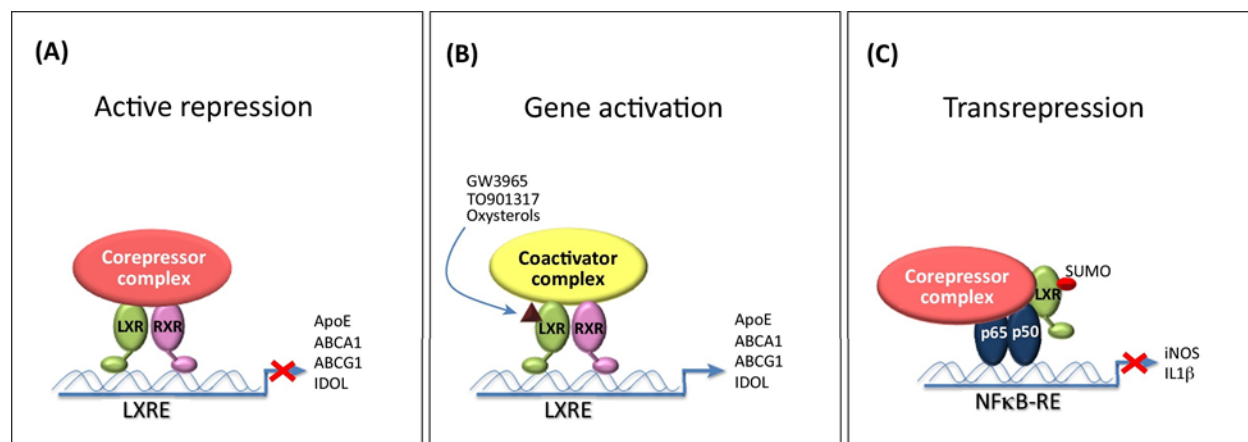
**Figure 26.** LXR $\alpha$  and LXR $\beta$  proteins (Bunay et al., 2020). LXR  $\beta$  and LXR $\alpha$ 's different splice variants are comprised of 4 domains: the N-terminal ligand-independent activation function domain, the DNA Binding Domain, Ligand-Binding Domain and the AF-2 (Activation Factor 2 – the C-terminal ligand-dependent transactivation sequence).

LXR  $\beta$  is ubiquitously expressed while LXR  $\alpha$  is mainly expressed in the spleen, adrenal gland, intestines, adipose tissue, macrophages, lung and kidney (Korach-Andre et al., 2015). The activation of LXRs is mediated by their natural ligands, the oxysterols which are oxidized derivatives of cholesterol. (Olkkonen et al., 2012). LXRs have multiple functions most importantly: cholesterol homeostasis, lipogenesis, inflammation, etc.. and are implicated in many

metabolic and neurodegenerative diseases in the Central as well as in the Peripheral Nervous System.

Two mechanisms of action are proposed for LXR activation. First, by direct activation; where LXR forms a heterodimer with the Retinoic X Receptor forming the LXR/RXR complex which is a ligand activated transcription factor heterodimer that binds to a specific LXR Responsive Element (LXRE) in the regulatory region of target genes. The LXRE is a two 5'-AGGTCA-sequences set a part by a direct repeat-4 (DR4) sequence (4 nucleotides), present in the promoter region of the targeted gene (Baranowski, 2008). If the heterodimer is not activated, the transcription is blocked by forming a complex with Nuclear Receptor Corepressor (NCoR) or Silencing Mediator of Retinoic Acid and Thyroid Hormone receptor (SMRT) (Figure 26A.). Once activated, by ligand binding, the corepressor is released and co-activators such as Peroxisome Proliferator Activated Receptor  $\gamma$  (PPAR $\gamma$ ) and Steroid receptor Coactivator-1 (SRC-1) bind the heterodimer. The recruitment of coactivators lead to chromatin remodeling and transcription of the target genes (Gabbi et al., 2014) (Figure 26B).

The second type of LXR activation is through transrepression, described in the regulation of NF- $\kappa$ B regulated proinflammatory genes. LXR is activated by ligand binding then sumoylated by proteins SUMO-2/3. The sumoylated LXR then interacts with the NCoR complex through the GPS2 subunit, inhibiting the release of the corepressor complex and transcription of NF- $\kappa$ B regulated genes (Gabbi et al., 2014) (Figure 26C)



Trends in Endocrinology & Metabolism

**Figure 26. LXR activation mechanisms of action (Courtney et al., 2016).**

**Direct activation:** **A.** Active repression of transcription by binding of the corepressor complex to LXR in the absence of ligands. **B.** the binding of LXR ligands lead to a conformational remodeling of LXR and the coactivator complex is recruited, replacing the corepressor complex thus activating gene expression. **Transrepression:** **C.** the activated LXR is sumoylated, then it interacts with the NCoR complex stabilizing it and inhibiting the expression of NF-κB regulated genes.

## 2. Oxysterols

Oxysterols are the oxidized derivatives of cholesterol and natural ligands of the LXR (Figure 27). Oxysterols play an important role in lipid and cholesterol metabolism; however, they are also implicated in other biological processes. The generation of oxysterols is mediated either by autoxidation of cholesterol or enzymatically mostly implicating the cytochromes P450 (Oikkonen et al., 2012).

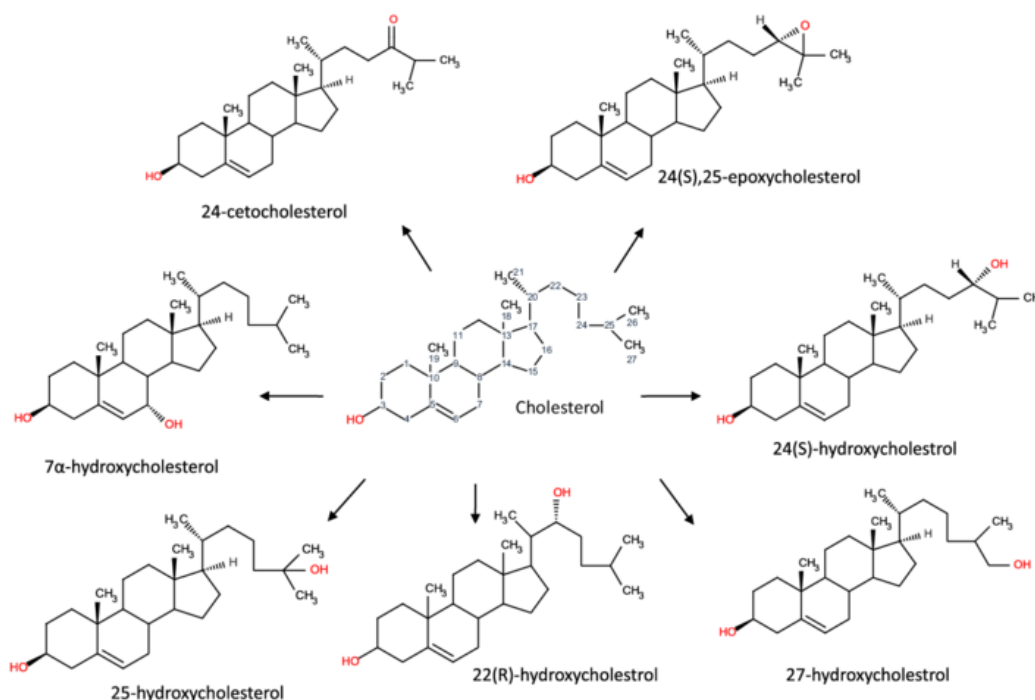


**Figure 27.** Oxysterols, the LXR natural ligands (Viennois et al., 2012). A representation of different oxysterols and their structure deriving from cholesterol oxidation.

### 3. Functions of Liver X Receptors: Cholesterol homeostasis and lipid biogenesis

LXRs are described as cholesterol sensors since they are activated by oxysterols and directly activate genes responsible in cholesterol transport and efflux when in excess. LXR direct targets are the ATP Binding Cassette Subfamily A Member 1 (ABCA1) as well as Apolipoprotein E (ApoE) which are membrane bound proteins involved in the export of excess cholesterol mediated through lipoproteins. Another LXR target is IDOL (Inducible Degradator of LDLR), an E3 ubiquitin ligase, that is responsible for degrading LDLR (Low Density Lipoprotein Receptor), thus limiting cholesterol uptake from extracellular sources. Oxysterols, independently from LXRs, can negatively regulate SREBP2 (Sterol regulatory element-binding protein 2) therefore modulate cholesterol biosynthesis and can promote the esterification of cholesterol. Hence, LXR and oxysterols work in synergy with SREBP2 – regulator of cholesterol biosynthesis – to maintain cholesterol homeostasis (G. Cermenati et al., 2013; Venkat Krishnan Sundaram et al., 2019).

LXR is also involved in lipid biogenesis by directly activating the SREBP1 (Sterol regulatory element-binding protein 1) that in turn regulates the expression of FASN (Fatty acid synthase) a key enzyme in fatty acid synthesis. It has been shown that in Schwann cells SREBP1c is the isoform involved in lipogenesis and its expression is mediated by RXR $\gamma$  (Norrmén et al., 2014), therefore LXR $\beta$ /RXR $\gamma$  heterodimer could be responsible for this function.

#### **4. Liver X Receptor and myelination**

Our team is interested in evaluating the role of LXRs in the myelination of the peripheral nervous system; a process requiring the availability of high lipid and cholesterol levels. Our team has described the presence of natural LXRLigands; 24(S)-Hydroxycholesterol (24-OH), 25-Hydroxycholesterol (25-OH) and 27-Hydroxycholesterol (27-OH) in the sciatic nerves and the MSC80 Schwann cell line (Makoukji et al., 2011).

Makoukji et al., demonstrated the implication of LXR in myelin proteins gene expression. The activation of LXR by its natural ligand 25-OH or by its synthetic ligand TO901317 (TO9) lead to the repression of myelin gene protein expression; both Peripheral Myelin Protein (PMP22) and Myelin Protein Zero (MPZ) were downregulated. LXR $\alpha/\beta$   $-/-$  double knock-out showed the expected upregulation of PMP22 and MPZ transcripts, however the protein levels did not mirror the same expression status but expressed lower levels of PMP22 and MPZ proteins in the sciatic nerves and MSC80 Schwann cell line (Makoukji et al., 2011). Moreover, the LXR double knock-out mouse model showed thinner myelin sheath in sciatic nerves further validating these results. The downregulation of myelin genes in Schwann cells by TO9 and 25-OH treatment were paralleled with the inhibition of the canonical Wnt signaling components, known for their crucial role in myelin gene expression (Tawk et al., 2011). The expression levels of  $\beta$ -catenin, a major player in the Wnt signaling pathway, were reduced and its recruitment at the level of myelin gene promoters of PMP22 and MPZ was hindered by 25-OH (G. Shackleford et al., 2013).

However LXRs deletion in the CNS did not show the same consequences as in the PNS, LXR deletion downregulated myelin genes expression and  $\beta$ -catenin was not downregulated after LXR activation. LXR deletion, in an oligodendrocyte cell line 158-N and in the brain, decreased the transcriptional and protein levels expression of the myelin genes (G. Shackleford et al., 2013), and thinner myelin sheath were observed in the cerebellum of LXR double knock-out mice (Meffre et

al., 2015). The effect of LXR knock-out was further evaluated in different regions of the brain. LXR deletion showed that the expression of major myelin protein transcripts depends on the age and region of the brain as well as the isoform of the nuclear receptor LXR. Highly myelinated regions of the brain namely the spinal cord, cerebellum, corpus callosum and optic nerve responded differently to LXR knock-out mouse model (G. G. Shackleford et al., 2017).

In order to further understand the mechanism responsible for the decreased levels of PMP22 and MPZ in the sciatic nerve after LXR deletion, the implication of oxidative stress was put into question. The deleterious consequences of oxidative stress on the myelin sheath proteins has been previously described in neurodegenerative diseases. Treating sciatic nerves with Paraquat, a free radical producing molecule, was shown to lead to the disorganization and aggregation of myelin proteins in the sciatic nerve (M. Hichor et al., 2017).

In a recent study, Hichor *et al.* described increased levels of oxidative stress in LXR double knock-out SNs that would be responsible for disrupting the correct protein folding of the myelin proteins. The increased activation of antioxidant responses through the Nuclear factor (erythroid-derived 2) like 2 (Nrf2) signaling pathway was also described. Treating the LXR double knock-out mice with N-acetylcystein (NAC), a Reactive Oxygen Species (ROS) scavenger, decreased oxidative stress levels and had beneficial consequences on myelin thickness, nerve conduction and locomotion. The regulation of the Nrf2 antioxidant pathway by LXR was evaluated by treating the MSC80 cell line with the TO9 agonist. TO9 increased the expression of Nrf2 protein levels followed by the expression of antioxidant proteins, therefore showing the role of LXR in the regulation of antioxidative response and highlighting its protective role as potential therapeutic target for increased oxidative stress in demyelinating diseases (Mehdi Hichor et al., 2018).

## **5. Liver X Receptor in pathology.**

The LXR has been most described in Diabetic Peripheral Neuropathy (DPN). Neuropathy is a very prevalent complication of diabetes and most diabetic patients develop DPN, affecting their sensory and motor functions and present symptoms such as allodynia and reduced nerve conduction velocity.

Streptozotocin (STZ) induced diabetes in rats showed decreased levels of LXR $\beta$  and neurosteroids. The activation of LXR by its synthetic agonist GW3965 specific to both LXR $\alpha$  and LXR $\beta$ , exerted neuroprotective effects by increasing the expression of neurosteroid levels in the SN, recovering them to normal levels in the SN of diabetic mice, and promoting cholesterol utilization by increasing the expression of the Steroidogenic acute regulatory protein (StAR) and enzymes responsible for the conversion of cholesterol into neuroactive steroids. The treatment with GW3965 increased expression levels of LXR targets such as ABCA1 and ABCG1 with a tendency of restoring MPZ and PMP22 levels (Gaia Cermenati et al., 2010). The role of LXR was further highlighted when the lipid composition of the diabetic sciatic nerves were evaluated. Cholesterol and glycolipid levels were significantly decreased. The levels of fatty acids (FAs) saturation were also altered in the sciatic nerves of diabetic mice and a significant decrease in mono-unsaturated FAs was observed. Enzymes involved in lipogenesis and FA desaturation such as FA desaturases 1 and 2, SREBP1c, FASN, Stearoyl-CoA Desaturase (SCD) 1 and 2 and acetyl-CoA carboxylase  $\alpha$  (ACACA) were all down regulated in DPN (Gaia Cermenati et al., 2012). The treatment with GW3965 restored their levels of expression back to normal conditions and myelin DPN induced abnormalities were not observed. Another orientation in the implication of LXR and DPN was recently described by Eid *et al.*, where a cross talk between LXR $\beta$  and NADPH Oxidase 4 (Nox-4) was described. Oxidative stress is known for its deleterious effects and DPN is no exception to it. In DPN, LXR $\beta$  levels are decreased and high levels of Nox4 are detected. The LXR activation by its synthetic agonist TO9 played a protective role by decreasing NADPH oxidase activity and restored myelin proteins; MPZ and Pmp22 mRNA and protein expression were back to normal levels accompanied by enhanced behavioral performance (Eid et al., 2020).

All these findings show, that in a pathological context, LXR plays a protective role against oxidative stress, corrects dyslipidemia and positively regulates expression of myelin gene.

In a recent review, Sundaram *et al.* highlight the role of LXR in the physiology and pathology of the PNS and underlines the necessity of finding an isoform and cell specific activator of the LXR in order to circle around LXR activation induced liver dyslipidemia and systemic reverse cholesterol transport. Sundaram *et al.* further called attention towards the possible regulation of cholesterol through LXR in different functions of the sciatic nerve cellular components and the potential therapeutic role of LXRs; not only in the case of diabetes but also in Charcot-Marie Tooth

type 1A (CMT1A) or Malignant Peripheral Nerve Sheath Tumor (MPNST) (Venkat Krishnan Sundaram et al., 2019).

Investigations on the role of LXR in the PNS are still at their beginning and require further research however, targeting LXR as potential therapeutic agent in PNS pathologies seems very promising.



## CHAPTER II: MATERIAL AND METHODS

### 1. Ethical approval procedures

All aspects of animal care were approved by the National Ethic Committee (No. 2016092216181520). For each experiment, particular care was taken to minimize any suffering of the animals. The number of transgenic mice and their corresponding controls was reduced to the minimum required for statistical precision. Animals were housed in a pathogen free facility on a 12-hour light dark cycle at 21°C and *ad libitum* access to food and water. Animals were euthanized by isoflurane overdose and cervical dislocation.

### 2. Genotyping

Mouse genomic DNA was extracted from tail biopsies. The biopsies were incubated in lysis buffer pH 8.3 (200 mM NaCl, 0.1% SDS, 5 mM EDTA pH 8, 100 mM Tris pH 8.5) with 1 mg/ml proteinase K at 55°C overnight. The DNA was precipitated using isopropanol followed by washes with 70% ethanol, dried and resuspended with RNase free water. PCR was performed using Kapa Buffer (KK 5121, Kapa Biosystems), LXR $\alpha$ , LXR $\beta$ , Dhh Cre and D9 Mit 10 (for internal control) primers to distinguish the different phenotypes (Table 1). 18 $\mu$ l PCR mixture (Table 2) were added to 2 $\mu$ l of DNA for each sample.

PCR conditions were as follows: 1 cycle for 2 minutes at 94°C, 1 cycle for 30 seconds at 94°C, 37 cycles of 30 seconds at 57°C and 1 cycle for 60 seconds at 72°C. The amplified material was run on 1.2% agarose gel containing 5 $\mu$ l of Ethidium bromide, for 20 minutes at 145 V and observed after exposure to UV light.

Gene	Forward primer sequence (5' - 3')	Reverse primer sequence (3' - 5')
LXR $\alpha$	GTG TAA CAG GCG CTC CTT CT	GGG CAA AGC GCT GTT GTC G
LXR $\beta$	GCC ACT AAC CCC ACA TTA CCG TGA	AGG TGC CAG GGT TCT TGC AGT TG
Dhh Cre	CCT TCT CTA TCT GCG GTG CT	ACG GAC AGA AGC ATT TTC CA
D9 Mit 10	TAA CCA ACC CTT CAA GGC AC	AAT CCT TGG CTG AAG GGA AT

**Table 1.** Genotyping primer sequences.

	LXR $\alpha$ (Volume / sample)	LXR $\beta$ (Volume / sample)	Dhh Cre (Volume/ sample)
Forward Primer LXR $\alpha$	0.6 $\mu$ l	-	
Reverse Primer LXR $\alpha$	0.6 $\mu$ l	-	
Forward Primer LXR $\beta$	-	0.6 $\mu$ l	
Reverse Primer LXR $\beta$	-	0.6 $\mu$ l	
Forward Primer Dhh Cre	-	-	0.4 $\mu$ l
Reverse Primer Dhh Cre	-	-	0.4 $\mu$ l
Forward Primer D9 Mit 10	-	-	0.4 $\mu$ l
Reverse Primer D9 Mit 10	-	-	0.4 $\mu$ l
Kappa Buffer	10 $\mu$ l	10 $\mu$ l	10 $\mu$ l
RNase free water	6.8 $\mu$ l	6.8 $\mu$ l	6.8 $\mu$ l
Total volume	18 $\mu$ l	18 $\mu$ l	18 $\mu$ l

**Table 2.** PCR mixture for the detection of LXR $\alpha$ , LXR $\beta$  and Dhh expression.

### 3. Behavioral testing and electrophysiological assessment

#### A. Locotronic

The locotronic technique was used to assess the psychomotor skills of mice. The mice have to cross a horizontal ladder, while the machine is recording a detailed modeling of their movement, to reach a safe place. Average time taken to reach the safe place, front paw and hind paw slips were automatically registered. The experiment was repeated three times and the data presented is the average of the triplicates. The test was performed without traps on 8 weeks old animals n=12 for Control and n=8 for LXR $\beta$  SC KO group.

#### B. Grip strength

The grip strength test is a technique that evaluates the mice forelimbs and combined all limbs' muscle force. The mice grasp on a metal grid and are pulled backwards in the horizontal plane;

the force applied by the mice as well as the time spent for each experiment is measured by the machine. Each test is repeated three times with a 30 minutes rest period in-between. The test was performed on 8 weeks old animals (n=14 for Control and n=9 for LXR $\beta$  SC KO group).

### **C. Hot Plate**

The hot plate test was used for the detection of pain sensitivity in mice. The noxious stimulus is an electrically heated plate at 52°C, in compliance with Office of Ethics and Compliance of the Institutional Animal Care and Use Program. The latency of response; such as hind paw licking and/or shaking, or jumping after noxious stimuli induction was recorded. Maximum experimentation time was 30 seconds regardless of the response. The mice were transferred to a recipient containing cold water to avoid any damage. The test was performed on 8 weeks old animals (n=16 for Control and n=8 for LXR $\beta$  SC KO group).

### **D. Compound Muscle Action Potential (CMAP)**

The compound muscle action potential (CMAP) is a sensitive, minimally invasive electrophysiological technique used for the assessment of nerve conduction. CMAP measurements have been indispensable for the detection and monitoring of neuromuscular disorders, neuropathies, myopathies and demyelination.

All measurements were performed using Dantec® Keypoint® Focus EMG / NCS / EP System (Natus) with Disposable Subdermal Needle Electrode (natus neurology, 019-476600). Control (n=4) and LXR $\beta$  SC specific KO (n=7) 8 weeks old mice were anesthetized by intra-peritoneal injection of 100 mg/kg Ketamine and 10 mg/kg Xylazine and kept on heating pads to ensure a body temperature of  $\pm$  37°C. Ocry-gel (Ocry Gel; Laboratoire TVM, France) was applied to protect and hydrate the corneal epithelium of the mice during anesthesia. Absence of podal withdrawal reflex was evaluated before the beginning of each procedure.

The stimulating needle electrodes are inserted subcutaneously in the hindlimb at the level of the sciatic notch and at the proximal part of the tail towards the body, whereas, the recording needle electrodes are inserted subcutaneously at the level of the tibialis anterior muscle. The recording needles are inserted in a parallel manner with a minimal distance, between the two, required to avoid any risk of needles contact. The ground electrode was also inserted subcutaneously, at the

level of the unmeasured hindlimb. In this study both left and right hindlimb CMAP measurements were recorded. Sciatic nerve fiber stimulation is evaluated by the magnitude of response recorded in the muscles, referred to as the Amplitude which is measured in millivolts (mV). Supramaximal stimulus is the stimulation at which the highest amplitude (response) is recorded. The stimulation mode used during the measurements is the 1 pulse stimulation for 0.1ms, starting from 1 milliampere (mA). Another crucial parameter measured in CMAP is the latency, which represents the delay in milliseconds (ms) between the initiation stimulus and the muscle fibers response. Figure 1 is a representation model of CMAP recordings.

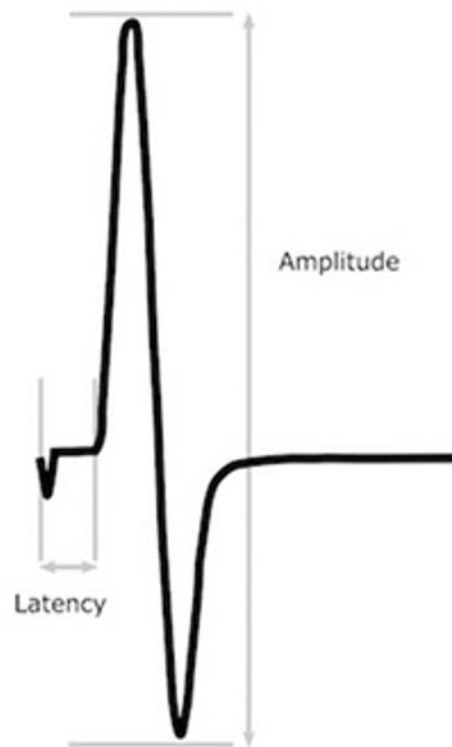


**Figure 1.** Representative image of CMAP response and calculations of Latency and Amplitude (Pollari et al., 2018).

## 4. Histological characterization of the Sciatic nerves

### A. Transmission Electron Microscopy

The sciatic nerves were extracted from 8-week-old Control (n=3) and LXR $\beta$  SC KO (n=3) mice and fixed in with 4% paraformaldehyde, 2.5% glutaraldehyde, and 0.1 M phosphate buffer, pH 7.4. Tissues were immersed in the same fixative solution at 4 °C overnight. The nerve samples were washed with 0.1M phosphate buffer then stained with a solution of 4% OsO<sub>4</sub> and 0.2M phosphate buffer and incubated in the dark for 2 hours. After incubation, samples were washed and then incubated with 0.1M phosphate buffer at 4°C overnight. The stained sciatic nerve samples were then washed with a series of ethanol and finally with an epon - propylene oxide 1:1 solution. The nerves were molded in epoxy resin then degassed in a vacuum chamber at 37°C for 3 hours then at 60°C for 24 hours to allow polymerization of the resin. The ultrathin sections were cut on an ultramicrotome (8800 Ultratome III; LKB Bromma) and collected on 300-mesh nickel grids. Staining was performed on drops of 4% aqueous uranyl acetate and Reynolds's lead. Imaging was performed in a JEOL jem-1011 electron microscope and digitalized with DigitalMicrograph software<sup>®</sup>.

### B. Oil Red O and Masson's Trichrome Staining

Sciatic nerve adipose tissue and collagen deposition were assessed by Oil Red O and Masson's Trichrome classic staining, respectively. Fresh sciatic nerves were dissected and included in OCT, the blocks were cryosectioned at a 10  $\mu$ m thickness using a Leica CM3050 S cryostat at -20 °C and mounted on TESPA ((3-Aminopropyl) triethoxysilane) (Cat #A3648) pre-treated glass slides. Masson's Trichrome and Oil Red O staining were carried out at the Histology Platform HistIm of Institut Cochin, Paris. In Oil Red O stained SN sections, neutral lipid droplets stained dark red and myelin sheath stained faint red. In Masson's Trichrome stained SN sections, myelin sheath stained purple, collagen stained blue and nuclei stained dark brown. Images were digitally captured using an AxioCam ICc1 Rev.4 (O) camera mounted on a Zeiss AxioObserver microscope (Z1, Carl Zeiss SAS, Le Pecq, France) using the ZEN 2012 software (Carl Zeiss SAS). Processing of Trichrome images was performed using Image J, U. S. National Institutes of Health, Bethesda, Maryland, USA with the Colour Deconvolution plugin (Ruifrok et al., 2001) . A total of nine 8-week-old mice were used for this experiment, Control n= 5 and LXR $\beta$  SC KO n=4.

## **C. Immunofluorescence**

### **a. Sample preparation**

Teased sciatic nerves (n=3 per group) were air dried for 1 hour and kept at -80°C (Description in Section 5.a.). When used, the samples were post fixed with methanol for 10 minutes then washed with PBS.

Cross sections of control and LXR $\beta$  SC KO sciatic nerves (Control n=3; LXR $\beta$  SC KO n=3) were prefixed with 4% PFA fixed and washed thoroughly with PBS then included in OCT. Cross sections were then mounted on TESPA pre-coated slides.

Fresh SN cross sections of ToF-SIMS samples (WT (C57Bl6/J) n=3, Flox Control n=2, LXR $\beta$  SC KO n=4 at 8 weeks old) were mounted on TESPA pre-coated slides and post fixed with 4% paraformaldehyde for 10 minutes then washed with PBS.

All the samples were permeabilized with a solution of 0.1% Tween-20 and 0.25% Triton-X for 10 minutes and washed thoroughly.

### **b. Labelling**

All Samples were blocked for 1 h with blocking buffer (PBS containing 2% BSA, 5% Donkey Serum and 0.1% Tween-20). Then incubated at 4°C with the primary antibodies diluted in blocking buffer overnight in a humidified chamber. Followed by PBS washes and incubation with the secondary antibodies diluted in blocking buffer for 1 hour at room temperature in a humidified chamber. The samples were washed by PBS and stained by Hoechst staining for 10 minutes. Slides

were then washed and mounted. Primary antibodies and their respective secondary antibodies are presented in Table 3.

<b>Primary Antibody</b>	<b>Company, Reference</b>	<b>Concentration</b>	<b>Secondary Antibody</b>	<b>Company, Reference</b>	<b>Concentration</b>
Anti-MPZ Antibody	AVES, PZO	1/500	Donkey Anti Chicken Cy3	Jackson 703-005-155	1/500
Anti-NFH Antibody	Millipore, AB1989	1/000	Donkey Anti Rabbit Alexa Fluor 488	Jackson 711-545-152	1/1000
Anti-SMI 312 Antibody	Biolegend, 837904	1/1000	Donkey Anti Mouse Alexa Fluor 488	Jackson 715-545-150	1/500
Anti-ZO1 Antibody	Invitrogen 61-7300	1/500	Donkey Anti Rabbit Alexa Fluor 488	Jackson 711-545-152	1/250
Anti-Thy1/CD90 Antibody	Abcam Ab3105	1/500	Donkey Anti-Rat Alexa Fluor 647	Jackson 705-605-147	1/500
Anti-SOX10 Antibody	R&D Systems AF2864	1/250	Donkey anti-Goat Cy3	Jackson 705-165-147	1/500
Anti-Krox20 Antibody	Pr.Meijer	1/100	Donkey anti Rabbit Alexa Fluor 488	Jackson 711-545-152	1/200
Bisbenzimidide Hoechst 33342	Sigma, B2261	1/3000	--	--	--

**Table 3.** Primary and secondary antibodies used for immunofluorescent staining.

## D. Fluorescence imaging

Fluorescence images were collected using a CMOS camera (ORCA-Fusion Digital CMOS camera C14440-20UP, Hamamatsu Photonics France, Massy, France) mounted on a Zeiss AxioObserver microscope (Z1, Carl Zeiss SAS, Le Pecq, France) using the ZEN 2012 software (Carl Zeiss SAS). Processing of the images was performed using Image J, U. S. National Institutes of Health, Bethesda, Maryland, USA.

## 5. Biophysical characterization by Atomic Force Microscopy

Atomic Force Microscopy (AFM) has long been a reliable technique for measuring the physical properties of materials at an atomic scale. And recently it has been playing an undeniably essential role in determining the structural and biomechanical properties of biological samples.

The AFM consists of four major parts: a cantilever with a sharp tip, mounted underneath it; a piezo-scanner that drives the cantilever (sample holder); a laser diode and a position sensitive detector (Figure 2).

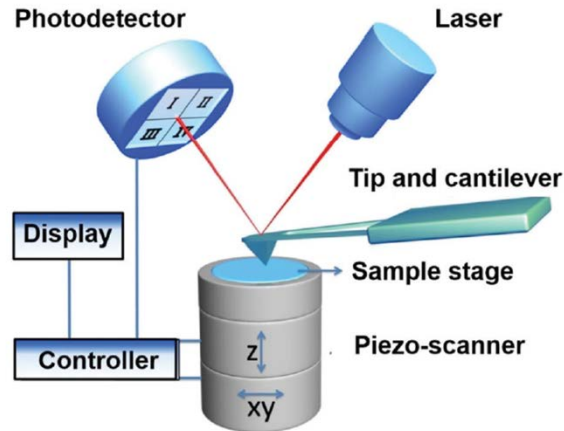


**Figure 2.** Schematic representation of the AFM (Shan et al., 2015)

The tip at the end of the spring like cantilever scans the surface of the sample in either contact or tapping mode, the movements are detected by laser reflection, and give rise to a topographic representation of the sample. Another application for AFM is measuring the mechanical properties of the sample called force spectroscopy, such as the Young's elastic modulus. A vertical force is applied by the tip to the sample; the forces of attraction and repulsion between the probe and sample are detected and presented as a force curve (Figure 3).



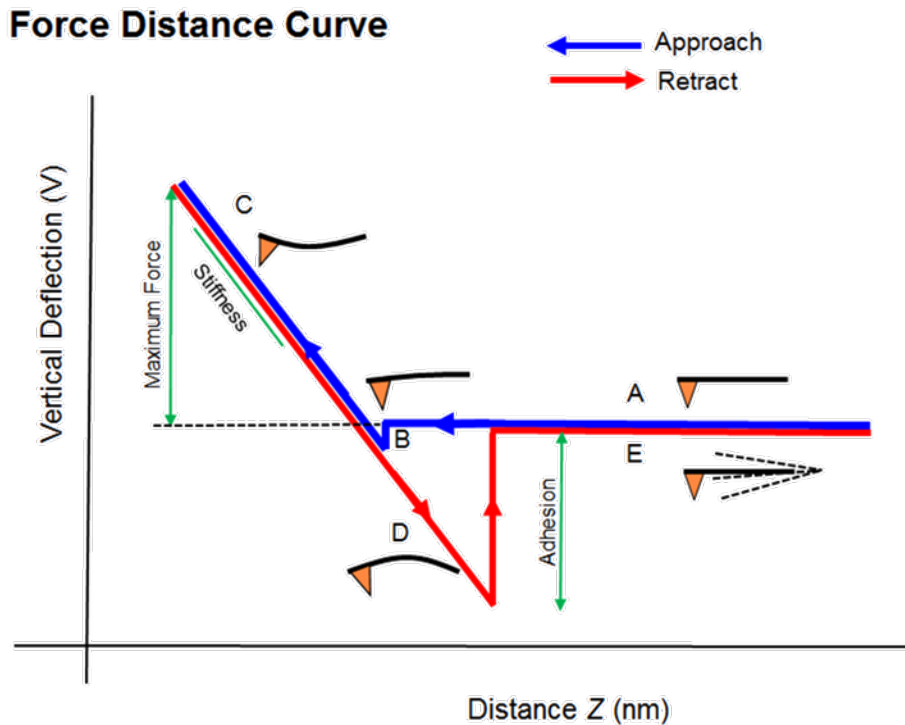


**Figure 3.** Schematic representation of a force distance curve (Paar, 2020).

### a. Sample preparation: Nerve teasing

Sciatic nerves of Control (n=3) and transgenic mouse model LXR $\beta$  SC KO mice (n=3) were dissected then immediately immersed in ice cold PBS and teased. The epineurium was first removed using fine forceps, releasing the nerve fascicles. The fascicles were then transferred on TESPA ((3-Aminopropyl-triethoxysilane) (Cat #A3648) pre-treated glass slides in order to increase surface adherence. With the use of tungsten needles (Cat # 10130-05), the fibers were separated and teased (Figure 4). The fresh samples were then directly stored at -80 C, no fixation was used in this process. These samples were used for AFM, SEM and immunofluorescence imaging of teased nerve fibers.

Before AFM measurements the samples were immersed in PBS for 30 minutes for rehydration.

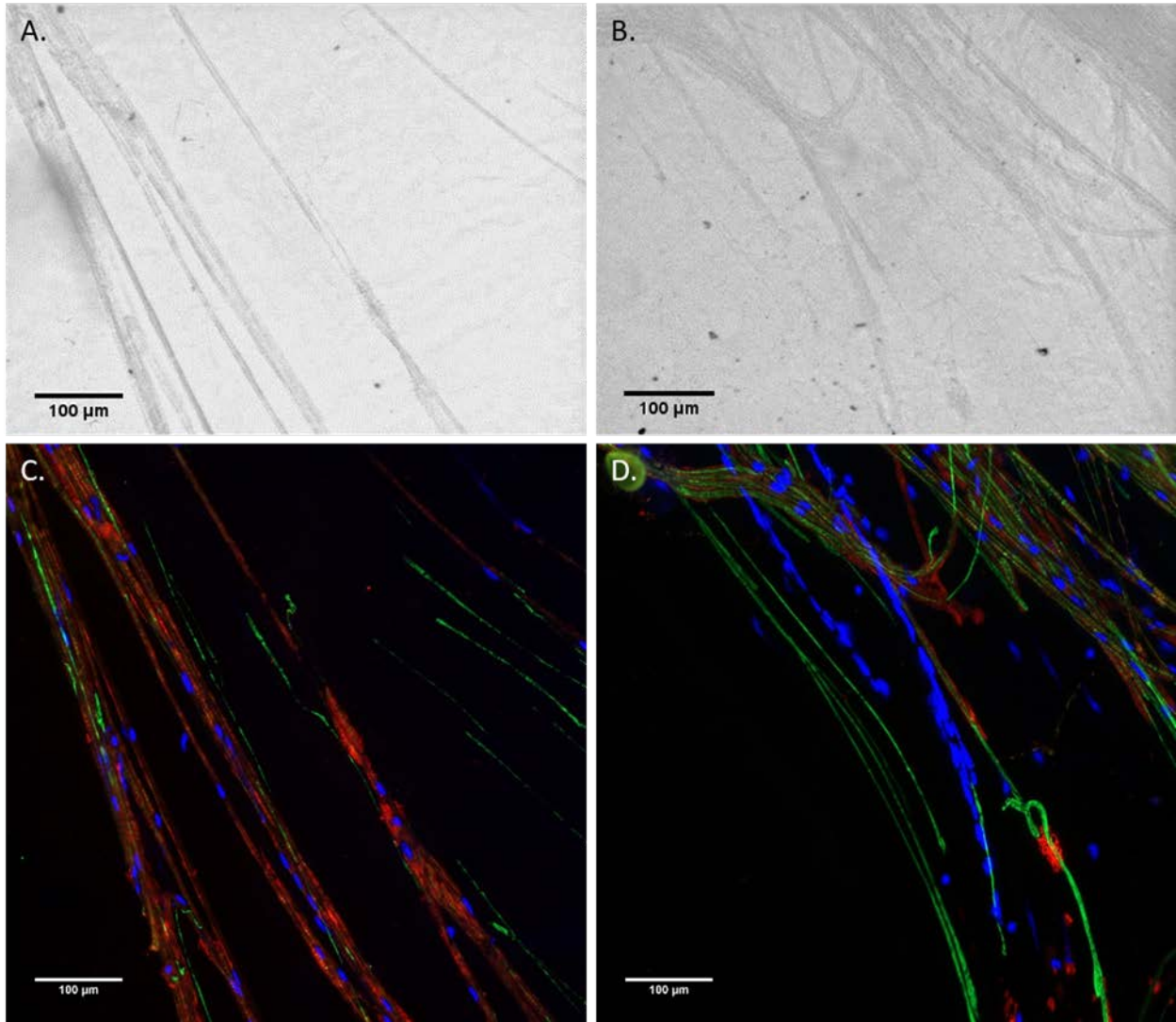


**Figure 4.** Nerve teased fibers of Control and LXR $\beta$  SC KO sciatic nerves at 8 weeks. Light imaging of **A.** Control and **B.** LXR $\beta$  SC KO teased nerve fibers. Immunofluorescent imaging of **C.** Control and **D.** LXR $\beta$  SC KO teased nerve fibers. Neurofilaments were marked by anti- NFH (Green), Myelin sheath was marked by anti-P0 (Red), and the nuclei by Hoechst. Scale Bar =100  $\mu$ m.

## **b. AFM measurements**

Structural and mechanical measurements were performed on teased sciatic nerve fibers at respective loading forces 25 nN, 75 nN and 131.6 nN using the Agilent 5420 SPM/AFM (Agilent Technologies, Santa Clara, California, USA) coupled to an optical bottom-view system. Triangular V shape silicium (Si) cantilever with a pyramidal tip shape with a spring constant of 0.2 N/m (Point Probes, Non-contact, High frequency, Agilent technology) were used as AFM probes. All data were processed and analyzed using Pico view 1.14. Topography imaging was performed in tapping mode to reduce any deformation to the sample. Elastic properties of the teased sciatic nerve fibers were then evaluated by assessing the force ( $F$ ) – indentation ( $\delta$ ) relationship during compression. However, these quantities are not measured directly, but need to be calculated from the deflection of the cantilever ( $d$ ) and the sample height ( $z$ ) presented in deflection in function of distance curves (force curve) for each compression. Typically, force curves are analyzed in a given range of loading forces. Thus, deflection values must first be converted into loading force values. Since cantilever springs are linear springs for small deflections, Hooke's law can be applied:

$$F = kc \cdot d.$$

( $kc$ ) represents the force constant of the cantilever, ( $d$ ) is its deflection, and ( $F$ ) is the corresponding loading force exerted by the cantilever.

When the cantilever is free, the deflection is not necessarily zero, e.g., because of stresses in the cantilever, which will deform it even without an external load. Therefore, the offset must be subtracted from all deflection values. This offset is obtained by calculating deflection when the tip is touching the sample. The indentation  $\delta$ , is given by the difference between the sample base height  $z$  and the deflection of the cantilever  $d$ :

$$\delta = z - d.$$

Moreover, the offsets should be subtracted from the deflection and piezo position values.

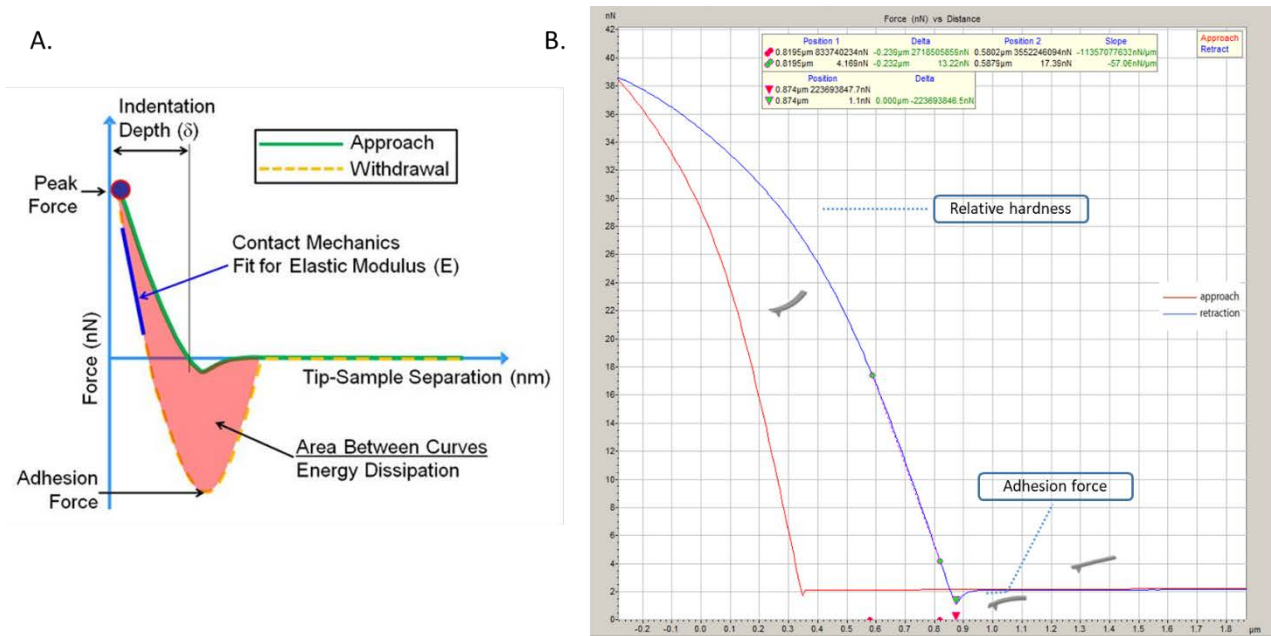


**Figure 5.** **A.** Schematic representation of the Elastic Modulus calculations from the force curve (BBML, 2020) . **B.** Annotated force curve obtained in our study.

Based on literature, we determined the elastic Young's modulus of the samples using the Hertz-Sneddon model corrected for pyramidal indenters (Rico et al., 2005). The Hertzian model describes the elastic indentation of an infinitely extended sample such as our nerve fiber sample.

For a sharp-pyramidal tip, the tip-sample force ( $F$ ) is proportional to the square of the sample indentation ( $\delta$ ), and its relation is given by the following equation:

$$F = \frac{E * \tan\alpha}{\sqrt{2} * (1 - \nu^2)} * \delta^2$$

$E$  is the elastic Young's modulus,  $\alpha$  is the half-opening angle to the face of the tip ( $\alpha = 10.7^\circ$ ) and ( $\nu$ ) is the Poisson's ratio of the sample ( $\nu = 0.5$ )

Since the curve obtained is force as a function of  $z$  (sample height) and not according to the indentation ( $\delta$ ), a corrected slope of the curve has to be calculated such as:

$$Slope = \frac{Force}{\delta^2}$$

Thus, the equation used to calculate the Young's modulus in this study transforms to:

$$E = \frac{\text{slope} * \sqrt{2} * (1 - \nu^2)}{\text{Tan } \alpha}$$

## 6. Scanning Electron Microscopy (SEM)

The sciatic nerve fibers (n=3 per group) were teased (described in section 5.a.) and stored at -80°C. A total of 20 Control SN teased fibers and 28 LXRβ SC KO SN fibers were measured at 8 weeks. Before SEM measurements, the samples were immersed in PBS for 30 minutes for rehydration and gold coated under vacuum for 1 minute at 20 kPa for conductivity. Samples were then observed with a JEOL JSM-6700F field emission scanning electron microscope (Seron technologies, Korea) at a voltage of 5 kV.

## 7. Lipid composition of the SN characterization using the Time of Flight – Secondary Ion Mass Spectrometry (ToF-SIMS)

ToF SIMS is a surface analytical technique with high detection sensitivity and depth resolution, it has long been a powerful tool for the chemical analysis of biological samples. ToF-SIMS uses a primary ion beam to irradiate the surface of a sample followed by mass spectrometry of the emitted secondary ions. The secondary ions emitting from the irradiation of the surface sputter are accelerated on their way towards a detector. Each secondary ion has a specific energy distribution and mass (mass to charge ratio:  $m/z$ ) which determines their arrival time (time of flight) to the detector (Figure 6). The mass spectrum is the plot of ion signal intensity in function of  $m/z$ , which elucidates the chemical identity of the secondary ions.

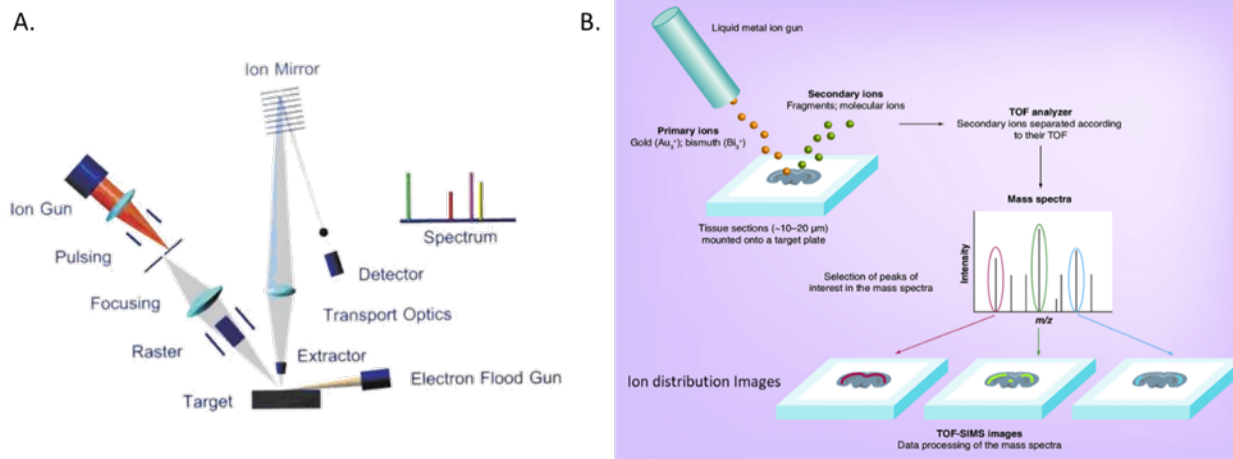


**Figure 6.** **A.** Schematic representation of the ToF-SIMS (Wahab et al., 2016). **B.** Schematic representation of ToF-SIMS procedure and illustration of ion distribution on surface sample (Sugden et al., 2011).

ToF-SIMS is capable of presenting a topographical distribution of the surface chemical elements. ToF-SIMS images are obtained by rastering the primary ion beam and collecting the mass spectrum at each pixel (J. Lee, 2011).

### a. Sample preparation

A total of nine 8-week-old mice were used for this experiment divided as the following: Group 1 (n=3) C57BL/6J mice were considered as wild type control, group 2 (n=2) C57BL/6J background mice with inserted P Lox sites (Flox) considered as control for the transgenic mice, and group 3 divided into two subgroups, left and right sciatic nerves of transgenic LXR $\beta$  Schwann Cell specific Knock Out mice (n=4).

The sciatic nerves of the 8-week-old mice were dissected and spot frozen in liquid nitrogen. The nerves were then immediately placed in cryomolds and covered with Optimum Cutting Temperature (OCT) compound. The molds were immersed in cold isopentane for 30 seconds. Once solidified, the blocks were transferred into cryotubes and stored at -80°C until cryosectioning.

10  $\mu$ m thick cross sections of sciatic nerves were obtained by cutting the frozen blocks with a Leica CM3050 S cryostat at -20 °C. The cross sections were then deposited on ITO (Indium-Tin-Oxide) – coated conductive slides and maintained frozen until analysis.

Before analysis, the samples were imaged by an optical microscope (Olympus BX 51 fitted with  $\times 1.25$ – $\times 50$  lenses, Olympus France SAS, Rungis, France) equipped with an SC30 camera, monitored by Stream motion 1.9 software (Olympus, Rungis, France), then dried under vacuum and set on the sample holder.

### **b. ToF-SIMS imaging**

A standard commercial TOF-SIMS IV (ION-TOF GmbH, Münster, Germany) reflectron-type TOF mass spectrometer was used for MSI experiments. The primary ion source was a bismuth-manganese alloy liquid metal ion gun.  $\text{Bi}^{3+}$  cluster ions were selected. Primary ions reach the sample surface with a kinetic energy of 25 keV and at an angle of incidence of  $45^\circ$ . Secondary ions are accelerated to a kinetic energy of 2 keV, fly through a field free region and are reflected (effective flight path  $\sim 2$  m) before being post-accelerated to a kinetic energy of 10 keV just before hitting a hybrid detector, composed by a micro-channel plate, a scintillator, and a photomultiplier. A low-energy electron flood gun was activated between two primary ion pulses to neutralize the sample surface (Gilmore et al., 2002). In this study, we used the so-called ‘high current bunched mode’ to set the primary ion column (Sodhi, 2004). Because of the very low initial kinetic energy distribution of the secondary ions, the relationship between the time-of-flight and the square root of  $m/z$  is always linear over the whole mass range. In this study, only negative ion mode images were recorded.

The mass calibration was always internal, and signals used for initial calibration were those of  $\text{H}^-$ ,  $\text{C}^-$ ,  $\text{CH}^-$ ,  $\text{CH}_2^-$ ,  $\text{C}_2^-$ , and  $\text{C}_4\text{H}^-$  for the negative ion mode. Structure attributions or assignments of ion peaks were made according to the instrument resolution ( $M/\Delta M = 3000$ , full width half-maximum [fwhm], at  $m/z$  500), accuracy, and the valence rule. Moreover, mass spectra of reference compounds have been recorded and compared to spectra recorded *in situ* to confirm the assignments. Finally, the biological relevance of the attribution was also taken into account and mass assignments were also confirmed or at least reinforced with the help of the literature (Tahallah et al., 2008).

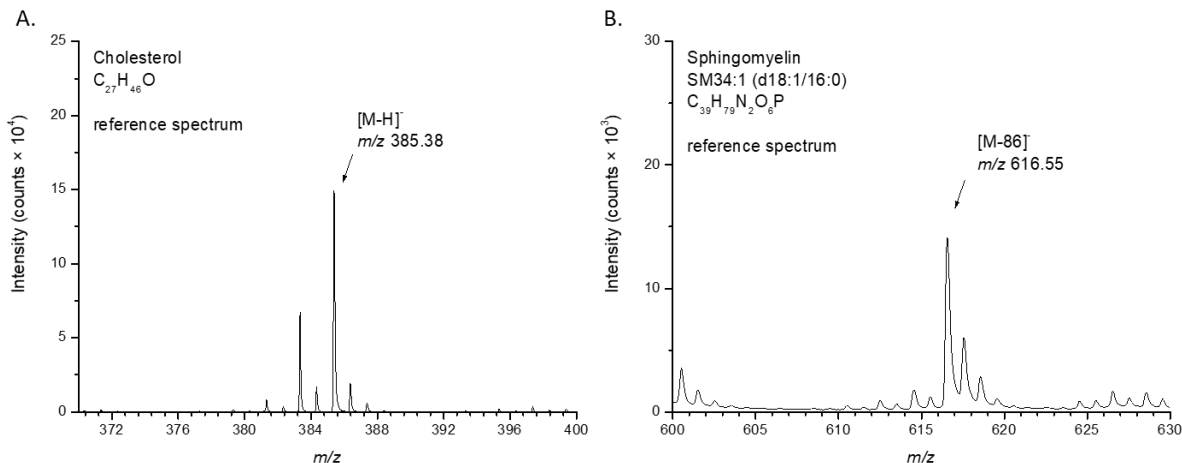


**Figure 7.** A. Cholesterol reference spectra. B. Sphingomyelin reference spectra.

Images were recorded with a field of view of  $100\ \mu\text{m} \times 100\ \mu\text{m}$  and  $128 \times 128$  pixels giving a pixel size of  $1\ \mu\text{m} \times 1\ \mu\text{m}$ . The name of the compound and the  $m/z$  value of the peak centroid, the maximal number of counts in a pixel (MC) and the total number of counts (TC) are written below each image. The color scale, specified to the right side of the images, corresponds to the  $[0, \text{MC}]$  intervals. The raw data were acquired using SurfaceLab 6.7 and processed using SurfaceLab 7.0 (ION-TOF GmbH, Münster, Germany). Spectra were processed with OriginPro 7.5.

Negative ion mode images were recorded for each selected area. All the images were recorded with exactly the same primary ion fluence (also called primary ion dose density, PIDD) of  $5.02 \times 10^{12}$  ions/cm<sup>2</sup>, well below the so-called static-SIMS limit, thus ensuring little sample damage and the maximum of intact secondary ion emission for the recording of two successive images on the same area (Vickerman, 2011).

Three adjacent sections were analyzed from each sciatic nerve in order to assess the instrumental and experimental variability (Bich et al., 2013). In the case of multiple zone measurement per section, the values were averaged.

Before each acquisition, the instrument settings are optimized by adjusting the three following parameters. Z value is the distance between the secondary ion extractor and the sample surface. The ‘Adjust Z’ function is used to finely and automatically tune the z-height of the sample. The ‘Adjust CC’ function (charge compensation) permits to adjust the voltages of the secondary ion optics (reflectron, lenses and deflection plates) to the exact kinetic energy of the secondary ions, *i.e.* taking into account any deficit of kinetic energy due to the insulating character of the tissue



surface. Generally, this deficit of energy for tissue samples is in the range of ~1% (Seyer et al., 2010). Finally, negative ion images are precisely aligned to the optical one (from the video camera of the spectrometer), and the acceptances are eventually re-centered. Negative ions detected at  $m/z$  253.22, 255.23, 277.22, 279.23, 281.25, 283.26, 385.33, 540.28, and 616.55 are studied. Each ion peak area is noted and the average with the coefficient of variation (CV) were calculated.

## 8. Primary co-culture of dissociated DRGs at E13.5

Schwann cells were isolated from the DRGs of C57Bl/6J mice at E13.5, the technique was previously described by Kim & Maurel (Protocols for Neural Cell Culture, 2009, Ch15).

The DRGs were first dissected in an L15 media (Table 4), then incubated in a trypsin solution. The Trypsin effect was stopped with the DRG isolation Media and triturated for cell dissociation. The DRG cells of each embryo were plated into a 35 mm dish in a DMEM serum containing media and NGF to ensure neuronal survival (Table 5). 16 to 18 hours following the isolation, the media is changed to a Neurobasal serum free, supplemented with B27 and NGF (Table 6). In 7 days, the neuronal network develops, Schwann cell precursors proliferate due to the presence of neurons. Fibroblast like cells form a layer underneath the network, their proliferation is limited by the absence of serum.

Component	Concentration	Reference
L-15 Leibovitz's	Base medium	11415-049 GIBCO
Antibiotic/ Antimycotic	1X	15240-062 GIBCO
Heat inactivated HS		26050-088/10500-064 GIBCO

**Table 4.** DRG Isolation Media

Component	Concentration	Reference
DMEM high glucose	Base medium	11960-044 GIBCO
L Glutamine or Glutamax	2Mm	35050-061 GIBCO
Heat inactivated HS		26050-088/10500-064 GIBCO
2.5S NGF	50ng/ml	R&D 1156 NG
Antibiotic/ Antimycotic	1X	15240-062 GIBCO

**Table 5.** DRG Plating Media

Component	Concentration	Reference
Neurobasal Medium	Base medium	21103-049 GIBCO
L Glutamine or Glutamax	2Mm	35050-061 GIBCO
2.5S NGF	50ng/ml	R&D 1156 NG
B27 supplement	1X	17504-044 GIBCO
Antibiotic/ Antimycotic	1X	15240-062 GIBCO

**Table 6.** Neurobasal Media

## 9. Evaluation of mRNA expression levels by RT-qPCR

The sciatic nerves (Control n=3; LXR $\beta$  SC KO n=3) were harvested and RNA was directly extracted using the TRIzol reagent (Ambion Life Technologies 15596018) in accordance with manufacturer's instructions with some minor modifications. Reverse transcription of 500 ng of RNA per sample was performed according to prescribed protocols using MMLV Reverse Transcriptase (Sigma M1302) and Random Primers (Promega C1181). Quantitative Real Time qPCR was then performed by adding 3.5 ng of cDNA to a master mix containing Absolute SYBR ROX 2X mix (Thermo AB1162B), and primers for the gene of interest for a total volume of 7  $\mu$ l per well in a 384-well plate. The experiments were carried out on the BioRad CFX384. The list of primer sequences is summarized in Table 7.

Gene	Gene name	Forward Sequence	Reverse Sequence
LXR $\alpha$	<i>Liver X Receptor <math>\alpha</math></i>	ACAGAACCTCAAGATGCAGGAG	AACCCTATCCCTAAAGCAACCC
LXR $\beta$	<i>Liver X Receptor <math>\beta</math></i>	AAGCAGGTGCCAGGGTTCT	TGCATTCTGTCTCGTGGTTGT
ABCA1	<i>ATP Binding Cassette Subfamily A Member 1</i>	TGGTGATGCGGAAGTTTCTG	TTGTCACAACCTGGCTTCAGG
SREBP1c	<i>Sterol Regulatory Element Binding Protein 1c</i>	TTGAGGATAGCCAGGTCAAAGC	AAAGCGAGGCCAAAGGATTG
SREBP2	<i>Sterol Regulatory Element Binding Protein 2</i>	AAGTCCTGCAGCCTCAAGTG	ATTGGCTGTCTGCGTCAAC
FASN	<i>Fatty Acid Synthase</i>	AGTTCATGAAGCTGGGGATG	ACAGCCTCAGAGCGACAATATC
HMGCR	<i>3-Hydroxy-3-Methylglutaryl-CoA Reductase</i>	CAGCAGATTTGCTCGTCTACAG	ACTGCCAGAATCTGCATGTC
APOE	<i>Apolipoprotein E</i>	TGCTGTTGGTCACATTGCTG	TAATCCCAGAAGCGGTTTCAGG
KROX20 (Egr2)	<i>Early growth response protein 2</i>	TGCACCTAGAAACCAGACCTTC	TGCCCGCACTACAATATTG
SOX10	<i>SRY-Box Transcription Factor 10</i>	ACTACAAGAGTGCCACCTG	TGTCTGGGGTGGTTGGAG
DHH	<i>Desert Hedgehog</i>	ATCCACGTATCGGTCAAAGC	AGTCACCACGATGTAGTTCCC
S100 $\beta$	<i>S100 calcium-binding protein B</i>	TGGTTGCCCTCATTGATGTC	TCTCCATCACTTTGTCACCAC
MPZ	<i>Myelin Protein Zero</i>	ATCTCTTTTACCTGGCGCTACC	ACTGGATGCGCTCTTTGAAG
PMP22	<i>Peripheral Myelin Protein 22</i>	TCTGGCAGAACTGTACCACATC	TGGCAGAAGAACAGGAACAGAG
SGMS1	<i>Sphingomyelin Synthase 1</i>	AAAGCTTCAGTGGCTGATGG	TTCTCCGGTCTGTGCTGTC
SGMS2	<i>Sphingomyelin Synthase 2</i>	AACTGTCGTGCTCACACTTAC	TTCATGCGCTACGAGAATGC
TBP	<i>TATA Box Binding Protein</i>	CAGCAGTTCAGTAGCTATGAG	CTCTGCTCTAACTTTAGCACCT

**Table 7.** Primer sequences.

## 10. Statistical Analysis

All data were analyzed using GraphPad Prism v.6 and were reported as average values and standard deviation. Differences between averages of multiple groups were compared by one-way analysis of variance (ANOVA). Then followed by Tukey's post hoc test for identifying the sources of those differences. Two group comparisons were conducted by Student's t test. P values  $\leq 0.05$  were considered statistically significant and indicated as the following \*P < 0.05, \*\*P < 0.01, \*\*\*P < 0.001, and \*\*\*\*P < 0.0001.

## CHAPTER III: RESULTS

### *Context of the Study:*

Previous studies, led by our team, have shown that LXR  $\alpha/\beta$   $-/-$  total mutants show dysregulation of myelin gene expression, thinner myelin sheaths and elevated oxidative stress levels (Mehdi Hichor et al., 2018; Makoukji et al., 2011). Previous findings and our unpublished data have called attention to LXR $\beta$  being the most prominent and functional isoform in the sciatic nerve. However, no previous study specifically deleted the single isoform LXR $\alpha$  or  $\beta$  in Schwann cells. Thus, we were interested in using a specific knock-out model of the LXR $\beta$  isoform uniquely in Schwann cells; the myelinating glia of the PNS.

We constructed this mouse model by cross breeding LXR $\beta$  floxed mice with Desert Hedgehog: Cre mice as well as LXR $\alpha$  Floxed mice with Dhh Cre mice. Only the LXR $\beta$  Schwann Cell specific Knock-Out (LXR $\beta$  SC KO) mice manifested severe behavioral and locomotive deficits and the presence of very few myelinated axons. Therefore, in this study, we aimed to understand the consequences of LXR $\beta$  SC KO on the structural integrity, biophysical properties and lipid homeostasis of the sciatic nerves.

### 1. LXR $\beta$ specific deletion in Schwann Cells presents deleterious consequences on behavioral performance, myelination and nerve conduction.

#### 1.1. Animal model design

As stated previously, we were interested in evaluating the role of LXR $\beta$  specifically in SCs based on our previous data. However, it was mandatory to also evaluate the consequences of LXR $\alpha$  specific deletion in SCs. LXR $\alpha$  Schwann cell specific knock-out mouse model did not present a phenotype, no abnormalities were observed in histology (Figure 1) or behavioral assessment (Data not shown).

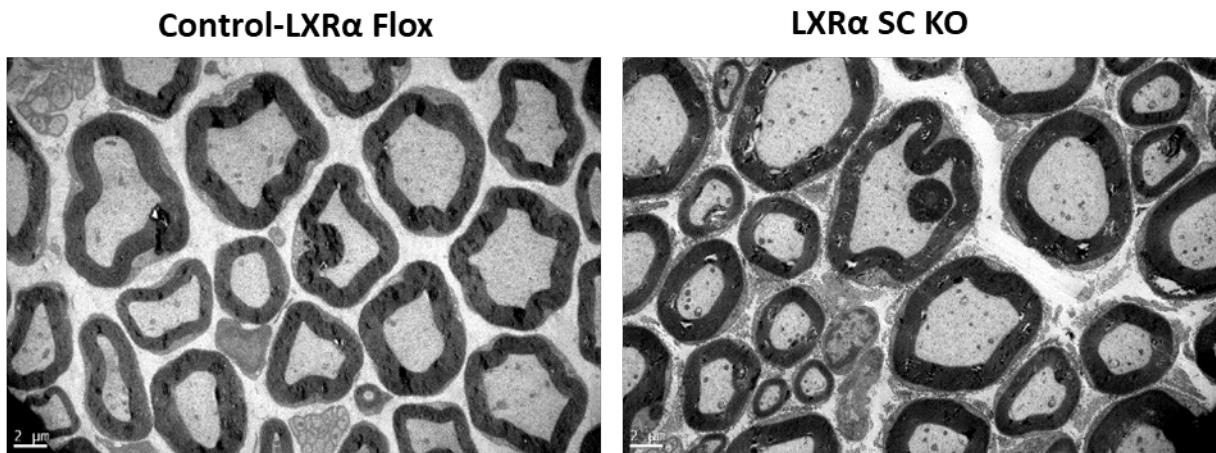


**Figure 1.** Transmission Electron Microscopy (TEM) of ultra-thin sciatic nerve sections of Control (LXR $\alpha$  floxed mice) and LXR $\alpha$  SC specific knock-out mice at 20 weeks. Scale bar = 2 $\mu$ m.

*The Liver X Receptor  $\beta$  Schwann cell specific knock out mouse model.*

The mouse model is obtained by cross breeding  $LXR\beta^{f/+}$ : Dhh-Cre and  $LXR\beta$  floxed mice. In order to obtain  $LXR\beta$  SC specific KO mice, we crossbred  $LXR\beta$  floxed mice expressing Desert Hedgehog Dhh: Cre recombinase ( $LXR\beta^{f/+}$ : Dhh-Cre) and transgenic  $LXR\beta$  floxed mice (Figure 2). Once Cre recombinase is expressed, under the control of Dhh at E13, it will subsequently delete the floxed  $LXR\beta$  gene specifically in the Schwann cells, and thus, we obtain our Schwann cell specific  $LXR\beta$  KO mouse model ( $LXR\beta$  SC KO or  $LXR\beta^{f/f}$ : Dhh-Cre). Specific ablation of  $LXR\beta$  in the SCs leads to a 50% decrease of its mRNA expression levels in the sciatic nerve of the mice and does not affect significantly  $LXR\alpha$  expression, therefore  $LXR\alpha$  is not compensating the reduction in  $LXR\beta$  expression (Figure 3).

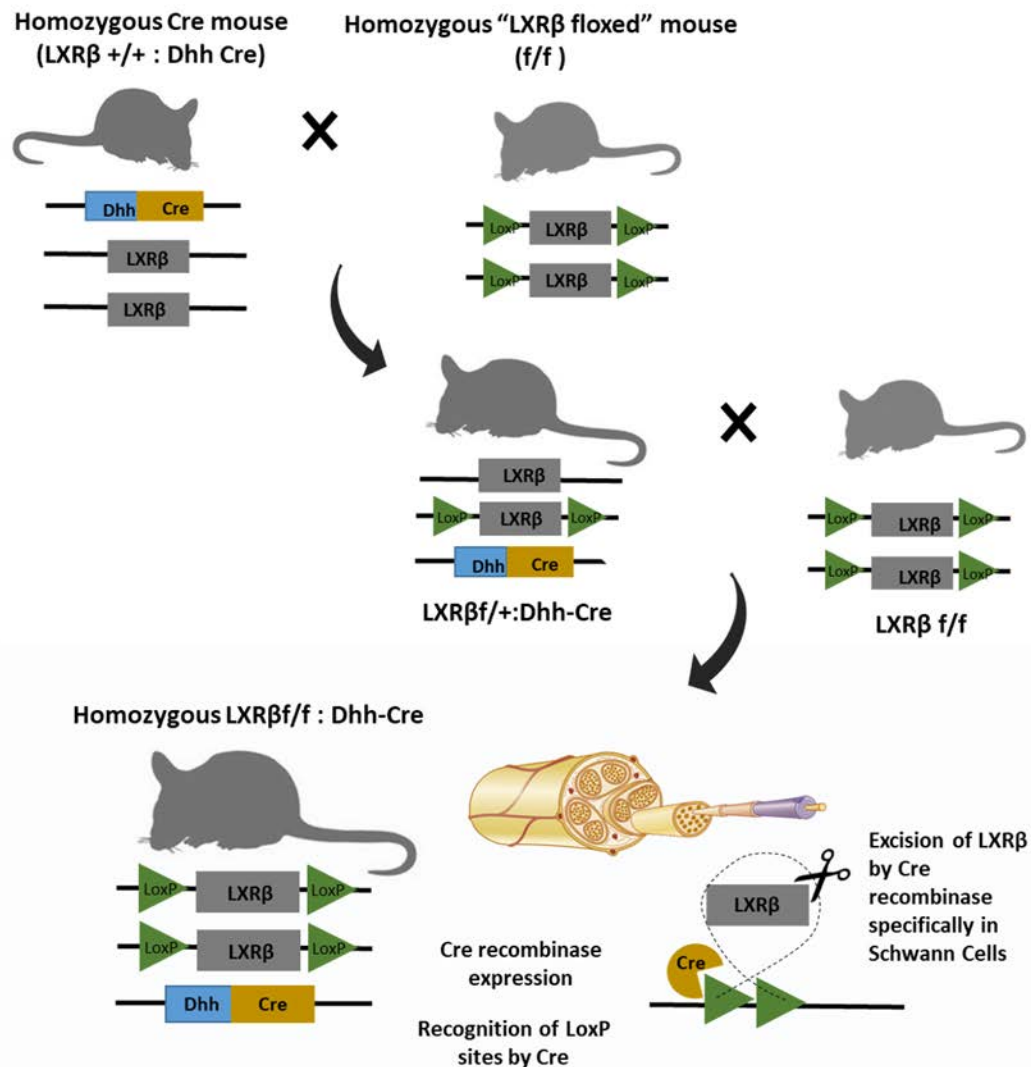


**Figure 2.** Cre-lox Schwann cell specific  $LXR\beta$  knock out mouse model.

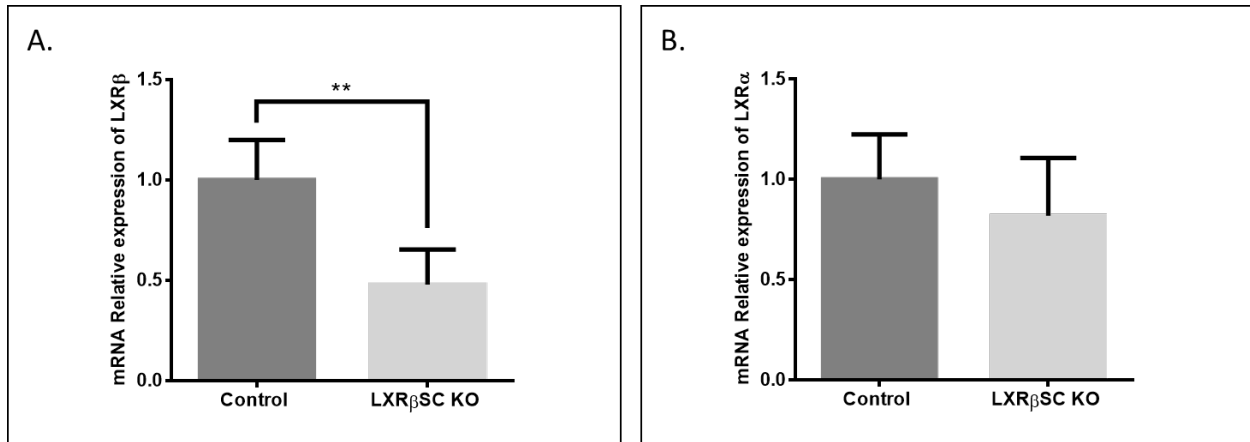


**Figure 3. mRNA expression levels of LXRβ and LXRα in control and LXRβ SC KO sciatic nerves of 8 weeks old mice.** RT-qPCR analysis of (A) LXRβ and (B) LXRα mRNA expression levels (n=3 Control, n=3 LXRβ SC KO). TBP was used for normalization. Results are represented by the mean +/- SD. Statistical significance was assessed by an unpaired Student t test with \* P<0.05, \*\* P<0.01, \*\*\*P<0.001.

### LXRβ floxed mice

LoxP sites were inserted into the mice genome around the nr1h2 (LXRβ) gene, the gene is therefore floxed or flanked by LoxP. Each LoxP (locus of X over P1) sequence is 34 base pairs long and consists of two 13 base pairs repeats separated by an asymmetric 8 base pairs sequence. The nr1h2 gene contains 10 exons with the coding region starting from exon3. The two LoxP sites are inserted in the same orientation into the genome of the mouse; one upstream of exon 3 and the second downstream of exon 7 of the nr1h2 gene (Figure 4). The floxed region also contains the Ligand Binding Domain and DNA Binding Domain thus the deletion of the floxed regions would be removing crucial domains necessary for the function of the LXRβ protein.

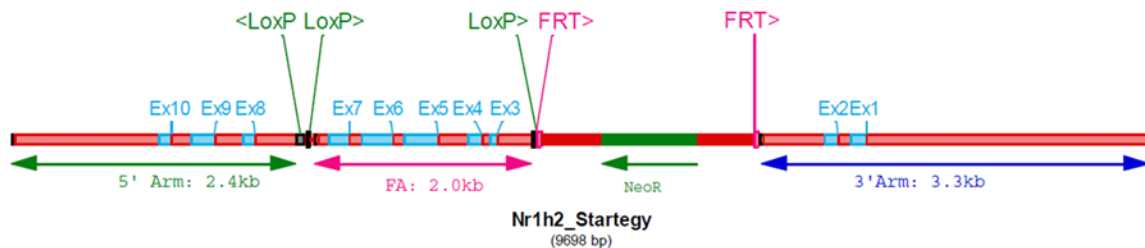


**Figure 4. LoxP site insertion for LXRβ conditional knock out.**

The insertion of LoxP sites surrounding the Liver X Receptors (nr1h2 and nr1h3) into an SV129 background was performed by ICS (K69-DG57) and then backcrossed to the C57BL6/J



background for 10 generations by the lab of Pr. Mangelsdorf 's Lab (Mansuy-Aubert et al., 2015). Every five generations the C57BL6/J is re-injected to avoid genetic drift.

In this study, we were only interested in the knock-out of the  $\beta$  isoform of the Liver X Receptor (nr1h2) in the PNS. Therefore with series of breeding and genotyping we were able to obtain LXR $\beta$  Floxed mice (LXR $\beta^{f/f}$ ) and eliminated the Lox P sites surrounding LXR $\alpha$  (nr1h3).

LXR $\beta$  Flox mice are considered as a suitable control for our LXR $\beta$  SC KO model, only presenting LoxP sites around the LXR $\beta$  gene but do not express the Cre recombinase. As mentioned, the mice were brought to a C57BL6/J background, thus Wild type C57BL6/J mice were added in some cases as controls in experiments.

### **Desert Hedgehog (Dhh) Cre mice**

Dhh Cre mice are transgenic mouse models that express the Cre recombinase enzyme derived from the bacteriophage P1. Cre recombinase recognizes Lox P sites and excises the DNA sequence between them. The expression of Cre recombinase in our model is under the control of a promoter: the Desert Hedgehog Homologue (Dhh) gene. In the PNS, the Dhh gene is only expressed in Schwann Cell Precursors in the Peripheral Nervous System starting Embryonic day 12.5 (Parmantier et al., 1999). Therefore, using Dhh as a promoter enables the knock out model to be Schwann cell specific. Dhh Cre mice were purchased from The Jackson Laboratory; FVB (Cg)-Tg(Dhh-cre)1/Mejr/J (012929) mice generated by Pr. Dies Meijer. The mice were backcrossed into C57BL6/J for ten generations. Every five generations, the C57BL6/J is re-injected to avoid genetic drift. In order to obtain our LXR $\beta^{f/+}$ : Dhh-Cre mice we crossbreed LXR $\beta$  floxed mice with Dhh-Cre mice.

## **1.2. Phenotypic description of the LXR $\beta$ Schwann cells specific knock-out mouse model.**

The LXR $\beta$  SC specific KO transgenic mice exhibit striking locomotion difficulties. As early as 8 weeks, some would manifest motor coordination problems, loss of tail movement and tremor to complete paralysis of the hindlimbs. The LXR $\beta$  SC specific KO also show some phenotypic characteristics like a curved back and weight loss at early timepoints. Behavioral testing was carried out by our team. Locotronic, grip strength and hot plate behavioral tests respectively

assessed locomotor coordination, muscle force and response to nociceptive stimuli. In all of the stated behavioral tests, there was a significant difference between the results of the Control and LXR $\beta$  SC KO mice. LXR $\beta$  SC KO mice had a higher margin for errors, showed less muscle strength in all limbs and longer time to react to a nociceptive stimulus (Figure 5). All LXR $\beta$  SC KO mice died around 30 weeks of age.

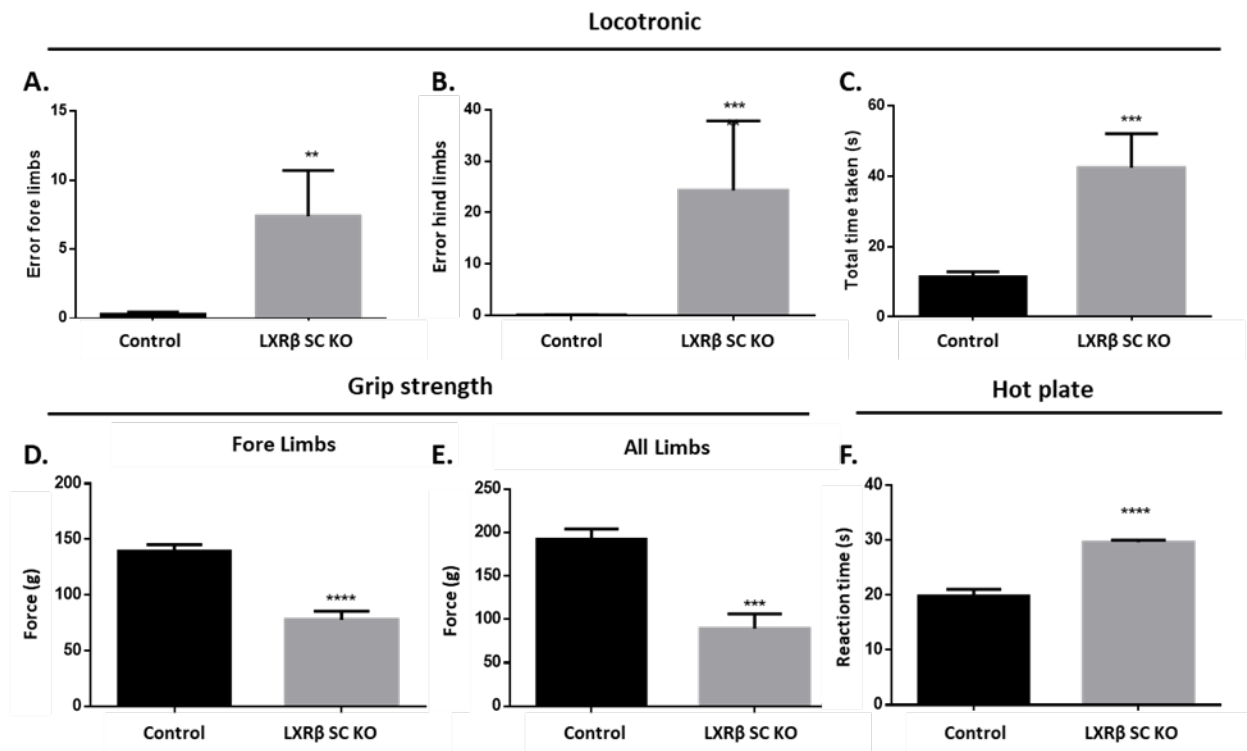


**Figure 5. Behavioral tests on Control and LXR $\beta$  SC KO at 8 weeks.** Locotronic test: A. Total error fore limbs, B. Total error hind limbs, C. Total test time (Control n=12; LXR $\beta$  SC KO n=8). Grip strength test: D. Fore limbs, E. All limbs (Control n=14; LXR $\beta$  SC KO n=9). F. Hotplate test (Control n=16; LXR $\beta$  SC KO n=8). Results are represented by the mean  $\pm$  SD. Statistical significance was assessed by an unpaired Student t test with \* P<0.05, \*\* P<0.01, \*\*\*P<0.001.

Surprisingly, when dissected, the sciatic nerves of the LXR $\beta$  SC specific KO mice were completely translucent (Figure 6). Control sciatic nerves at 8 weeks as well as at 20 weeks are white and well defined however LXR $\beta$  SC KO sciatic nerves were transparent and thinner.

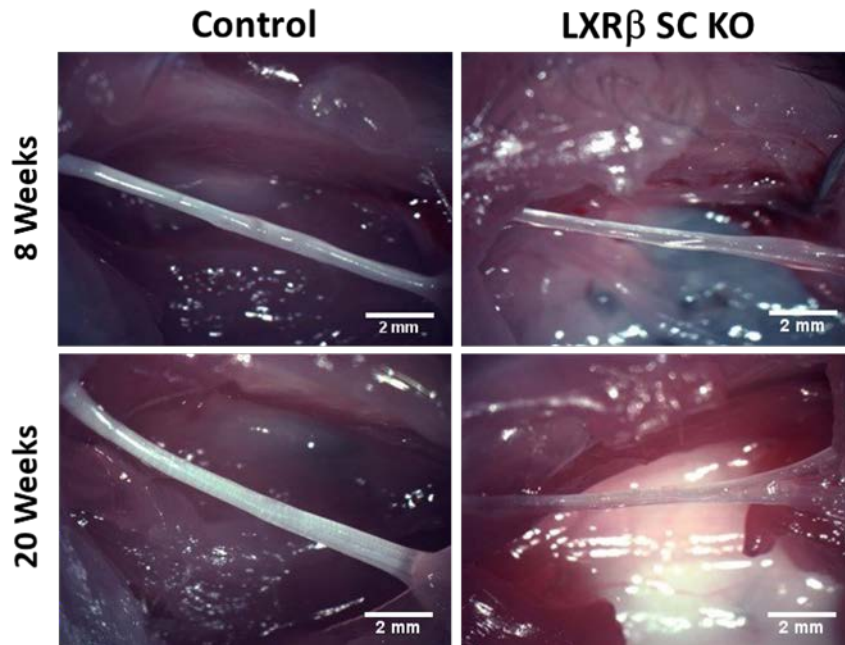


**Figure 6. Images of Control and LXR $\beta$  SC KO sciatic nerves at 8 and 20 weeks of age.**

The ultrastructure of the sciatic nerves was visualized with Transmission Electron Microscopy (TEM) at 8 weeks (Figure 5). These images revealed a vast difference between the Control and LXR $\beta$  SC KO sciatic nerve organization and structure. LXR $\beta$  SC KO sciatic nerves showed less myelinated nerve fibers than the controls, a dominance of unmyelinated fibers bundled together as well as different myelin content between the two sciatic nerves of the same LXR $\beta$  SC KO mice (Figure 7). Due to this observed heterogeneous myelination, we gave the nomination thick for LXR $\beta$  SC KO nerves presenting more myelinated fibers and the thin nomination for the for LXR $\beta$  SC KO nerves presenting less myelinated fibers. Subsequently, we measured the characteristics of both left and right sciatic nerves in all experiments.

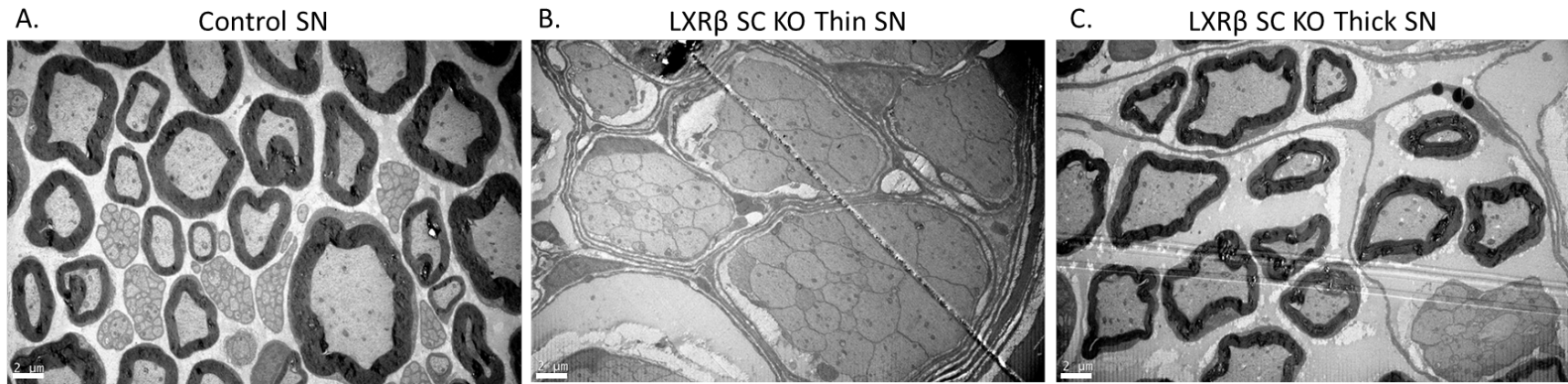


**Figure 7.** TEM images of transversal sections of sciatic nerves at 8 weeks of age. (A) Control and (B) LXR $\beta$  SC KO thin SN (C) LXR $\beta$  SC KO thick SN. Scale bar= 2 $\mu$ m.

### **1.3. Electrophysiological assessment of nerve conduction in LXR $\beta$ SC KO mice.**

We wanted to assess the state of sciatic nerve conduction in LXR $\beta$  SC KO mice by using a sensitive and minimally invasive electrophysiological technique. Hence, we recorded nerve conduction using the Compound Muscle Action Potential (CMAP) where sciatic nerve stimulation is evaluated by the magnitude of response recorded in the muscles (Figure 8). CMAP measurements have been indispensable for the detection and monitoring of neuromuscular disorders, neuropathies, myopathies and demyelination.

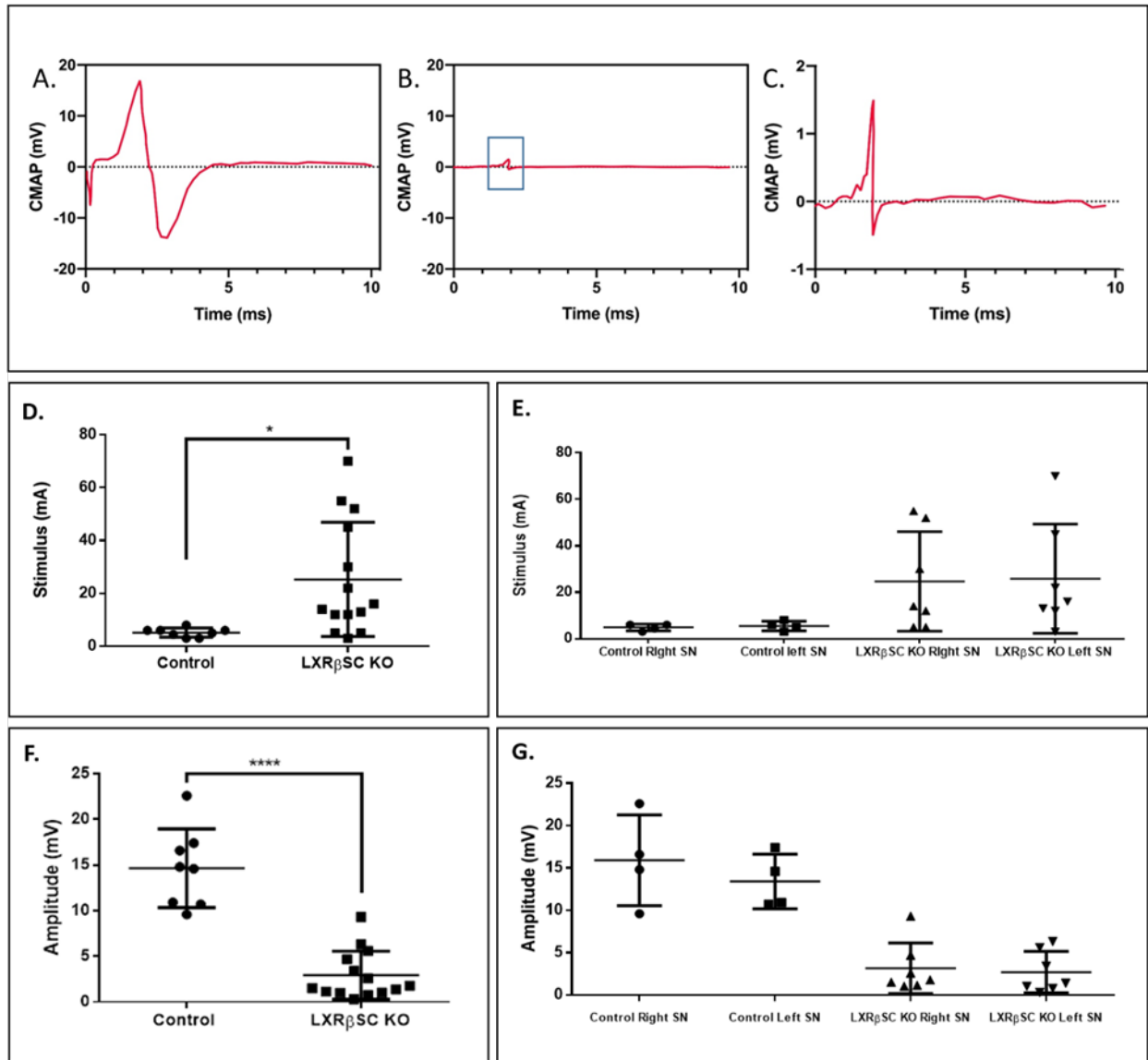


**Figure 8.** Compound Muscle Action Potential (CMAP) measurements in Control and LXRβ SC KO mice at 8 weeks. Representative curve of CMAP measurement in **A.** Control and **B.** LXRβ SC KO mice at 8 weeks. **C.** Enlarged curve of LXRβ SC KO CMAP measurement. **D.** CMAP Supramaximal stimulation values of Control and LXRβ SC KO mice at 8 weeks. **E.** Comparison of supramaximal stimulation values between left and right SNs of both groups. **F.** CMAP Amplitude of response to stimulation in Control and LXRβ SC KO mice at 8 weeks. **G.** Comparison of Amplitude values between left and right SNs of both groups. Data expressed as means ± SDs of the samples, (n=4 Controls, n=7 LXRβ SC KO); Statistical significance was assessed by a Student's T test, \*p<0.05, \*\*\*\*p<0.0001.

As stated, the stimulation of the sciatic nerve is evaluated by the magnitude of response recorded in the muscles, which is referred to as the Amplitude. The stimulations at which we recorded the highest response were around 3 to 5 mA for controls. However, it was not always the case for the LXR $\beta$  SC KO mice. There was a significant difference between the average stimulation of Controls and LXR $\beta$  SC KO mice; in some cases, a stimulation higher than 50 mA was required to obtain a response at the level of LXR $\beta$  SC KO mice muscle fibers. Also, the amplitude of response in LXR $\beta$  SC KO mice, despite the high stimulations, did not exceed 10 mV. The average response amplitude for Controls was  $14.65 \pm 4.3$  mV, yet, it was significantly lower for the LXR $\beta$  SC KO mice, where they registered an average response amplitude of  $2.9 \pm 2.6$  mV. Another crucial parameter measured by CMAP, that could play a role in detecting pathology is the latency. Latency represents the delay between sciatic nerve stimulation and detection of muscle fiber response. Recorded CMAP latency in control mice is between 0.9 to 1 milliseconds. On the other hand, LXR $\beta$  SC KO mice response to stimulation took more time than the controls: latency recordings were between 0.9 to 6 milliseconds. These results further confirm the observed signs of pathology (Figure 9). No significant difference was observed between left and right sciatic nerves in CMAP measurements.

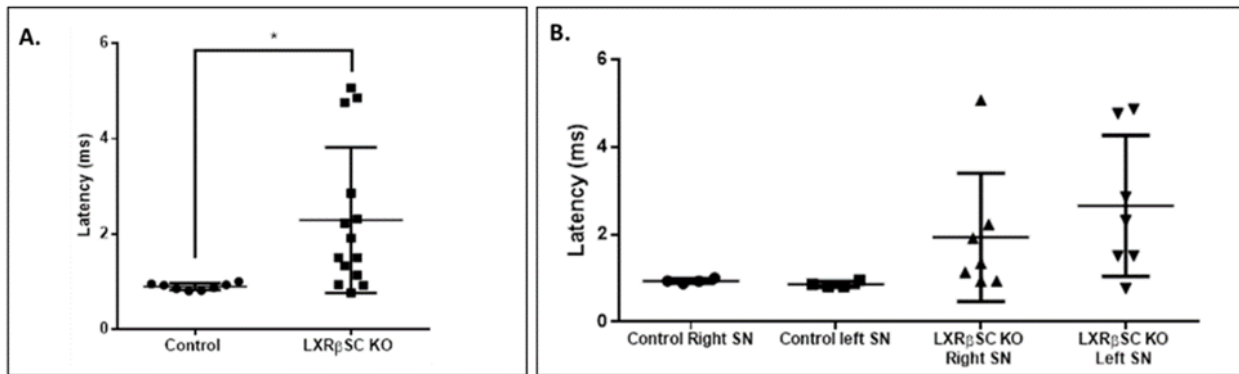


**Figure 9. Compound Muscle Action Potential (CMAP) measurements in control and LXR $\beta$  SC KO mice at 8 weeks. A. CMAP latency (in milliseconds) measurements in Control and LXR $\beta$  SC KO. B. Comparison of latency measurements between left and right SNs of both groups. Data expressed as means  $\pm$  SDs of the samples, (n=4 Controls, n=7 Left & Right LXR $\beta$  SC KO); Statistical significance was assessed by a Student's T test, \*  $p < 0.05$ .**

## 2. LXR $\beta$ specific deletion does not affect the biophysical properties of the nerve fibers but leads to sciatic nerve structural reorganization.

### 2.1. Investigating the effect of LXR $\beta$ SC KO on the structural characteristics of the sciatic nerve fibers

After observing the remarkable difference between the morphology as well as the electrophysiological recordings between the two groups, we were interested in further understanding the implications of LXR $\beta$  SC KO on the structural, physical and biochemical properties of the SNs. Structural organization, membrane composition and fluidity are directly related to the functioning of the sciatic nerves, therefore by evaluating these properties, we might be able to understand the observed phenotype and hope to be able to explain the effect of the LXR $\beta$  SC KO on the SNs.

Atomic Force Microscopy (AFM) has long been a reliable technique for measuring the physical properties of all types of samples. And recently, it has been playing an undeniably essential role in determining the structural and biomechanical properties of biological samples as those of the nervous system. By using the AFM, we were able to first measure the apparent diameter of our teased sciatic nerve fibers. Using the tapping mode, we obtained a topographic representation of the teased nerve fibers and were able to calculate its apparent diameter (Figure 10).

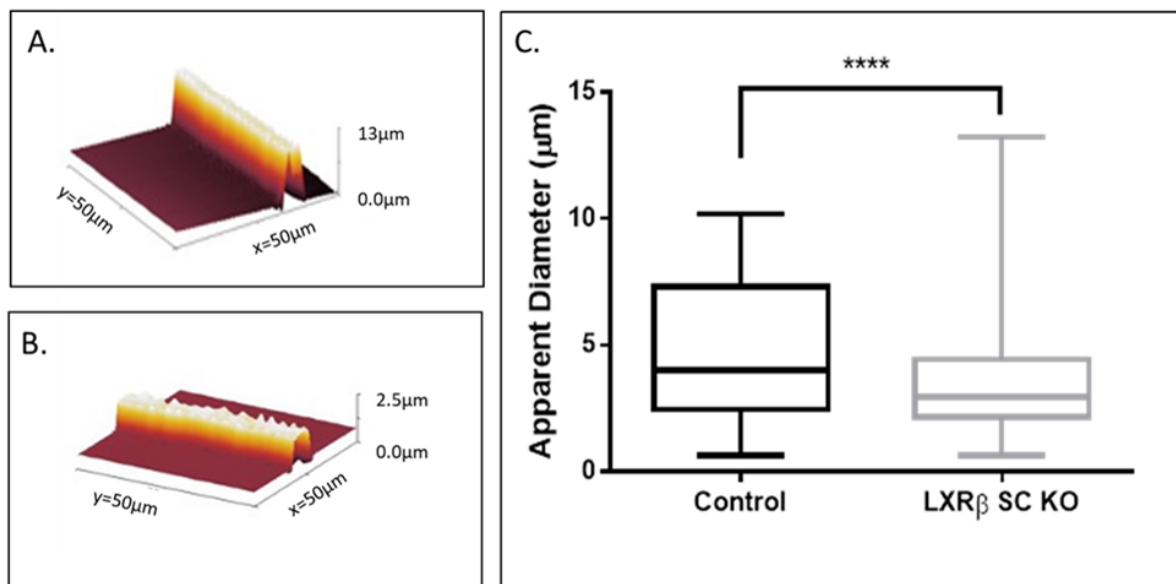


**Figure 10.** AFM measurements of Control and LXR $\beta$  SC KO teased nerve fibers at 8 weeks. Three-dimensional rendering of **A.** Control and **B.** LXR SC KO isolated



nerve fibers topography. **C. AFM Apparent diameter ( $\mu\text{m}$ ) of teased sciatic nerve fibers of 8 weeks Control vs. LXR $\beta$  SC KO mice.** Data expressed as means  $\pm$  SDs of the samples, (n=3, N=114 Controls, n=3, N=179 LXR $\beta$  SC KO); Statistical significance was assessed by a Student's T test, \*\*\*\* p<0.0001.

As expected, there was a significant difference between the apparent diameters of the two groups at 8 weeks. The mean apparent diameter of the Control group was  $4.6 \pm 2.5 \mu\text{m}$  and the mean apparent diameter of the LXR $\beta$  SC KO group was  $3.550 \pm 2.026 \mu\text{m}$  (Figure 9). No significant difference between left and right SN apparent diameter was observed in any of the groups. The AFM measurements were seconded by a high definition imaging of the isolated fibers using Scanning Electron Microscopy (SEM). SEM imaging allowed the observation of the nerve fibers (not feasible by AFM) and the analysis confirmed the observed difference between wild type and KO nerve fibers apparent diameter, where the average apparent diameter of the Control isolated nerve fibers is calculated at  $5.3 \pm 3.2 \mu\text{m}$  and at  $2.9 \pm 3.4 \mu\text{m}$  for the LXR $\beta$  SC KO (Figure 11).

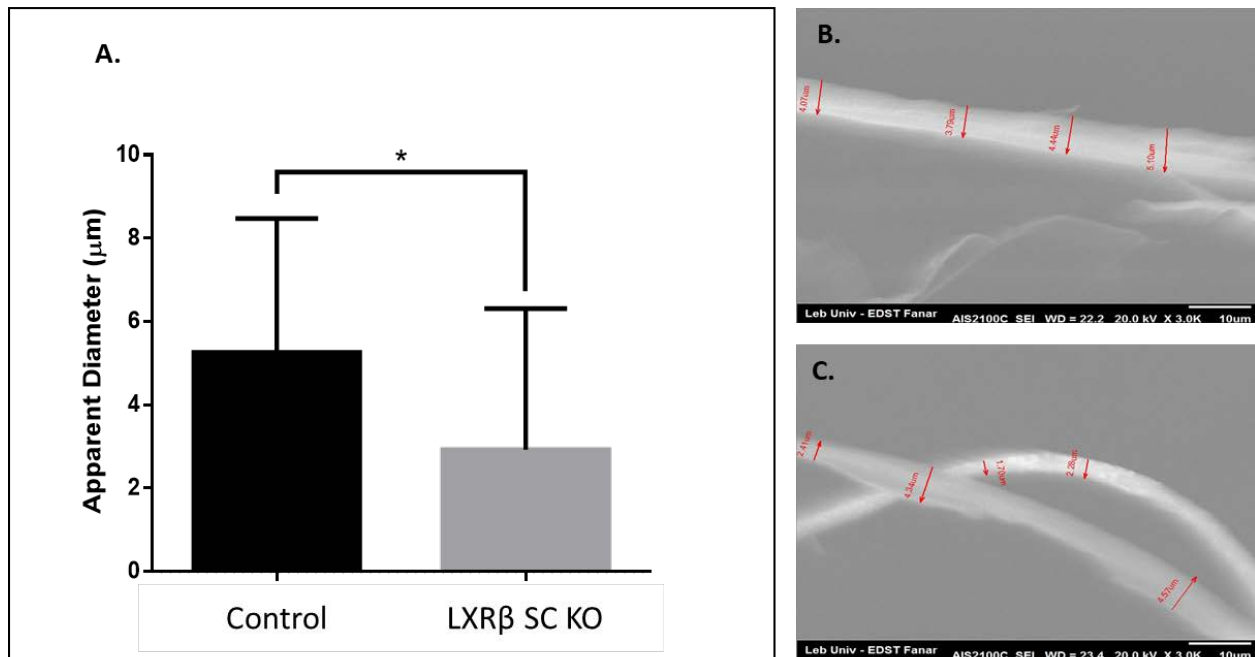


**Figure 11. Scanning Electron Microscopy (SEM).** A. SEM Apparent diameter measurement of sciatic nerve fibers of Control vs. LXR $\beta$  SC KO at 8 weeks. **SEM images of nerve fibers B. Control, C. LXR $\beta$  SC KO** at 8 weeks. Data expressed as means  $\pm$  SDs of the samples, (n=3, N=20 Control 8 weeks, n=3, N=28 LXR $\beta$  SC KO); Statistical significance was assessed by a Student's T test, \* p<0.05.

Many factors could be the responsible for these structural differences such as the myelination status of the sciatic nerve fibers, the number of unmyelinated axons present in the SN and axonal size. Myelination in the PNS depends basically on the diameter of the axons and on the axon-glia interaction. Myelin sheath properties affect conduction velocity, and its lipid composition plays a crucial role in membrane fluidity and physical characteristics. Therefrom, we proceeded by evaluating the myelination status of our nerve fibers by immunofluorescence staining.

We stained the teased nerve fibers for a myelin protein and a neurofilament marker respectively MPZ and NFH (Figure 12). Immunofluorescent imaging revealed that the majority of the LXR $\beta$  SC KO nerve fibers did not stain positive for MPZ. This could imply that there are less myelinated fibers in the LXR $\beta$  SC KO sciatic nerves in comparison with the Control sciatic nerves. These results are in line with Electron Microscopy observations on the LXR $\beta$  SC KO sciatic nerves (Figure 6).

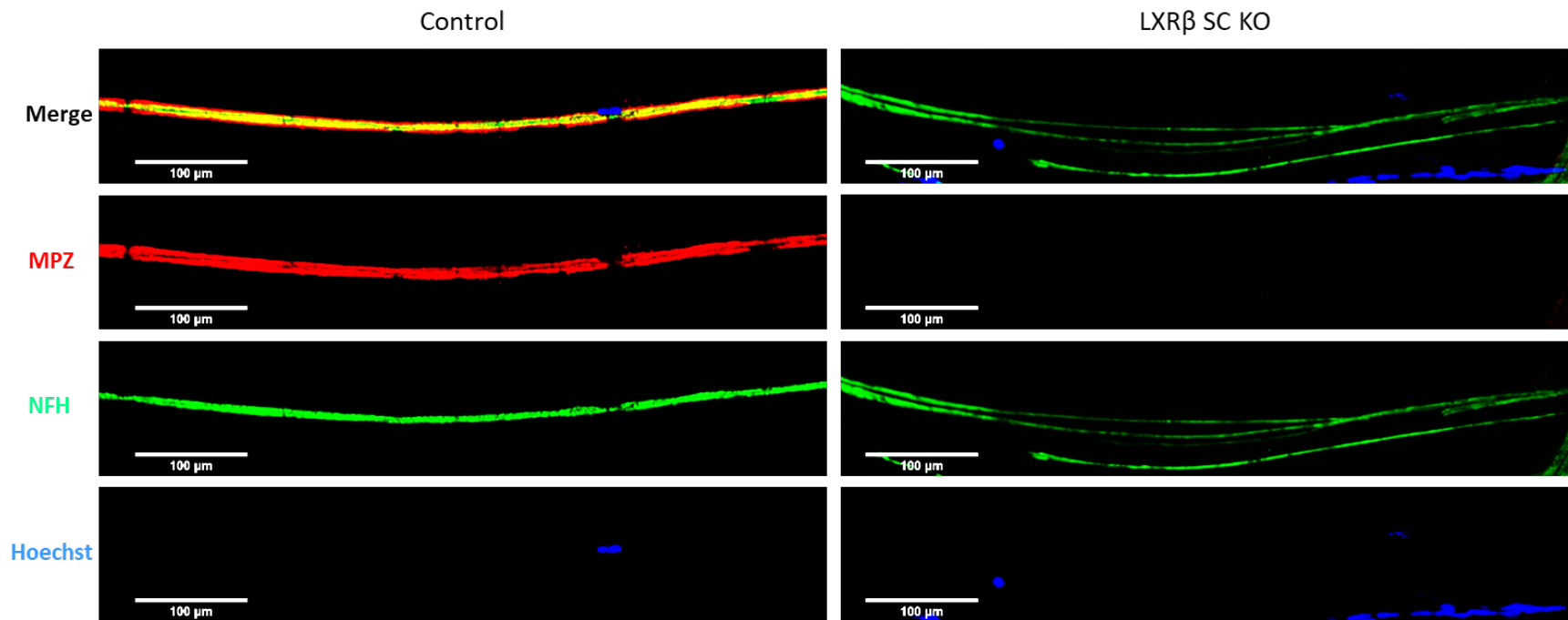


**Figure 12.** Immunofluorescent representative images of teased sciatic nerve fibers of Control and LXR $\beta$  SC KO mice at 8 weeks. Neurofilaments were marked by anti- NFH (Green), Myelin sheath was marked by anti-P0 (Red), and the nuclei by Hoechst.

## 2.2. Investigating the effect of LXR $\beta$ SC KO on the biomechanical properties sciatic nerve fibers.

We then carried our investigation, and assessed if the absence of myelin has a consequence on the biomechanical properties of the sciatic nerve fibers, by measuring the elastic modulus of the nerve fibers using the AFM. We started by applying a 131.6 nN force to the teased sciatic nerve fibers, the Young's modulus of elasticity was calculated by averaging at least 5 force measurements per fiber (Figure 13).

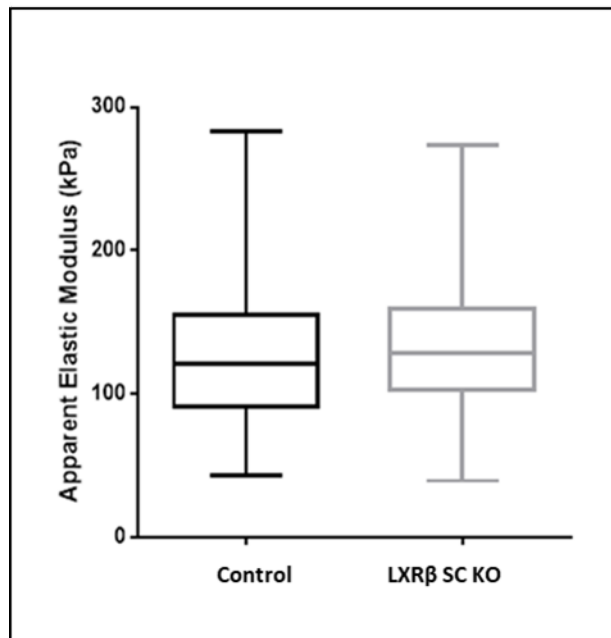


**Figure 13.** AFM apparent elastic modulus measurement of Control vs. LXR $\beta$  SC KO SN fibers at 8 weeks with a 131.6nN applied force. Data expressed as means  $\pm$  SDs of the samples, (Control 8 weeks n=3, N=82 Fiber,  $\pm$ 410 measurement. LXR $\beta$  SC KO 8 weeks, n=3, N=147 fibers,  $\pm$ 735 measurements); Statistical significance was assessed by a Student's T test.

Membrane elasticity measurements reflect on the physical integrity of the fibers. To our surprise, no difference was observed between the apparent elastic modulus of 8-week-old Control and LXR $\beta$  SC KO teased sciatic nerve fibers. The average apparent elastic modulus of 8 week old Control SN teased fibers was  $127.4 \pm 48.6$  kPa and  $136.7 \pm 45.5$  kPa for LXR $\beta$  SC KO. No difference between left and right SN measurements were observed. We further continued the study

by applying different forces to the nerve fibers. We decided to apply 75 nN and 25 nN forces to be able to compare our results to previous studies (Figure 14).

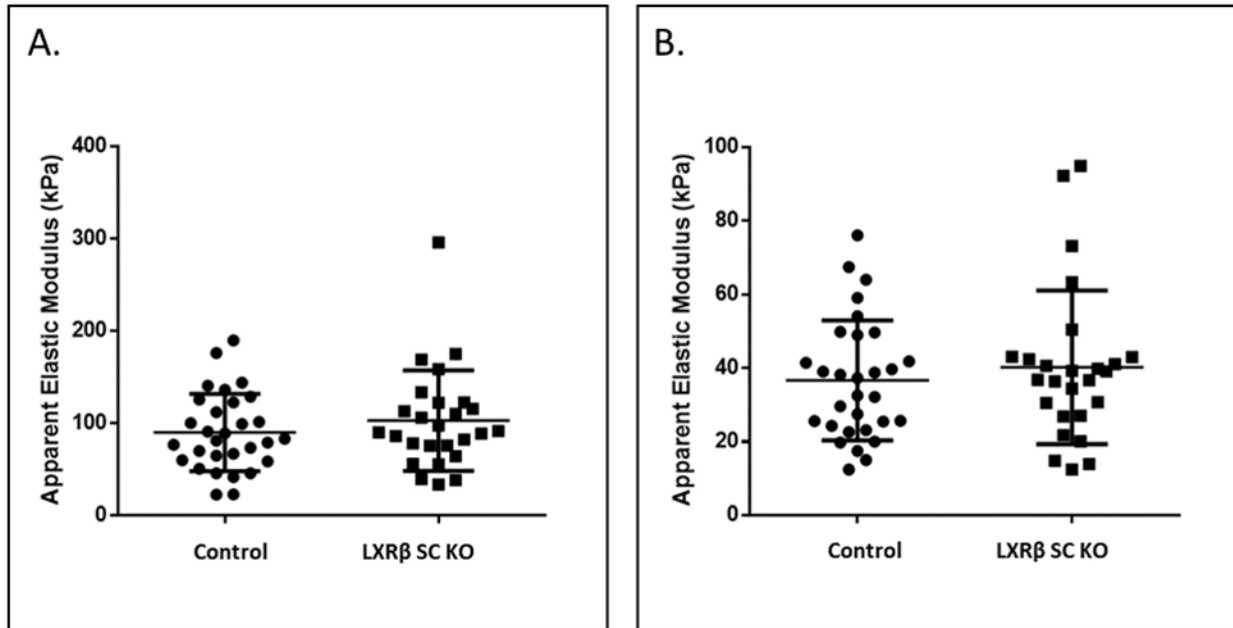


**Figure 14.** AFM apparent elastic modulus measurement of Control vs. LXRβ SC KO SN fibers at 8 weeks using **A.** 75 nN as the applied force, **B.** 25 nN as the applied force. Data expressed as means  $\pm$  SDs of the samples, (Control 8 weeks n=3, N=30 Fiber, 150 measurement. LXRβ SC KO 8 weeks, n=3, N=26 fibers, 130 measurements); Statistical significance was assessed by a Student's T test.

The application of both 75 nN and 25 nN forces by AFM did not show a difference between the two groups elastic measurements. The average apparent elastic modulus of 8 week old Control nerve fibers at an applied force of 75 nN was  $90.1 \pm 41.7$  kPa and  $103.0 \pm 54.4$  kPa for LXRβ SC KO. And the average apparent elastic modulus at an applied force of 25nN was  $36.6 \pm 16.3$  kPa for 8 week old Control SN nerve fibers and  $40.2 \pm 20.9$  kPa for LXRβ SC KO. No difference between left and right SN fiber measurements were observed for both applied forces.

We then compared all the data of applied force measurements and we observed a tendency; LXRβ SC KO measurements showed a slightly higher apparent elastic modulus than the wild type in all applied forces (Figure 15). Therefore, myelin is not the factor affecting the nerve fibers' stiffness.

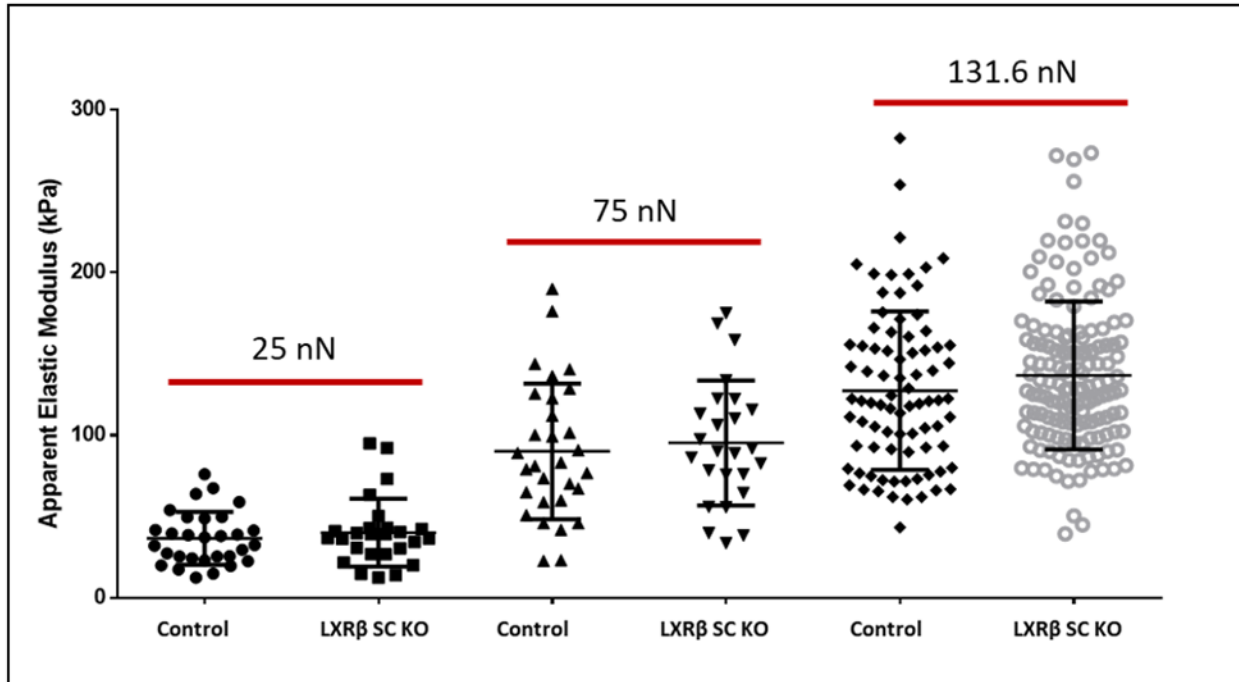


**Figure 15.** AFM apparent elastic modulus measurements of Control vs. LXR $\beta$  SC KO SN fibers at 8 weeks with applied forces 25 nN, 75 nN and 131.6 nN. Data expressed as means  $\pm$  SDs of the samples.

Recent studies have confirmed the role of the basal lamina (BL) and the ECM components as the main players in PNS nerve fiber protection from external injuries. Rosso et al. suggest that it is only when the BL and ECM are compromised that we observe a change in the biomechanical properties of the nerve fibers (Rosso et al., 2014a).

However, in our model, we observe a lack of myelination maybe due to a decrease in SC presence, which are principally the ones responsible for the formation of the BL. We could not really explain our results, therefore we put forward numerous hypotheses.

We first started by evaluating if there is a relationship between nerve fiber apparent diameter and its apparent elastic modulus. No correlation was found between these two parameters which correlates with previous studies in which they have mentioned their inability to find a correlation between the apparent diameter and apparent elastic modulus in nerve fibers. (See Box 4).

#### BOX 4 – Nerve fiber’s Young Modulus during development

The characterization of isolated nerve fibers from sciatic nerves by AFM has been till present, only investigated in the adult stages. Therefore, we decided to assess the Young’s elastic modulus of teased nerve fibers from wild type mice (C57Bl/6) during development. In mice, the second post-natal week – around P10 – corresponds to the peak of myelination, around P23 the myelination is almost complete and at 8 weeks the myelination starts to be maintained. We wanted to evaluate if, in the current setting, a correlation between myelination and nerve fiber stiffness would exist. Even though in different settings, the literature has been suggesting the absence of a direct correlation between myelination and nerve fiber stiffness.

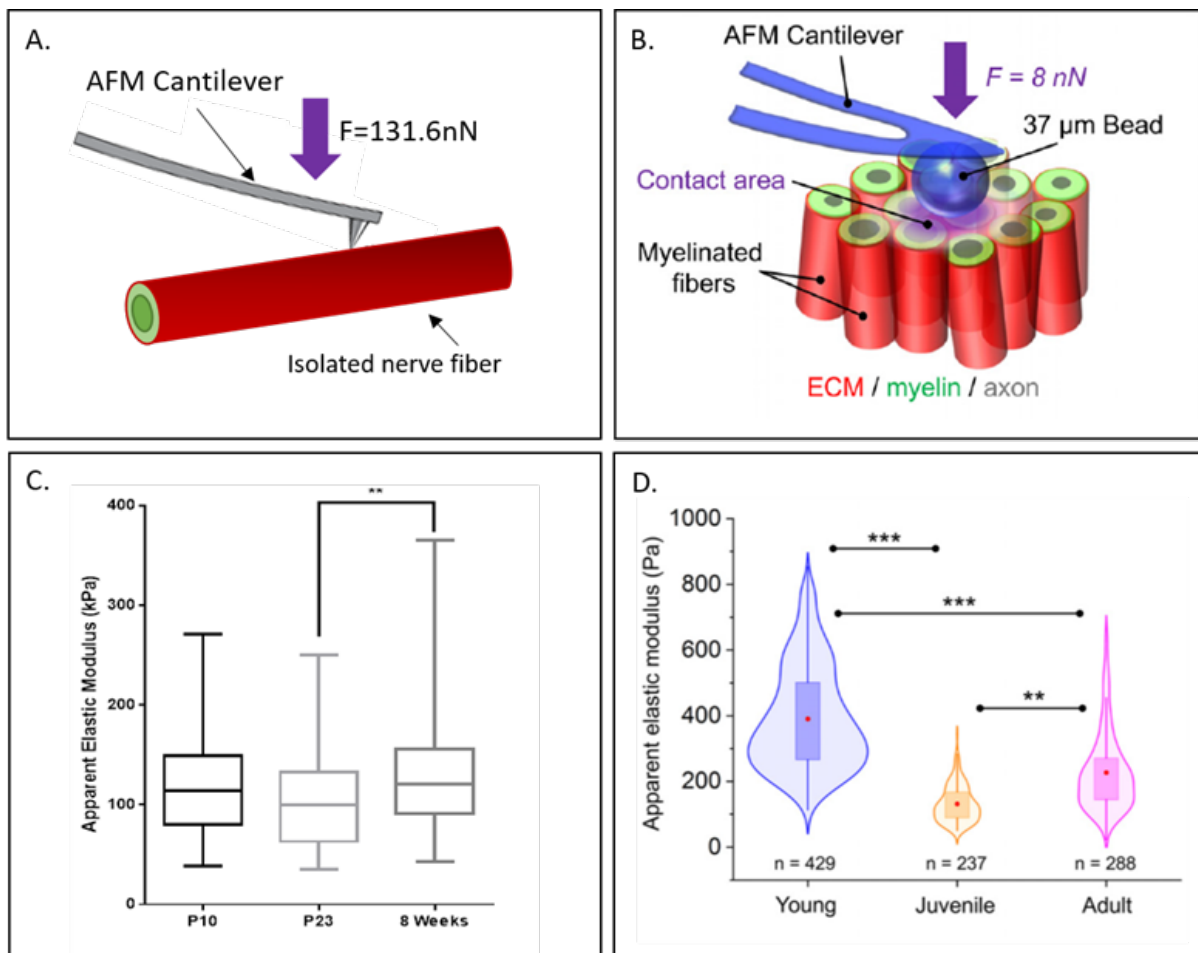


**Figure 16. AFM apparent elastic modulus measurements of nerve fibers at different developmental stages.**

**A.** Scheme of isolated nerve fiber measurement by AFM in our study. **B.** Scheme of sciatic nerve section measured by AFM from (Rosso et al., 2019). **C.** AFM apparent elastic measurement of nerve fibers at P10, P23 and 8 weeks at an applied force of 131.6nN. Young's modulus of elasticity was calculated by averaging at least 5 force measurements per fiber. Data expressed as means  $\pm$  SDs of the samples, (Wild Type P10 n=3, N=57, P23 n=3, N= 68, Wild Type 8 weeks n=3, N=82). Statistical significance was assessed by one way ANOVA with Tukey comparison test, \*\*p<0.01, \*\*\*p<0.001. **D.** Figure from (Rosso et al., 2019) - Apparent elastic moduli of sciatic nerve cross sections measured in developing nerves in young, juvenile, and adult mice (five mice per group) with an applied force of 8nN. Data are presented as violin plots showing data distribution with overlaid box-plots. Red dot= mean; box= 25th and 75<sup>th</sup> percentile. n indicates the total number of force spectroscopy curves. \*\* indicates a significant difference with p<0.001 and \*\*\* with p<0.0001 obtained using a Mann-Whitney test.

Our results show that with the applied force of 131.6nN, the apparent elastic modulus of the teased nerve fibers measured at P10 is  $120.2 \pm 46.5$  kPa, at P23 is  $104.9 \pm 45.0$  kPa and at 8 weeks is  $127.46 \pm 48.6$  kPa (Figure 16 C.). We do not observe a correlation between the nerve fiber's stiffness and myelination, however we observe a significant difference between the nerve fiber's stiffness at P23 and 8 weeks. We were surprised to observe this difference and could not explain this result. However, a recent study conducted by G. Rosso and colleagues in 2019 described this heterogeneous biphasic state of PNS tissue stiffness on SN cross sections (Rosso et al., 2019). The P23 developmental stage in our study (Figure 16 C.) would correspond to the juvenile group in their study (Figure 16 D.) showing a drop in its elastic modulus at that stage explained roughly by a decrease of collagen type 1 expression and a multitude of factors. This observation helped us further evaluate the important role of ECM components in the nerve fibers' stiffness.

Then we postulated two other hypotheses in order to understand our findings. The first one would be an increase of ECM components around the axons to provide protection and the second hypothesis would be a change in SN lipid composition in an attempt to restore the elasticity.



### 2.3. Assessment of cellular organization and collagen deposition in the sciatic nerves of LXR $\beta$ SC KO mice.

ECM and BL components are mostly collagen type I, II and IV, laminin, fibronectin and sulfate proteoglycan. Collagen presence can be easily observed by the use of the classic Masson's Trichrome stain. Histology observations of the sciatic nerves at 8 weeks stained with Masson's Trichrome (Figure 17) revealed a significant increase of collagen deposition (Area %) in LXR $\beta$  SC KO sciatic nerves.

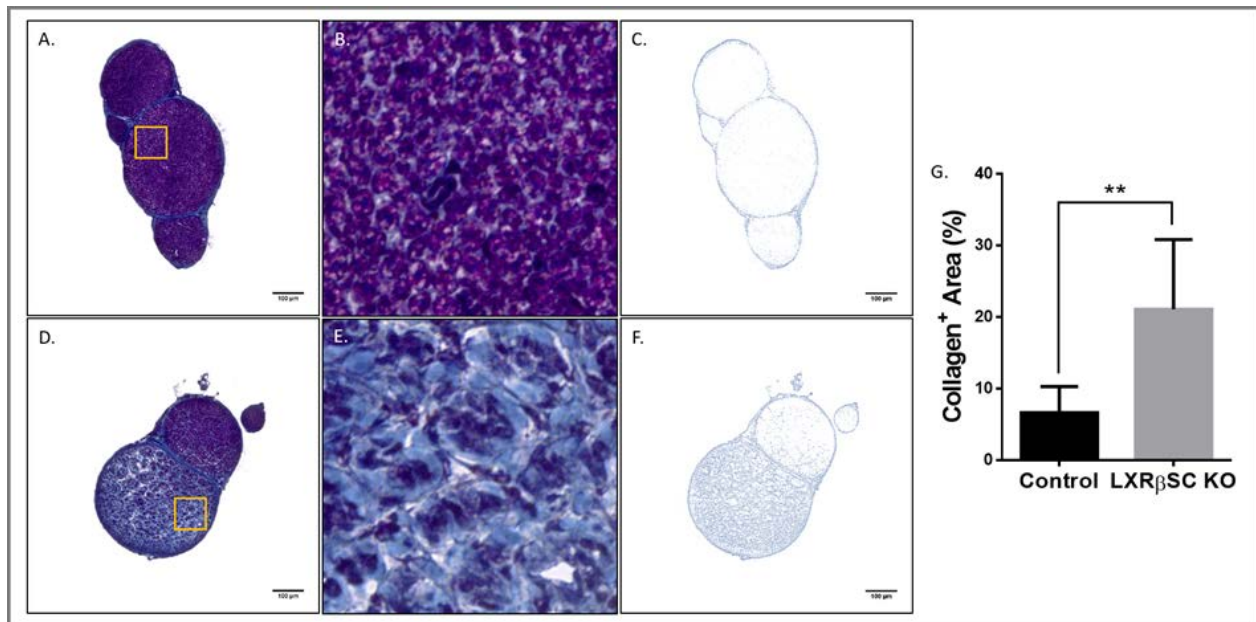


**Figure 17.** Masson's Trichrome stain of the sciatic nerve of 8 weeks old mice. Light microscopy image of the SN, myelin sheath stain purple, collagen stain blue and nuclei stain dark brown. **A.** Control group representative image. **B.** Zoomed in ROI of 100\*100  $\mu$ m of Control section. **C.** Blue channel representing collagen of the Control SN. **D.** LXR $\beta$  SC KO group representative image. **E.** Zoomed in ROI of 100\*100  $\mu$ m of LXR $\beta$  SC KO section. **F.** Blue channel representing collagen of the LXR $\beta$  SC KO SN. **G.** Analysis of collagen positive area over sample area (%). Data expressed as means  $\pm$  SDs of the samples, (n=5 Controls, n=4 LXR $\beta$  SC KO); Statistical significance was assessed by a Student's T test, \*\*p<0.01.

We observed a 3 fold increase going from 6.64 $\pm$ 3.66% in 8 week Control SNs to a 21.09 $\pm$ 9.71% collagen deposition in LXR $\beta$  SC KO SNs. We also observed significant irregularities in nerve fiber grouping architecture between the two groups.

These results support the first hypothesis postulated in order to understand the tendency of LXR $\beta$  SC KO SN fibers' higher apparent Young modulus of elasticity. Since in our model the extent of SC presence is questionable and based on ongoing research that describe the effect of SC absence on SN architecture, we were intrigued to assess the factors that would intervene and might increase ECM component expression.

Therefore, we stained THY1, a marker of endoneurial cells, in control and LXR $\beta$  SC KO sciatic nerves. We observed a higher expression of THY1 in the LXR $\beta$  SC KO SNs compared to their controls littermates which might explain the increase in collagen deposition (Figure 18).

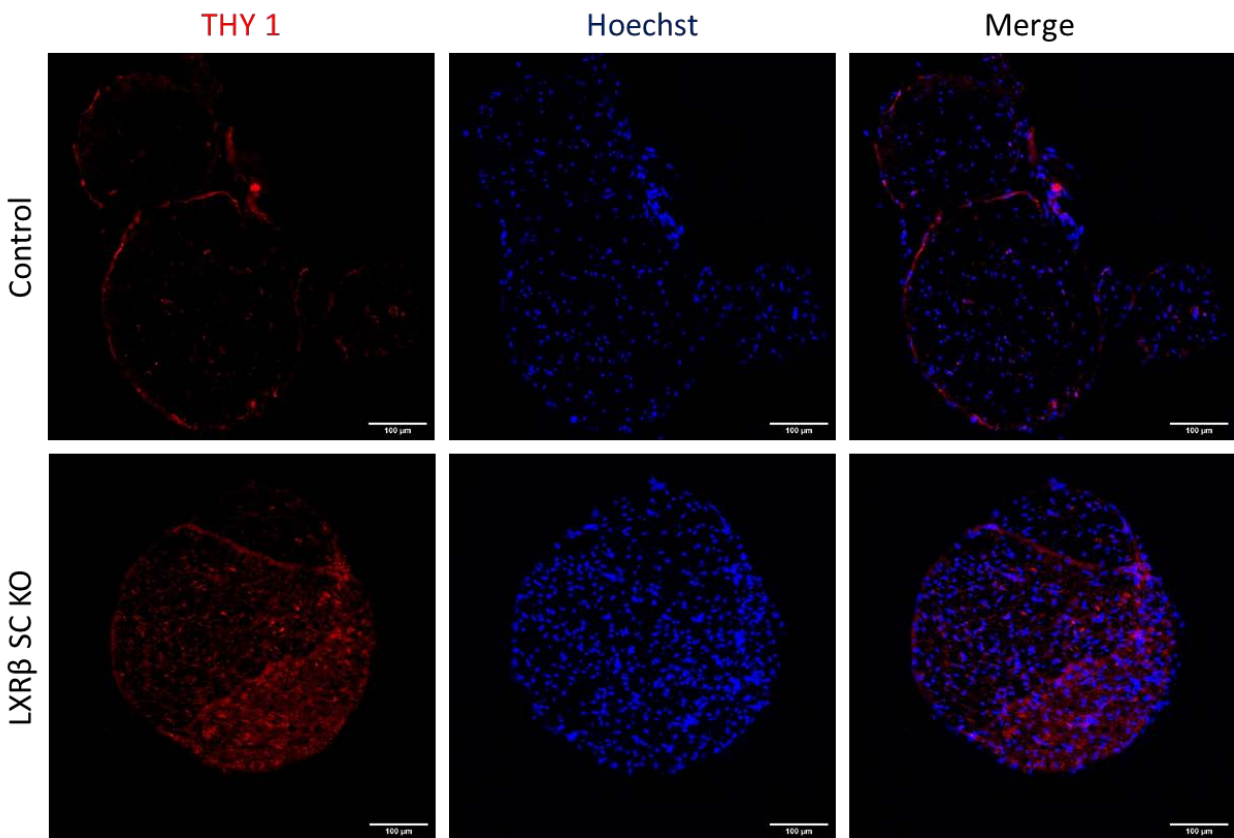


**Figure 18.** Immunohistochemical assessment of endoneurial cell presence in Control and LXR $\beta$  SC KO sciatic nerve cross section at 8 weeks. Nerve sections were stained with anti-Thy1/CD90 (Red) to detect endoneurial cells. Nuclei were stained with Hoechst (Blue) (Control n=3, LXR $\beta$  SC KO n=3) Scale bar = 100 $\mu$ m.

Based on the observation of the EM images and on different KO animal models affecting SC integrity described in the literature, we decided to additionally evaluate perineurial infiltration in the SNs. The perineurium is formed by layers of perineurial cells that form tight-junctions between them, to structure the nerve. We stained our samples with ZO-1, a tight junction marker highly expressed by the perineurial cells in the SN. To our surprise, ZO-1 which is supposed to mark the outlines of the nerve bundles in normal conditions, was abundantly present inside the endoneurial space of the LXR $\beta$  SC KO sciatic nerve (Figure 19).

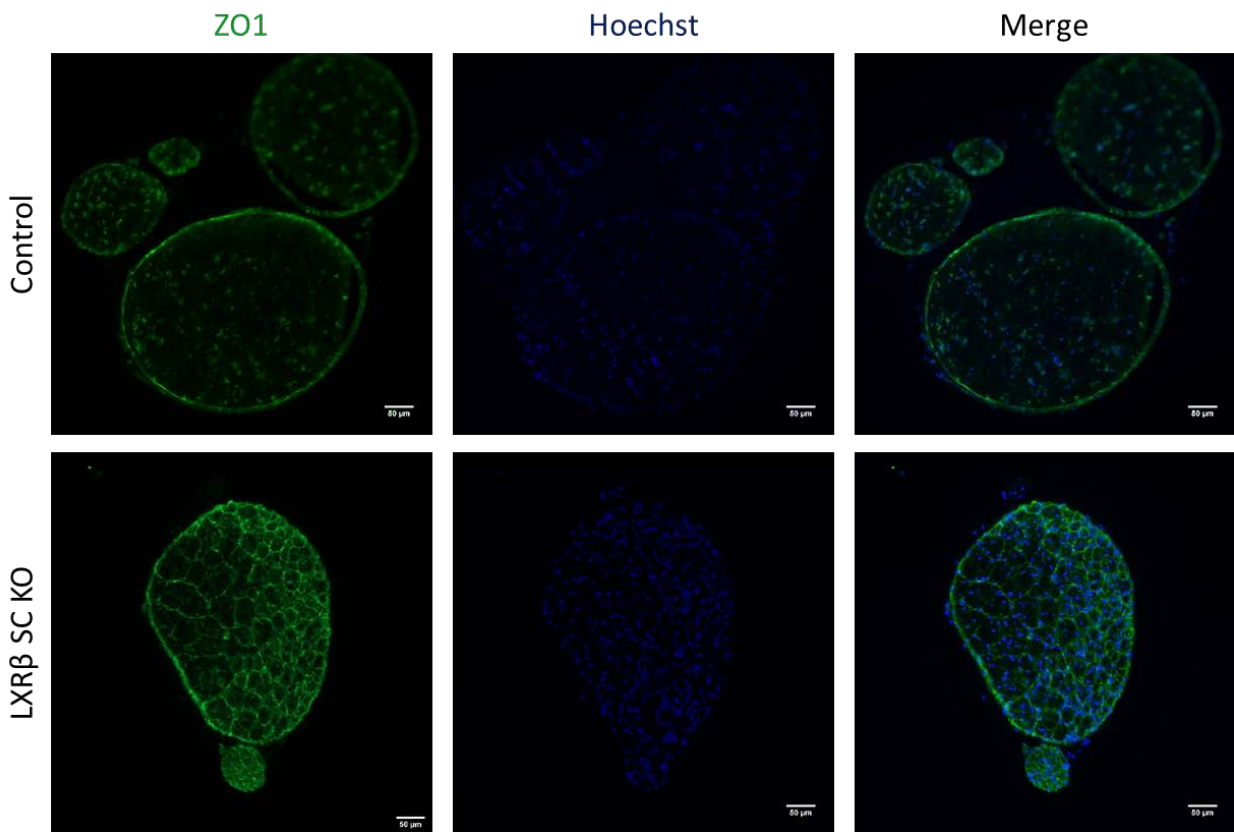


**Figure 19.** Immunohistochemical assessment of perineurial cells presence in Control and LXR $\beta$  SC KO sciatic nerve cross section at 8 weeks. Nerve sections were stained with anti-ZO1 (Green) to detect endoneurial cells. Nuclei were stained with Hoechst (Blue) (Control n=3, LXR $\beta$  SC KO n=3). Scale bar = 50 $\mu$ m.

Not only was it present inside the nerve bundles but it was expressed in an organized but unconventional way, where perineurial cells attempt to reorganize the nerve bundles in reduced presence of Schwann cells. Numerous smaller size nerve bundles were observed to be formed by ZO-1 positive cells in the LXR $\beta$  SC KO sciatic nerves.

Our results show that LXR $\beta$  SC KO does not alter the mechanical properties of the nerve fibers, however, that might be due to the involvement of the other cellular components of the SNs. In absence of myelination or reduced SC presence, we describe an infiltration of perineurial cells, higher staining for THY1 and increased collagen deposition in the LXR $\beta$  SC KO SNs which might be a strategy to maintain SN integrity.

### 3. LXR $\beta$ specific deletion in Schwann cells alters sciatic nerve lipid composition and homeostasis.

The second hypothesis postulated was the alteration of the SN lipid composition in our animal model. We stained for Oil Red O in order to visualize lipid distribution in the SN cross sections (Figure 20). Interestingly Oil Red O staining in LXR $\beta$  SC KO showed irregularities in lipid distribution when compared to their controls. Lipid distribution in LXR $\beta$  SC KO sciatic nerves is not homogeneous, normal lipid distribution can be observed in one nerve bundle but the second would show less amounts to complete absence of lipids (Figure 20 B).

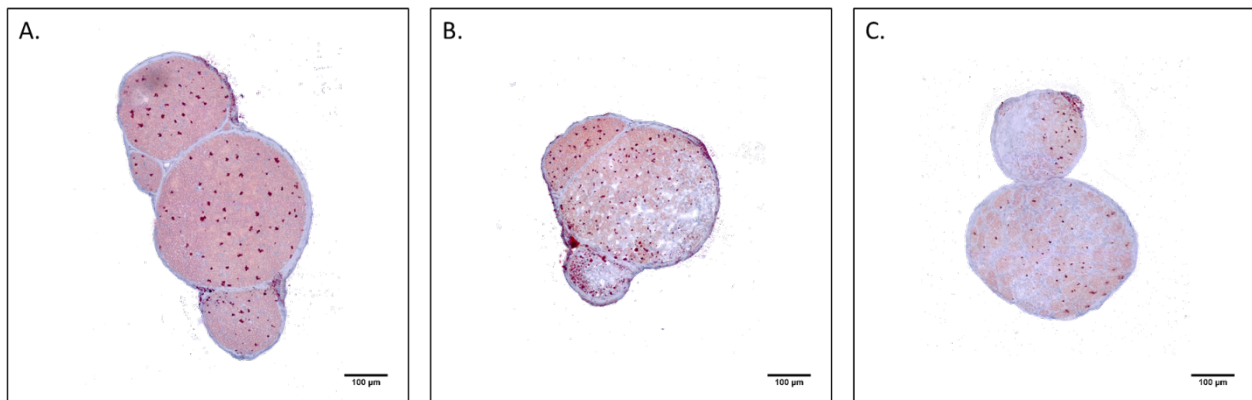


**Figure 20.** Oil Red O stain of the sciatic nerve of 8-week-old mice. Light microscopy image of the SN, neutral lipid droplets stain dark red and myelin sheath stains faint red **A.** Control group representative image, **B.** LXR $\beta$  SC KO representative image 1. **C.** LXR $\beta$  SC KO representative image 2, (n=5 Controls, n=4 LXR $\beta$  SC KO). Scale bar= 100 $\mu$ m.

We continued evaluating the effect of LXR $\beta$  KO on the SN lipid composition by using the time-of-flight secondary ion mass spectrometry (ToF SIMS). ToF SIMS is a mass spectrometry technique that offers a semi quantitative composition of the SN as well as surface molecular composition imaging of the sample (Images 21&22).

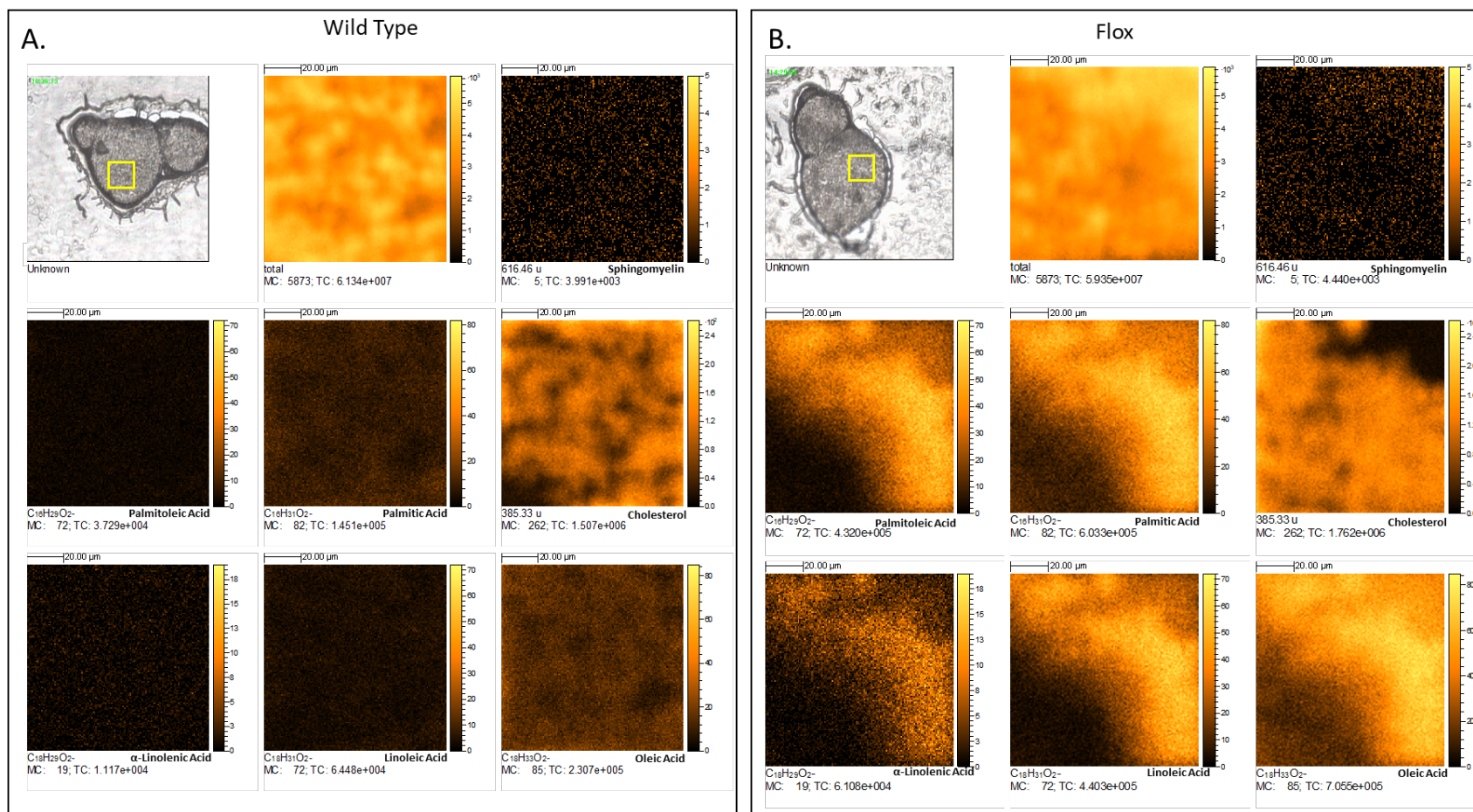


**Figure 21.** ToF-SIMS ion images of Wild type (C57Bl6/j) and Flox sciatic nerve cross section at 8 weeks old in negative ion mode. Below each ion image is the name of the selected species, with maximal number of counts in a pixel (MC). From left to right; optical image of the cross section, ToF SIMS image of total lipids measured in the 100\*100 μm<sup>2</sup> ROI, SM fragment 616.46, Palmitoleic Acid C16:1 m/z 253.21, Palmitic Acid C16:0 m/z 255.23, cholesterol m/z 385.33, α-linoleic acid C18:3 m/z 277.21, linoleic acid C18:2 m/z 279.23 and Oleic Acid C18:1m/z 281.24 (Wild type n=3, Flox Control n=2, LXRβ SC KO left n=4, LXRβ SC KO right n=4). Scale bar =20μm.

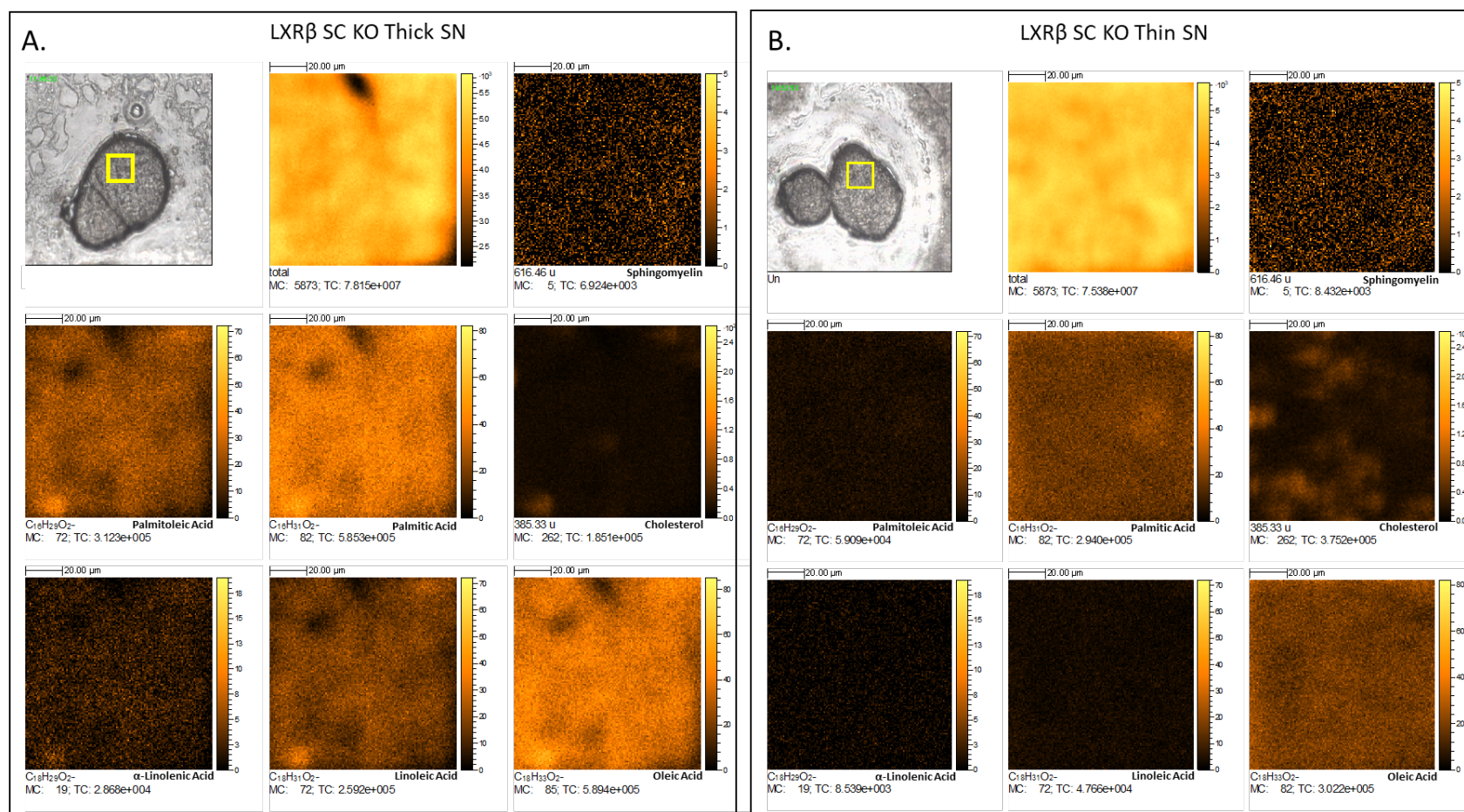


**Figure 22.** ToF-SIMS ion images of thick and thin LXRβ SC KO sciatic nerve cross section at 8 weeks old in negative ion mode. Below each ion image is the name of the selected species, with maximal number of counts in a pixel (MC). From left to right; optical image of the cross section, ToF SIMS image of total lipids measured in the 100\*100 μm<sup>2</sup> ROI, SM fragment 616.46, Palmitoleic Acid C16:1 m/z 253.21, Palmitic Acid C16:0 m/z 255.23, cholesterol m/z 385.33, α-linolenic acid C18:3 m/z 277.21, linoleic acid C18:2 m/z 279.23 and Oleic Acid C18:1m/z 281.24 (Wild type n=3, Flox Control n=2, LXRβ SC KO left n=4, LXRβ SC KO right n=4) . Scale bar =20μm.

TOF SIMS results showed no significant difference between the groups for 16 carbon chain saturated and unsaturated fatty acids measurements as well as for the 18 carbon chain FAs (Figure 23). However, FAs measurements had important error bars highlighting the variability of the samples. Unsaturated over saturated ratio (C18:1/C18:0) also did not show any significant difference between the groups (data not shown). We stained the ToF SIMS measured ROIs with myelin and neurofilament markers (MPZ and SMI 312) to observe the status of myelination of each section. The staining further confirmed the heterogeneity of the measured regions (Figure 24).

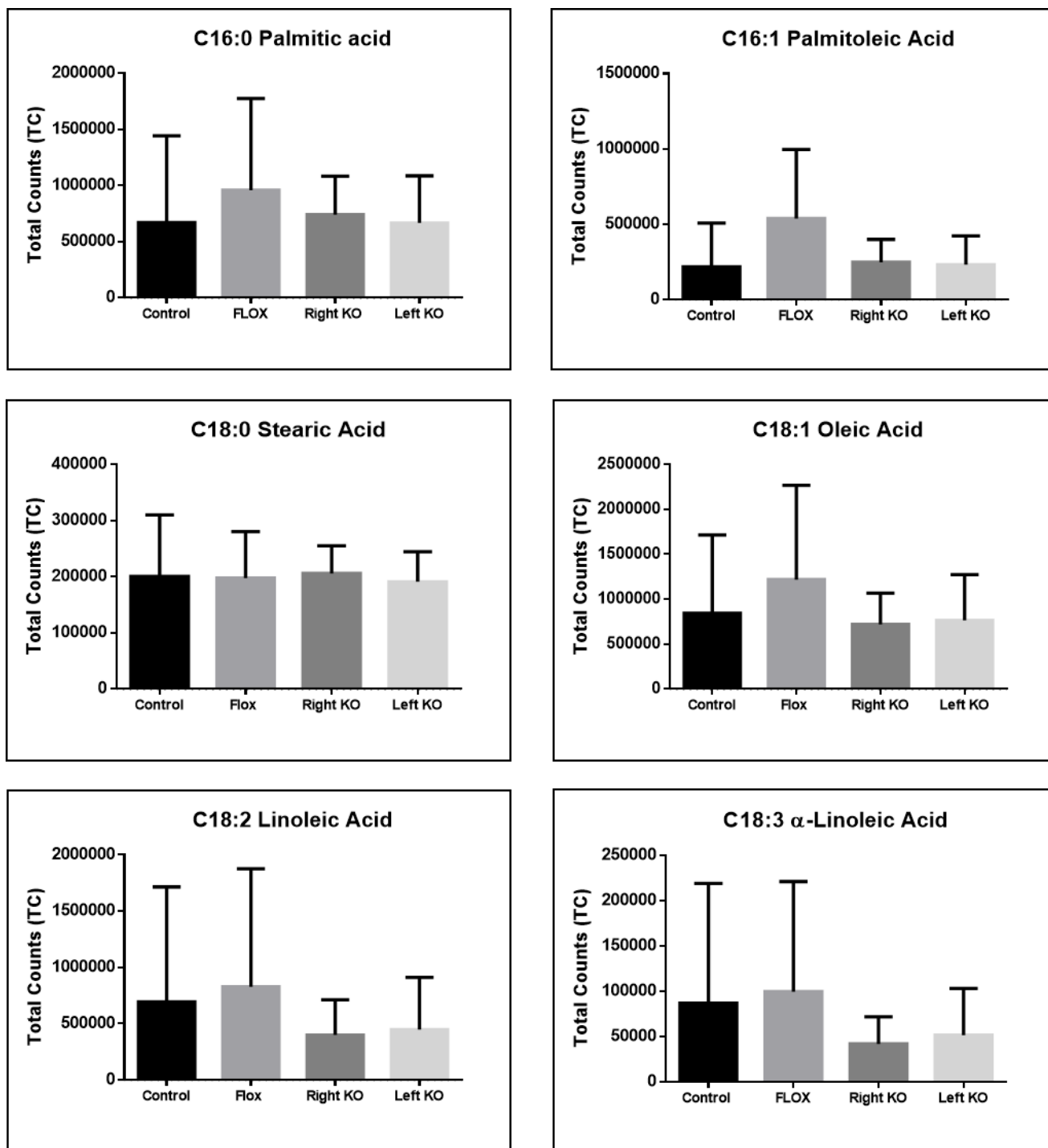


**Figure 23.** Total Counts recorded in ToF-SIMS negative ion mode for Palmitic Acid  $m/z$  255.23, Palmitoleic Acid  $m/z$  253.21, Stearic Acid  $m/z$  283.26, Oleic Acid  $m/z$  281.24, Linoleic Acid 279.23, and  $\alpha$ -Linoleic Acid  $m/z$  277.21 detected in the sciatic nerves (Wild type  $n=3$ , Flox Control  $n=2$ , LXR $\beta$  SC KO left  $n=4$ , LXR $\beta$  SC KO right  $n=4$ ). Columns and bars represent means and SDs of triplicates from each sample (one way ANOVA with Tukey comparison test, \*\* $p<0.01$ , \*\*\* $p<0.001$ ).



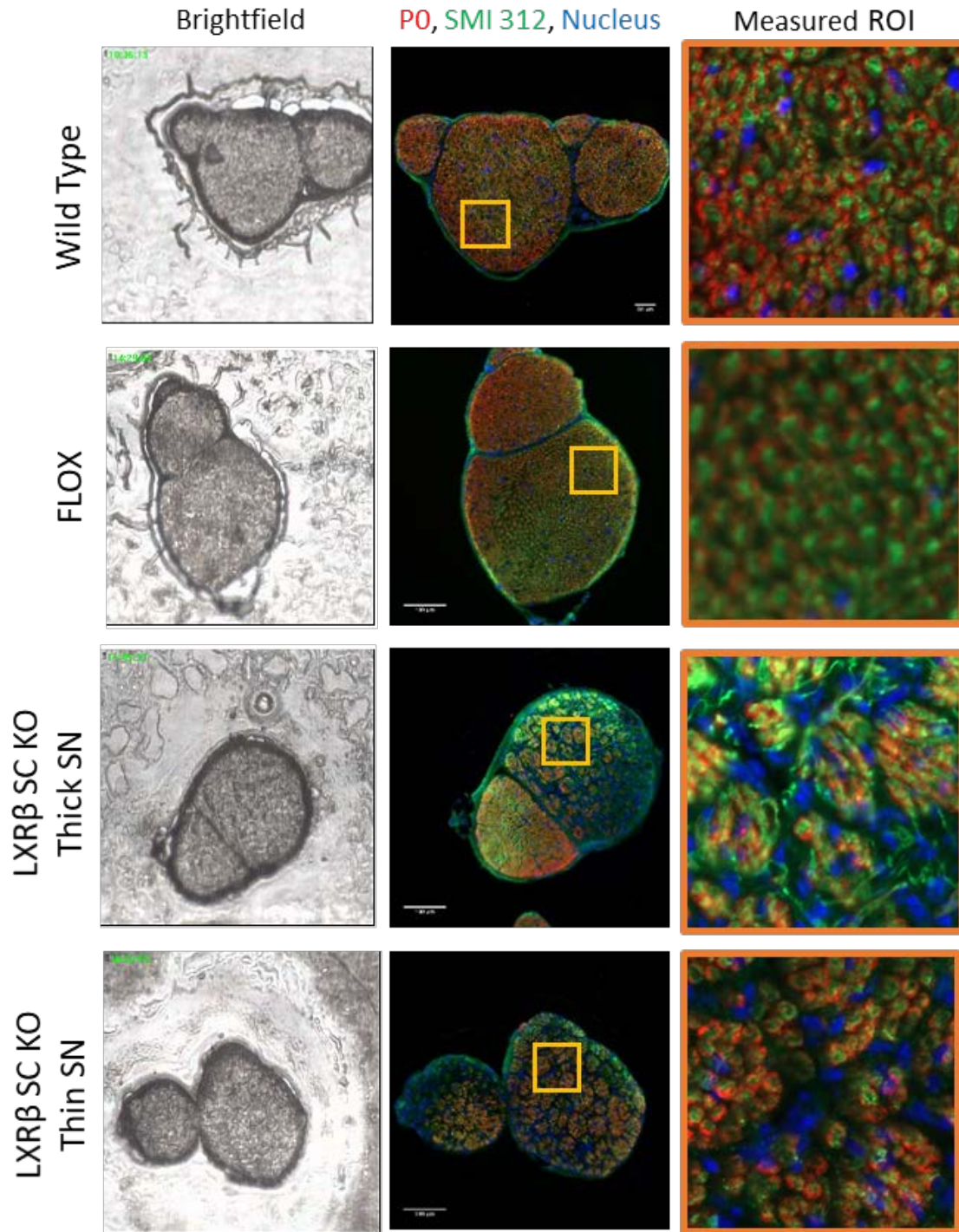


**Figure 24. Assessment of myelination in sciatic nerve cross sections used for ToF SIMS measurements.** The left panel contains optical images of the samples. The middle panel contains the cross sections of the sciatic nerves stained with anti-MPZ (Red) for myelin, anti-SMI 312 (Green) for neurofilaments and Hoechst (Blue) for nuclei, Scale bar = 100 $\mu$ m. The right panel contains the immunofluorescent images of ToF SIMS measured ROIs (100 $\mu$ m\*100 $\mu$ m).

We then evaluated mRNA expression of key enzymes responsible for the regulation and biosynthesis of fatty acids. No significant difference was observed between control and LXR $\beta$  SC KO mRNA expression levels of SREBP1c and FASN in the SNs of 8 weeks old mice (Figure 25). We did not expect significant difference between the groups after describing the scarce presence of myelinated axons and also knowing that LXR $\beta$  is directly involved in the regulation of SREBP1c and increase FA synthesis. The infiltration of other cellular types might be a plausible explanation for the lack of difference between the two groups.

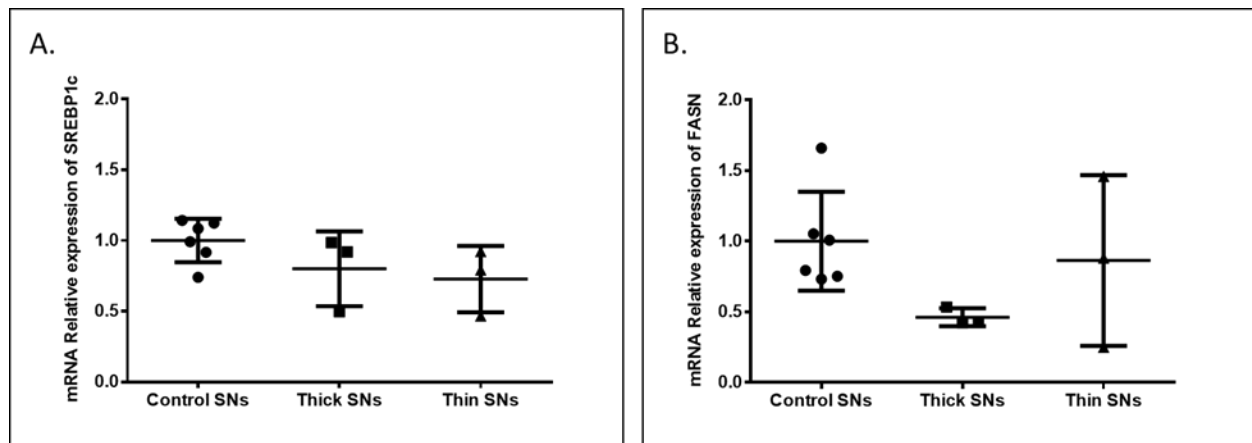


**Figure 25.** mRNA expression levels of SREBP1c and FASN in control and LXR $\beta$  SC KO thick and thin SNs of 8week old mice. RT-qPCR analysis of (A) SREBP1c and (B) FASN mRNA expression levels (n=3 Control, n=3 LXR $\beta$  SC KO). TBP was used for normalization. Results are represented by the mean +/- SD. Statistical significance was assessed by a one-way ANOVA follow by a Post hoc test with \* P<0.05, \*\* P<0.01, \*\*\*P<0.001.

We then evaluated the consequences of LXR $\beta$  SC KO on the SN cholesterol homeostasis. ToF SIMS measurements showed that cholesterol concentration in LXR $\beta$  SC KO SNs was 10 folds lower than in controls (Figure 26).

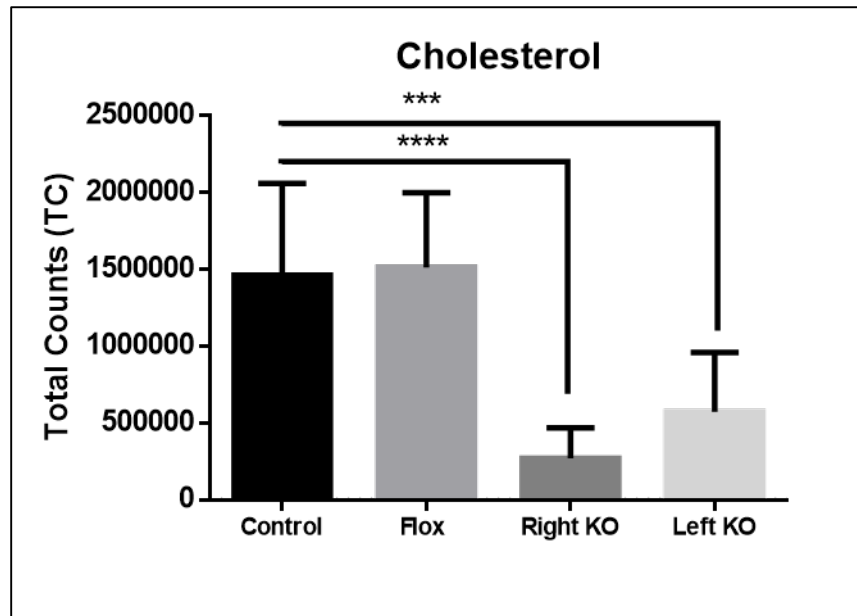


**Figure 26.** Total Counts recorded in ToF-SIMS negative ion mode for Cholesterol *m/z* 385.33 detected in the sciatic nerves (Wild type n=3, Flox Control n=2, LXR $\beta$  SC KO left n=4, LXR $\beta$  SC KO right n=4). Columns and bars represent means and SDs of triplicates from each sample (one way ANOVA with Tukey comparison test, \*\*p<0.01, \*\*\*p<0.001).

A result that could be expected due to the presence of few myelinated nerve fibers, and since the largest portions of SN cholesterol resides in myelin. ToF SIMS imaging also portrayed a clustering of cholesterol in LXR $\beta$  SC KO samples but no interpretation could be extrapolated from the imaging (Figure 21).

mRNA levels of the major regulator of cholesterol biosynthesis SREBP2 and the key enzyme involved in cholesterol *de novo* biosynthesis HMGCR were significantly down regulated. These results might be explained by the absence of myelination or reduced presence of SCs; the SN cellular component that are responsible for the majority of the *de novo* cholesterol production.

Conversely, the mRNA levels of ABCA1 and ApoE; the LXR direct targets responsible for cholesterol transport and efflux, were significantly increased (Figure 27).

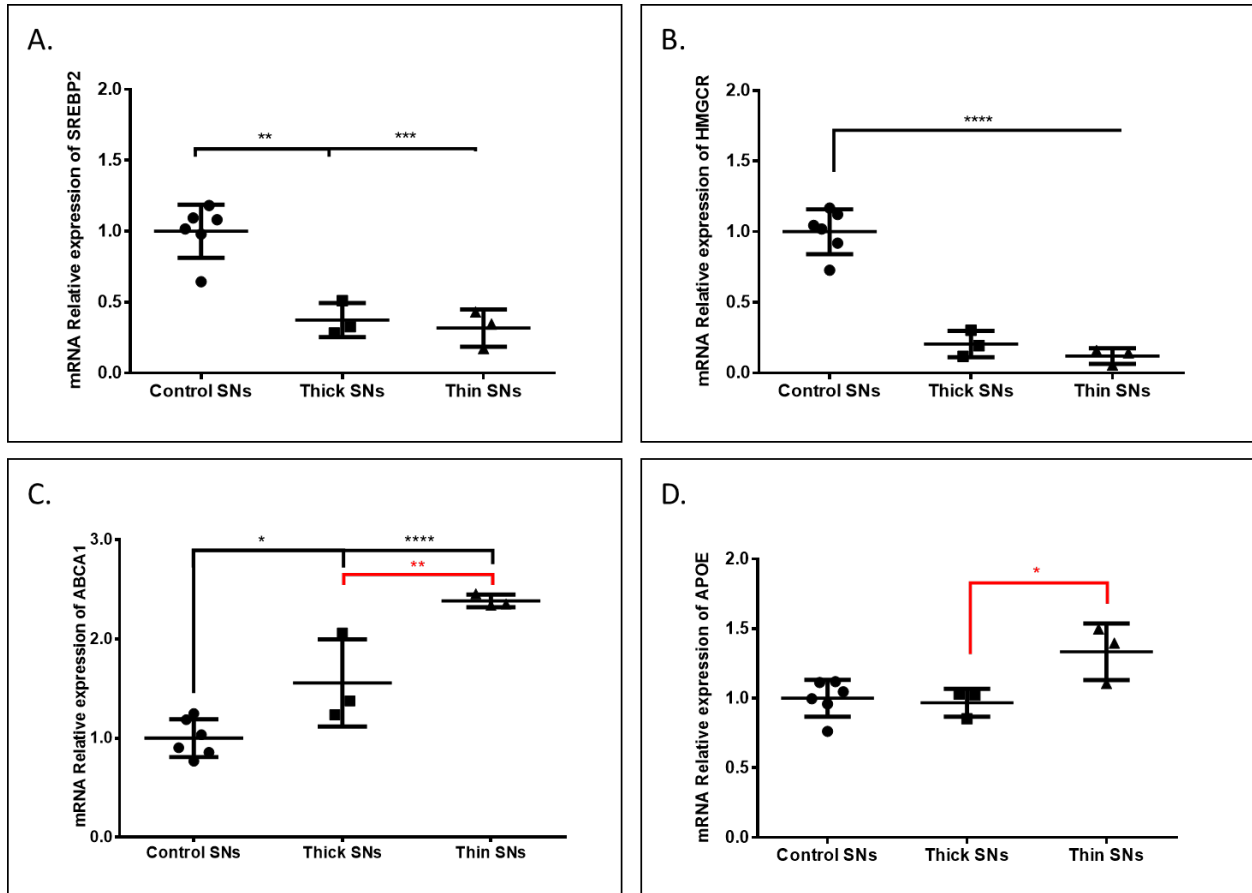


**Figure 27.** mRNA expression levels of SREBP2, HMGCR, ABCA1 and APOE in control and LXR $\beta$  SC KO thick and thin SNs of 8week old mice. RT-qPCR analysis of (A) SREBP2 (B) HMGCR, (C) ABCA1 and (D) APOE mRNA expression levels (n=3 Control, n=3 LXR $\beta$  SC KO). TBP was used for normalization. Results are represented by the mean +/- SD. Statistical significance was assessed by a one-way ANOVA follow by a Post hoc test with \* P<0.05, \*\* P<0.01, \*\*\*\*P<0.001.

Our results show that LXR $\beta$  SC KO profoundly disrupts cholesterol homeostasis in the sciatic nerves, however, we do not know which cellular component of the SN is responsible for the increase of expression of the LXR targets thus increasing cholesterol transport and efflux.

To our surprise, a highly enriched component of the myelin sheath was abundantly present in the SN of LXR $\beta$  SC KO that present very few myelinated fibers. ToF SIMS measurements revealed a 4 fold increase in Sphingomyelin concentration in the SN of LXR $\beta$  SC KO, and imaging revealed the homogeneous distribution of sphingomyelin in the measured ROIs of both control and LXR $\beta$

SC KO SNs (Figure 21&22). Additionally, a tendency of an increased, yet not significant, Sulfatide concentration was observed in the LXR $\beta$  SC KO SNs (Figure 28).

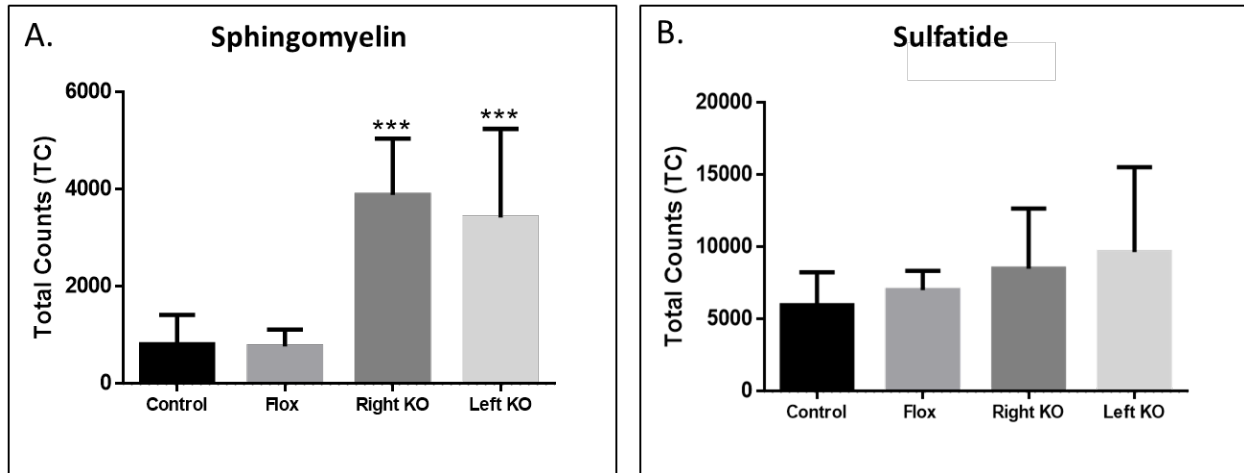


**Figure 28.** Total Counts recorded in ToF-SIMS negative ion mode for Sphingomyelin  $m/z$  616.46 subtracting noise at  $m/z$  615.45 and Sulfatide  $m/z$  540.28 detected in the sciatic nerves (Wild type  $n=3$ , Flox Control  $n=2$ , LXR $\beta$  SC KO left  $n=4$ , LXR $\beta$  SC KO right  $n=4$ ). Columns and bars represent means and SDs of triplicates from each sample (one way ANOVA with Tukey comparison test, \*\* $p<0.01$ , \*\*\* $p<0.001$ ).

The mRNA levels of the enzymes responsible for sphingomyelin synthesis at the level of the Golgi apparatus and plasma membrane respectively, SGMS1 and 2, did not show a significant difference between the two groups (Figure 29)

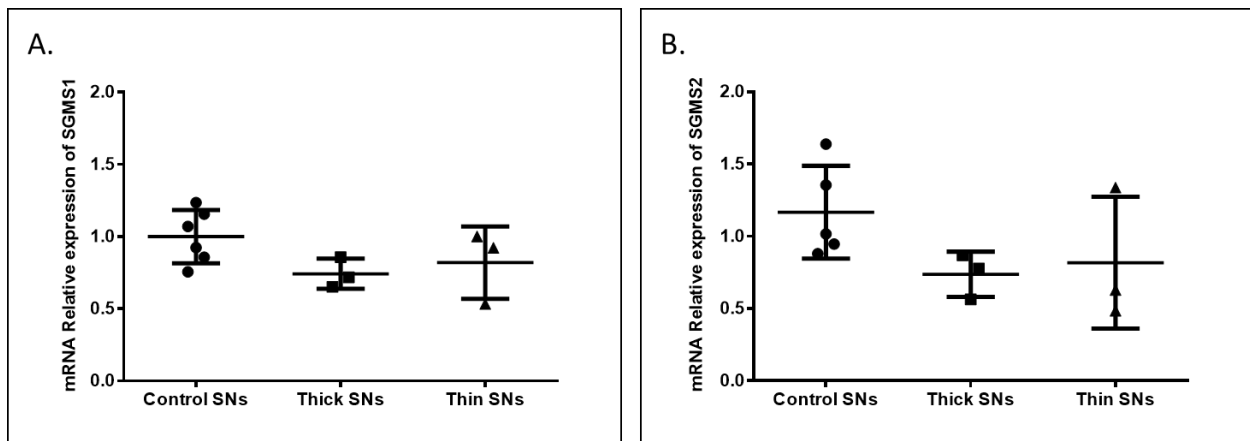


**Figure 29.** mRNA expression levels of SGMS1 and SGMS2 in control and LXR $\beta$  SC KO thick and thin SNs of 8week old mice. RT-qPCR analysis of (A) SGMS1 and (B) SGMS2 mRNA expression levels ( $n=3$  Control,  $n=3$  LXR $\beta$  SC KO). TBP was used for normalization. Results are represented by the mean  $\pm$  SD. Statistical significance was assessed by a one-way ANOVA follow by a Post hoc test with \*  $P<0.05$ , \*\*  $P<0.01$ , \*\*\* $P<0.001$ .

Concisely, our results show that the LXR $\beta$  SC KO completely disrupted the lipid homeostasis of the sciatic nerves. Fatty acid concentrations are not significantly different; however, they show high variability, perhaps a different approach should be applied to have a more specific idea of the concentration of FAs in the SNs of our different groups.

The decrease in cholesterol concentrations could be expected due to the reduced presence of myelin. However, the increase in sphingomyelin concentrations had never been described before in a similar context. Many questions remain unanswered and would require further research to be understood.

#### 4. LXR $\beta$ is crucial for SC survival, differentiation and myelination.

In order to fully understand the phenotype of our LXR $\beta$  SC KO mice and explain the lack of myelination, we first started by evaluating the mRNA level of expression of myelin proteins MPZ and PMP22 (Figure 30).

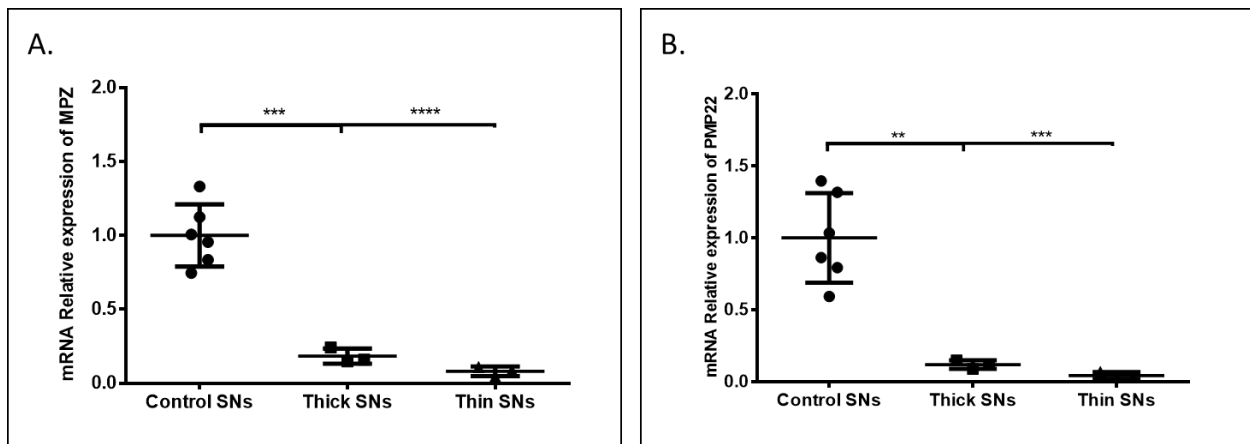


**Figure 30.** mRNA expression levels of MPZ and PMP22 in control and LXR $\beta$  SC KO thick and thin SNs of 8week old mice. RT-qPCR analysis of (A) MPZ and (B) PMP22 mRNA expression levels (n=3 Control, n=3 LXR $\beta$  SC KO). TBP was used for normalization. Results are represented by the mean +/- SD. Statistical significance was assessed by a one-way ANOVA follow by a Post hoc test with \* P<0.05, \*\* P<0.01, \*\*\*P<0.001.

A very significant decrease in PMP22 and MPZ mRNA levels were detected in line with the observed phenotype, though, this result is in complete opposition with previous findings, where the KO of LXR $\beta$  would increase myelin protein transcription. Therefore, we evaluated the possibility of reduced presence of SCs in the SNs of LXR $\beta$  SC KO mice. We evaluated the mRNA expression levels of different SC markers; such as S100 $\beta$ , Dhh, Krox20 and SOX10. All of the

following showed a very important decrease in expression in the SNs of LXR $\beta$  SC KO mice (Figure 31), further confirming the reduced presence of Schwann cells in the sciatic nerves as a result of LXR $\beta$  SC knock-out.

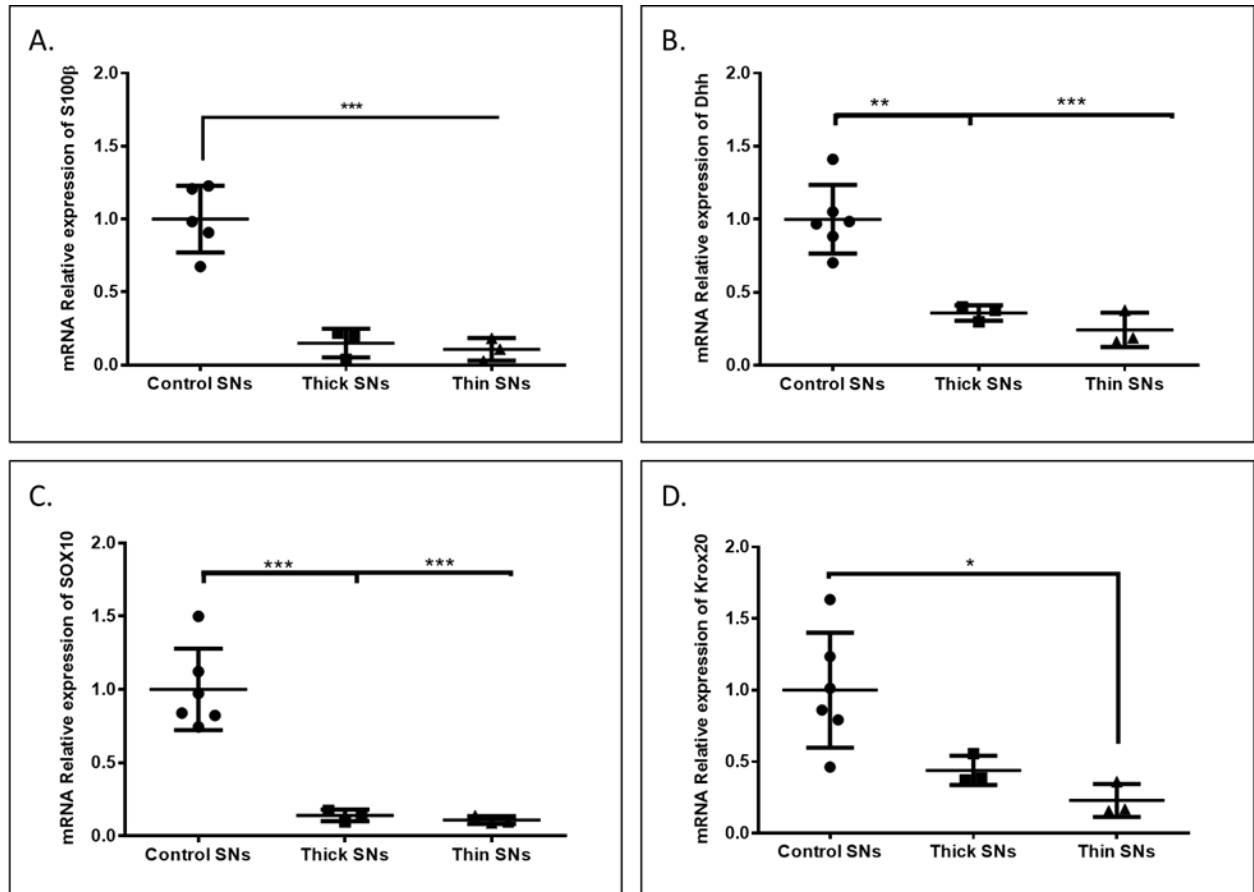


**Figure 31.** mRNA expression levels of S100 $\beta$ , Dhh, Sox10 and Krox20 in control and LXR $\beta$  SC KO thick and thin SNs of 8week old mice. RT-qPCR analysis of (A) S100 $\beta$ , (B) Dhh, (C) Sox10 and (D) Krox20 mRNA expression levels (n=3 Control, n=3 LXR $\beta$  SC KO). TBP was used for normalization. Results are represented by the mean  $\pm$  SD. Statistical significance was assessed by a one-way ANOVA follow by a Post hoc test with \* P<0.05, \*\* P<0.01, \*\*\*P<0.001.

We then stained for Krox20 and Sox10 TFs to observe and evaluate the amount of Krox20 and Sox10 positive cells (Figure 32). The absence of myelin had hinted at the inability of SCs to myelinate, therefore, observing a very significantly reduced number of Krox20 positive cells in the LXR $\beta$  SC KO SNs was not really a surprise. However, the near absence of Sox10 positive cells in LXR $\beta$  SC KO SNs was unexpected, which means that SCs or their precursors are most likely not present at this time point.

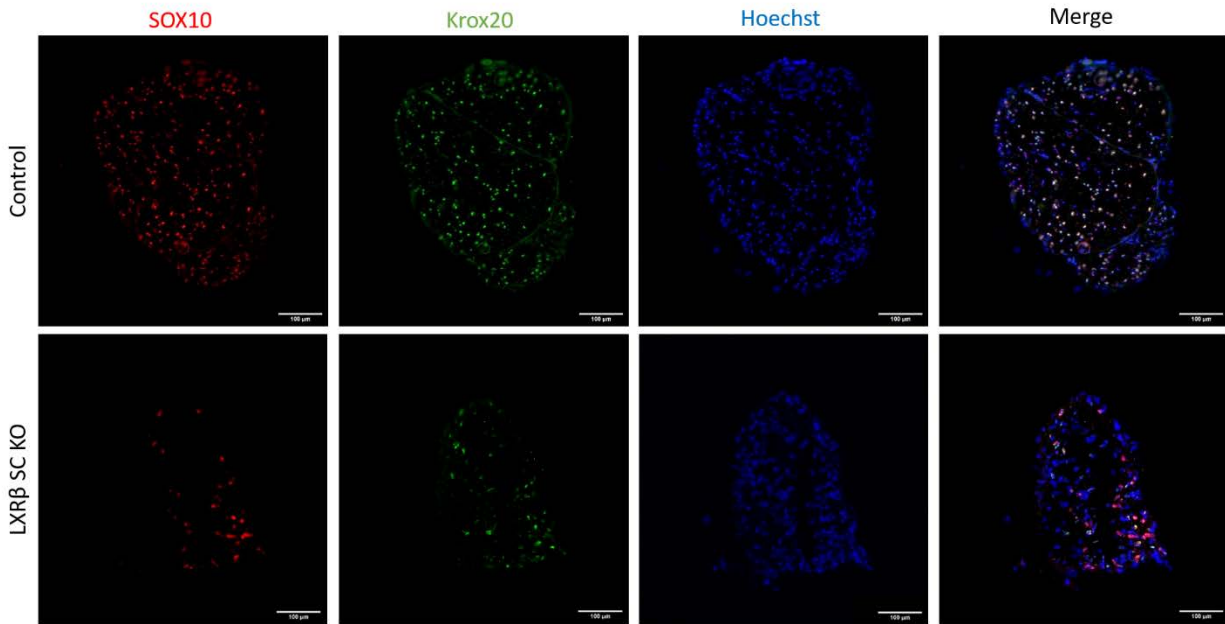


**Figure 32. Immunohistochemical assessment of Schwann cell presence in Control and LXR $\beta$  SC KO sciatic nerve cross section at 8 weeks.** Nerve sections were stained with anti SOX10 (Red) to detect SC lineage, anti Krox20 to detected myelinating SCs (Green) and Nuclei were stained with Hoechst (Blue). Scale bar = 100 $\mu$ m.

The ongoing research in our lab evaluated the effect of LXR $\beta$  SC KO on the development and survival of the SCs (unpublished work of VK Sundaram). We observed by electron microscopy as well as immunofluorescence that the absence of SCs even goes back to embryonic stages. Even at E18.5 electron microscopy imaging of the LXR $\beta$  SC KO SN reveals the absence of iSCs (Figure 33).



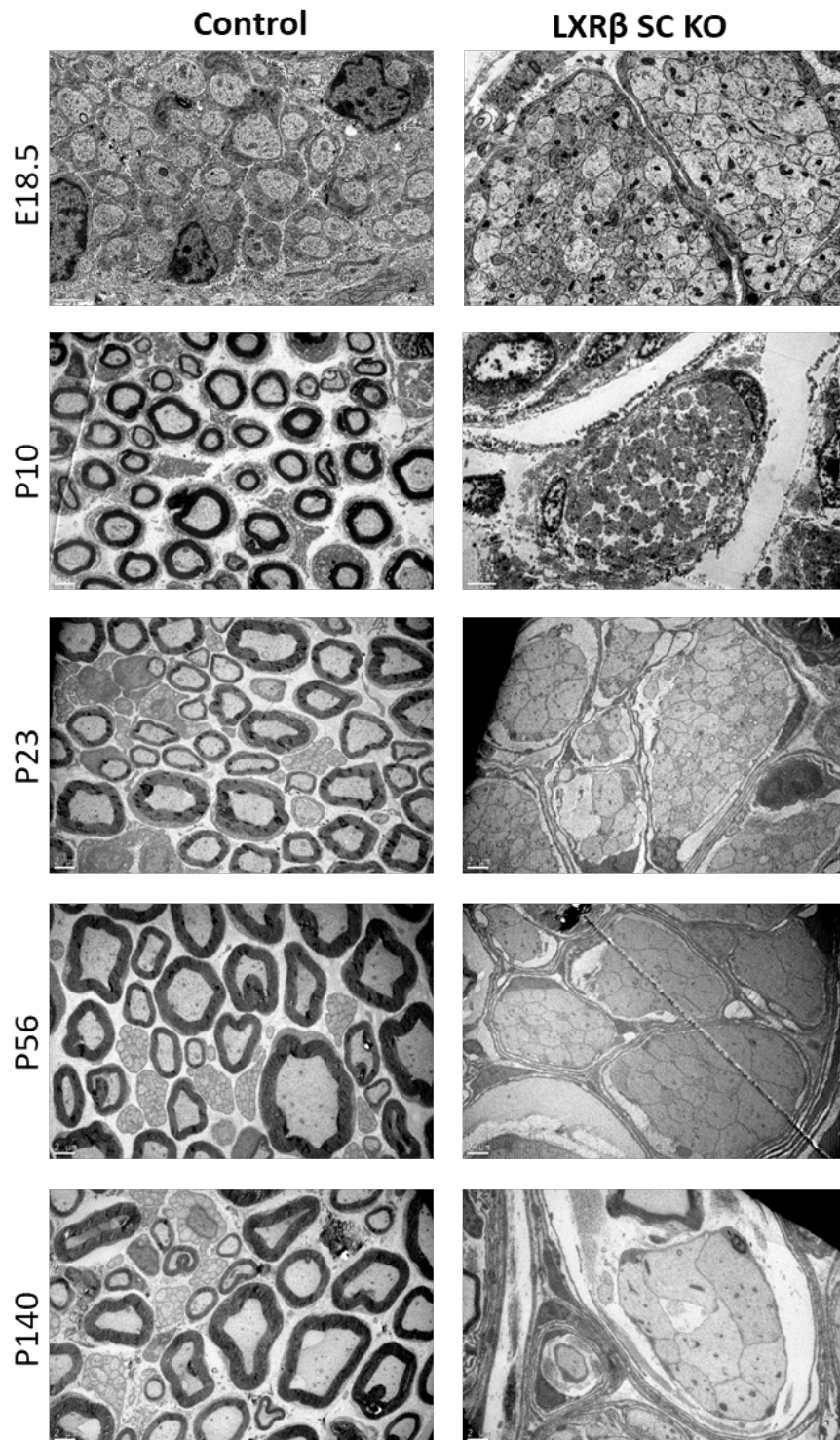


**Figure 33.** Transmission Electron Microscopy of sciatic nerve ultra-thin sections at different developmental stages (E18.5, P10, P23, P56 and P140) of both control and LXR $\beta$  SC KO mice. Scale bar = 1 $\mu$ m for embryonic nerve sections. Scale bar = 2 $\mu$ m for postnatal nerve sections.

We then resorted to culturing dissociated DRGs from both control and LXR $\beta$  SC KO embryos at E13.5, where a small population of SCP are still present at the level of DRGs at that time.

The dissociated DRG cocultures show that, around DIV7 (day *in vitro*) and DIV8, the LXR $\beta$  knocked out SCs detach from axons and start dying (Figure 34). No previous studies have described the stages of SC development in cultured embryonic DRGs.

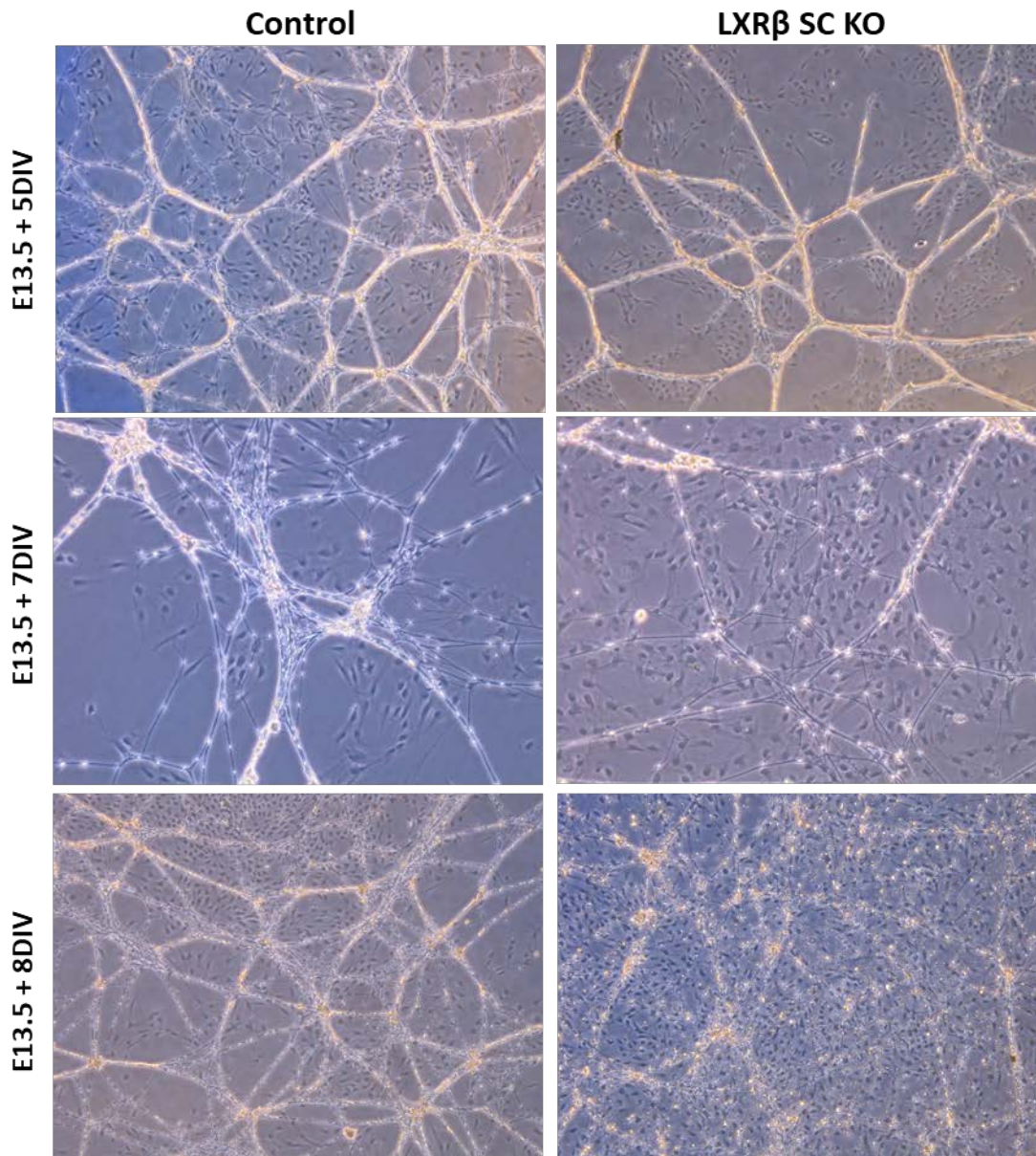


**Figure 34.** Development of dissociated DRG co-cultures *in vitro* from control and LXR $\beta$  SC KO mice at E13.5. Images of co-cultured DRGs at timepoints 5, 7 and 8 days *in vitro*, 10X magnification.

In order to identify the SC developmental stage at DIV7, we conducted a study to understand the different SC developmental stages of *in vitro* cultured dissociated DRGs. This study was recently published in *Frontiers In cellular Neuroscience*.

1 **Retracing Schwann cell developmental transitions in embryonic**  
2 **dissociated DRG/Schwann cell cocultures in mice**

3

4 **Venkat Krishnan Sundaram <sup>1\*</sup>, Tatiana El Jalkh <sup>1,3</sup>, Rasha Barakat <sup>1,2</sup>, Camille Julie**  
5 **Isabelle Fernandez <sup>1</sup>, Charbel Massaad <sup>1</sup> & Julien Grenier <sup>1\*</sup>**

6

7 1. Université de Paris, INSERM UMRS 1124, Faculty of Basic and Biomedical Sciences, Paris,  
8 France.

9 2. Université de Paris, INSERM UMRS 1016, Institut Cochin, Paris, France.

10 3. Lebanese University, EC2M, Faculty of Sciences II, Fanar, Lebanon

11

12 **\*Correspondance :**

13 Venkat Krishnan SUNDARAM

14 [venkatkrishnan.sundaram@u-paris.fr](mailto:venkatkrishnan.sundaram@u-paris.fr)

15 <https://orcid.org/0000-0001-6024-6959>

16

17 Julien GRENIER

18 [julien.grenier@u-paris.fr](mailto:julien.grenier@u-paris.fr)

19 <https://orcid.org/0000-0002-1897-1329>

20

21

**22 Author Contributions:**

23 *Conceptualization:* VKS JG & CM

24 *Formal analysis:* VKS

25 *Experiments:* VKS, TEJ, RB & CJIF

26 *Methodology:* VKS TEJ & JG.

27 *Validation:* CM.

28 *Visualization:* JG.

29 *Writing – original draft:* VKS.

30 *Writing – review & editing:* All authors.

31

**32 Acknowledgements:**

33 The authors thank the *Animal House Core Facility* and the *Cyto2BM Molecular Biology Platform* of  
34 BioMedTech Facilities (INSERM US36/CNRS UMS2009) for the animals and research services  
35 pertaining to the generation of qPCR data. The authors also thank the SCM microscopy platform for the  
36 services pertaining to confocal imaging. The authors would also like to thank Prof. Dies MEIJER,  
37 University of Edinburgh, for the Krox20 and Oct6 antibodies. We also thank Prof. Rhona MIRSKY and  
38 Prof. Kristjan R JESSEN, University College London, for the critical reading of the preprint and for their  
39 inputs.

40

**41 Funding:**

42 No specific funding was sought for this study. VKS was funded by a PhD fellowship from the French  
43 Ministry of Research and Innovation and is currently funded by Université de Paris. RB is funded by a  
44 research fellowship from INSERM U1016, Institut Cochin, Paris. TEJ is funded by a Doctoral fellowship  
45 from Université de Paris and the National Council for Scientific Research Lebanon (CNRS-L). CJIF is  
46 funded by INSERM UMRS1124.

47

**48 Conflict of interest:**

49 The authors declare that there is no conflict of interest.

50 **Abstract:**

51 Embryonic Dissociated Dorsal Root Ganglia cultures are often used to investigate the role of novel  
52 molecular pathways or drugs in Schwann cell development and myelination. These cultures largely  
53 recapitulate the order of cellular and molecular events that occur in Schwann cells of embryonic nerves.  
54 However, the timing of Schwann cell developmental transitions, notably the transition from Schwann Cell  
55 Precursors to immature Schwann cells and then to myelinating Schwann cells, has not been estimated  
56 so far in this culture system. In this study, we determined the expression profiles of Schwann cell  
57 developmental genes during the first week of culture and then compared our data to the expression  
58 profiles of these genes in developing spinal nerves. This helped in identifying that Schwann Cell  
59 Precursors transition into immature Schwann Cells between the 5<sup>th</sup> and 7<sup>th</sup> day *in vitro*. Furthermore, we  
60 also investigated the transition of immature cells into pro-myelinating and myelinating Schwann cells  
61 upon the induction of myelination *in vitro*. Our results suggest that Schwann cell differentiation beyond  
62 the immature stage can be observed as early as 4 days post the induction of myelination in cocultures.  
63 Finally, we compared the myelinating potential of coculture-derived Schwann cell monocultures to  
64 cultures established from neonatal sciatic nerves and found that both these cultures system exhibit  
65 similar myelinating phenotypes. In effect, our results allow for a better understanding and interpretation  
66 of coculture experiments especially in studies that aim to elucidate the role of a novel actor in Schwann  
67 Cell development and myelination.

68

69 **Keywords: Schwann cell development, Dissociated DRG/SC cocultures, Schwann Cell**  
70 **Precursors, immature Schwann Cells, myelinating Schwann cells**

## 71 **Introduction:**

72 Dissociated Dorsal Root Ganglia (DRG) cultures from mouse embryos have long been utilized as a  
73 resourceful model for exploring the nuances of Schwann cell development *in vitro* (Taveggia and Bolino,  
74 2018). The co-culture system provides a solid experimental framework to study different aspects of  
75 Schwann cell development such as proliferation, migration, differentiation and myelination of axons  
76 (Päiväläinen et al., 2008; Taveggia and Bolino, 2018). Furthermore, it recapitulates the different aspects  
77 of Schwann cell development that is observed *in vivo*. Hence, dissociated DRG cultures form an  
78 indispensable part of studies that aim to understand the role of a novel actor in Schwann cell development  
79 and differentiation.

80  
81 It is well known that temporal differences exist between Schwann cell development in Dissociated  
82 DRG/SC coculture *in vitro*, and in developing spinal nerves *in vivo*. In developing spinal nerves of mice,  
83 Neural Crest Cells (NCC), destined to a glial fate differentiate into Schwann Cell Precursors (SCP) and  
84 appear in the DRGs at around E11 (Jacob, 2015). Then, the SCPs start migrating on nascent axons  
85 between E12.5 and E13.5 to populate their peripheral targets. However, at around E15.5 in mice, SCPs  
86 undergo a transition into immature Schwann cells (iSC) that further differentiate into either myelinating  
87 or non-myelinating Schwann cells, perinatally (Monk et al., 2015; Fledrich et al., 2019; Jessen and Mirsky,  
2019).

88  
89 Nevertheless, these observations cannot be used to extrapolate the timing of Schwann cell  
90 developmental transitions *in vitro* because of certain technical issues. Firstly, the DRGs are dissected  
91 from mouse embryos towards the end of the 2<sup>nd</sup> week of gestation (E12.5 or E13.5). At this stage, SCP  
92 *in vivo* have already started departing from the DRGs and begun migrating on developing axons (Jessen  
93 et al., 1994; Jessen and Mirsky, 2005). However, once dissected and dissociated, the E13.5 DRG cells  
94 give rise to sensory neurons and Schwann cell precursors once again *in vitro* (Ratner et al., 2005; Kim  
95 and Maurel, 2009; Kim and Kim, 2018). This is rendered possible because of a reservoir of sensory  
96 neurons and SCP located inside the DRGs that repopulate the culture (**Figure 1**). Therefore, a significant  
97 portion of *in vivo* developmental events are repeated in cell culture albeit with a phase difference. Our  
98 objective in this study is to better understand these temporal differences in cocultures in an effort to  
99 provide a better experimental and inferential framework.

100 To this end, we first delineated the mRNA expression profiles of the genes expressed in SCP (*Dhh*, *Mpz*,  
101 *Cnp*, *Plp*, *Mbp*, *Cad19* and *Tfap2a*) and iSC (*Krox20*). We then compared them to their profiles *in vivo*  
102 described in previous high-throughput studies conducted on embryonic peripheral nerves that provide  
103 extensive data on the differential expression of genes during Schwann Cell developmental transitions  
104 (Buchstaller et al., 2004; D'Antonio et al., 2006) This analysis helped us in determining the exact time  
105 window when SCP transition into iSC in Dissociated DRG/SC cocultures. Furthermore, we also verified  
106 that iSC at DIV7 transition into pro-myelinating (pro-mSC) and myelinating Schwann cells (mSC) upon  
107 the induction of myelination by the addition of Ascorbic Acid (AA) to DIV7 cocultures. Finally, we  
108 investigated if SC monocultures established from DIV7 cocultures possess the same myelinating  
109 potential as monocultures established from neonatal sciatic nerves.

110 Taken together, our results show that SCP transition into iSC between DIV5 and DIV7 in cocultures.  
111 Furthermore, we have also observed that the iSC/mSC transition in co-cultures occurs as early as 4 days  
112 post Ascorbic acid treatment. As for Schwann cell monocultures, SC obtained from DIV7 cocultures  
113 differentiate into mSC similar to SC isolated from neonatal sciatic nerves, further suggesting that the cells  
114 at DIV7 are comparable to neonatal Schwann cells in culture. In conclusion, our data provides a holistic  
115 understanding of the Schwann Cell Precursor/immature Schwann Cell/myelinating Schwann Cell  
116 transition in embryonic DRG/SC cocultures which is crucial for designing rigorous *in vitro* assays to study  
117 Schwann cell embryonic development and embryonic phenotypes of different Schwann cell mutants.

## 118 **Materials and methods:**

### 119 **Animals and Tissue Harvesting**

120 Timed pregnant C57Bl6/J mice at E13.5 were purchased from Janvier Labs. The pregnant mice were  
121 first anesthetized with isoflurane and sacrificed using cervical dislocation. Embryos were surgically  
122 removed and placed in ice-cold L-15 media. DRGs were harvested from these embryos based on existing  
123 protocols (Kim and Kim, 2018; Taveggia and Bolino, 2018). All aspects of animal care and animal  
124 experimentation were performed in accordance with the relevant guidelines and regulations of INSERM  
125 and Université de Paris (authorization APAFIS#7405-2016092216181520).

### 126 **Dissociated DRG/SC cocultures**

127  
128 A total of 40 DRGs were harvested from each embryo. DRGs were then trypsinized (0.25% Trypsin in  
129 HBSS1X) for 30min at 37°C. Trypsinization was stopped using L-15 media containing 10% Horse Serum  
130 (Gibco). DRGs were then spun down at 1500 rpm for 5min. The supernatant was removed, and the  
131 tissues were resuspended in *DRG plating medium* (refer to *Media Compositions* in Supplementary  
132 Methods). The tissues were then triturated 10-20 times using flamed Pasteur pipettes until a  
133 homogenous cell suspension was obtained. For each time point (DIV1, DIV3, DIV5, DIV7), dissociated  
134 DRGs were plated on 12 well plates containing 14mm coverslips coated with Poly L Lysine (Sigma) and  
135 Collagen (R&D Systems). 40 DRGs from each embryo were plated into 8 wells at approximately 5  
136 dissociated DRGs per well. 2 wells were assigned to each time point. The cells were first plated with  
137 DRG plating medium for 16h. The following day the medium was replaced with Supplemented  
138 Neurobasal medium to promote neurite growth and Schwann cell proliferation for a period of 7 days.  
139 Media was changed every 48 hours. Myelination was induced at DIV7 by changing the media to DRG  
140 plating medium supplemented with 50µg/mL Ascorbic Acid (Sigma).

### 141 **Schwann cell monocultures**

142 SC monocultures were established using previously detailed protocols (Kim and Kim, 2018). Briefly,  
143 dissociated DRGs were obtained from E13.5 and were cultured on uncoated 35mm petri dishes (approx.  
144 40 DRGs/Embryo) as explained above. At DIV7, the neurite network (neurons + Schwann cells) was  
145 mechanically lifted from the plate using a sterile 27<sup>L1/2</sup> G needle. The network was then enzymatically  
146 digested (0.25% Trypsin, 0.1% Collagenase in HBSS1X) for 30 min at 37°C. Digestion was stopped by  
147 the addition of *Schwann Cell Plating Media* and the cell suspension was centrifuged at 1500rpm for 5min.  
148 The pellet was then triturated 5 – 6 times using a 1mL pipette tip. To obtain highly pure cultures without  
149 contaminating fibroblasts, the cell suspension was subjected to immunopanning to remove Thy1.2+ve  
150 fibroblasts as described elsewhere (Lutz, 2014). About 500000 Schwann cells were obtained from each  
151 embryo after immunopanning and the cells were plated on 14mm Poly L Lysine coated glass coverslips  
152 at a density of 50000 cells/coverslip. Schwann cells were expanded using defined *Schwann Cell*  
153 *Proliferation Media* (see supplementary methods) for 48h. To induce differentiation, cell cultures were  
154 treated with *Schwann Cell Differentiation Media* (Proliferation media without Forskolin but supplemented  
155 with 1mM dbcAMP) for a period of 48h.

156

### 157 **Immunohistochemistry**

158 E13.5 and E16.5 embryos were surgically removed from the pregnant mouse and placed on ice cold L-  
159 15 media. The head, the thoracic region along with the ventral internal organs and the tail were dissected.  
160 The lumbar region along with the hindlimbs were fixed overnight with 4% PFA at 4°C. The following day,  
161 the embryos were extensively washed with PBS1X and incubated overnight in Antigen Retrieval Buffer  
(10mM Sodium Citrate, 0.05% Tween20, pH 6.0) at 4°C. The following day, the samples were boiled in



162 the antigen retrieval buffer for 5 min and immediately placed in ice cold 30% sucrose solution. The  
163 samples were then dehydrated in Sucrose overnight at 4°C. The following day, samples were embedded  
164 in 4% Agarose and placed on the vibratome such that the caudal aspect of the embryo was facing the  
165 chuck, the rostral aspect was facing upwards, and the lateral aspect was facing the blade. 50µm serial  
166 transverse sections of the lumbar region was made and transferred to a 12 well plate containing PBS1X.  
167 Sections were quickly washed in PBS1X and then stored at -20°C in a cryoprotectant (30% Glycerol,  
168 30% Ethylene Glycol in PBS1X) until immunostaining.

169 Immunostaining was performed by washing the sections first with PBS1X followed by incubation in 0.1M  
170 Glycine for 1 hour. Sections were permeabilized and blocked with blocking buffer (0.5% Triton X100,  
171 0.1% Tween20, 2% BSA and 5% Normal Donkey Serum) for 1 hour followed by incubation with primary  
172 antibodies against Neurofilament SMI312, Sox10 and Tfp2α for 36h at 4°C (refer to *Supplementary*  
173 *Methods* for primary and secondary antibody references and concentrations). Sections were then  
174 washed thrice (1h per wash) in PBS1X containing 0.1% Tween20 and were then incubated with the  
175 corresponding secondary antibodies for 1h at RT in the dark. The sections were then washed, and nuclei  
176 were stained using Hoechst 33342 dye. Samples were then mounted on slides using Permaflour (Thermo  
177 Fisher Scientific) and stored at 4°C till confocal imaging.

178

179

### **Immunocytochemistry**

180

181 DRG/SC cocultures and Schwann cell monocultures at different conditions were first fixed with 4% PFA  
182 at RT for 30 mins. The coverslips were then washed with PBS1X and stored at -20°C in a cryoprotectant  
183 until immunostaining.

184

185 Immunostaining was first performed by washing the coverslips first with PBS1X followed by incubation  
186 in Antigen Retrieval Buffer (refer to *Immunohistochemistry*) preheated to 95°C for 3min. Samples were  
187 then washed with PBS1X and incubated in 0.1M Glycine solution for 30 minutes followed by  
188 permeabilization (0.25% Triton X100 0.1% Tween 20 in PBS1X, 20 min at RT) and blocking (2% BSA,  
189 0.1% Tween 20, 10% Normal Donkey Serum, 1h at RT). Coverslips were then incubated with primary  
190 antibodies against, Neurofilament SMI312, Sox10, Tfp2α, Oct6, Krox20 and Ki67 overnight at 4°C (refer  
191 to *Supplementary Methods* for primary and secondary antibody references and concentrations). The  
192 following day, the coverslips were washed thrice with PBS1X (10 min per wash) and incubated with  
193 corresponding secondary antibodies for 1h at RT in the dark. Samples were then washed, and nuclei  
194 were stained with Hoechst 33342 dye. Samples were then mounted on slides using Permafluor (Thermo  
195 Fisher Scientific) and stored at 4°C till confocal imaging.

194

### **Imaging and Image analysis**

195

196 Confocal imaging of tissues sections and coverslips were performed on the LSM710 microscope. Images  
197 were obtained as z-stacks and analyzed in ImageJ. For each experimental condition, 3 – 4 biological  
198 replicates (embryos) and 3 technical replicates/biological replicate were analyzed. Cell counting was  
199 performed on z-projections (Max intensity) using the Analyze particles function after thresholding the  
200 images. Data was exported to Microsoft excel and graphs were plotted using Prism v8.0

200

201

### **Total RNA isolation**

202

203 Total RNA was extracted from each sample using 1mL of TRIzol reagent (Ambion Life Technologies  
204 15596018) on ice as described in the manufacturer's instructions with slight modifications. Briefly, 100%  
205 Ethanol was substituted for Isopropanol to reduce the precipitation of salts. Also, RNA precipitation was  
carried out overnight at -20°C in the presence of glycogen. The following day, precipitated RNA was

206 pelleted by centrifugation and washed at least 3 times with 70% Ethanol to eliminate any residual  
207 contamination. Tubes were then spin dried in vacuum for 5 minutes and RNA was resuspended in 20µL  
208 of RNA resuspension buffer containing 0.1mM EDTA, pH 8. RNA was then stored at -80°C till RTqPCR.

### 209 **RNA quality, integrity and assay**

210 RNA quantity was assayed using UV spectrophotometry on Nanodrop One (Thermo Scientific). Optical  
211 density absorption ratios A260/A280 & A260/A230 of the samples were above 1.8 and 1.5, respectively.  
212 The yield (mean ± SD) for each time point is as follows: DIV1 (26.74 ± 2.57 ng/µL), DIV3 (61.3 ± 8.01  
213 ng/µL), DIV5 (51.86 ± 10.8 ng/µL), and DIV7 (77.34 ± 24.04 ng/µL). The extraction protocol used in the  
214 study was also validated using Agilent Bioanalyzer (RIN value 9.0 and above).

### 215 **RTqPCR**

216 250ng of Total RNA was reverse transcribed with Random Primers (Promega C1181) and MMLV  
217 Reverse Transcriptase (Sigma M1302) according to prescribed protocols. Quantitative Real time PCR  
218 (qPCR) was performed using Absolute SYBR ROX 2X qPCR mix (Thermo AB1162B) as a fluorescent  
219 detection dye. All reactions were carried out in a final volume of 7µl in 384 well plates with 300 nM gene  
220 specific primers, around 3.5ng of cDNA (at 100% RT efficiency) and 1X SYBR Master Mix in each well.  
221 Each reaction was performed in triplicates. All qPCR experiments were performed on BioRad CFX384  
222 with a No-Template-Control (NTC) to check for primer dimers and a No-RT-Control (NRT) to check for  
223 any genomic DNA contamination.

### 224 **Primer design and efficiency:**

225 All primers used in the study were designed using the Primer 3 plus software  
226 (<https://primer3plus.com/cgi-bin/dev/primer3plus.cgi>). Splice variants and the protein coding sequence  
227 of the genes were identified using the Ensembl database ([www.ensembl.org](http://www.ensembl.org)). Constitutively expressed  
228 exons among all splice variants were then identified using the ExonMine database  
229 (<https://imm.medicina.ulisboa.pt/group/exonmine/ack.html>) (Mollet et al., 2010). Primer sequences that  
230 generated amplicons spanning two constitutively expressed exons were then designed using the Primer  
231 3 plus software. For detailed information on Primer sequences used in the study, refer to the  
232 Supplementary Methods. The amplification efficiencies of primers were calculated using serial dilution of  
233 cDNA molecules. Briefly, cDNA preparations from all the time points were pooled and serially diluted  
234 three times by a factor of 10. qPCR was then performed using these dilutions and the results were plotted  
235 as a standard curve against the respective concentrations of cDNA. Amplification efficiency (E) was  
236 calculated by linear regression of standard curves using the following equation:

$$237 E = 10^{-(1/\text{slope of the standard curve})}$$

238 Primer pairs that exhibited a theoretical Amplification Efficiency (E) of 1.9 to 2.1 (95% - 105%) and an R<sup>2</sup>  
239 value (Determination Coefficient) of 0.98 and above were chosen for this study.

### 240 **qPCR statistical analysis and Data Visualization**

241 qPCR readouts were analyzed in Precision Melt Analysis Software v1.2. The amplicons were subjected  
242 to Melt Curve analysis and were verified for a single dissociation peak at a Melting Temperature (T<sub>m</sub>) >  
243 75°C as expected from the primer constructs. The C<sub>q</sub> data was exported to Microsoft Excel for further  
244 calculations. Each biological sample had 3 technical replicates thereby generating 3 individual C<sub>q</sub> values.  
245 The arithmetic mean of the triplicates was taken to be the C<sub>q</sub> representing the biological sample. The  
246 standard deviation (SD) of the triplicates was also calculated and samples that exhibited SD>0.20 were  
247 considered inconsistent. In such cases, one outlier C<sub>q</sub> was removed to have at least duplicate C<sub>q</sub> values  
248 for each biological sample and an SD<0.20.

249 For the DIV1 to DIV7 longitudinal dataset, reference gene validation was performed according to our  
250 qPCR data analysis workflow (Sundaram et al., 2019). Briefly, 10 conventional reference genes were  
251 chosen and screened using Coefficient of variation (CV) analysis and NormFinder (Supplementary Table  
252 S1) in R (<https://moma.dk>) (Andersen et al., 2004). The algorithm predicted *Tbp* and *Ppia* to be the most  
253 stable references. The normalization factor was then determined as the mean Cq value of *Tbp* and *Ppia*  
254 for each sample (Supplementary Table S1). For the comparison of DIV7 vs Schwann cell monocultures,  
255 reference gene validation was performed using CV analysis. *Mrp10* and *Sdha* exhibited the least  
256 collective variation (CV = 22%) and they were subsequently used for calculating the normalization factor.  
257 Relative expression of target genes was quantified using the  $2^{-\Delta\Delta C_t}$  method (Livak and Schmittgen, 2001;  
258 Schmittgen and Livak, 2008) and data was visualized using Prism v8.0.

259 To assess statistical difference in relative RNA quantities between groups, One-way ANOVA was  
260 performed in Graph Pad Prism v8.0. If statistical significance was observed between the means of the  
261 groups, Tukey's post hoc was performed to compare all the groups with each other. The alpha value  
262 threshold was set at 5% and the P-values are represented as follows: P<0.05 - \*, P<0.01 - \*\*, P<0.001 -  
263 \*\*\*.

264

265 **Results:**

266

267 **Progression of dissociated DRG/SC cocultures:**

268 We first documented the cellular composition of DRGs at E13.5 as well as the progression of the culture  
269 at Days *in Vitro* (DIV) 1, DIV3, DIV5 and DIV7 (**Figure 1**). DRGs at E13.5 are comprised of sensory  
270 neurons with axonal projections towards the dorsal roots and the peripheral nerve. They are also  
271 comprised of neural crest derivatives (Sox10<sup>+</sup> cells). Once dissected and dissociated, we observed a  
272 very sparse population of dissociated cells that comprised of neurons and neural crest derivatives  
273 (Sox10<sup>+</sup> cells) at DIV1. At DIV3, however, we could see a neurite network gradually being formed with  
274 cells located on top of neuronal extensions. These cells are presumably migratory Schwann cell  
275 precursors. The neurites then grew out and established a well-connected network by DIV5. Schwann  
276 cells now densely populated neurites. Not much difference was observed between DIV5 and DIV7 except  
277 that more connections were established in the neurite-Schwann cell network (**Figure 1**). From these  
278 observations, we could only deduce that Schwann cell precursors appear between DIV1 and DIV3 and  
279 they continue to populate the culture during the first 7 days.

280

281

282 **Expression profiles of Schwann cell developmental genes:**

283 We then determined the expression profiles of Schwann cell developmental genes using RTqPCR  
284 (**Figure 2A**). The genes that we assayed include *Dhh*, *Mpz*, *Mbp*, *Plp* and *Cnp* which are expressed in  
285 the Schwann cell lineage from the SCP stage *in vivo* (Jessen and Mirsky, 2019). We also assayed *Cad19*  
286 and *Tfap2a* which are expressed in SCP but are downregulated in iSC *in vivo* (Stewart et al., 2001;  
287 Takahashi and Osumi, 2005). Finally, we also assayed *Krox20* mRNA levels which are upregulated as  
288 SCP transition into iSC in embryonic nerves (Topilko et al., 1994; Ghislain and Charnay, 2006)

289 *Dhh* showed a stark 14-fold increase between DIV1 and DIV3. Although the profile seemed to project a  
290 downward trajectory after DIV3, the levels of *Dhh* did not vary significantly between DIV3 and DIV7. *Mpz*  
291 displayed an initial spike between DIV 1 and DIV3 by about 12 folds, which was similar to *Dhh*. However,  
292 the quantity of *Mpz* gradually increased and reached about 17 folds at DIV7. *Cnp* expression increased  
293 by about 7-folds between DIV1 and DIV3 and maintained a stable profile till DIV7. *Plp* showed an initial  
294 peak at DIV3 by about 7-folds, which was comparable to that of *Cnp*. However, *Plp* expression  
295 momentarily dropped at DIV5 and reached a plateau by DIV7. *Mbp* displayed a modest but statistically  
296 significant increase by 2-folds between DIV1 and DIV3. However, the expression did not increase  
297 significantly beyond DIV3. *Krox20* expression did not vary significantly between DIV1 to DIV5. However,  
298 at DIV7 we observed a sudden spike by about 4-folds. *Cad19* expression increased almost linearly  
299 between DIV1 and DIV5. However, between DIV5 and DIV7, we observe a drop in its expression level.  
300 *Tfap2a* maintains a flat profile from DIV1 and DIV3. It begins to decline after DIV3 and drops significantly  
301 to about 0.5 folds at DIV7.

302

303 **Expression of Tfap2α protein in Dissociated DRG/SC cocultures:**

304 The downregulation of Tfap2α protein levels in SCP is essential for their transition into iSC *in vivo*  
305 (Stewart et al., 2001). Consequently, we assayed the expression of Tfap2α in dissociated cultures using  
306 ICC (**Figure 2B**). We observed the expression of the protein at DIV1, DIV3 and DIV5. However, at DIV7  
307 we observed a huge reduction in Tfap2α immunoreactivity to background levels. This observation is also  
308 corroborated with the reduction in Tfap2α mRNA levels between DIV5 and DIV7 (**Figure 2A**). The  
309 reduction in Tfap2α immunofluorescence is also observed *in vivo* wherein SCP at E13.5 in sciatic nerve  
310 transverse sections express the protein whereas iSC at E16.5 do not (**Figure 2C**). These results  
collectively suggest that SCP in DRG/SC cocultures transition into iSC between DIV5 and DIV7.

311 **iSC/mSC transition in dissociated DRG/SC cocultures:**

312

313 We next sought to determine if iSC at DIV7 transition into pro-myelinating SC (pro-mSC) and myelinating  
314 SC (mSC) in cocultures upon the induction of myelination. In embryonic nerves, iSC differentiate into  
315 pro-mSC and mSC perinatally (E16.5 + around 4 days) (Salzer, 2015; Fledrich et al., 2019). These stages  
316 of Schwann cell development are characterized by the expression of Oct6 (pro-mSC) and Krox20 (mSC)  
317 transcription factors (Topilko et al., 1994; Jaegle et al., 1996, 2003). However, myelination *in vitro*  
318 requires the addition of Ascorbic Acid (AA) to cocultures to promote the formation of SC basal lamina  
319 and SC intrinsic epigenetic modifications which are prerequisites to promote further Schwann cell  
320 differentiation (Eldridge et al., 1987, 1989; Bacallao and Monje, 2015; Huff et al., 2020).

321 We treated cocultures at DIV7 with Ascorbic Acid and assayed Oct6 (**Figure 3A**) and Krox20 (**Figure**  
322 **3B**) immunoreactivity after 4 days of treatment. We observed the presence of Oct6<sup>+</sup> and Krox20<sup>+</sup>  
323 Schwann cells located on top of the axons once the differentiation process is stimulated by AA addition.  
324 These results show that SC at DIV7 differentiate into pro-mSC and mSC after AA supplementation which  
325 is comparable to the perinatal iSC/mSC transition *in vivo*.

326

327 **Myelinating potential of Coculture derived SC monocultures:**

328 SC monocultures are established from enzymatic digestion of neonatal mouse sciatic nerves in a  
329 plethora of recent studies because the preparation technique is less cumbersome. Neonatal nerves  
330 contain underdeveloped connective tissues and unmyelinated fibers and can be easily digested to render  
331 copious amounts of primary SC (Monje, 2020). Myelination can be induced in these cells by the addition  
332 of cAMP in substantially large concentrations (Arthur-Farraj et al., 2011; Bacallao and Monje, 2015). We  
333 therefore wanted to investigate if primary SC monocultures established from DIV7 cocultures are  
334 comparable to cultures established from neonates. We isolated SC from DIV7 cocultures using  
335 immunopanning and expanded them in culture for 48h (Proliferation) following which these cells were  
336 treated with cAMP for another 48h (Differentiation) according to prescribed protocols employing neonatal  
337 SC cultures (Arthur-Farraj et al., 2011). We assessed for the presence of pro-mSC and mSC using Oct6  
338 and Krox20 mRNA and protein expression using DIV7 cells as experimental controls (**Figure 4**).

339 mRNA expression levels of Oct6 and Krox20 do not vary much between DIV7 dissociated DRG/SC  
340 coculture and SC monocultures in proliferation medium but we noticed a stark increase in Oct6 mRNA  
341 levels by about 12 folds and Krox20 mRNA by about 18 folds when SC monocultures were treated with  
342 cAMP to induce differentiation (**Figure 4A**). This increased mRNA levels also corresponded with an  
343 increase in Oct6 and Krox20 immunoreactivity (**Figure 4B, 4C, quantified in 4D**) where we observed  
344 about 80% of Sox10<sup>+</sup> SC also stained positive for Oct6 and about 60% of SC stained positive for Krox20  
345 on an average. Very similar results are also observed in SC monocultures derived from neonatal sciatic  
346 nerves (Arthur-Farraj et al., 2011)

347 Furthermore, we also inspected the mRNA and protein levels of the SCP marker Tfap2 $\alpha$ . Interestingly,  
348 Tfap2 $\alpha$  mRNA levels are further downregulated by about 0.5 folds between DIV7 dissociated DRG/SC  
349 coculture and Proliferative SC monocultures (**Figure 4A**). Besides, we could not detect any Tfap2 $\alpha$ <sup>+</sup> cells  
350 in all the three conditions (Supplemental Figure S2). These results suggest that SC monocultures  
351 established from DIV7 cocultures are comparable to primary cultures established from neonatal sciatic  
352 nerves with regard to the change in SC phenotype upon cAMP addition. Furthermore, we also observed  
353 that these monocultures do not express the SCP marker Tfap2 $\alpha$  at the protein level. Taken together,  
354 these results provide further evidence that DIV7 SC are phenotypically different from SCP that arise in  
355 DRG/SC cocultures between DIV1 and DIV5 and they are rather similar to neonatal SC in culture.

356

357 **Discussion:**

358  
359 The objective of this study was to determine the SCP/iSC/mSC transition in DRG/SC cocultures using  
360 the expression profiles of Schwann cell developmental genes (*Dhh*, *Mpz*, *Cnp*, *Plp*, *Mbp*, *Krox20*, *Cad19*,  
361 *Tfap2a*). We first determined the expression profiles of these genes between DIV1 and DIV7. In addition  
362 to the mRNA data, we used Tfap2 $\alpha$  ICC as a confirmatory experiment to distinguish between SCP and  
363 iSC in the coculture model. Furthermore, we induced myelination by the addition of Ascorbic Acid at DIV7  
364 to verify that the iSC transition into pro-mSC and mSC *in vitro*. Additionally, we also compared the  
365 myelinating potential of SC monocultures established from DIV7 cocultures to that of monocultures  
366 established from neonatal nerves. A detailed schematic of our experimental approach is detailed in  
367 **Figure 5A**.

368

369 **The SCP/iSC transition**

370  
371 The expression profiles of SC lineage genes have been previously documented in gene profiling studies  
372 on murine embryonic nerves (Buchstaller et al., 2004; D'Antonio et al., 2006). Seminal reviews on  
373 Schwann cell developmental markers and other gene-specific expression profiling studies have been  
374 published in the last couple of decades and they give us a holistic understanding of the SC developmental  
375 transitions in embryonic and postnatal peripheral nerves (Jessen et al., 1994; Jessen and Mirsky, 2005;  
376 Woodhoo and Sommer, 2008; Monk et al., 2015). A summary of the current consensus on the  
377 expression profiles of these genes *in vivo* along with the relevant literature is presented in **Figure 5B**.

378  
379 When comparing our mRNA expression data to these profiles, we find that our data seem to largely  
380 comply and concur with the order of molecular events observed in embryonic spinal nerves. For instance,  
381 the expression of *Dhh*, *Mpz*, *Mbp* & *Plp* is upregulated in SCP at around E12.5 in mice (Jessen and  
382 Mirsky, 2005; Woodhoo and Sommer, 2008). In DRG cultures, *Dhh*, *Mpz*, *Mbp* and *Plp* expression is  
383 increased at DIV3 (**Figure 2A**). These observations suggest that SC in coculture either increase their  
384 endogenous expression of these SCP markers or that they proliferate extensively between DIV1 and  
385 DIV3. We find that the latter is more plausible as SC in cocultures continue to proliferate from DIV1 all  
386 through DIV7 (*Supplementary Figures, Figure S1 for Ki67 staining in cocultures*). Moreover, it is worth  
387 noting that the cells have already attained the SCP state at the time of dissection (E13.5) (Jacob, 2015).

388  
389 Data on *Cnp* expression in SCP of embryonic nerves is inconclusive. We analyzed three separate studies  
390 that sought to trace *Cnp* expression in the PNS (Gravel et al., 1998; Yuan et al., 2002; Deng et al., 2014).  
391 One study demonstrated that *Cnp* is expressed in the satellite cells of DRGs at E14.5 and at the ventral  
392 roots at E17.5 but did not comment on its expression in SCPs (Deng et al., 2014). The other two studies  
393 dealt with post-natal time points. Nonetheless, our observations suggest that *Cnp* mRNA is upregulated  
394 in SCP from DIV3 in culture. This observation, however, needs to be verified *in vivo*.

395  
396 *Krox20* is expressed at two different time points during the development of the PNS (Topilko et al., 1994;  
397 Voiculescu et al., 2000; Couplier et al., 2010). At around E10.5, it is first expressed in the boundary cap  
398 cells that are located at the dorsal and ventral roots. This is followed by its increased expression as SCP  
399 transition into iSC at around E15.5 in peripheral nerves. Indeed, it is one of the genes used in the study  
400 that can categorically distinguish between SCP and iSC at the mRNA expression level. In our study,  
401 *Krox20* expression does not change significantly between DIV1 and DIV5. We then see a sudden spike  
402 in its expression between DIV5 and DIV7 suggesting that SCP transition to iSC in this time-period (**Figure**  
403 **2A**).

404  
405 To test this hypothesis, we further looked at the expression profile of *Tfap2a*, which is expressed in NCC  
406 and SCP but not in iSC (Stewart et al., 2001) (**Figure 2A**). The downregulation of this transcription factor  
407 is indeed required for SCP to transition into iSC in developing nerves (Stewart et al., 2001; Jacob, 2015).

404 Consistent with this observation, *Tfap2a* levels drop by 50% between DIV5 and DIV7 thus providing  
405 further evidence of the SCP/iSC transition between DIV5 and DIV7. Furthermore, *Tfap2a*  
406 immunoreactivity in dissociated DRG/SC cocultures starkly reduces at DIV7 (**Figure 2B**) congruent with  
407 its downregulated expression in iSC *in vivo* (**Figure 2C**). Finally, we also assayed the expression levels  
408 of *Cad19*, which is the only known gene that is uniquely expressed in SCP but neither in Neural Crest  
409 Cells nor in iSC (Jessen and Mirsky, 2005, 2019; Takahashi and Osumi, 2005). *Cad19* expression *in*  
410 *vitro* was the highest around DIV3 and DIV5 but it reduced again at DIV7 reaching to levels comparable  
411 to DIV3. It is to be noted that all these changes in mRNA expression occur despite continuous  
412 proliferation of SC in this time period (Supplementary Data, Figure S1) suggesting that cells indeed  
413 downregulate *Cad19* and *Tfap2a* between DIV5 and DIV7.

414 Taken together, these results give a clear picture of Schwann cell developmental transitions in embryonic  
415 cocultures during which SCP proliferate and also presumably migrate on developing neurites between  
416 DIV1 and DIV5. At DIV5, SCP begin their transition into iSC and at DIV7 most of the cells present on  
417 neurites are iSC.

418  
419 It is interesting to note that SCP monocultures established directly from E12.5 dissociated mouse  
420 peripheral nerves transition into iSC in cultures after 4 DIV (E12.5 + 4DIV) which corresponds exactly to  
421 their timing *in vivo* (Dong et al., 1999). However, it takes up to 7 DIV to achieve this transition in DRG/SC  
422 cocultures. One plausible reason for this difference is the fact that SCP monocultures are expanded in  
423 the presence of a fixed concentration of Neuregulin to mimic the trophic support from axons that in turn  
424 drives their differentiation to iSC (Dong et al., 1995; Leimeroth et al., 2002). In cocultures however, the  
425 media is not supplemented with Neuregulin and neurites have to first emanate from the dissociated soma  
426 and achieve significant growth during the first 72h. Therefore, it is possible that optimal levels of axonal  
427 Neuregulin are not present in the coculture system until DIV5 thereby causing a delay in the SCP/iSC  
428 transition. This hypothesis can also be extended to other axo-glia signaling pathways such as Notch  
429 signaling which is also crucial for the SCP/iSC transition (Woodhoo et al., 2009). In effect, we think that  
430 the delay in the SCP/iSC transition in cocultures is largely driven by the fact that sufficient axonal  
431 extensions (and therefore axonal differentiation and axonal cues) are only achieved between DIV5 and  
432 DIV7. However, this hypothesis warrants further experimentation.

### 433 ***The iSC/mSC transition***

434  
435 iSC *in vivo* give rise to promyelinating and myelinating SC perinatally which is about 4 days after iSC  
436 emanate from SCP (Salzer, 2015; Fledrich et al., 2019). Therefore, we hypothesized that if the cells at  
437 DIV7 are indeed iSC, then they should transition into pro-mSC and mSC upon the addition of Ascorbic  
438 Acid. We were able to observe Oct6<sup>+</sup> and Krox20<sup>+</sup> cells after 4 days of Ascorbic Acid (AA)  
439 supplementation (**Figure 3**). However, Oct6 expression *in vivo* is only transient, and it promotes the  
440 differentiation of pro-mSC to mSC (Jaegle et al., 1996, 2003). In other words, perinatal SC *in vivo*  
441 sequentially express Oct6 and Krox20 but fully mature myelinating SC do not express Oct6 postnatally.

442 Our data show that both these cellular phenotypes are present after 4 days of AA supplementation  
443 suggesting that iSC/mSC transition is still ongoing at this timepoint. It is also equally possible that the  
444 cells that express Krox20 at DIV7 + 4 days AA expressed Oct6 before and they have already transitioned  
445 to mSC. Therefore, further experiments are required to assess the advent and the successive extinction  
446 of Oct6 expression in this coculture system. Nevertheless, our results clearly demonstrate that iSC at  
447 DIV7 transition into mSC as early as after 4 days of AA supplementation which is comparable to their  
448 transition *in vivo*.

449 As for SC monocultures, the phenotype of SC in culture; irrespective of the source, is highly peculiar as  
450 these cells express several makers of the Schwann cell lineage including those of SCP, iSC and the  
repair phenotype that arises post nerve injury (Monje, 2020). In our study, we wanted to determine the

451 myelination potency of coculture derived SC monocultures and compare that to SC monocultures  
452 established from neonatal nerves which largely comprise of iSC and pro-mSC (Monje, 2020) (**Figure 4**).  
453 Our observations demonstrate firstly that SC monocultures derived from DIV7 cocultures are similar to  
454 cultures established from neonatal peripheral nerves in their potential to differentiate into mSC. Secondly,  
455 and more importantly, they show that DIV7 SC in monoculture are distinct from SCP that arise between  
456 DIV1 and DIV5 in cocultures as they lack Tfp2 $\alpha$  immunoreactivity both in proliferative and in  
457 differentiative conditions (Supplementary figure S2). However, we have not investigated any fine  
458 phenotypic differences between neonatal SC monocultures and coculture-derived SC monocultures as  
459 it falls beyond the ambit of the present study. Nevertheless, it is an important criterion that remains to be  
460 ascertained. That being said, it would also be equally interesting to isolate SCP from cocultures before  
461 DIV5 and compare them to SCP derived directly from embryonic nerves at E12.5 to ascertain phenotypic  
462 differences, if any.

463 In summation and as highlighted above, our study demonstrates for the first time that the SCP/iSC  
464 transition indeed occurs in embryonic DRG/SC cocultures between DIV5 and DIV7. The further  
465 differentiation of iSC to mSC can also be observed in this model as early as 4 days post AA  
466 supplementation. These observations serve as a powerful frame of reference to design, execute and  
467 comprehend coculture experiments using different Schwann cell mutants that aim to ascertain the role  
468 of specific genes or experimental conditions in Schwann cell development and myelination.

469



470 **References**

471

- 472 Andersen, C., Jensen, J., and Orntoft, T. (2004). Normalization of Real • Time Quantitative Reverse  
473 Transcription • PCR Data : A Model • Based Variance Estimation Approach to Identify Genes  
474 Suited for Normalization , Applied to Bladder and Colon Cancer Data Sets. *Cancer Res.* 64, 5245.  
475 doi:10.1158/0008.
- 476 Arthur-Farraj, P., Wanek, K., Hantke, J., Davis, C. M., Jayakar, A., Parkinson, D. B., et al. (2011).  
477 Mouse schwann cells need both NRG1 and cyclic AMP to myelinate. *Glia* 59, 720–733.  
478 doi:10.1002/glia.21144.
- 479 Bacallao, K., and Monje, P. V. (2015). Requirement of cAMP Signaling for Schwann Cell Differentiation  
480 Restricts the Onset of Myelination. *PLoS One* 10, e0116948. doi:10.1371/journal.pone.0116948.
- 481 Buchstaller, J., Sommer, L., Bodmer, M., Hoffmann, R., Suter, U., and Mantei, N. (2004). Efficient  
482 Isolation and Gene Expression Profiling of Small Numbers of Neural Crest Stem Cells and  
483 Developing Schwann Cells. *J. Neurosci.* 24, 2357–2365. doi:10.1523/JNEUROSCI.4083-03.2004.
- 484 Culpier, F., Decker, L., Funalot, B., Vallat, J. M., Garcia-Bragado, F., Charnay, P., et al. (2010).  
485 CNS/PNS boundary transgression by central glia in the absence of schwann cells or Krox20/Egr2  
486 function. *J. Neurosci.* 30, 5958–5967. doi:10.1523/JNEUROSCI.0017-10.2010.
- 487 D'Antonio, M., Michalovich, D., Paterson, M., Droggiti, A., Woodhoo, A., Mirsky, R., et al. (2006). Gene  
488 profiling and bioinformatic analysis of Schwann cell embryonic development and myelination. *Glia*  
489 53, 501–515. doi:10.1002/glia.20309.
- 490 Deng, Y., Kim, B., He, X., Kim, S., Lu, C., Wang, H., et al. (2014). Direct visualization of membrane  
491 architecture of myelinating cells in transgenic mice expressing membrane-anchored EGFP.  
492 *genesis* 52, 341–349. doi:10.1002/dvg.22751.
- 493 Dong, Z., Brennan, A., Liu, N., Yarden, Y., Lefkowitz, G., Mirsky, R., et al. (1995). Neu differentiation  
494 factor is a neuron-glia signal and regulates survival, proliferation, and maturation of rat schwann  
495 cell precursors. *Neuron* 15, 585–596. doi:10.1016/0896-6273(95)90147-7.
- 496 Dong, Z., Sinanan, A., Parkinson, D., Parmantier, E., Mirsky, R., and Jessen, K. R. (1999). Schwann  
497 cell development in embryonic mouse nerves. *J. Neurosci. Res.* 56, 334–348.  
498 doi:10.1002/(sici)1097-4547(19990515)56:4<334::aid-jnr2>3.0.co;2-%23.
- 499 Eldridge, C. F., Bartlett Bunge, M., and Bunge, R. P. (1989). Differentiation of axon-related Schwann  
500 cells in vitro: II. Control of myelin formation by basal lamina. *J. Neurosci.* 9, 625–638.  
501 doi:10.1523/jneurosci.09-02-00625.1989.
- 502 Eldridge, C. F., Bunge, M. B., Bunge, R. P., and Wood, P. M. (1987). Differentiation of axon-related  
503 Schwann cells in vitro. I. Ascorbic acid regulates basal lamina assembly and myelin formation. *J.*  
504 *Cell Biol.* 105, 1023–1034. doi:10.1083/jcb.105.2.1023.
- 505 Fledrich, R., Kungl, T., Nave, K. A., and Stassart, R. M. (2019). Axo-glia interdependence in peripheral  
506 nerve development. *Development* 146. doi:10.1242/dev.151704.
- 507 Ghislain, J., and Charnay, P. (2006). Control of myelination in Schwann cells: A Krox20 cis-regulatory  
508 element integrates Oct6, Brn2 and Sox10 activities. *EMBO Rep.* 7, 52–58.  
509 doi:10.1038/sj.embor.7400573.
- 510 Gravel, M., Polo, A. Di, Valera, P. B., and Braun, P. E. (1998). Four-kilobase sequence of the mouse  
511 CNP gene directs spatial and temporal expression of lacZ in transgenic mice. *J. Neurosci. Res.*  
512 53, 393–404. doi:10.1002/(SICI)1097-4547(19980815)53:4<393::AID-JNR1>3.0.CO;2-1.
- 513 Huff, T. C., Sant, D. W., Camarena, V., Van Booven, D., Andrade, N. S., Mustafi, S., et al. (2020).  
514 Vitamin C regulates Schwann cell myelination by promoting DNA demethylation of pro-myelinating  
515 genes. *J. Neurochem.* doi:10.1111/jnc.15015.

- 516 Jacob, C. (2015). Transcriptional control of neural crest specification into peripheral glia. *Glia* 63, 1883–  
517 1896. doi:10.1002/glia.22816.
- 518 Jaegle, M., Ghazvini, M., Mandemakers, W., Piirsoo, M., Driegen, S., Levavasseur, F., et al. (2003).  
519 The POU proteins Brn-2 and Oct-6 share important functions in Schwann cell development.  
520 *Genes Dev.* 17, 1380–1391. doi:10.1101/gad.258203.
- 521 Jaegle, M., Mandemakers, W., Broos, L., Zwart, R., Karis, A., Visser, P., et al. (1996). The POU factor  
522 Oct-6 and Schwann cell differentiation. *Science (80- )*. 273, 507–510.  
523 doi:10.1126/science.273.5274.507.
- 524 Jessen, K. R., Brennan, A., Morgan, L., Mirsky, R., Kent, A., Hashimoto, Y., et al. (1994). The Schwann  
525 cell precursor and its fate: A study of cell death and differentiation during gliogenesis in rat  
526 embryonic nerves. *Neuron* 12, 509–527. doi:10.1016/0896-6273(94)90209-7.
- 527 Jessen, K. R., and Mirsky, R. (2005). The origin and development of glial cells in peripheral nerves. *Nat*  
528 *Rev Neurosci* 6, 671–682. doi:nrn1746 [pii]n10.1038/nrn1746.
- 529 Jessen, K. R., and Mirsky, R. (2019). Schwann cell precursors; multipotent glial cells in embryonic  
530 nerves. *Front. Mol. Neurosci.* 12, 69. doi:10.3389/fnmol.2019.00069.
- 531 Kim, H. A., and Maurel, P. (2009). “Primary Schwann Cell Cultures,” in (Humana Press), 253–268.  
532 doi:10.1007/978-1-60761-292-6\_15.
- 533 Kim, J., and Kim, H. A. (2018). “Isolation and expansion of Schwann cells from transgenic mouse  
534 models,” in *Methods in Molecular Biology* (Humana Press Inc.), 39–48. doi:10.1007/978-1-4939-  
535 7649-2\_3.
- 536 Leimeroth, R., Lobsiger, C., Lüssi, A., Taylor, V., Suter, U., and Sommer, L. (2002). Membrane-bound  
537 neuregulin1 type III actively promotes Schwann cell differentiation of multipotent progenitor cells.  
538 *Dev. Biol.* 246, 245–258. doi:10.1006/dbio.2002.0670.
- 539 Livak, K. J., and Schmittgen, T. D. (2001). Analysis of relative gene expression data using real-time  
540 quantitative PCR and the  $2^{-\Delta\Delta CT}$  Method. *Methods* 25, 402–408. doi:10.1006/meth.2001.1262.
- 541 Lutz, A. B. (2014). Purification of Schwann Cells from the Neonatal and Injured Adult Mouse Peripheral  
542 Nerve. *Cold Spring Harb. Protoc.* 2014, pdb.prot074989. doi:10.1101/pdb.prot074989.
- 543 Mollet, I. G., Ben-Dov, C., Felício-Silva, D., Grosso, A. R., Eleutério, P., Alves, R., et al. (2010).  
544 Unconstrained mining of transcript data reveals increased alternative splicing complexity in the  
545 human transcriptome. *Nucleic Acids Res.* 38, 4740–4754. doi:10.1093/nar/gkq197.
- 546 Monje, P. V. (2020). Schwann Cell Cultures: Biology, Technology and Therapeutics. *Cells* 9, 1848.  
547 doi:10.3390/cells9081848.
- 548 Monk, K. R., Feltri, M. L., and Taveggia, C. (2015). New insights on schwann cell development. *Glia*  
549 63, 1376–1393. doi:10.1002/glia.22852.
- 550 Päiväläinen, S., Nissinen, M., Honkanen, H., Lahti, O., Kangas, S. M., Peltonen, J., et al. (2008).  
551 Myelination in mouse dorsal root ganglion/Schwann cell cocultures. *Mol. Cell. Neurosci.* 37, 568–  
552 578. doi:10.1016/j.mcn.2007.12.005.
- 553 Ratner, N., Williams, J. P., Kordich, J. J., and Kim, H. A. (2005). Schwann Cell Preparation from Single  
554 Mouse Embryos: Analyses of Neurofibromin Function in Schwann Cells. *Methods Enzymol.* 407,  
555 22–33. doi:10.1016/S0076-6879(05)07003-5.
- 556 Salzer, J. L. (2015). Schwann cell myelination. *Cold Spring Harb. Perspect. Biol.* 7, 1–26.  
557 doi:10.1101/cshperspect.a020529.
- 558 Schmittgen, T. D., and Livak, K. J. (2008). Analyzing real-time PCR data by the comparative C(T)  
559 method. *Nat. Protoc.* 3, 1101–8.
- 560 Stewart, H. J., Brennan, A., Rahman, M., Zoidl, G., Mitchell, P. J., Jessen, K. R., et al. (2001).  
561 Developmental regulation and overexpression of the transcription factor AP-2, a potential regulator

562 of the timing of Schwann cell generation. *Eur. J. Neurosci.* 14, 363–72. doi:10.1046/j.0953-  
563 816x.2001.01650.x.

564 Sundaram, V. K., Sampathkumar, N. K., Massaad, C., and Grenier, J. (2019). Optimal use of statistical  
565 methods to validate reference gene stability in longitudinal studies. *PLoS One* 14, e0219440.  
566 doi:10.1371/journal.pone.0219440.

567 Takahashi, M., and Osumi, N. (2005). Identification of a novel type II classical cadherin: Rat cadherin19  
568 is expressed in the cranial ganglia and Schwann cell precursors during development. *Dev. Dyn.*  
569 232, 200–208. doi:10.1002/dvdy.20209.

570 Taveggia, C., and Bolino, A. (2018). “DRG neuron/schwann cells myelinating cocultures,” in *Methods in*  
571 *Molecular Biology* (Humana Press Inc.), 115–129. doi:10.1007/978-1-4939-7862-5\_9.

572 Topilko, P., Schneider-Maunoury, S., Levi, G., Baron-Van Evercooren, A., Chenoufi, A. B. Y.,  
573 Seitanidou, T., et al. (1994). Krox-20 controls myelination in the peripheral nervous system. *Nature*  
574 371, 796–799. doi:10.1038/371796a0.

575 Voiculescu, O., Charnay, P., and Schneider-Maunoury, S. (2000). Expression pattern of a Krox-20/Cre  
576 knock-in allele in the developing hindbrain, bones, and peripheral nervous system. *genesis* 26,  
577 123–126. doi:10.1002/(SICI)1526-968X(200002)26:2<123::AID-GENE7>3.0.CO;2-O.

578 Woodhoo, A., Alonso, M. B. D., Droggiti, A., Turmaine, M., D’Antonio, M., Parkinson, D. B., et al.  
579 (2009). Notch controls embryonic Schwann cell differentiation, postnatal myelination and adult  
580 plasticity. *Nat. Neurosci.* 12, 839–847. doi:10.1038/nn.2323.

581 Woodhoo, A., and Sommer, L. (2008). Development of the schwann cell lineage: From the neural crest  
582 to the myelinated nerve. *Glia* 56, 1481–1490. doi:10.1002/glia.20723.

583 Yuan, X., Chittajallu, R., Belachew, S., Anderson, S., McBain, C. J., and Gallo, V. (2002). Expression of  
584 the green fluorescent protein in the oligodendrocyte lineage: A transgenic mouse for  
585 developmental and physiological studies. *J. Neurosci. Res.* 70, 529–545. doi:10.1002/jnr.10368.

586

587

588 **Figure Legends**

589 **Figure 1: Progression of DRG/SC cocultures between Days in Vitro (DIV)1 & DIV7.**

590 DRGs were dissociated and cultured from E13.5 embryos. The DRGs at the time of dissections contained SMI312+  
591 neurons and Sox10+ glial cells. The cells sparsely populated the culture at DIV1. In the next 5 days, the neuron-SC  
592 network expanded and established a well-connected network by DIV 7 containing Sox10+ SC situated on top of  
593 SMI312+ axonal extensions. Images shown here are representative images chosen arbitrarily. Although the area  
594 covered by axons increases progressively between DIV1 and DIV7, not all regions of the culture are equally dense  
595 at DIV7. SMI312 – Neuronal Marker, Sox10 – SC lineage marker, Hoechst – Nuclear Staining. SC: Spinal Cord, DR:  
596 Dorsal root, VR: Ventral root, DRG: Dorsal Root Ganglia. Scale bar = 100µm

597

598 **Figure 2: Transition of Schwann cell Precursors to immature Schwann cells in DRG/SC Cocultures.**

599 (A) mRNA expression profiles of Schwann cell lineage markers assessed through RTqPCR. Relative expression  
600 was calculated using DIV1 as the experimental calibrator. To assess statistical difference in relative RNA quantities  
601 between groups, One-way ANOVA was performed. If statistical significance was observed between the means of  
602 the groups, Tukey's post hoc was performed to compare all the groups with each other. The alpha value threshold  
603 was set at 5% and the P-values are represented as follows: P<0.05 - \*, P<0.01 - \*\*, P<0.001 - \*\*\*.

604 (B) ICC performed on dissociated cultures between DIV1 and DIV7. SCP were identified using Tfp2α staining,  
605 Sox10 was used as a SC lineage marker, Neurons were identified using SMI312 staining, and Hoechst dye was used  
606 to stain all nuclei. Scale bar = 100µm

607 (C) IHC performed on hind limb cross sections of E13.5 and E16.5 embryos. SCP were identified using Tfp2α  
608 staining, Sox10 was used as a SC lineage marker, Neurons were identified using SMI312 staining, and Hoechst dye  
609 was used to stain all nuclei. Scale bar = 100µm

610

611 **Figure 3: Transition of immature SC to myelinating SC in DRG/SC cocultures.**

612 Cocultures at DIV7 were treated with Ascorbic Acid (AA) for a period of 4 days. ICC was performed to assess the  
613 presence of Oct6+ (A) and Krox20+ (B) Schwann cells. Sox10 was used as a SC lineage marker, SMI312 was used  
614 to stain neurons and Hoechst dye was used to stain all nuclei. Scale bar = 100µm

615

616 **Figure 4: Myelinating potential of Coculture derived SC monocultures.**

617 SC monocultures were established from DIV7 DRG/SC cocultures using immunopanning and were differentiated  
618 using cAMP.

619 (A) Relative mRNA of Oct6, Krox20 and Tfp2α assessed across DIV7, SC monocultures in Proliferation (Prolif.) and  
620 in Differentiation (Diff.) DIV7 was used as the experimental control. To assess statistical difference in relative RNA  
621 quantities between groups, One-way ANOVA was performed. If statistical significance was observed between the  
622 means of the groups, Tukey's post hoc was performed to compare all the groups with each other. The alpha value  
623 threshold was set at 5% and the P-values are represented as follows: P<0.05 - \*, P<0.01 - \*\*, P<0.001 - \*\*\*.

624 (B) ICC performed on dissociated cultures at DIV7 as well as in SC monocultures in proliferation and in  
625 differentiation. Pro-mSC were identified using Oct6 staining, Sox10 was used as a SC lineage marker, Neurons  
626 were identified using SMI312 staining, and Hoechst dye was used to stain all nuclei. SMI312 is not applicable in  
627 SC monocultures due to the absence of axons. Scale bar = 100 $\mu$ m

628 (C) ICC performed on dissociated cultures at DIV7 as well as in SC monocultures in proliferation and in  
629 differentiation. mSC were identified using Krox20 staining, Sox10 was used as a SC lineage marker, Neurons were  
630 identified using SMI312 staining, and Hoechst dye was used to stain all nuclei. SMI312 is not applicable in SC  
631 monocultures due to the absence of axons. Scale bar = 100 $\mu$ m

632 (D) Quantification of Sox10, Oct6 and Krox20 immunoreactivity. The purity of SC cultures was assessed by  
633 calculating the total number of Sox10+ cells in culture. Oct6 and Krox20 immunoreactivity was quantified as the  
634 ratio of the total number of Oct6+ and Krox20+ cells to Sox10+ cells and it is expressed as a percentage. To assess  
635 statistical differences, a non-parametric Mann Whitney test was performed. The alpha value threshold was set at  
636 5% and the P-values are represented as follows: P<0.05 - \*, P<0.01 - \*\*, P<0.001 - \*\*\*.

637

638 ***Figure 5: Experimental paradigm and literature review***

639 (A) Experimental design used in the study.

640 (B) Current consensus on the mRNA expression of SC lineage markers in embryonic peripheral nerves presented  
641 along with the corresponding literature. The empirical quantification presented herein has been extrapolated  
642 from microarray studies performed on murine embryonic nerves (Buchstaller et al., 2004; D'Antonio et al., 2006).

643

Figure 1.TIF

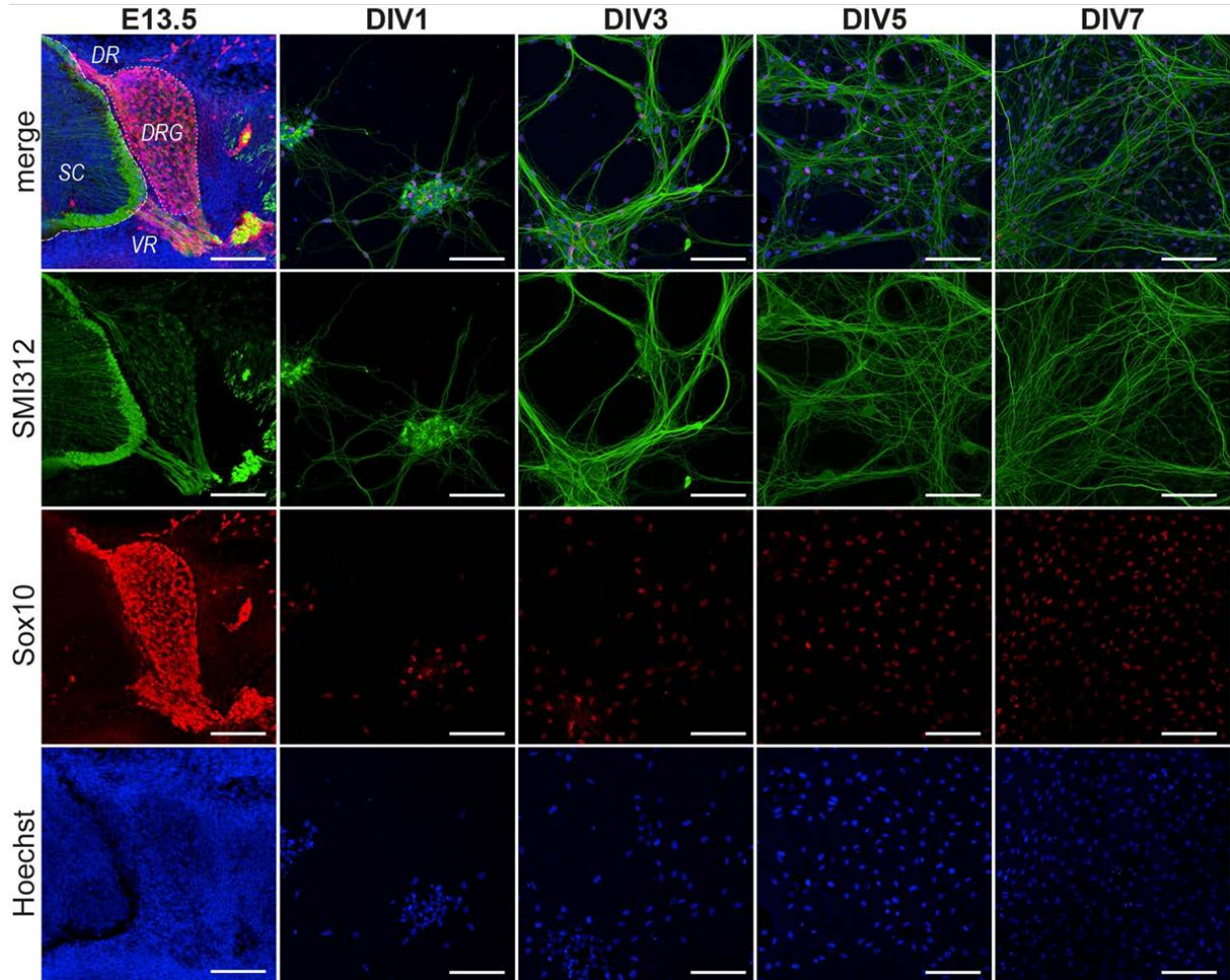


Figure 2.TIF

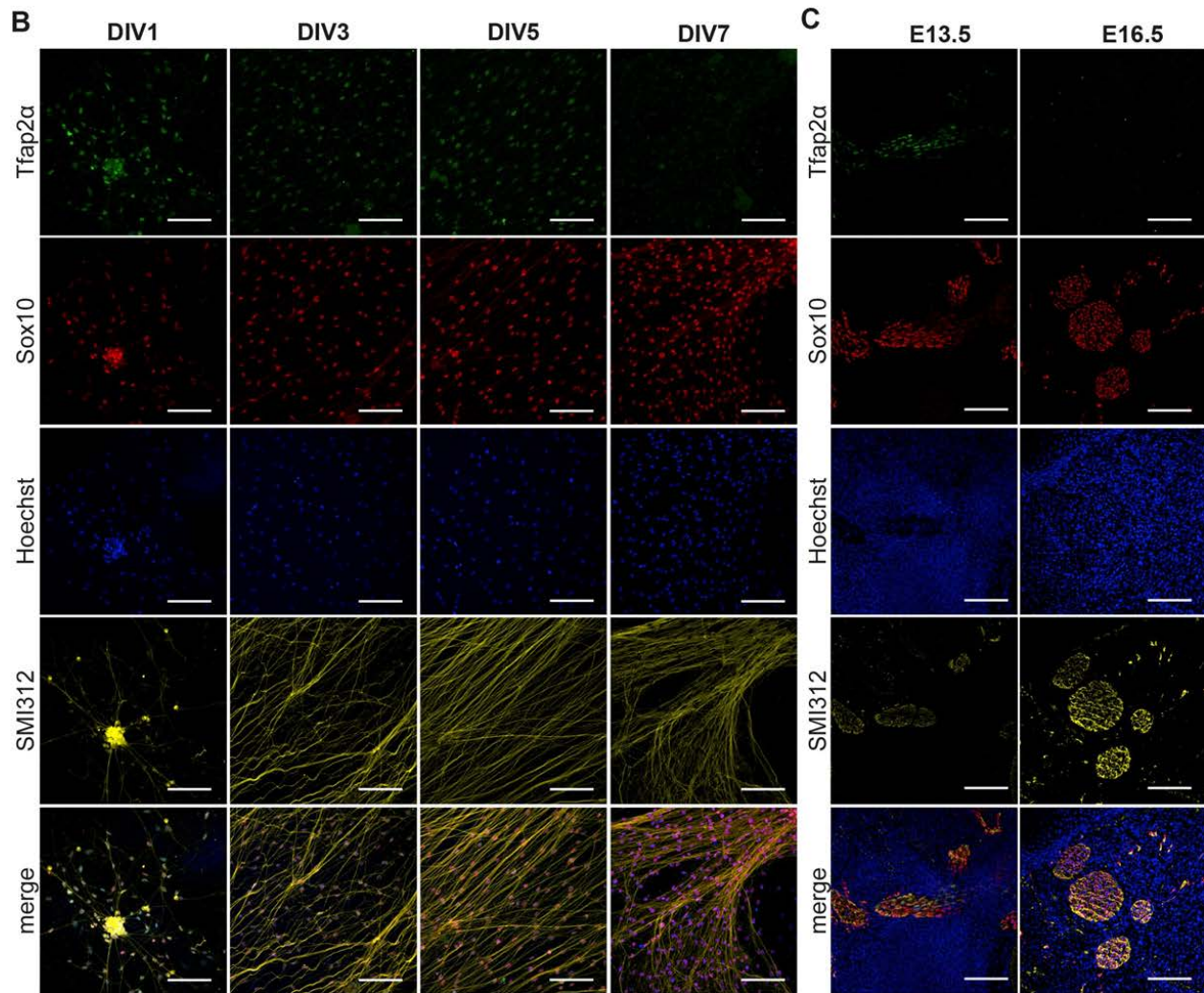
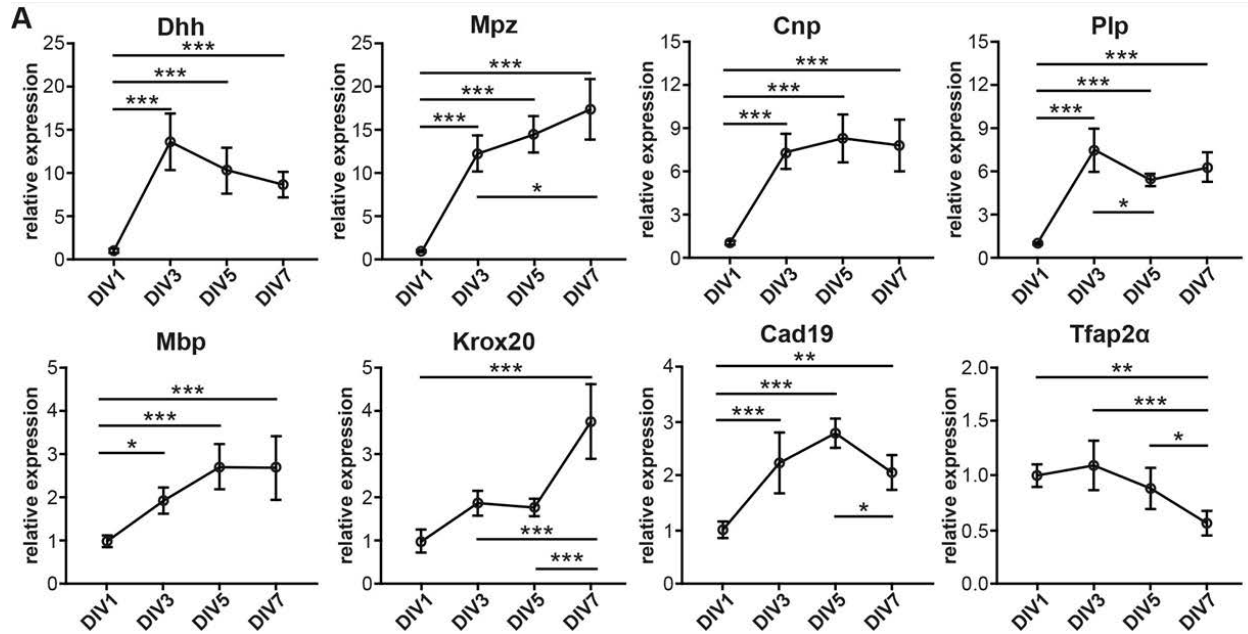


Figure 3.TIF

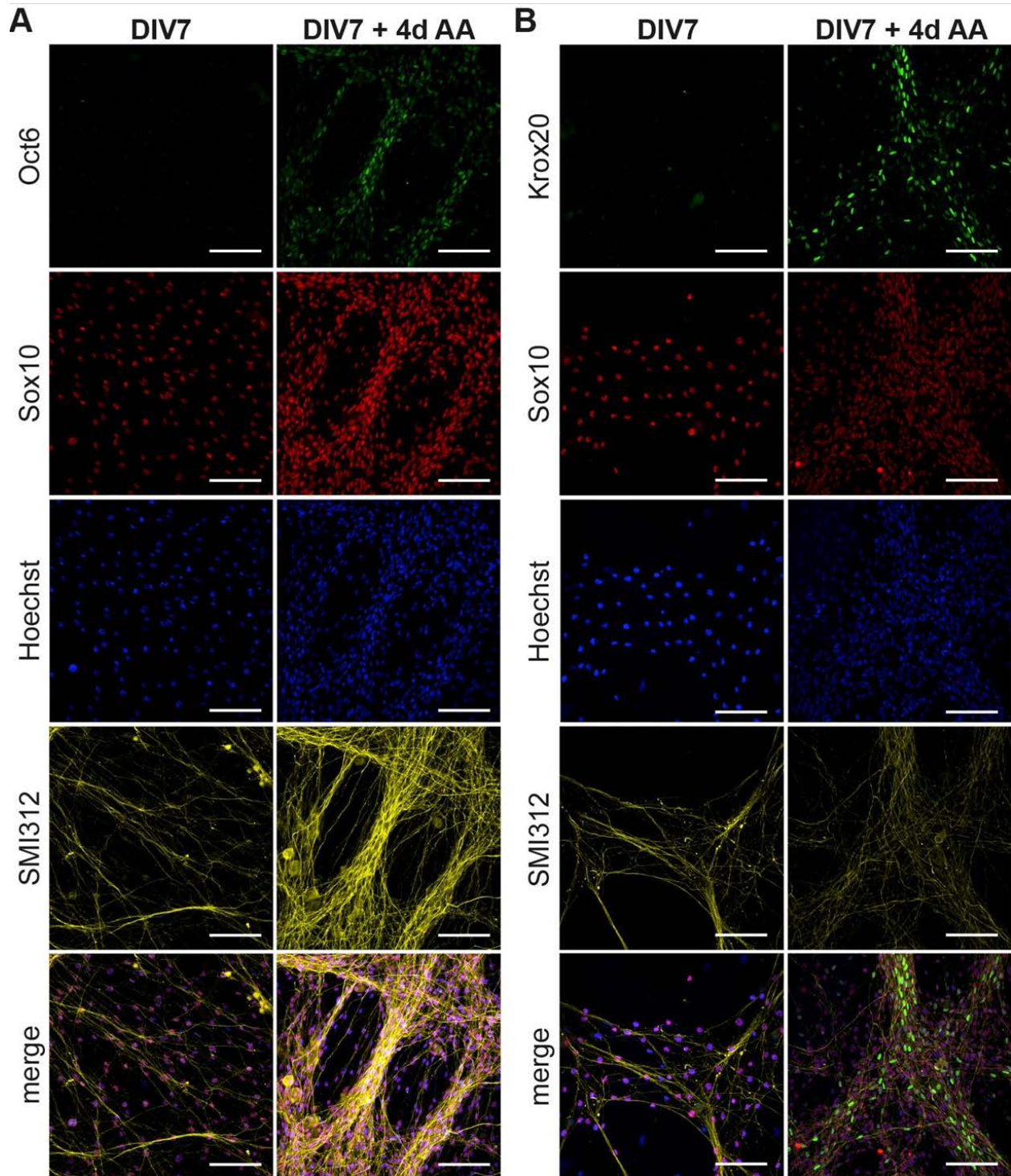




Figure 4.TIF

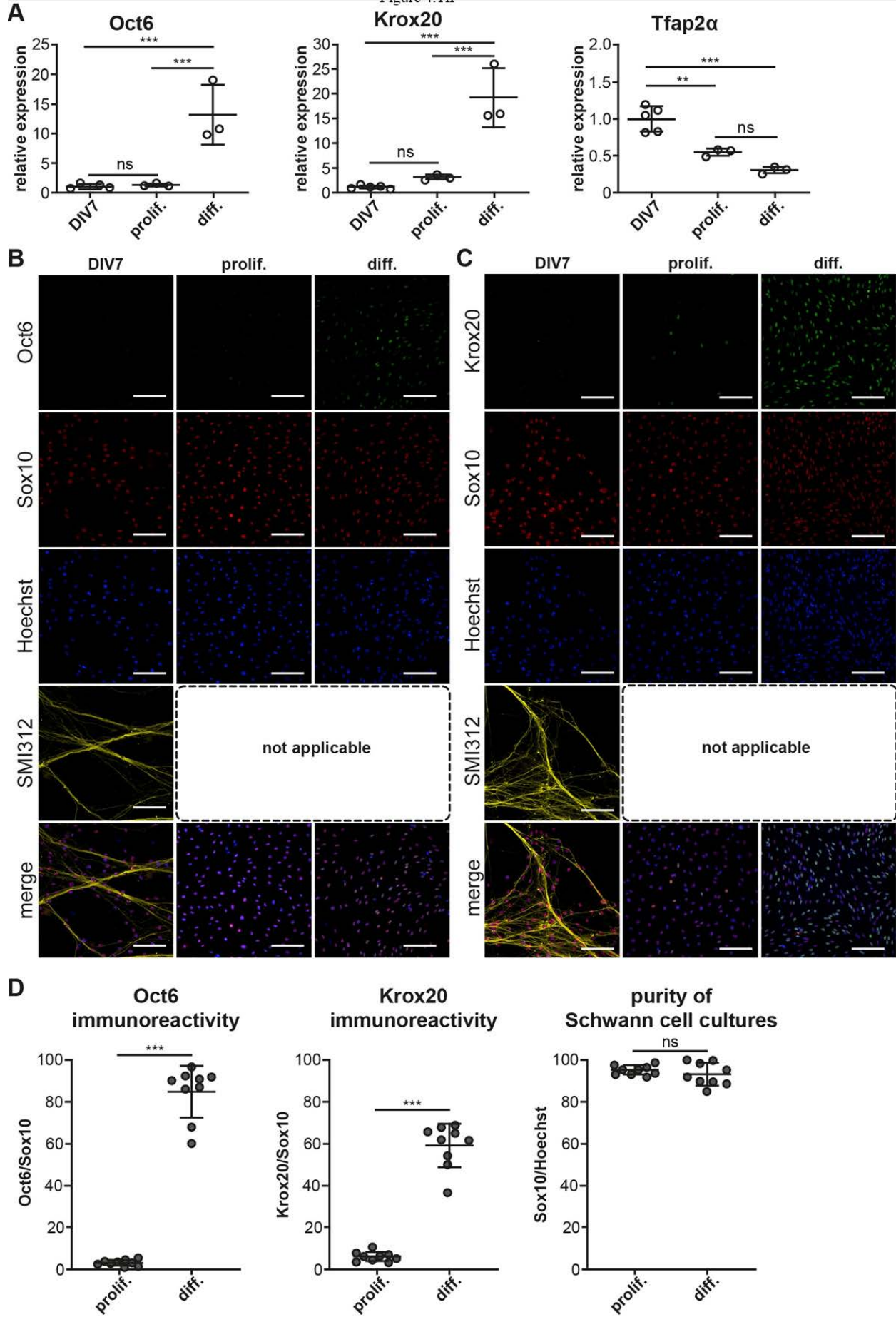
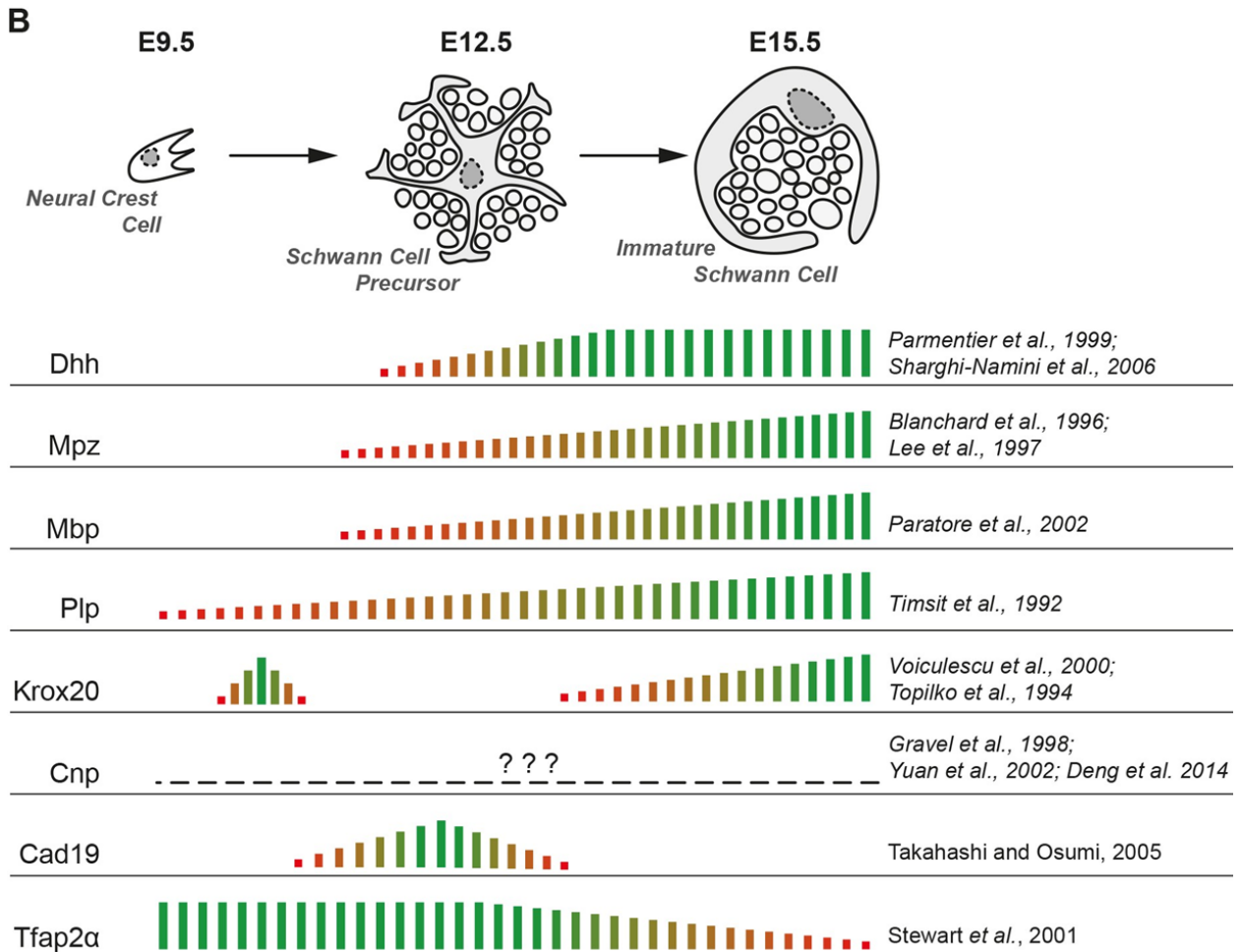
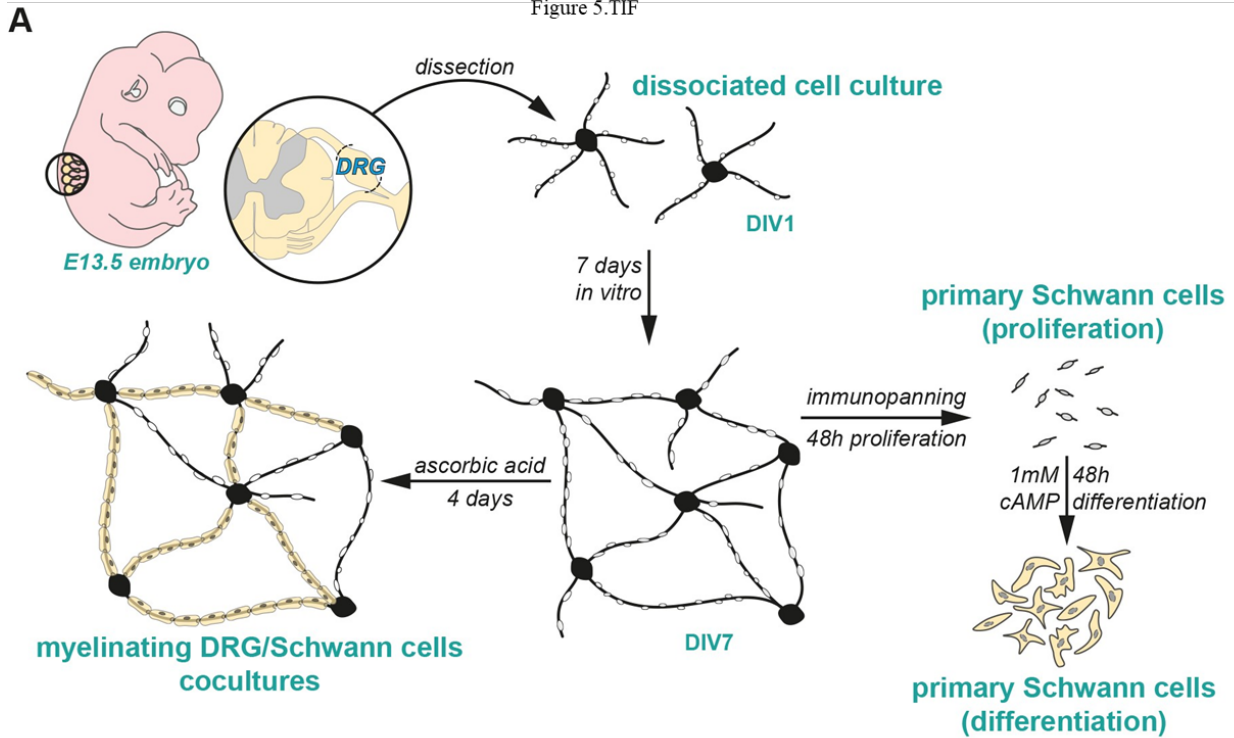


Figure 5.TIF



We have shown that the period between DIV5 to DIV7 corresponds to the transition from SC precursors to immature SCs and that plausibly cholesterol regulation by the LXR $\beta$  isoform is of much importance to that transition.

In summary, our results show that the LXR $\beta$  isoform is of crucial importance during this transition for SC survival, differentiation and maintaining the integrity of the peripheral nerves.

## CHAPTER IV: DISCUSSION

### 1. Consequences of LXR $\beta$ SC KO on mice behavioral performance and nerve ultrastructure.

The specific knock out of LXR $\beta$  in Schwann cells had significant consequences on the mice's behavioral performance. By mere observation, the phenotype of LXR $\beta$  SC KO mice can be detected, however, the behavioral and electrophysiological tests gave a thorough understanding of what was going on. Locomotoric results highlighted the difference with control mice by observing further limbs error in LXR $\beta$  SC KO mice and requiring a longer time to finish the test. These locomotive problems could result either of nerve conduction or muscular problems. The muscle strength was evaluated in fore limbs and all limbs, mutant mice showed less strength in all limbs in comparison to controls. To assess the contribution of the nerve part, we first evaluated the heat sensitivity using the hotplate test. The mutants showed no response to increased temperature and we had to ethically remove the mice off the hotplate after 30 seconds; this result shows the lack of response after nociceptive stimuli. The motor nerve conduction was evaluated by CMAP which also revealed a very significant difference between the mutants and the controls. These results highlight a very severe phenotype presenting sensory motor deficits which likely contribute to the motor coordination deficits and also reduced muscular strength.

The dissection of the sciatic nerve showed a flagrant difference in the anatomy of the nerve where LXR $\beta$  SC KO mice have thinner and translucent nerves, a phenomenon observed in *Gpr126*<sup>-/-</sup> mice and SOX 10 PNS mutants (Finzsch et al., 2010; Monk et al., 2011). The structural organization of sciatic nerve was evaluated by electron microscopy which revealed a severe lack of myelin in the mutant mice, also presenting heterogeneity between both nerves of the same mouse. At times some nerves would have close to no myelin and at other times would have a slightly higher number of myelinated axons, which might be explained by the extent of recombination efficiency of DhhCre in the mutant nerves.

We wanted to evaluate the consequences of reduced myelin presence on nerve fibers structural integrity, in a more physiological approach not requiring any fixation. We measured the apparent diameter of sciatic nerve teased fibers in PBS by AFM and observed a very significant difference between the two groups. LXR $\beta$  SC KO presented a smaller nerve fiber diameter however an

important variability was observed in this sample. We went ahead and acquired high-definition images of the nerves by SEM, since our AFM is not coupled to a microscope, which further confirmed our results by showing the same difference and confirmed the correct separation of the nerve fibers. We also assessed nerve myelination by staining the neurofilaments and the myelin protein MPZ, which showed the presence of very few myelinated axons in the mutant mice. Therefore, we can safely conclude that it is the lack of myelin that affects the apparent diameter of the nerve fibers that is observed both in AFM and SEM.

## 2. Maintenance of Sciatic nerve fiber biomechanical integrity in the LXR $\beta$ SC KO mutant mice by collagen deposition.

The absence of a bone structure around the peripheral nervous system, portrays it as more vulnerable to external injuries and stimuli however its very specific organization and composition compensate and provide this barrier protection. The nerve fibers are surrounded by three layers; the epineurium, perineurium and endoneurium. Additionally, the nerve fibers, if myelinated, are surrounded by Schwann cells in a 1:1 ratio which are also responsible for producing a basal lamina. If not myelinated, multiple smaller nerve fibers are wrapped by Remak Schwann cells.

In our study, the LXR $\beta$  SC KO led to reduced presence of myelinated fibers and consequently affected the nerve fiber diameter. Hence, we used AFM to assess the consequences of reduced myelin presence on the biomechanical properties of the sciatic nerve fibers by applying a force of compression and measuring the apparent elastic Young's Modulus, which gives the stiffness of nerve fibers.

We were then expecting to have consequences on the biomechanical properties of the teased sciatic nerve fibers of mutant mice, however, much to our surprise, our measurements did not show any significant difference between the apparent Young modulus of the mutant and the control nerve fibers. A recent study, working on a neuropathic Pmp22 $^{-/-}$  mouse model concluded that the basal lamina is the crucial player in maintaining the biomechanical properties of the nerve fibers. By chemically removing the basal lamina, the difference in the stiffness of the nerve fibers was observed in control vs. Pmp22 $^{-/-}$  (Rosso et al., 2014b). However, because of the reduced number of SCs at 8 weeks in LXR $\beta$  SC KO nerves, the formation of a basal lamina around the nerve fibers by SCs is doubtful. This made us question even more about the factor or cellular component

responsible for maintaining the nerve fibers integrity. Another study, led by the same team, described a heterogeneity of stiffness during development and once again, the myelination status is not the factor affecting the biomechanical properties. The apparent Young's modulus was measured in cross sections of sciatic nerves at different developmental stages divided in three groups: young, juvenile and adults corresponding to P5–P8, P26–P32, and P130–P217 respectively. The elastic moduli of the cross sections exhibited a heterogeneous biphasic state during maturation of the PNS tissue stiffness. A drop in juvenile nerve cross section stiffness was explained by a decrease of collagen type 1 expression and a multitude of ECM related factors, however not thoroughly proven (Rosso et al., 2019).

This enticed us to evaluate the other cellular components and factors that might be responsible for maintaining the integrity of the nerve fibers in the reduced presence of Schwann cells. We first started by evaluating the collagen content in the sciatic nerve which was very significantly increased in the LXR $\beta$  SC KO mice. This increased collagen content might be the factor responsible for maintaining the similar stiffness in the two groups and therefore the integrity of the nerve fibers.

Following the assessment of collagen deposition, we evaluated the presence of endoneurial cells, known for their contribution in the expression of the ECM component collagen. Thy1 staining, for endoneurial cell identification, was more noticeable in LXR $\beta$  SC KO sciatic nerves which might explain the increase of collagen deposition in the LXR $\beta$  SC specific mutants. Therefore, one explanation would be that collagen residues on the teased sciatic nerve fibers of LXR $\beta$  SC KO would lead to similar elastic moduli values.

The involvement of another player was also questioned. Based on the observation of the electron microscopy images, we noticed smaller nerve bundles engulfed by an unusual cell type which resembled perineurial cells in electron micrographs. Thus, we stained for ZO-1, a marker for perineurial cells in the PNS. To our surprise, the whole SN of LXR $\beta$  SC KO mice was restructured by these perineurial cells normally found around the endoneurial space. Another possible explanation for the absence of difference between the two groups would be that during the nerve teasing (sample preparation) the very small bundles were not completely separated from the perineurial cells rendering them more rigid, however, the number of measured nerve fibers is very

high which makes chances for this manipulation error very slim. Another hypothesis would be the involvement of these cells in the expression of ECM molecules in the absence of SCs.

### 3. Perineurial/Schwann cell communication

The infiltration of perineurial cells and fasciculation of the nerve fibers might not be the direct cause of maintaining the sciatic nerve fibers' stiffness in the LXR $\beta$  SC KO mice, yet, it shed the light on a structural reorganization of the SNs in the reduced presence of SCs. This nerve "minifasciculation" was previously described by many groups, especially Jessen and Mirsky with the Dhh $^{-/-}$  mouse model (Parmantier et al., 1999). The nerve conduction in Dhh mutants was not altered, myelination and axons seemed not very affected. However, minifasciculation by perineurial cells was observed, highlighting the role of Schwann cell expressed Dhh in leading a correct development of the sciatic nerve by communicating with perineurial cells through its receptor Patched (Ptc)/Smoothened (SMO).

They described the expression of Dhh as early as E13 in Schwann cells and detected the expression of patched Ptc/SMO in a population of perineurial cells found at that time point outside the nerve fascicle. The perineurial barrier was described as leaky, presenting a dispatched basal lamina, lacking the gap junction protein connexin 43 and in contrast to our findings, they report a decrease in collagen (Parmantier et al., 1999).

Two other studies describe the minifasciculation phenotype; the SOX10 mutants and Gpr126 mutants. However, in these cases, SC differentiation and myelination were affected. The deletion of SOX10 led to the absence of both myelinating and non myelinating Schwann cells and an increase in collagen deposition similar to our findings (Finzsch et al., 2010). The sciatic nerves of Gpr126 mutants had Schwann cells that were halted at the promyelinating stage, did not present any Remak bundles and the Dhh expression was not detected. (Monk et al., 2011). The authors state that the fasciculation is not directly related to Gpr126 expression but to the fact that Schwann cells are not differentiated or are absent.

Jessen and Mirsky put forward that the perineurium formation happens in two stages; the first would be the recruitment of the perineurial cells and is independent from SCs and Dhh signaling and the second is Dhh signaling dependent and is necessary for perineurial maturation and correct

development of the nerve (Parmantier et al., 1999). Another theory explained minifasciculation, in a different context, where the nerve myelin was injured by glycerol injections resulting in remyelination, and the authors describe the observed phenotype as endoneurial fibroblasts differentiation into perineurial cells (Fressinaud et al., 1987). The role of Dhh cannot be refuted in the correct nerve development, subsequently, both of these theories were postulated based at that time's conception of a mesenchymal origin of the perineurial cells. Furthermore, in a clinical setting, this minifasciculation is found in the benign tumor; intraneural perineurioma (Boyanton Jr et al., 2007).

In summary, our findings are in line with the literature and highlight the importance of Schwann cells in the correct development of peripheral nerves by the communication with perineurial cells. Understanding this communication would not only help understanding nerve development but would also be in favor of finding therapeutic targets for patients with intraneural perineurioma which is yet again characterized by a similar phenotype that we observed in our mutants.

#### 4. Alteration of lipid composition in LXR $\beta$ SC KO SNs

Another hypothesis we postulated in order to explain the observed phenotype is the alteration of the lipid composition of the sciatic nerves as consequences of LXR $\beta$  SC KO.

Using TOF-SIMS mass spectrometry imaging, we have shown that the lipid composition of the sciatic nerve was severely altered following LXR $\beta$  SC KO and the consequent reduced presence of Schwann cells and myelination. Our results do not mimic the findings of any other study. We did not observe any significant changes in fatty acid synthase expression, in FA composition or a shift in the saturation levels that may be close to a previous study describing lipid composition after demyelination and fasciculation induced by glycerol injections (Fressinaud et al., 1987).

Surprisingly, we observed an increased concentration of sphingomyelin in the sciatic nerves of the LXR $\beta$  SC KO. This increase has never been described before, nonetheless, different scenarios have been reported in numerous studies. Lipid composition of Diabetic show no change in sphingomyelin content (Gaia Cermenati et al., 2012) and CMT1A mice describe a decrease in sphingomyelin levels (Fledrich et al., 2018). One recent study even proposed that SM concentration in serum is a potential biomarker of neuropathies (Capodivento et al., 2017). A



previous study described increased sphingomyelin in the plasma membranes of maturing hippocampal neurons (Dolores Ledesma et al., 1999), which might be, in our case, a sort of compensation mechanism. The distribution of the sphingomyelin in our samples is homogenous which leads us to really consider the involvement of endoneurial cells and perineurial cells as a potential cellular components responsible for this increased concentration. The recently surged Sciatic Nerve Atlas (Gerber et al., 2021), allowed us to find the expression of SGMS1 and SGMS2 in all cellular types of the sciatic nerve. At P60, SGMS1 is expressed by all cell types in WT sciatic nerves, but particularly by epineurial cells, perineurial cells, and endothelial cells. Our ToF-SIMS measurements excluded the epineurium, therefore perineurial and endothelial cells are the potential candidates in this increased concentration of sphingomyelin. SGMS2 expression levels in the cells of the sciatic nerve are lower than those of SGMS1, but they are very important in perineurial cells. As a result, we can speculate that perineurial cells are involved in the increased expression of sphingomyelin, although another possibility may be the transport of sphingomyelin to the sciatic nerves.

Another finding was a 10-fold decrease in cholesterol concentration, which has been identified in several diseases and mouse models that affect myelination (Gaia Cermenati et al., 2012; Fledrich et al., 2018). Additionally, the expression of enzymes responsible for its biosynthesis and control was significantly downregulated. This observation was expected given the scarce number of myelinated axons, and myelin usually contains the largest pool of free cholesterol in the SN (Saher et al., 2015). However, the upregulation in ABCA1 and APOE mRNA levels measured in mutant might be a coping mechanism of the other cellular components of the SN. One possible hypothesis could be that oxysterols secreted by neurons and other cell types would not be utilized by SCs due to their reduced presence, causing oxysterols to enter neighboring cells and lead to the increase of ABCA1 and ApoE levels.

## 5. Unraveling the cause of reduced myelin presence

In this study, we describe the reduced presence of myelination and we have stated that it might be due to a reduced presence of Schwann cells. Therefore, in order to understand the LXR $\beta$  SC KO phenotype and validate our hypotheses, we evaluated the mRNA levels of myelin specific proteins MPZ and PMP22. As expected, they were significantly decreased in the nerves of the mutant mice.

We then examined the mRNA expression levels of SC markers, which were also significantly reduced in mutant mice. Immunostaining of SOX10 and Krox20 further confirmed these findings. In our model, the presence of myelinating SCs is reduced and the decreased expression of the glial marker SOX10 is also observed. The reduced presence of Krox20 positive cells could be caused by an arrest at earlier stages, similar to the Krox20<sup>-/-</sup> mouse model described by P. Topilko (Topilko et al., 1994), however the reduced presence of SOX10 would refute this hypothesis. We also showed, by electron microscopy, the absence of SCs up to E18.5. Therefore, we studied earlier stages of SC development and we cultured dissociated DRGs of control and LXR $\beta$  SC KO embryos at E13.5. We observed that LXR $\beta$  SC KO Schwann cells detached at DIV7/8, corresponding to the transition of SCP to iSCs.

Till present, we have not been able to tell if the Schwann cells are dying or if they are arrested at the iSC stage. The absence of SOX10 staining and the detachment of iSCs in LXR $\beta$  SC KO DRG co-cultures tend to support the hypothesis of iSC death as a result of LXR $\beta$  SC KO, emphasizing the crucial role of LXR $\beta$  in this transition. The ablation of LXR $\beta$  at E13, leading to SC death, would explain the severe phenotype of this mouse model, which was not previously observed in the LXR total mutants, where LXR was never expressed at any stage of its development and compensating pathways would have been activated.

One hypothesis for the death of iSCs is that, in the absence of LXR, the "sterol sensor," intracellular cholesterol accumulation leads to cellular death. Further research is needed to affirm or refute this hypothesis. However, the critical function of LXR expression during the SCP transition to iSCs cannot be denied.

## CHAPTER V: PERSPECTIVES AND CONCLUSION

The findings of this study open new questions that would require further investigation. Therefore, in this section, I discuss them and propose experiments that would help in the understanding and continuation of this work.

### 1. Which type of collagen is responsible for the maintenance of nerve fiber biomechanical integrity after LXR $\beta$ SC KO?

After observing the severity of the phenotype, the poor behavioral performance and reduced nerve conduction of the LXR $\beta$  SC KO mice, we questioned the biomechanical integrity of the nerve fibers in absence of myelination. Therefore, we measured the apparent Young's modulus by AFM. Our results were very surprising because we did not observe any difference between the two groups. Both our groups' measurements were in line with control measurements found in the literature. How did our nerves maintain the same stiffness? As discussed, one explanation, based on previous findings from the work of G. Rosso, is the involvement of ECM components and especially collagen type 1. On that account, we evaluated the presence of collagen, the main structural component of the ECM, by Masson Trichrome staining and our mutant nerves had a significantly higher collagen concentration in the SNs, which was an explanation to our findings. However, we did not evaluate which type of collagen or confirm the cellular type expressing them in the reduced presence of Schwann cells.

*Suggested experiment:*

To this extent, we suggest performing a single cell RNAseq in mutant peripheral nerves at 8 weeks would help us identify the type of collagen that is expressed and the cell type responsible for its expression. Furthermore, this experiment will also give us a clear idea of the different cell types that occupy the nerve following a drastic reduction in Schwann cell numbers.

### 2. Is the increase of sphingomyelin concentration a compensation for cholesterol reduction?

We detected a 4-fold increase in sphingomyelin levels and a 10-fold decrease of cholesterol levels in the mutant SNs. Since we described the reduction of myelinated fibers in the LXR SC KO SNs,

the cholesterol reduction was anticipated. Cholesterol plays a crucial role in membrane fluidity and conductance, thus its presence in the myelin sheath is crucial for the insulation of the axons. The increase in sphingomyelin levels arises from other cellular types of the SN, since we describe a reduced presence of SCs. We also highlight a heterogeneous distribution of the measured sphingomyelin by ToF-SIMS, therefore, we searched for sphingomyelin synthases expression in the newly surged Sciatic Nerve Atlas (Gerber et al., 2021) and found that its expression is mostly detected in perineurial cells in addition to epineurial cells. We then questioned if this increase in sphingomyelin concentration would be a mechanism for replacing cholesterol and an attempt for ensuring a better insulation of the axons?

*Suggested experiments:*

1. Evaluating the consequence of the increase in sphingomyelin vs cholesterol contents on membrane fluidity; Biomimetic membrane production by liposome extrusion with different sphingomyelin concentrations. Membrane fluidity evaluation by Fluorescence Recovery After Photobleaching (FRAP).
2. Assessing sphingomyelin content of perineurial cells from control and LXR $\beta$  SC KO SNs: Isolation and primary cell culture of perineurial cells from control and LXR $\beta$  SC KO sciatic nerves at 8 weeks and evaluation of sphingomyelin levels by Mass Spectrometry (MS).

### 3. Is the lipid alteration the cause or the consequence of the observed phenotype in LXR $\beta$ SC KO?

We described an altered lipid composition of the sciatic nerves of LXR $\beta$  SC KO at 8 weeks, which was explained by the absence of myelination and the reduced presence of SCs and involvement of other cell types of the SN. We also discussed the hypothesis of cholesterol accumulation because of LXR $\beta$  deletion during the SCP/iSCs transition that might be leading to embryonic cellular death, explaining the reduced number of SCs at post-natal timepoints.

*Suggested experiments:* Assessment of lipid composition of SNs during SCP/iSC transition and correlation with cell death.

1. HPLC-MS on control and LXR $\beta$  SC KO primary SCP cells cultured from sciatic nerves at E12.5 before the SCP/iSC transition.

2. The observation of possible cholesterol accumulation by filipin staining during the SCP/iSC transition in primary cells extracted from control and LXR $\beta$  SC KO sciatic nerves at E12.5.
3. Assessment of cellular death by Annexin V and co-staining with SOX10 to confirm Schwann cell death during the SCP/iSC transition in both primary cell culture and *in vivo*.

## Conclusion

In conclusion, our results describe the deleterious consequences of LXR $\beta$  SC KO on the SNs of 8 week old mice. We described poor behavioral and locomotive performances as well as reduced nerve conduction in the mutant mouse model, which are explained by the presence of very scarce myelinated nerve fibers. The reduced presence of myelin in LXR $\beta$  SC KO SNs affected the apparent diameter of the isolated nerve fibers however, it did not affect the biomechanical properties. We found that the major ECM component; collagen is responsible for maintaining the biomechanical properties of the nerve fibers in LXR $\beta$  SC KO.

Another consequence of LXR $\beta$  SC KO observed in this study is the structural reorganization of the SN by ZO-1 positive cells, predominantly expressed by perineurial cells, by creating smaller nerve fascicles. This reorganization and fasciculation of the sciatic nerve has been described in previous studies which highlight the role of Schwann cells in the correct development of the peripheral nerve and the importance of SC/Perineurial cells communication.

The consequences of LXR $\beta$  SC KO also affected sciatic nerve lipid composition. Decreased cholesterol concentration in the SNs of our mutants as well as the mRNA levels of the enzymes responsible for cholesterol biosynthesis and regulation were expected, since little myelinated axons were observed. However, we detected an increase in sphingomyelin levels which might be a compensation mechanism carried out by other cell types of the SN in an attempt of maintaining the integrity of the sciatic nerve.

The reason behind of all of these drastic differences between the two groups was not the ability of Schwann cells to myelinate but it was their reduced presence as early as E18.5 after LXR $\beta$  SC KO. By primary DRG cocultures from embryos at E12.5, we show that the LXR $\beta$  specific knock-out leads to the detachment and death of Schwann cell precursors during the transition to the immature stage. Based on these observations, we speculate a similar phenomenon is happening *in vivo* which would explain all these consequences.

Taken all together, our data show that the LXR  $\beta$  is crucial for correct peripheral nerve development, SC survival, differentiation and myelination.

## References

- Aggarwal, S., et al. (2011). Central nervous system myelin: structure, synthesis and assembly. *Trends in cell biology*, 21(10), 585-593.
- Alvarez-Prats, A., et al. (2018). Schwann-cell-specific deletion of phosphatidylinositol 4-kinase alpha causes aberrant myelination. *Cell reports*, 23(10), 2881-2890.
- Apfel, R., et al. (1994). A novel orphan receptor specific for a subset of thyroid hormone-responsive elements and its interaction with the retinoid/thyroid hormone receptor subfamily. *Molecular and cellular biology*, 14(10), 7025-7035.
- Arthur-Farraj, P., et al. (2011). Mouse schwann cells need both NRG1 and cyclic AMP to myelinate. *Glia*, 59(5), 720-733. doi:10.1002/glia.21144
- Baranowski, M. (2008). Biological role of liver X receptors. *J Physiol Pharmacol*, 59 Suppl 7, 31-55.
- Baron, W., et al. (2010). On the biogenesis of myelin membranes: sorting, trafficking and cell polarity. *FEBS letters*, 584(9), 1760-1770.
- BBML, B. B. a. M. L. (2020). GENERAL INTRODUCTION TO ATOMIC FORCE MICROSCOPY. Retrieved from <https://bbml.sitehost.iu.edu/afmintro.html>
- Bhatt, S., et al. (2013). Signals and switches in Mammalian neural crest cell differentiation. *Cold Spring Harb Perspect Biol*, 5(2). doi:10.1101/cshperspect.a008326
- Bich, C., et al. (2013). Study of experimental variability in TOF-SIMS mass spectrometry imaging of biological samples. *International Journal of Mass Spectrometry*, 337, 43-49.
- Birchmeier, C., et al. (2008). Neuregulin-1, a key axonal signal that drives Schwann cell growth and differentiation. *Glia*, 56(14), 1491-1497.
- Bosio, A., et al. (1996). Functional breakdown of the lipid bilayer of the myelin membrane in central and peripheral nervous system by disrupted galactocerebroside synthesis. *Proceedings of the National Academy of Sciences*, 93(23), 13280-13285.
- Boynton Jr, B. L., et al. (2007). Intraneural perineurioma: a systematic review with illustrative cases. *Archives of pathology & laboratory medicine*, 131(9), 1382-1392.
- Brady, S. (2005). *Basic neurochemistry: molecular, cellular and medical aspects*: Elsevier.
- Britsch, S., et al. (2001). The transcription factor Sox10 is a key regulator of peripheral glial development. *Genes Dev*, 15(1), 66-78. doi:10.1101/gad.186601
- Brown, M. (1997). Goldstein JL. *The SREBP pathway: regulation of cholesterol metabolism by proteolysis of a membrane-bound transcription factor*. *Cell*, 89, 331-340.
- Buchstaller, J., et al. (2004). Efficient isolation and gene expression profiling of small numbers of neural crest stem cells and developing Schwann cells. *J Neurosci*, 24(10), 2357-2365. doi:10.1523/JNEUROSCI.4083-03.2004
- Bunay, J., et al. (2020). Screening for Liver X Receptor modulators: where are we and for what use? *British Journal of Pharmacology*.
- Capodivento, G., et al. (2017). Sphingomyelin as a myelin biomarker in CSF of acquired demyelinating neuropathies. *Scientific reports*, 7(1), 1-9.
- Cassagne, C., et al. (1986). Fatty acid biosynthesis in the peripheral nervous system of normal and Trembler mice. *Biochimica et Biophysica Acta (BBA)-Lipids and Lipid Metabolism*, 875(3), 633-640.
- Cermenati, G., et al. (2012). Diabetes-induced myelin abnormalities are associated with an altered lipid pattern: protective effects of LXR activation. *J Lipid Res*, 53(2), 300-310.
- Cermenati, G., et al. (2013). Liver X receptors, nervous system, and lipid metabolism. *J Endocrinol Invest*, 36(6), 435-443. doi:10.3275/8941

- Cermenati, G., et al. (2010). Activation of the liver X receptor increases neuroactive steroid levels and protects from diabetes-induced peripheral neuropathy. *Journal of Neuroscience*, 30(36), 11896-11901.
- Chami, M., et al. (2017). Acid sphingomyelinase deficiency enhances myelin repair after acute and chronic demyelination. *PLoS One*, 12(6), e0178622.
- Chrast, R., et al. (2011). Lipid metabolism in myelinating glial cells: lessons from human inherited disorders and mouse models. *J Lipid Res*, 52(3), 419-434.
- Clark, J. K., et al. (2014). Mammalian Nkx2. 2+ perineurial glia are essential for motor nerve development. *Developmental Dynamics*, 243(9), 1116-1129.
- Coetzee, T., et al. (1996). Myelination in the absence of galactocerebroside and sulfatide: normal structure with abnormal function and regional instability. *Cell*, 86(2), 209-219.
- Cortes, V. A., et al. (2014). Physiological and pathological implications of cholesterol. *Front. Biosci*, 19, 416-428.
- Court, F. A., et al. (2006). Basal lamina: Schwann cells wrap to the rhythm of space-time. *Current opinion in neurobiology*, 16(5), 501-507.
- Courtney, R., et al. (2016). LXR regulation of brain cholesterol: from development to disease. *Trends in Endocrinology & Metabolism*, 27(6), 404-414.
- da Silva, T. F., et al. (2014). Peripheral nervous system plasmalogens regulate Schwann cell differentiation and myelination. *The Journal of clinical investigation*, 124(6), 2560-2570.
- De Preux, A.-S., et al. (2007). SREBP-1c expression in Schwann cells is affected by diabetes and nutritional status. *Molecular and Cellular Neuroscience*, 35(4), 525-534.
- Decker, L., et al. (2006). Peripheral myelin maintenance is a dynamic process requiring constant Krox20 expression. *J Neurosci*, 26(38), 9771-9779. doi:10.1523/jneurosci.0716-06.2006
- Demyelinating Disorders - Physiopedia.
- Dolores Ledesma, M., et al. (1999). Maturation of the axonal plasma membrane requires upregulation of sphingomyelin synthesis and formation of protein-lipid complexes. *The EMBO Journal*, 18(7), 1761-1771.
- Domènech-Estévez, E., et al. (2016). Akt regulates axon wrapping and myelin sheath thickness in the PNS. *Journal of Neuroscience*, 36(16), 4506-4521.
- Dong, Z., et al. (1999). Schwann cell development in embryonic mouse nerves. *Journal of neuroscience research*, 56(4), 334-348.
- Dykes, I. M., et al. (2011). Brn3a and Islet1 act epistatically to regulate the gene expression program of sensory differentiation. *Journal of Neuroscience*, 31(27), 9789-9799.
- Eid, S. A., et al. (2020). Targeting the NADPH Oxidase-4 and Liver X Receptor Pathway Preserves Schwann Cell Integrity in Diabetic Mice. *Diabetes*, 69(3), 448-464. doi:10.2337/db19-0517
- Emery, B. (2013). Playing the field: Sox10 recruits different partners to drive central and peripheral myelination. *PLoS Genet*, 9(10), e1003918. doi:10.1371/journal.pgen.1003918
- Erne, B., et al. (2002). Rafts in adult peripheral nerve myelin contain major structural myelin proteins and myelin and lymphocyte protein (MAL) and CD59 as specific markers. *Journal of neurochemistry*, 82(3), 550-562.
- Feltri, M. L., et al. (2016). How Schwann Cells Sort Axons: New Concepts. *The Neuroscientist : a review journal bringing neurobiology, neurology and psychiatry*, 22(3), 252-265. doi:10.1177/1073858415572361
- Feltri, M. L., et al. (2008). The function of RhoGTPases in axon ensheathment and myelination. *Glia*, 56(14), 1508-1517. doi:10.1002/glia.20752
- Fewou, S., et al. (2009). Functional dynamics of myelin lipids *Handbook of Neurochemistry and Molecular Neurobiology*.



- Fewou, S. N., et al. (2009). Functional Dynamics of Myelin Lipids\*. In A. Lajtha, G. Tettamanti, & G. Goracci (Eds.), *Handbook of Neurochemistry and Molecular Neurobiology: Neural Lipids* (pp. 239-265). Boston, MA: Springer US.
- Filbin, M. T., et al. (1990). Role of myelin Po protein as a homophilic adhesion molecule. *Nature*, *344*(6269), 871-872.
- Finzsch, M., et al. (2010). Sox10 is required for Schwann cell identity and progression beyond the immature Schwann cell stage. *J Cell Biol*, *189*(4), 701-712. doi:10.1083/jcb.200912142
- Fledrich, R., et al. (2018). Targeting myelin lipid metabolism as a potential therapeutic strategy in a model of CMT1A neuropathy. *Nature communications*, *9*(1), 1-14.
- Fressinaud, C., et al. (1986). Fatty acid composition of endoneurium and perineurium from adult rat sciatic nerve. *Journal of neurochemistry*, *46*(5), 1549-1554.
- Fressinaud, C., et al. (1987). Analysis of unsaturated fatty acids of endoneurium and perineurium from normal and degenerating rat sciatic nerve: Morphological correlations. *Journal of the neurological sciences*, *81*(1), 85-92.
- Fricker, F. R., et al. (2009). Sensory axon-derived neuregulin-1 is required for axoglial signaling and normal sensory function but not for long-term axon maintenance. *Journal of Neuroscience*, *29*(24), 7667-7678.
- Gabbi, C., et al. (2014). Action mechanisms of liver X receptors. *Biochemical and biophysical research communications*, *446*(3), 647-650.
- Gammill, L., et al. (2003). Neural crest specification: migrating into genomics. *Nature Reviews Neuroscience*, *4*, 795-805.
- Garbay, B., et al. (2000). Myelin synthesis in the peripheral nervous system. *Progress in neurobiology*, *61*(3), 267-304.
- Gault, C. R., et al. (2010). An overview of sphingolipid metabolism: from synthesis to breakdown. *Sphingolipids as signaling and regulatory molecules*, 1-23.
- Gerber, D., et al. (2021). Transcriptional profiling of mouse peripheral nerves to the single-cell level to build a sciatic nerve ATlas (SNAT). *Elife*, *10*, e58591.
- Giese, K. P., et al. (1992). Mouse P0 gene disruption leads to hypomyelination, abnormal expression of recognition molecules, and degeneration of myelin and axons. *Cell*, *71*(4), 565-576. doi:10.1016/0092-8674(92)90591-y
- Gilmore, I., et al. (2002). Electron flood gun damage in the analysis of polymers and organics in time-of-flight SIMS. *Applied surface science*, *187*(1-2), 89-100.
- Girault, J.-A., et al. (2002). Development of nodes of Ranvier. *Current opinion in neurobiology*, *12*(5), 476-485.
- Giuffre, B. A., et al. (2020). Anatomy, sciatic nerve. *StatPearls [Internet]*.
- Giussani, P., et al. (2020). The role of Sphingolipids in myelination and myelin stability and their involvement in childhood and adult demyelinating disorders. *Journal of neurochemistry*.
- Gould, R. M., et al. (1995). The number of Schmidt-Lanterman incisures is more than doubled in shiverer PNS myelin sheaths. *Journal of neurocytology*, *24*(2), 85-98.
- Hailemariam, T. K., et al. (2008). Sphingomyelin synthase 2 deficiency attenuates NFκB activation. *Arteriosclerosis, thrombosis, and vascular biology*, *28*(8), 1519-1526.
- Hall, B. K. (1999). *The neural crest in development and evolution*: Springer Science & Business Media.
- Hannun, Y. A. (1994). The sphingomyelin cycle and the second messenger function of ceramide. *The Journal of biological chemistry (Print)*, *269*(5), 3125-3128.
- Hayashi, A., et al. (2013). Sulfatide decrease in myelin influences formation of the paranodal axo-glial junction and conduction velocity in the sciatic nerve. *Glia*, *61*(4), 466-474.
- He, Y., et al. (2010). Yy1 as a molecular link between neuregulin and transcriptional modulation of peripheral myelination. *Nat Neurosci*, *13*(12), 1472-1480. doi:10.1038/nn.2686

- Heape, A., et al. (1986). A quantitative developmental study of the peripheral nerve lipid composition during myelinogenesis in normal and trembler mice. *Developmental Brain Research*, 25(2), 181-189.
- Heffernan, C., et al. (2017). Nectin-like 4 Complexes with Choline Transporter-like Protein-1 and Regulates Schwann Cell Choline Homeostasis and Lipid Biogenesis in Vitro. *J Biol Chem*, 292(11), 4484-4498. doi:10.1074/jbc.M116.747816
- Hichor, M., et al. (2017). Paraquat Induces Peripheral Myelin Disruption and Locomotor Defects: Crosstalk with LXR and Wnt Pathways. *Antioxid Redox Signal*, 27(3), 168-183. doi:10.1089/ars.2016.6711
- Hichor, M., et al. (2018). Liver X Receptor exerts a protective effect against the oxidative stress in the peripheral nerve. *Scientific reports*, 8(1), 1-13.
- Hoshi, T., et al. (2007). Nodal protrusions, increased Schmidt-Lanterman incisures, and paranodal disorganization are characteristic features of sulfatide-deficient peripheral nerves. *Glia*, 55(6), 584-594.
- Jacob, C., et al. (2014). HDAC1 and HDAC2 control the specification of neural crest cells into peripheral glia. *J Neurosci*, 34(17), 6112-6122. doi:10.1523/jneurosci.5212-13.2014
- Jaegle, M., et al. (2003). The POU proteins Brn-2 and Oct-6 share important functions in Schwann cell development. *Genes Dev*, 17(11), 1380-1391. doi:10.1101/gad.258203
- Jagalur, N. B., et al. (2011). Functional dissection of the Oct6 Schwann cell enhancer reveals an essential role for dimeric Sox10 binding. *Journal of Neuroscience*, 31(23), 8585-8594.
- Jessen, K. R., et al. (2005). The origin and development of glial cells in peripheral nerves. *Nature Reviews Neuroscience*, 6(9), 671-682.
- Jessen, K. R., et al. (2019). Schwann cell precursors; multipotent glial cells in embryonic nerves. *Frontiers in molecular neuroscience*, 12, 69.
- Joseph, N. M., et al. (2004). Neural crest stem cells undergo multilineage differentiation in developing peripheral nerves to generate endoneurial fibroblasts in addition to Schwann cells. *Development*, 131(22), 5599-5612.
- Kao, S. C., et al. (2009). Calcineurin/NFAT signaling is required for neuregulin-regulated Schwann cell differentiation. *Science*, 323(5914), 651-654. doi:10.1126/science.1166562
- Kim, T., et al. (1999). Myelin glycosphingolipid/cholesterol-enriched microdomains selectively sequester the non-compact myelin proteins CNP and MOG. *Journal of neurocytology*, 28(4), 281-293.
- Korach-Andre, M., et al. (2015). Liver X receptors as regulators of metabolism. *Biomol Concepts*, 6(3), 177-190. doi:10.1515/bmc-2015-0007
- Kucenas, S. (2015). Perineurial glia. *Cold Spring Harbor perspectives in biology*, 7(6), a020511.
- Kucenas, S., et al. (2008). CNS-derived glia ensheath peripheral nerves and mediate motor root development. *Nature neuroscience*, 11(2), 143-151.
- Kucenas, S., et al. (2009). A selective glial barrier at motor axon exit points prevents oligodendrocyte migration from the spinal cord. *Journal of Neuroscience*, 29(48), 15187-15194.
- Lajtha, A., et al. (2009). *Handbook of Neurochemistry and Molecular Neurobiology: Neural Lipids* (Vol. 14): Springer Science & Business Media.
- Lee, A. G. (2001). Myelin: delivery by raft. *Current Biology*, 11(2), R60-R62.
- Lee, J. (2011). Time-of-flight secondary ion mass spectrometry-fundamental issues for quantitative measurements and multivariate data analysis.
- Lee, S., et al. (2014). PMP22 is critical for actin-mediated cellular functions and for establishing lipid rafts. *J Neurosci*, 34(48), 16140-16152. doi:10.1523/JNEUROSCI.1908-14.2014
- Li, Z., et al. (2012). Impact of sphingomyelin synthase 1 deficiency on sphingolipid metabolism and atherosclerosis in mice. *Arteriosclerosis, thrombosis, and vascular biology*, 32(7), 1577-1584.
- Ma, Q., et al. (1999). Neurogenin1 and neurogenin2 control two distinct waves of neurogenesis in developing dorsal root ganglia. *Genes Dev*, 13(13), 1717-1728. doi:10.1101/gad.13.13.1717

- Makoukji, J., et al. (2011). Interplay between LXR and Wnt/beta-catenin signaling in the negative regulation of peripheral myelin genes by oxysterols. *J Neurosci*, *31*(26), 9620-9629. doi:10.1523/jneurosci.0761-11.2011
- Maldonado, E. N., et al. (2008). FA2H is responsible for the formation of 2-hydroxy galactolipids in peripheral nervous system myelin. *J Lipid Res*, *49*(1), 153-161.
- Mansuy-Aubert, V., et al. (2015). Loss of the liver X receptor LXR $\alpha/\beta$  in peripheral sensory neurons modifies energy expenditure. *Elife*, *4*, e06667.
- Marcus, J., et al. (2006). Sulfatide is essential for the maintenance of CNS myelin and axon structure. *Glia*, *53*(4), 372-381.
- Martini, R., et al. (1995). Mice doubly deficient in the genes for P0 and myelin basic protein show that both proteins contribute to the formation of the major dense line in peripheral nerve myelin. *J Neurosci*, *15*(6), 4488-4495. doi:10.1523/jneurosci.15-06-04488.1995
- Martini, R., et al. (1995). Protein zero (P0)-deficient mice show myelin degeneration in peripheral nerves characteristic of inherited human neuropathies. *Nature genetics*, *11*(3), 281-286.
- Maurel, P., et al. (2007). Nectin-like proteins mediate axon Schwann cell interactions along the internode and are essential for myelination. *J Cell Biol*, *178*(5), 861-874. doi:10.1083/jcb.200705132
- McDonnell, L. A., et al. (2007). Imaging mass spectrometry. *Mass spectrometry reviews*, *26*(4), 606-643.
- McFerrin, J., et al. (2017). NTE/PNPLA6 is expressed in mature Schwann cells and is required for glial ensheathment of Remak fibers. *Glia*, *65*(5), 804-816.
- Meffre, D., et al. (2015). Liver X receptors alpha and beta promote myelination and remyelination in the cerebellum. *Proc Natl Acad Sci U S A*, *112*(24), 7587-7592. doi:10.1073/pnas.1424951112
- Meier, C., et al. (1999). Developing Schwann cells acquire the ability to survive without axons by establishing an autocrine circuit involving insulin-like growth factor, neurotrophin-3, and platelet-derived growth factor-BB. *Journal of Neuroscience*, *19*(10), 3847-3859.
- Michailov, G. V., et al. (2004). Axonal neuregulin-1 regulates myelin sheath thickness. *Science*, *304*(5671), 700-703. doi:10.1126/science.1095862
- Monje, P. V. (2015). To myelinate or not to myelinate: fine tuning cAMP signaling in Schwann cells to balance cell proliferation and differentiation. *Neural Regen Res*, *10*(12), 1936-1937. doi:10.4103/1673-5374.169622
- Monk, K. R., et al. (2015). New insights on Schwann cell development. *Glia*, *63*(8), 1376-1393.
- Monk, K. R., et al. (2011). Gpr126 is essential for peripheral nerve development and myelination in mammals. *Development*, *138*(13), 2673-2680.
- Montani, L., et al. (2018). De novo fatty acid synthesis by Schwann cells is essential for peripheral nervous system myelination. *Journal of Cell Biology*, *217*(4), 1353-1368.
- Morell, P., et al. (1970). The biosynthesis by brain microsomes of cerebroside containing nonhydroxy fatty acids. *Archives of biochemistry and biophysics*, *141*(2), 738-748.
- Morell P., Q. R. (1999). Myelin Formation Structure and Biochemistry. In A. B. Siegel GJ, Albers RW, et al. (Ed.), *Basic Neurochemistry: Molecular, Cellular and Medical Aspects* (6th ed.). Philadelphia: Lippincott-Raven.
- Munro, S. (2003). Lipid rafts: elusive or illusive? *Cell*, *115*(4), 377-388.
- Naef, R., et al. (1998). Many facets of the peripheral myelin protein PMP22 in myelination and disease. *Microsc Res Tech*, *41*(5), 359-371. doi:10.1002/(sici)1097-0029(19980601)41:5<359::aid-jemt3>3.0.co;2-l
- Nave, K. A., et al. (2014). Myelination of the nervous system: mechanisms and functions. *Annu Rev Cell Dev Biol*, *30*, 503-533. doi:10.1146/annurev-cellbio-100913-013101
- Newbern, J., et al. (2010). Nrg1/ErbB signaling networks in Schwann cell development and myelination. *Semin Cell Dev Biol*, *21*(9), 922-928. doi:10.1016/j.semdb.2010.08.008

- Newbern, J. M., et al. (2011). Specific functions for ERK/MAPK signaling during PNS development. *Neuron*, 69(1), 91-105. doi:10.1016/j.neuron.2010.12.003
- Norrmén, C., et al. (2014). mTORC1 controls PNS myelination along the mTORC1-RXR $\gamma$ -SREBP-lipid biosynthesis axis in Schwann cells. *Cell reports*, 9(2), 646-660.
- Norton, W., et al. (1984). Isolation and characterization of myelin. Myelin. by Morell, P., Plenum, New York, 147-195.
- Noutsi, P., et al. (2016). Assessment of Membrane Fluidity Fluctuations during Cellular Development Reveals Time and Cell Type Specificity. *PLoS One*, 11(6). doi:10.1371/journal.pone.0158313
- O'Brien, J. S., et al. (1967). Lipid composition of myelin from the peripheral nervous system: intradural spinal roots. *Journal of neurochemistry*, 14(3), 357-365.
- Olkkonen, V. M., et al. (2012). Oxysterols and their cellular effectors. *Biomolecules*, 2(1), 76-103. doi:10.3390/biom2010076
- Paar, A. (2020). Atomic force microscopy (AFM). Retrieved from <https://wiki.anton-paar.com/en/atomic-force-microscopy-afm/>
- Parmantier, E., et al. (1999). Schwann cell-derived Desert hedgehog controls the development of peripheral nerve sheaths. *Neuron*, 23(4), 713-724.
- Patton, K. T., et al. (2018). *Anthony's Textbook of Anatomy & Physiology-E-Book*: Elsevier Health Sciences.
- Pertusa, M., et al. (2007). Transcriptional control of cholesterol biosynthesis in Schwann cells by axonal neuregulin 1. *J Biol Chem*, 282(39), 28768-28778. doi:10.1074/jbc.M701878200
- Poitelon, Y., et al. (2020). Myelin Fat Facts: An Overview of Lipids and Fatty Acid Metabolism. *Cells*, 9(4), 812.
- Pollari, E., et al. (2018). In Vivo Electrophysiological Measurement of Compound Muscle Action Potential from the Forelimbs in Mouse Models of Motor Neuron Degeneration. *JoVE (Journal of Visualized Experiments)*(136), e57741.
- Pratt, J. H., et al. (1969). Lipid class and fatty acid composition of rat brain and sciatic nerve in alloxan diabetes. *Diabetes*, 18(8), 556-561. doi:10.2337/diab.18.8.556
- Prendergast, A., et al. (2014). Neural crest cells and peripheral nervous system development *Neural crest cells* (pp. 255-286): Elsevier.
- Purves, D. (2018). *Neuroscience* (6th Edition ed.).
- Purves, D., et al. (2001). Increased conduction velocity as a result of myelination. *Neuroscience*.
- Raasakka, A., et al. (2020). How Does Protein Zero Assemble Compact Myelin? *Cells*, 9(8), 1832. doi:10.3390/cells9081832
- Radhakrishnan, A., et al. (2010). Chapter 298 - The SREBP Pathway: Gene Regulation through Sterol Sensing and Gated Protein Trafficking. In R. A. Bradshaw & E. A. Dennis (Eds.), *Handbook of Cell Signaling (Second Edition)* (pp. 2505-2510). San Diego: Academic Press.
- Richard, L., et al. (2012). Endoneurial fibroblast-like cells. *Journal of neuropathology and experimental neurology*, 71(11), 938-947.
- Richard, L., et al. (2014). Characterization of endoneurial fibroblast-like cells from human and rat peripheral nerves. *Journal of Histochemistry & Cytochemistry*, 62(6), 424-435.
- Rico, F., et al. (2005). Probing mechanical properties of living cells by atomic force microscopy with blunted pyramidal cantilever tips. *Physical Review E*, 72(2), 021914.
- Riebeling, C., et al. (2013). Ceramide in the regulation of neuronal development: two faces of a lipid *Madame Curie Bioscience Database [Internet]*: Landes Bioscience.
- Rigaud, M., et al. (2008). Species and strain differences in rodent sciatic nerve anatomy: implications for studies of neuropathic pain. *Pain*, 136(1-2), 188-201.
- Ross, M. A. (2014). Sciatic nerve *Encyclopedia of the Neurological Sciences* (pp. 110-111): Elsevier Inc.
- Rosso, G., et al. (2019). Mechanical changes of peripheral nerve tissue microenvironment and their structural basis during development. *APL bioengineering*, 3(3), 036107.

- Rosso, G., et al. (2014a). Unravelling crucial biomechanical resilience of myelinated peripheral nerve fibres provided by the Schwann cell basal lamina and PMP22. *Scientific reports*, 4, 7286.
- Rosso, G., et al. (2014b). Unravelling crucial biomechanical resilience of myelinated peripheral nerve fibres provided by the Schwann cell basal lamina and PMP22. *Scientific reports*, 4(1), 1-8.
- Rothe, T., et al. (1991). Uptake of endoneurial lipoprotein into Schwann cells and sensory neurons is mediated by low density lipoprotein receptors and stimulated after axonal injury. *Journal of neurochemistry*, 57(6), 2016-2025.
- Ruifrok, A. C., et al. (2001). Quantification of histochemical staining by color deconvolution. *Anal Quant Cytol Histol*, 23(4), 291-299.
- Saher, G., et al. (2009). Cholesterol regulates the endoplasmic reticulum exit of the major membrane protein P0 required for peripheral myelin compaction. *Journal of Neuroscience*, 29(19), 6094-6104.
- Saher, G., et al. (2011). Cholesterol: a novel regulatory role in myelin formation. *The Neuroscientist*, 17(1), 79-93.
- Saher, G., et al. (2015). Cholesterol in myelin biogenesis and hypomyelinating disorders. *Biochimica Et Biophysica Acta (BBA)-Molecular and Cell Biology of Lipids*, 1851(8), 1083-1094.
- Salzer, J., et al. (2016). Myelination. *Current Biology*, 26(20), R971-R975.
- Salzer, J. L. (2015). Schwann cell myelination. *Cold Spring Harb Perspect Biol*, 7(8), a020529. doi:10.1101/cshperspect.a020529
- Sancho, S., et al. (2001). Regulation of Schwann cell proliferation and apoptosis in PMP22-deficient mice and mouse models of Charcot–Marie–Tooth disease type 1A. *Brain*, 124(11), 2177-2187. doi:10.1093/brain/124.11.2177
- Schanthaveerappa, T., et al. (1962). A perineurial epithelium. *J. Cell Biol*, 14, 343-346.
- Schmitt, S., et al. (2015). Metabolism and functions of lipids in myelin. *Biochim Biophys Acta*, 1851(8), 999-1005. doi:10.1016/j.bbalip.2014.12.016
- Schreiner, S., et al. (2007). Hypomorphic Sox10 alleles reveal novel protein functions and unravel developmental differences in glial lineages. *Development*, 134(18), 3271-3281. doi:10.1242/dev.003350
- Schwenk, R. W., et al. (2010). Fatty acid transport across the cell membrane: regulation by fatty acid transporters. *Prostaglandins, Leukotrienes and Essential Fatty Acids (PLEFA)*, 82(4-6), 149-154.
- Seyer, A., et al. (2010). Localization of flavonoids in seeds by cluster time-of-flight secondary ion mass spectrometry imaging. *Analytical chemistry*, 82(6), 2326-2333.
- Shackelford, G., et al. (2013). Differential regulation of Wnt/beta-catenin signaling by Liver X Receptors in Schwann cells and oligodendrocytes. *Biochem Pharmacol*, 86(1), 106-114. doi:10.1016/j.bcp.2013.02.036
- Shackelford, G. G., et al. (2017). Liver X Receptors differentially modulate central myelin gene mRNA levels in a region-, age- and isoform-specific manner. *J Steroid Biochem Mol Biol*, 169, 61-68. doi:10.1016/j.jsbmb.2016.02.032
- Shan, Y., et al. (2015). The structure and function of cell membranes examined by atomic force microscopy and single-molecule force spectroscopy. *Chemical Society Reviews*, 44(11), 3617-3638.
- Shanthaveerappa, T., et al. (1966). Perineurial epithelium: a new concept of its role in the integrity of the peripheral nervous system. *Science*, 154(3755), 1464-1467.
- Shanthaveerappa, T. R., et al. (1966). Perineurial epithelium: a new concept of its role in the integrity of the peripheral nervous system. *Science*, 154(3755), 1464-1467. doi:10.1126/science.154.3755.1464
- Siegel, G. J. (1999). *Basic neurochemistry: molecular, cellular and medical aspects*.
- Sodhi, R. N. (2004). Time-of-flight secondary ion mass spectrometry (TOF-SIMS):—versatility in chemical and imaging surface analysis. *Analyst*, 129(6), 483-487.

- Sugden, M., et al. (2011). Time-of-flight secondary ion mass spectrometer: a novel tool for lipid imaging. *Clinical Lipidology*, 6(4), 437-445.
- Sundaram, V. K., et al. (2019). Liver X Receptors and Their Implications in the Physiology and Pathology of the Peripheral Nervous System. *Int J Mol Sci*, 20(17). doi:10.3390/ijms20174192
- Sundaram, V. K., et al. (2019). Liver X receptors and their implications in the physiology and pathology of the peripheral nervous system. *Int J Mol Sci*, 20(17), 4192.
- Svaren, J., et al. (2008). The molecular machinery of myelin gene transcription in Schwann cells. *Glia*, 56(14), 1541-1551. doi:10.1002/glia.20767
- Tahallah, N., et al. (2008). Lipid mapping in human dystrophic muscle by cluster-time-of-flight secondary ion mass spectrometry imaging. *J Lipid Res*, 49(2), 438-454. doi:10.1194/jlr.M700421-JLR200
- Taveggia, C., et al. (2005). Neuregulin-1 type III determines the ensheathment fate of axons. *Neuron*, 47(5), 681-694. doi:10.1016/j.neuron.2005.08.017
- Tawk, M., et al. (2011). Wnt/beta-catenin signaling is an essential and direct driver of myelin gene expression and myelinogenesis. *J Neurosci*, 31(10), 3729-3742. doi:10.1523/jneurosci.4270-10.2011
- Topilko, P., et al. (1994). Krox-20 controls myelination in the peripheral nervous system. *Nature*, 371, 796-799. doi:10.1038/371796a0
- Trapp, B. D., et al. (1978). Essential fatty acid deficiency and CNS myelin: Biochemical and morphological observations. *Journal of the neurological sciences*, 37(3), 249-266.
- Trapp, B. D., et al. (1995). Polarization of myelinating Schwann cell surface membranes: role of microtubules and the trans-Golgi network. *Journal of Neuroscience*, 15(3), 1797-1807.
- van Echten-Deckert, G., et al. (2006). Sphingolipid metabolism in neural cells. *Biochimica et Biophysica Acta (BBA)-Biomembranes*, 1758(12), 1978-1994.
- van Paassen, B. W., et al. (2014). PMP22 related neuropathies: Charcot-Marie-Tooth disease type 1A and Hereditary Neuropathy with liability to Pressure Palsies. *Orphanet journal of rare diseases*, 9, 38-38. doi:10.1186/1750-1172-9-38
- Verheijen, M. H., et al. (2009). SCAP is required for timely and proper myelin membrane synthesis. *Proceedings of the National Academy of Sciences*, 106(50), 21383-21388.
- Verheijen, M. H., et al. (2003). Local regulation of fat metabolism in peripheral nerves. *Genes & development*, 17(19), 2450-2464.
- Vickerman, J. C. (2011). Molecular imaging and depth profiling by mass spectrometry—SIMS, MALDI or DESI? *Analyst*, 136(11), 2199-2217.
- Viennois, E., et al. (2012). Selective liver X receptor modulators (SLiMs): what use in human health? *Molecular and cellular endocrinology*, 351(2), 129-141.
- Vogl, M. R., et al. (2013). Sox10 cooperates with the mediator subunit 12 during terminal differentiation of myelinating glia. *J Neurosci*, 33(15), 6679-6690. doi:10.1523/jneurosci.5178-12.2013
- Wahab, R., et al. (2016). *Protocols and Methods for Developing Green Immobilized Nanobiocatalysts for Esterification Reactions*.
- Wattenberg, B. W. (2019). Intra-and intercellular trafficking in sphingolipid metabolism in myelination. *Advances in biological regulation*, 71, 97-103.
- Willem, M., et al. (2006). Control of peripheral nerve myelination by the beta-secretase BACE1. *Science*, 314(5799), 664-666. doi:10.1126/science.1132341
- Woodhoo, A., et al. (2009). Notch controls embryonic Schwann cell differentiation, postnatal myelination and adult plasticity. *Nature neuroscience*, 12(7), 839-847. doi:10.1038/nn.2323
- Xue, J., et al. (2019). Sphingomyelin Synthase 2 Inhibition Ameliorates Cerebral Ischemic Reperfusion Injury Through Reducing the Recruitment of Toll-Like Receptor 4 to Lipid Rafts. *Journal of the American Heart Association*, 8(22), e012885.

- Zhou, Y., et al. (2020). Subcellular diversion of cholesterol by gain-and loss-of-function mutations in PMP22. *Glia*, 68(11), 2300-2315.
- Zhou, Y., et al. (2019). PMP22 regulates cholesterol trafficking and ABCA1-mediated cholesterol efflux. *Journal of Neuroscience*, 39(27), 5404-5418.
- Zöller, I., et al. (2008). Absence of 2-hydroxylated sphingolipids is compatible with normal neural development but causes late-onset axon and myelin sheath degeneration. *Journal of Neuroscience*, 28(39), 9741-9754.